J

Aramco
Journal
of **Technology**

J

Aramco
Journal
of Technology

Contents

Magnetically Labeled Hybrid Nanosurfactant for Upstream Oil and Gas Operations

Dr. Nouf M. AlJabri, Hussain A. Shateeb, Mustafa A. Alsaffar and Dr. Amr I. Abdel-Fattah

Abstract /

Nanoencapsulation and targeted chemical delivery techniques have transformed many fields, such as pharmaceutical drug delivery for medical treatment and diagnosis, and which can similarly transform several upstream oil and gas operations. This article describes the dual nanoencapsulation of superparamagnetic iron oxide nanoparticles (SPIONs) and petroleum sulfonate surfactants to produce a hybrid nanosurfactant in high salinity water (56,000 ppm) using an inexpensive, scalable, and straightforward synthesis protocol. This novel magnetically labeled nanofluid is designed to: (1) enhance the residual oil mobilization via altering the rock's wettability and reducing the interfacial tension (IFT), and (2) enable in situ monitoring of injected fluids when combined with electromagnetic surveys.

Nanofluids encapsulating a petroleum sulfonate surfactant and three different concentrations of 5-nm SPIONs were prepared using a two-step nanoencapsulation method. Both colloidal and chemical stability of the prepared formulations were tested at 90 °C for over a year. The results showed that all the formulations exhibited remarkable long-term colloidal and chemical stability under these close-to-reservoir conditions. Transmission electron microscopy (TEM) images confirmed the encapsulation of the SPIONs.

The SPION's nanofluids have successfully reduced the IFT between the crude oil and water by more than three orders of magnitude — from ~25 mN/m down to ~0.01 mN/m. These IFT and stability results demonstrate a strong synergy between the SPIONs and the petroleum sulfonate surfactant. It is worth noting that this novel encapsulation platform enables the encapsulation of a wide range of nanoparticles to generate a library of multifunction nanofluids to support several upstream applications.

Introduction

The unique properties of nanoparticles, such as high surface-to-volume, nano-size, and potential compatibility with subsurface fluids attracted considerable attention to improving the chemical enhanced oil recovery (EOR) either as additives or as nanofluid flooding[1, 2]. Nanofluids are fluids that consist of nanoparticles of one phase (solid, liquid, or gas) suspended in continuous medium of another phase to form chemically and colloidally stable dispersions. The carrier medium is usually comprised of aqueous or low thermoconductive fluids, while the dispersed phase of nanoparticles may vary from metal oxides to carbon-based nanoparticles, to carbides. The nanofluids' novel properties have prospered with many subsurface applications such as improving heavy oil production[3], EOR[4, 5], and boosting the fracturing fluid properties[6].

The oil mobilization using nanofluid flooding has been widely studied, and many plausible mechanisms are proposed in the literature. These mechanisms are: The rocks' wettability alteration, interfacial tension (IFT) reduction, disjoining pressure, and in situ Pickering emulsion. The disjoining pressure in porous media to mobilize the residual oil is proposed as a mean plausible mechanism during nanofluid flooding[1, 7]. In this mechanism, nanoparticles form a wedge film at the interface between the oil and rocks' surface, which allows for increasing the disjoining pressure and releasing the oil from the surface.

Other studies have investigated the synergy effect between the nanoparticles and the base fluid, which leads to reduce the IFT significantly beyond the values of using nanoparticles or surfactants alone[8, 9]. The repulsive interactions between nanoparticles and surfactants force surfactants to be located at the interface, rather than to stay in the solution, leading to lower IFT than the use of surfactant or nanoparticles. It is important to note that at high salinity ($\geq$ 25,000 ppm) the ions will diminish this effect due to the ion's influence on the nanoparticle's surface charge.

An alternative mechanism, which also may play a possible role in the synergistic effect, is the effect of zwitterionic surfactants or Janus nanoparticles[10]. In this situation, the dual functionality and anisotropic properties of nanoparticles will enable the nanoparticles' selective adsorption at the interface[11, 12].

Figure 1 is an illustration of the proposed mechanisms of oil displacements using nanofluids.

Among nanoparticles, the superparamagnetic iron oxide nanoparticles (SPIONS) exhibit unique properties that can be exploited for several reservoir applications such as fluid mapping, IFT reduction, and rock surface wettability alteration. They are difficult to remain suspended in high salinity formation water. This work demonstrates the use of a nanosurfactant as a base fluid to produce smart nanofluid, through encapsulation of SPIONs within the oil core of nanosurfactant droplets. In this work, we developed the magnetically labeled nanofluid using an inexpensive and straightforward synthesis route. Interestingly, the SPION's nanofluid exhibited remarkable colloidal stability at 90 °C and in 56,000 ppm for over a year. Transmission electron microscopy (TEM) results confirmed the encapsulation of five SPIONs into nanosurfactant droplets. The SPIONs' nanofluid showed a significant reduction in IFT compared to a conventional nanosurfactant.

Experimental Work

Material

Uncoated iron oxide nanoparticles (IONPs), with average particles of 50 nm, were used in this study. Also, SPIONs (5 nm, 5 mg/mL) in toluene were purchased from Millipore Sigma. The magnetization of the SPIONs for 5 nm is ≥ 30 emu/g (at ambient temperature under 4,500 Oe). The SPIONs were hydroponically coated to allow their solubility in oil/internal phase of nanosurfactant for an efficient encapsulation. Petronate HL/L (61 wt% active) as petroleum sulfonate surfactant was obtained from Sonneborn.

The co-surfactant used is a zwitterionic cocamidopropyl hydroxysultaine surfactant (Cola®Teric CBS), with 48 wt% of active ingredients without further purification. A brine analogue (around 60,000 mg/L of total dissolved solids) was used to synthesize the base fluid as well as to test the high salinity impact on the formulations.

Encapsulation of SPIONS into Nanosurfactant

The IONPs, at different concentrations, were encapsulated into nanosurfactants to produce three nanofluid formulations. Different volumes of IONP solutions (0.3 mL, 0.6 mL, and 0.9 mL) were added to 5.0 wt% of Petronate HL/L, which followed with the addition of deionized (DI) water (5.6 mL). To prepare the nanofluid, 1.0 mL of the HL/L IONPs phase was added to 1.5 mL of the CBS solution phase (4.0 wt%), and mixed for 5 minutes before the addition of 52.0 mL of brine analogue, Fig. 2. To optimize the encapsulation and maximize the colloidal stability, we have explored particles' encapsulation out of oil cores, an external encapsulation method (EEM). This was produced similarly to the aforementioned approach except that the particles were added to the CBS phase, not to the HL/L.

To maximize the encapsulation efficiency, 5 nm SPIONs were encapsulated into nanosurfactant droplets. For that, 5 nm SPIONs in toluene (5 mg/mL) were mixed at different ratios with as received Petronate HL/L, Table 1. The toluene was removed from the

Fig. 1 *An illustration of the proposed mechanisms of oil displacements using nanofluids.*
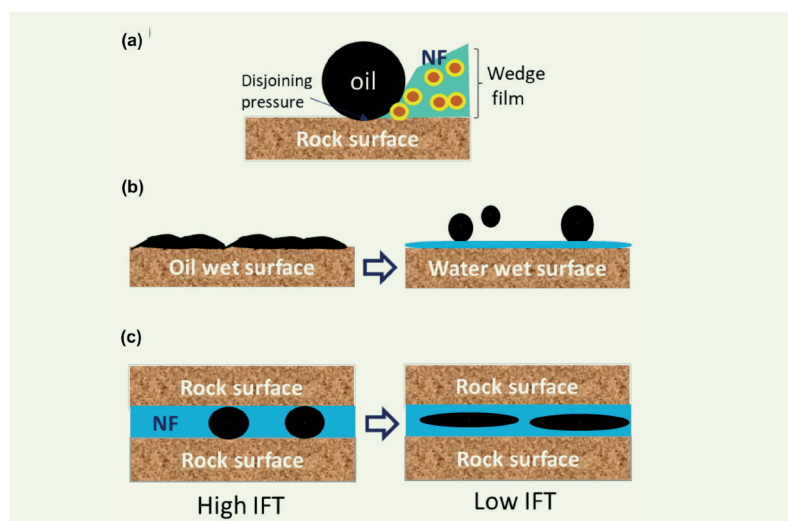
Fig. 2 *A schematic of (a) internal encapsulation, and (b) external encapsulation methods.*
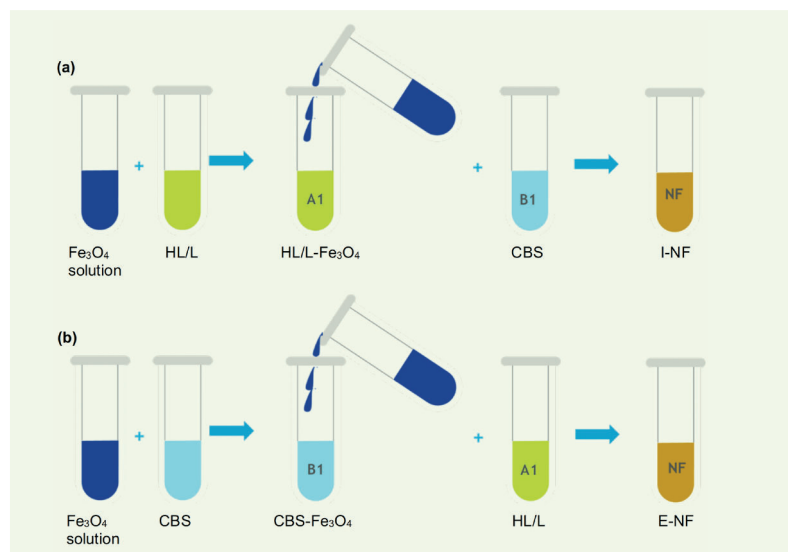
mixture and residue dried at 95 °C overnight to eliminate any possible impact of toluene on the IFT. DI water (5.6 mL) was added to the HL/L encapsulated SPIONs to complete the first step of the encapsulation. Then, the surfactant phase was prepared by dissolving 0.49 g of CBS (48 wt% active ingredient) in 6.0 mL of DI water. Both phases were mixed separately at the ambient condition until each solution become homogeneous. To prepare the nanofluid, 1.0 mL of the HL/L SPIONs phase was added to 1.5 mL of the CBS phase and mixed for 5 minutes before the addition of 52.0 mL of brine analog.

Table 1 *The amount of 5 nm SPIONS in Petronate HL/L (surfactant phase).*

Sample ID	Petronate HL/L (g)	5 nm SPIONs*(mL)	wt% of SPIONs in 5 wt% Petronate HL/L Solution
Nanofluid-1	0.5	0.3	0.02
Nanofluid-2	0.5	0.6	0.039
Nanofluid-3	0.5	0.9	0.083

Cryogenic TEM (Cryo-TEM)

As-prepared nanofluids were drop-cast on a copper grid with 1.2 μm holes on a 5 nm carbon support film substrate. Plunge freezing was performed on a Gatan CP3 Cryoplunge at Harvard University's Center of Nanoscale Systems (CNS) using liquid ethane as the cryogen. Samples were imaged on FEI Tecnai Arctica Cryo-TEM at the Harvard CNS at 200 kV accelerating voltage.

IFT Measurements

The impact of the nanofluids on the oil mobility was determined by measuring the IFT values after treating the samples with I-NF-1, I-NF-2, I-NF-3, and E-NF-1, E-NF-2, E-NF-3, respectively. The IFT study was conducted using a KRÜSS Spinning Drop Tensiometer. Crude oil (0.8908 g/ml) was used and the temperature was fixed at 90.0 ± 0.4 °C. Each nanofluid was filled in the capillary tube, followed with introducing the filtered crude oil. The oil droplet's diameter was measured every two minutes for 30 minutes.

Results and Discussions

Encapsulation Method Evaluation

Similar to any EOR fluid, nanofluid chemical/colloidal stability is a crucial element that should be evaluated before the injection in the reservoir. The nanofluid's stability is influenced by the particles' charge, size, concentrations, and encapsulation compartment space. Therefore, we designed and evaluated two possible encapsulation methods to produce nanofluid with maximum encapsulation efficiency and stability.

The internal encapsulation method (IEM) strives to encapsulate nanoparticles in the oil core of the nanosurfactant droplets. In contrast, the EEM is designed to encapsulate the nanoparticles outside of the oil cores. The IONP's size was fixed at 50 nm with the IONP concentrations of 0.02 wt%, 0.04 wt%, and 0.08 wt%, respectively. Three samples, namely, I-NF-1, I-NF-2, and I-NF-3 were prepared using IEM, and the other three, E-NF-1, E-NF-2, and E-NF-3, were prepared by the EEM.

All the prepared nanofluids were incubated at 90 °C, photographed, and monitored to record any physical change. Notably, the EEM yielded unstable colloids despite the IONP's concentration. After 24 hours of incubation, samples E-NF-1, E-NF-2, and E-NF-3 exhibited aggregation, which become a complete phase separation after three days only, Fig. 3. This aggregation is attributed to the incomplete encapsulations of SPIONs in the aqueous phase of the nanosurfactant. Also, encapsulating SPIONs in the CBS phase has influenced the rheological properties of the co-surfactant and disturbed the nanofluid stability accordingly.

The IEM resulted in remarkably stable nanofluids during the initial stability at 90 °C, Fig. 4. The IONP's size was fixed at 50 nm with the IONP concentrations of 0.02 wt%, 0.04 wt%, and 0.08 wt%, respectively. To extend the phase behavior study, the nanofluids were transferred to tightly sealed pressure tubes and incubated in an oven at 90 °C. The SPION's nanofluids stability was checked and photographed regularly, and interestingly, all the samples showed long-term stability.

This can be explained by encapsulating the particles in the oil core of the nanosurfactant, providing enough shell to protect the particles from the extreme conditions and high ion concentration. Therefore, the IEM was selected as an optimum encapsulation method to produce high salinity and high temperature stable nanofluids.

Fig. 3 *Images of the three nanofluid formulations prepared by the EEM of IONPs in the CBS phase: (a) t = 0 h, (b) t = 24 h, (c) t = 48 h, and (d) 72 h.*
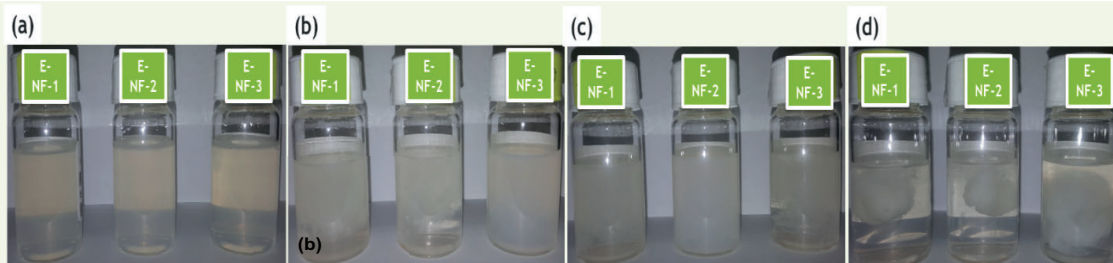
Fig. 4 *Images of the three nanofluid formulations prepared by the IEM of IONPs in the HL/L phase: (a) t = 0 h, (b) t = 24 h, (c) t = 48 h, and (d) 72 h.*
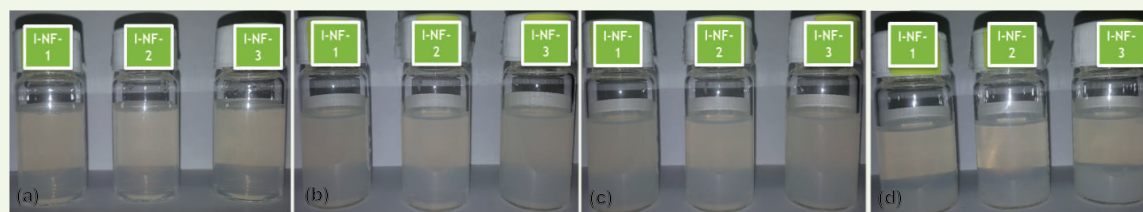
IFT Measurements

The presence of IONPs in the nanosurfactant's droplets is expected to alter the surfactant's rheological properties, therefore, lower IFT values can be achieved compared to conventional nanosurfactants. The IFT measurements between crude oil and the prepared nanofluids were conducted using a spinning drop tensometer. The results confirmed a significant reduction in IFT values when the nanofluids were introduced. I-NF-1, I-NF-2, and I-NF-3 have successfully reduced the IFT to 0.021 mN/m, 0.018 mN/m, and 0.022 mN/m, respectively, Fig. 5.

Interestingly, the nanofluids lowered the IFT 50% less than the nanosurfactant alone or particles alone, confirming the synergy between the nanosurfactants and IONPs. Notably, increasing the IONP's concentration beyond 0.02 wt% did not contribute to a further reduction in the IFT values, indicating that the 0.02 wt% is the optimum concentration.

Loading Efficiency Optimization

To increase the IONP's loading in the nanosurfactant's oil droplets, we further reduced the particle size from 50 nm, as an average, to 5 nm. The formulations were prepared by encapsulating 0.02 wt%, 0.04 wt%, and 0.08 wt% of five SPIONs using the aforementioned IEM. All the formulations, despite the SPION's concentrations and sizes, exhibited colloidal and chemical stability after 11 months at 90 °C, Fig. 6.

To ensure a fair comparison, we fixed all the parameters, including particle concentration (0.04 wt%) and varied the particle size only to analyze the size effect on the loading efficacy, and therefore on the IFT. Figure 7 shows the impact of the particle's size on the IFT and the synergy between the nanosurfactant and the IONPs. The IFT significantly decreased to 0.02 mN/m compared to 0.04 mN/m in the case of using the nanosurfactant only. Reducing the particle size from 50 nm to 5 nm has successfully reduced the IFT to 0.01 mN/m. This result suggests that more of the SPIONs were encapsulated in the nanosurfactant droplets, which improved the synergic effect. These results confirm the nanofluid's potential for EOR applications.

Cryo-TEM Characterization

Nanofluid flooding is one of the most economical utilizations of nanoparticles in EOR due to the synergic effect between the particles and base fluids. In this

Fig. 5 *The IFT results of I-NF-1, I-NF-2, and I-NF-3, successfully reduced to 0.021 mN/m, 0.018 mN/m, and 0.022 mN/m, respectively.*
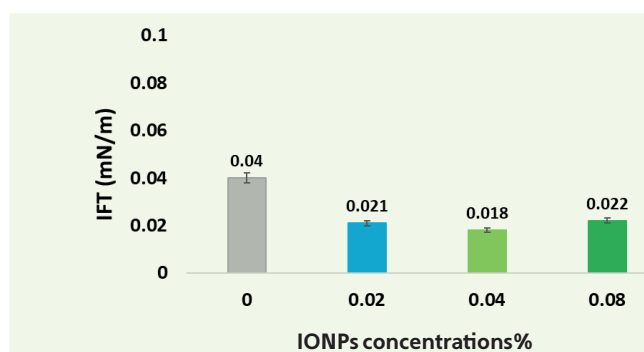
Fig. 6 *Images of the three nanofluid formulations prepared by the IEM of the SPIONs at 5 nm.*
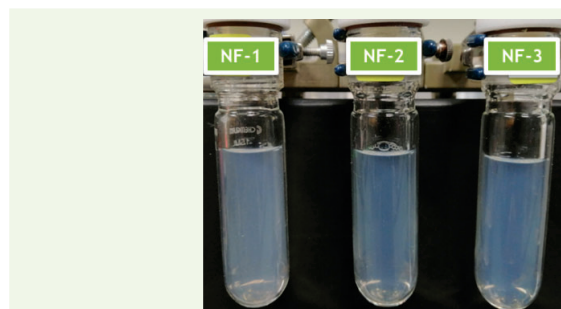
work, the superior performance and remarkable stability of the nanofluids are owing to the presence of IONPs/SPIONs in the nanosurfactant droplets. We characterized nanofluids using cryo-TEM to confirm the encapsulation of the IONPs/SPIONs. The SPIONs encapsulated free nanosurfactant shows some multilayer oil swollen micelles attributed to the coalescence of smaller nanosurfactant vesicles together, Fig. 8a. The nanofluids' images confirmed the SPIONs encapsulation within the nanosurfactant droplets, and in some cases, it was observed that multiple SPIONs were encapsulated in one nanosurfactant droplet, Fig. 8b.

Fig. 7 *The impact of the particle's size on the IFT and the synergy between the nanosurfactant and the IONPs.*
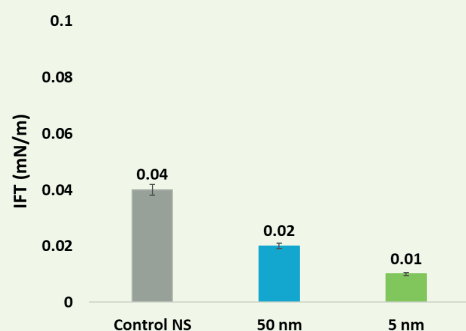
Fig. 8 *A cryo-TEM image of (a) SPIONs free nanofluid, and (b) SPIONs nanofluid image included to demonstrate some newly observed structures. The nanosurfactant in the middle has a smaller sphere encapsulated within a larger sphere (size ~40 nm) (not all of the IONPs are demonstrated with arrows). The total concentration of the IONPs in the image are equal to 0.003 wt%.*
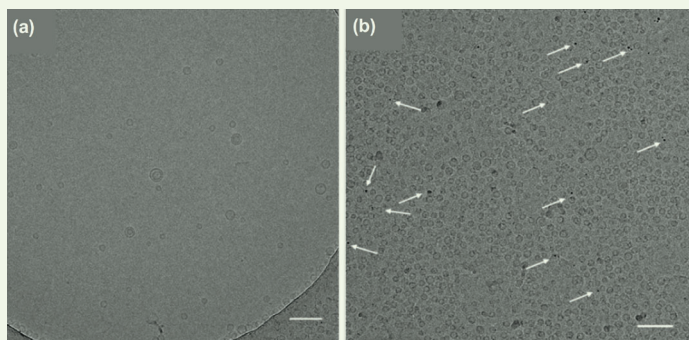
This observation is in alignment with the reduction in IFT values after reducing the particle size to 5 nm. It is important to note that the cryo-TEM cannot be provided with a higher resolution and it is hard to distinguish smaller than 5 nm SPIONs within the nanosurfactant core, due to the technique limitations. It is not possible to obtain all SPION encapsulated nanofluids in a focal plane, as the samples are beam sensitive. Therefore, a large number of the encapsulated SPIONs are potentially out of the focus plane and were not visible.

Conclusions

We report the synthesis of SPION encapsulated nanofluids using two different encapsulation procedures for reservoir applications. We studied the influence of particle size, coating, and the concentration of the SPION's particles on the nanofluid's stability and ability to reduce the crude oil/water IFT. Cryo-TEM images confirmed the encapsulation of SPIONs in the nano-sized oil droplets. The phase behavior and IFT results indicated the synergy between the SPIONs and

the petroleum sulfonate surfactant in the prepared nanofluids. The IFT value was decreased to 0.01 mN/m at 0.04 wt% of the 5 nm SPION concentration.

Our findings suggest that the size of the SPIONS has no direct influence on the nanofluid's colloidal stability while beneficially affecting its ability to mobilize oil. In-depth analysis is ongoing to understand the type of synergy between the magnetic nanoparticles and the petroleum sulfonate surfactant. Based on the IFT reduction and remarkable colloidal stability of the investigated nanofluids under close to reservoir condition, we believe that they can be utilized for a number of reservoir applications. This outlined encapsulation method can be generalized to synthesize multiple nanofluids with a variety of surfactants and nanoparticles.

Acknowledgments

References

1. Rezk, M.Y. and Allam, N.K.: "Impact of Nanotechnology on Enhanced Oil Recovery: A Mini-Review," *Industrial & Engineering Chemistry Research*, Vol. 58, Issue 36, August 2019, pp. 16287-16295.

2. Druetta, P. and Picchioni, F.: "Polymer and Nanoparticles Flooding as a New Method for Enhanced Oil Recovery," *Journal of Petroleum Science and Engineering*, Vol. 177, June 2019, pp. 479-495.

3. Alomair, O.A., Matar, K.M. and Alsaeed, Y.H.: "Nanofluids Application for Heavy Oil Recovery," SPE paper 171539, presented at the SPE Asia Pacific Oil and Gas Conference and Exhibition, Adelaide, Australia, October 14-16, 2014.

4. Pereira, A.O. and Miranda, C.R.: "Exploring the Potentialities of Nanoscience to Enhanced Oil Recovery Process: A Multiscale Computational Approach," OTC paper 26241, presented at the Offshore Technology Conference Brasil, Rio de Janeiro, Brazil, October 27-29, 2015.

5. Hendraningrat, L., Engeset, B., Suwarno, S. and Torsæter, O.: "Improved Oil Recovery by Nanofluids Flooding: An Experimental Study," SPE paper 163335, presented at the SPE Kuwait International Petroleum Conference and Exhibition, Kuwait City, Kuwait, December 10-12, 2012.

6. Fakoya, M.F. and Shah, S.N.: "Effect of Silica Nanoparticles on the Rheological Properties and Filtration Performance of Surfactant-Based and Polymeric Fracturing Fluids and Their Blends," *SPE Drilling & Completion*, Vol. 33, Issue 2, June 2018, pp. 100-114.

7. Wasan, D., Nikolov, A. and Kondiparty, K.: "The Wetting and Spreading of Nanofluids on Solids: Role of the Structural Disjoining Pressure," *Current Opinion in Colloid & Interface Science*, Vol. 16, Issue 4, August 2011, pp. 344-349.

8. Vatanparast, H., Shahabi, F., Bahramian, A., Javadi, A., et al.: "The Role of Electrostatic Repulsion on Increasing Surface Activity of Anionic Surfactants in the

Presence of Hydrophilic Silica Nanoparticles," *Scientific Reports*, Vol. 8, Issue 1, May 2018.

9. Betancur Márquez, S., Giraldo Pedroza, L.J., Carrasco-Marín, F., Riazi, M., et al.: "Importance of the Nanofluid Preparation for Ultra-Low Interfacial Tension in Enhanced Oil Recovery Based on Surfactant-Nanoparticle-Brine System Interaction," *ACS Omega*, Vol. 4, Issue 14, September 2019, pp. 16171-16180.

10. Wu, H., Gao, K., Lu, Y., Meng, Z., et al.: "Silica-Based Amphiphilic Janus Nanofluid with Improved Interfacial Properties for Enhanced Oil Recovery," *Colloids and Surfaces A: Physicochemical and Engineering Aspects*, Vol. 586, February 2020.

11. Zhang, L., Lei, Q., Luo, J., Zeng, M., et al.: "Natural Halloysites-Based Janus Platelet Surfactants for the Formation of Pickering Emulsion and Enhanced Oil Recovery," *Scientific Reports*, Vol. 9, Issue 1, January 2019.

12. Wang, K., Wang, G., Lu, C. and Wang, Y.: "Preparation of Amphiphilic Janus Particles and Their Application in Stabilizing Foams," *Micro & Nano Letters*, Vol. 13, Issue 3, December 2017, pp. 397-402.

About the Authors

Dr. Nouf M. AlJabri

Ph.D. in Chemical Engineering, King Abdullah University of Science and Technology

Dr. Nouf M. AlJabri is a Geophysicist with the Reservoir Engineering Technology Division at Saudi Aramco's Exploration and Petroleum Engineering Center – Advanced Research Center (EXPEC ARC). Nouf is spearheading the efforts to design and synthesize novel advanced materials to resolve key upstream challenges.

Previously, she was a visiting scientist working with Professor Timothy M. Swager at MIT.

Nouf received her M.S. degree and Ph.D. degree in Chemical Engineering from King Abdullah University of Science and Technology (KAUST), Thuwal, Saudi Arabia.

She is the recipient of several prestigious international awards.

Hussain A. Shateeb

A.S. in Industrial Chemistry Technology, Jubail Industrial College

Hussain A. Shateeb joined Saudi Aramco as an Apprentice Technician in the Vocational College Graduates (VCGNE) Training Program in August 2014. Upon attaining his degree in 2016, he then then joined the Reservoir Engineering Technology Division of Saudi Aramco's Exploration and Petroleum Engineering Center – Advanced Research Center (EXPEC ARC), where he works as a Lab Technician.

Hussain received his A.S. degree in Industrial Chemistry Technology from Jubail Industrial College, Jubail, Saudi Arabia.

Mustafa A. Alsaffar

A.S. in Industrial Chemistry Technology, Jubail Industrial College

Mustafa A. Alsaffar joined Saudi Aramco as an Apprentice Technician in the Vocational College Graduates (VCGNE) Training Program in 2011. Upon attaining his degree, he then then joined the Reservoir Engineering Technology Division of Saudi Aramco's Exploration and Petroleum Engineering Center – Advanced Research Center (EXPEC ARC), where he is a Lab Technician working mainly on the synthesizing and characterization of nanomaterials.

Mustafa received his A.S. degree in Industrial Chemistry Technology from Jubail Industrial College, Jubail, Saudi Arabia.

Dr. Amr I. Abdel-Fattah

Ph.D. in Chemical Engineering, University of New Mexico

Dr. Amr I. Abdel-Fattah is a Petroleum Engineering Consultant and Team Leader of the In-Situ Sensing and Intervention focus area in Saudi Aramco's Exploration and Petroleum Engineering Center – Advanced Research Center (EXPEC ARC). He joined EXPEC ARC's Reservoir Engineering Technology Division in late 2012 after working 16 years with the Los Alamos National Laboratory in New Mexico, U.S., where he reached a Senior Scientist status. Amr is currently spearheading a number of research and technology development programs in EXPEC ARC geared at utilizing nanotechnology for upstream oil and gas applications.

He has over 35 years of experience in subsurface energy and environmental applications of nanotechnology, colloid and interface science, and electrokinetics. Amr is a Society of Petroleum Engineers (SPE) Distinguished Lecturer, a founding Board Member of the International Association of Electrokinetics, a U.S. Representative on the International Board of Electrokinetics, a Technical Member on the Science Advisory Board of the International Association of Colloid and Interface Scientists, and a Guest Editor for the international *Journal of Colloids and Surfaces A*, and *Frontiers in Energy Research*.

He has published numerous papers in international journals, including some of the world's premier and most cited journals, and delivered numerous plenary and invited talks and lectures worldwide. Amr chaired the International Electrokinetics Conference in Santa Fe, NM, in 2008, in addition to several international workshops and conference sessions in the U.S., Canada, and Europe since 2005.

He received his B.S. degree in Civil Engineering and an M.Eng. in Geotechnical Engineering from Ain Shams University, Cairo, Egypt. Amr received his M.S. degree and his Ph.D. degree in Chemical and Nuclear Engineering from the University of New Mexico, Albuquerque, NM.

Thermochemical Pulse Fracturing of Tight Gas: Investigation of Pulse Loading on Fracturing Behavior

Ayman R. Al-Nakhli, Dr. Zeeshan Tariq, Dr. Mohamed Mahmoud and Dr. Abdulazeez Abdulraheem

Abstract /

Unconventional and tight gas reservoirs are located in deep and competent formations, which requires massive fracturing activities to extract hydrocarbons. Some of the persisting challenges faced by operators are either canceled or nonproductive fractures. Both challenges force oil companies to drill new substitutional wells, which will increase the development cost of such reservoirs.

A novel fracturing method was developed based on thermochemical pressure pulses. Reactive material of exothermic components are used to generate in situ pressure pulses, which are sufficient to create fractures. The reaction can vary from low-pressure pulses, to a very high loading — up to 20,000 psi — with short pressurization time.

In this study, finite element modeling (FEM) was used to investigate the impact of the generated pressure pulse load, by chemical reaction, on the number of induced fractures and fracture length. Actual tests of pulsed fracturing were conducted in lab-scale using several block samples compared with modeling work. There was a great relationship between the pressure load and fracturing behavior. The greater the pulse load and pressurization rate, the greater the number of created fractures, and the longer the induced fractures.

The developed novel fracturing method will increase stimulated reservoir volume of unconventional gas without introducing a lot of water into the formation. The new method can reduce formation breakdown pressure by approximately 70%, which will minimize the number of canceled fracturing.

Introduction

The continuous demand and increase on fossil fuels has made unconventional gas an attractive energy resource to support industrial development. Unconventional reservoirs are located in deep tight formations, which require special stimulation techniques to ensure economical production. The development progress in drilling, completion, and fracturing techniques made commercial production from such tight resources a game changer for reserves. As the formation is very tight, multistage fracturing was introduced to increase gas production from each well; however, more techniques need to be developed to improve permeability around induced fractures. Having such reservoirs in deep formations — with high stress — makes it very difficult to fracture using the conventional hydraulic fracturing method[1].

Unconventional gas is located in deep, tight, and highly stressed reservoirs. This resulted in three main challenges, which are high breakdown pressure, low drainage area around a fracture, and high drilling and completion costs. A low drainage area forces a gas producer to carry out horizontal drilling, and multistage fracturing that can reach up to 200 stages per well. A high breakdown pressure forces an operator to increase the completion pressure rating to manage fracturing such reservoirs. Even with a high rating, approximately 30% of the wells are annually canceled worldwide, due to high breakdown pressure that cannot be met with hydraulic fracturing[2].

There are mainly four types of cost associated with the development of tight gas wells, namely drilling and completion, fracturing, labor, and steel, Fig. 1[3]. With the development of horizontal drilling, fracturing activities are increasing, which represents 34% of the total cost. Subsequently, if the operator failed to fracture a well, the cost will be 100%, with the charges of drilling a replacement well. Locked potential is also another uncounted cost. Keeping in mind that approximately 30% of tight and unconventional gas wells are not productive globally, the costs of canceled fracturing turned out to be very high.

Discussion

Limitation of Hydraulic Fracturing

Currently, there is no foreseen or practical solution to overcome high breakdown pressure, which results in the cancelation of numerous fracturing jobs around the globe.

During the injection test, Fig. 2, slurry was pumped at 15 barrels per minute (bpm) with a wellhead pressure

The breakdown of the four main types of costs in the U.S. associated with the development of tight gas wells[3].
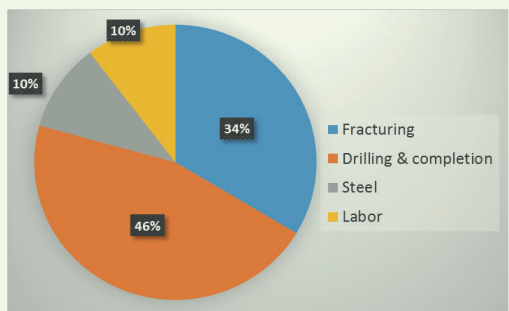
of 12,800 psi, and a downhole pressure of 18,700 psi. During the main hydraulic fracturing stage, Fig. 3, the pumping rate was increased to 20 bpm at a wellhead pressure of 13,800 psi. The bottom-hole pressure was approximately 19,000 psi, which was below the breakdown pressure required to initiate a fracture. Pumping was then canceled, due to reaching the completion limitation of 15,000 psi.

Fracturing Fundamentals and Development

Since the 1960s, there are fundamentally three types of formation fracturing: hydraulic fracturing, gas pulse, and explosives, Fig. 4[4]. Hydraulic fracturing is based on pumping a large amount of water into the formation to induce fractures. This type of fracturing is safe, and easy to apply. Consequently, one of the disadvantages of

Fig. 2 *A typical example of an injection test during hydraulic fracturing.*
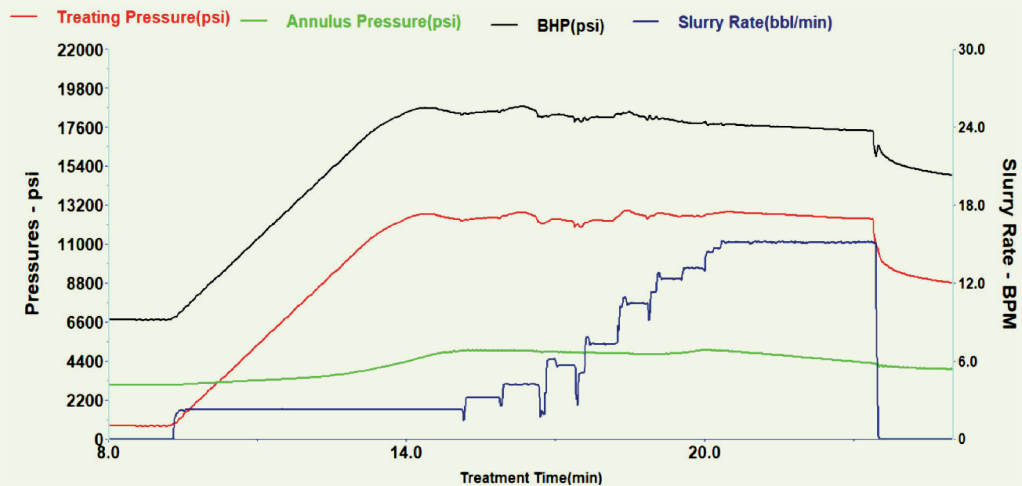
Fig. 3 *A typical example of a canceled hydraulic fracturing job, due to high breakdown pressure.*
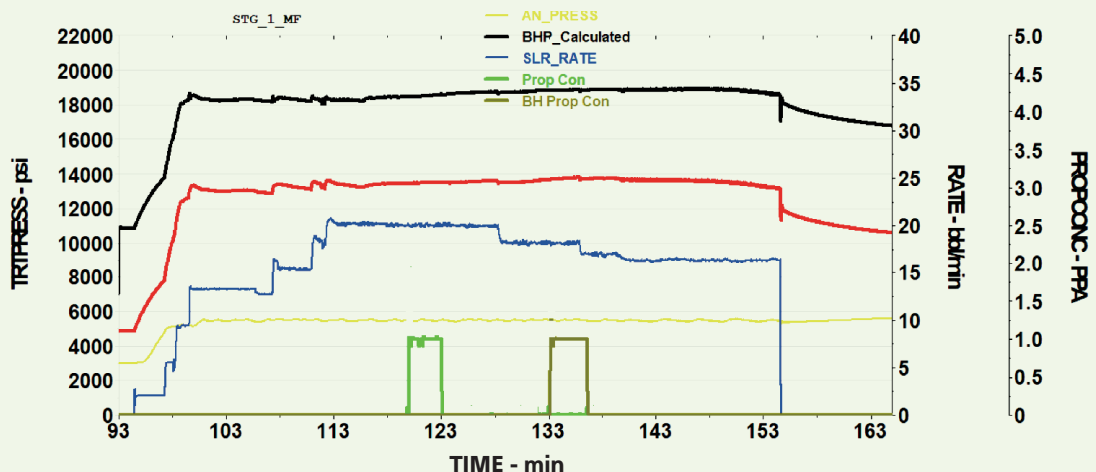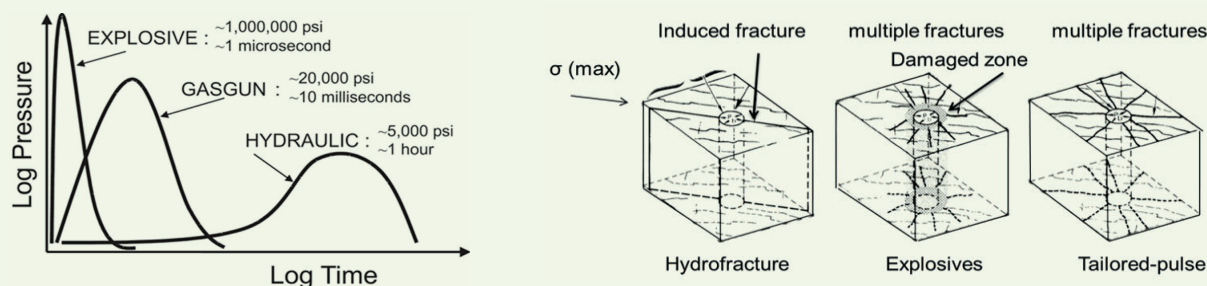
hydraulic fracturing in a tight formation, is the hydraulic pressure limitation that results in several fracturing cancelations. Moreover, fracturing fluid, whether slick water or cross-linked gel, is a damaging material for the formation. Introducing such fluid to a very tight formation can create water blockage and prevent gas transmissibility from a reservoir to an induced fracture[5].

During hydraulic fracturing, fluid is pumped from the surface with high pressure until a fracture is introduced in the formation and propagates to several hundred feet. Another type of fracturing is via using explosives, where an explosion-based fluid is introduced and activated downhole. During the field-testing of such fracturing, it was found that multiple fractures were created, with a compacted zone around the wellbore. A compacted zone is a damaged zone, which limits gas production.

A third type of fracturing is propellant-based fracturing, which also creates multiple fractures around a wellbore, as tested. Subsequently, during propellant testing, no compacted zone was found. A fourth and novel type of fracturing has recently been developed, based on exothermic reaction. The new method employs reactive chemicals to generate an in situ pressure pulse, which can be used as a stand-alone or hybridized method with hydraulic fracturing.

In this study, we strive to investigate the pressurization rate and pulse loading of thermochemical fracturing on induced fractures. An actual lab test and simulation was implemented[6].

In Situ Pressure Pulse Using Thermochemicals

Fracturing can be induced into a formation using an in situ pressure pulse, generated by thermochemicals. Figure 5 shows the pressure and temperature profiles of a typical thermochemical pulse generated in an autoclave system. Figure 6 shows the high-pressure, high temperature autoclave used for thermochemical pulse testing.
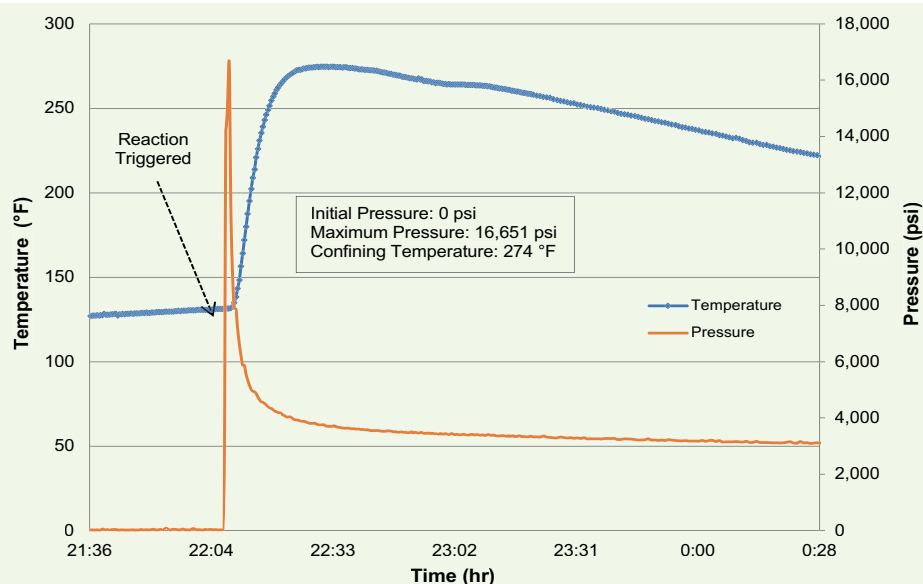
Fig. 6 *The high-pressure, high temperature autoclave system used for thermochemical pulse testing.*

Exothermic reaction, when it is activated downhole, can generate a significant amount of pressure. The in situ generated pressure can completely replace the required hydraulic pressure to fracture a formation, or can be hybridized with hydraulic fracturing to minimize the required wellhead pressure. So, when the new pulse fracturing treatment is used, three forces will be applied on the formation, which are hydraulic pressure, hydrostatic pressure from the wellbore column, and a pressure pulse generated by thermochemicals.

Therefore, all of these pressures can be applied to fracture a formation, and reduce the required wellhead pressure. As a result, the number of canceled fracturing stages around the world will be reduced, and likewise, the number of unproductive wells.

Impact of Pulse Rate and Loading on Induced Fractures

During formation fracturing, the pressurization rate can determine the number of induced fractures. When the pressurization rate, during fracturing, is microseconds, multiple fractures will be created, with an impacted zone around the wellbore. This type of fracturing is created using explosives only.

Another type of fracturing is pulse fracturing, where the pressurization rate is in milliseconds. This type of fracturing can be done using tailored gas or the newly developed thermochemical fracturing. Moreover, the thermochemical treatment is based on aqueous fluid, so it can be hybridized with hydraulic fracturing. In this type of pulse fracturing, multiple fractures will also be created without an impacted damaged zone, which makes it attractive for application.

A third type of fracturing is when the pressurization rate is slow and in minutes, which is hydraulic fracturing. During hydraulic fracturing, one main fracture is developed.

Chemical Pulse Testing

In this work, we strive to study the effect of pulse load and pressurization rates on induced fractures. An autoclave system was used to measure the pulse loading

with different chemical formulas. It was found that the pressure pulse load can vary from 500 psi up to 19,600 psi, Fig. 7[1]. The pressurization rate also can vary from days to milliseconds by changing the reaction behavior. In situ reservoir pressure can positively impact the magnitude of the pressure pulse. The higher the in situ pressure prior to triggering the reaction, the higher the pressure pulse magnitude, Fig. 8.

The pressure pulse was conducted in an autoclave with various initial pressure, from zero up to 1,800 psi. The initial pressure was subtracted from the recorded peak pressure and the results were plotted. The figure shows that the higher the initial pressure, the greater the pressure pulse magnitude. At an initial pressure of zero, the pressure pulse was approximately 2,000 psi. When the initial pressure was increased to 1,800 psi, the pressure pulse, using the same formula, was measured at 3,150 psi. This shows that the pulse magnitude was increased by 1,150 psi, due to the in situ pressure.

Numerical Modeling of Pulse Loading

To study the impact of pulse loading and the pulse

Fig. 7 *Thermochemical pulse fracturing can vary, up to 19,600 psi[1].*
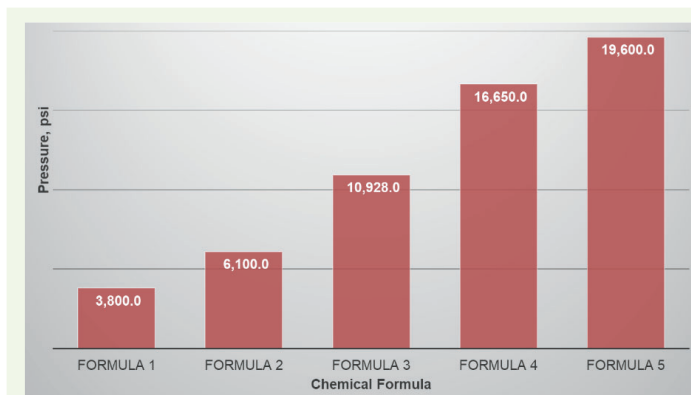
Fig. 8 *The impact of in situ pressure on the peak of the thermochemical pulse.*
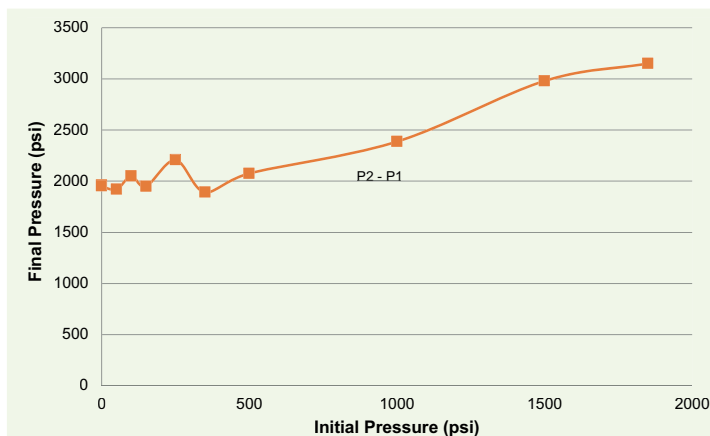
pressurization rate, numerical modeling was done using the finite element analysis simulator ABAQUS. The objective of this numerical study is to investigate the impact of pulse magnitude and the rate on the induced fracture shape and depth. Figure 9 shows the 3D finite element model (FEM) cement block used for this study. The block model has a central borehole with homogeneous porosity and permeability texture, Table 1[7].

The cement block was modeled using a concrete damage plasticity model in the ABAQUS software. A stress-strain relationship and damage parameters were used as proposed models[8]. Equations 1 and 2 were used to calculate the compressive and tensile damage parameters.

The compressive damage parameter, d_c, can be written as:

$$d_c = 1 - \frac{\sigma_c E_c^{-1}}{\varepsilon_c\,pl\left(\frac{1}{b_c} - 1\right) + \sigma_c E_c^{-1}} \qquad 1$$

The tensile damage parameter, d_t, can be written as:

$$d_t = 1 - \frac{\sigma_t E_c^{-1}}{\varepsilon_t\,pl\left(\frac{1}{b_t} - 1\right) + \sigma_t E_c^{-1}} \qquad 2$$

where d_c is the compressive damage parameter, d_t is the tensile damage parameter, σ_c is the compressive strength of the mortar cement, σ_t is the tensile strength of the mortar cement, E_c is the modulus of elasticity of the cement, $\varepsilon_c\,pl$ and $\varepsilon_t\,pl$ are the plastic strains that corresponds to the compressive and tensile strength respectively, and b_c and b_t are the constant parameters.

Figure 10 shows the used sensitivity of the breakdown pressure with respect to Young's modulus, and Fig. 11 shows the sensitivity of the breakdown pressure with respect to Poisson's ratio.

Pulse Fracturing Experiment

As a base case, the $8 \times 8 \times 8$" cement block, with a $1\frac{1}{2}$" borehole in the middle, was used to carry out pulse fracturing with thermochemicals. The cement block was placed in a biaxial frame and 4,000 psi of stress was applied in all horizontal directions. Thermochemical fluid was injected at room temperature. Then, the block temperature was increased by an internal heater. Upon reaching the designed triggering temperature, the reaction was activated at 150 °F, and a pressure pulse was generated.

The block temperature was increased to 288 °F, due to the exothermic reaction, and generated a pressure pulse up to 4,000 psi, Fig. 12. Four fractures were created in all directions, Fig. 13. This result, of having multiple fractures with pulse loading is matching the theoretical prediction described earlier. The results obtained from the experimental work of pulse fracturing was modeled using ABAQUS software. Moreover,

Fig. 9 *A 3D image of the FEM cement block used for the study.*
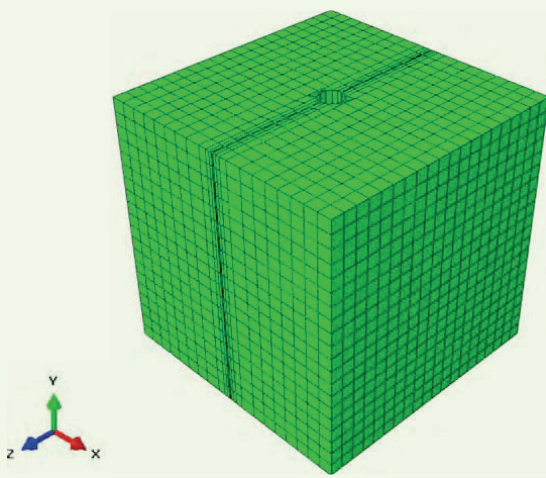
Table 1 *The input parameters of the FEM cement block.*

Model Parameters	Value	Units
Dimension of the FEM block	101.6 × 101.6 × 101.6	mm³
Density	2.31	g/cc
Young's modulus	38	GPa
Poisson's ratio	0.3	—
Unconfined compressive strength	40	MPa
Scratch strength	60	MPa
Thermochemical fluid viscosity	0.1	cp
Permeability	0.005	mD
Porosity	12.3	%
Tensile strength	—	—

Fig. 10 *The sensitivity of breakdown pressure with Young's modulus.*
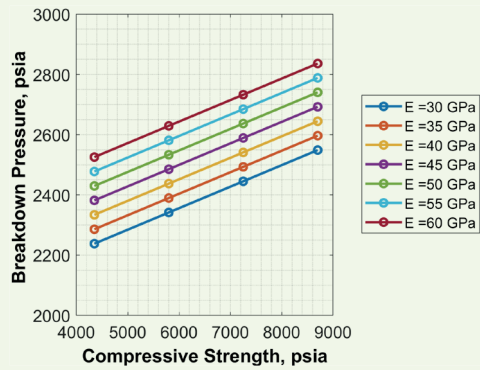
Fig. 11 *The sensitivity of breakdown pressure with Poisson's ratio.*
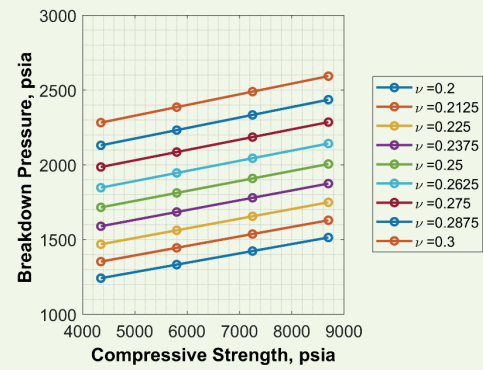
Fig. 12 *The biaxial frame test of pulsed fracturing at 4,000 psi confined stress for the cement block.*
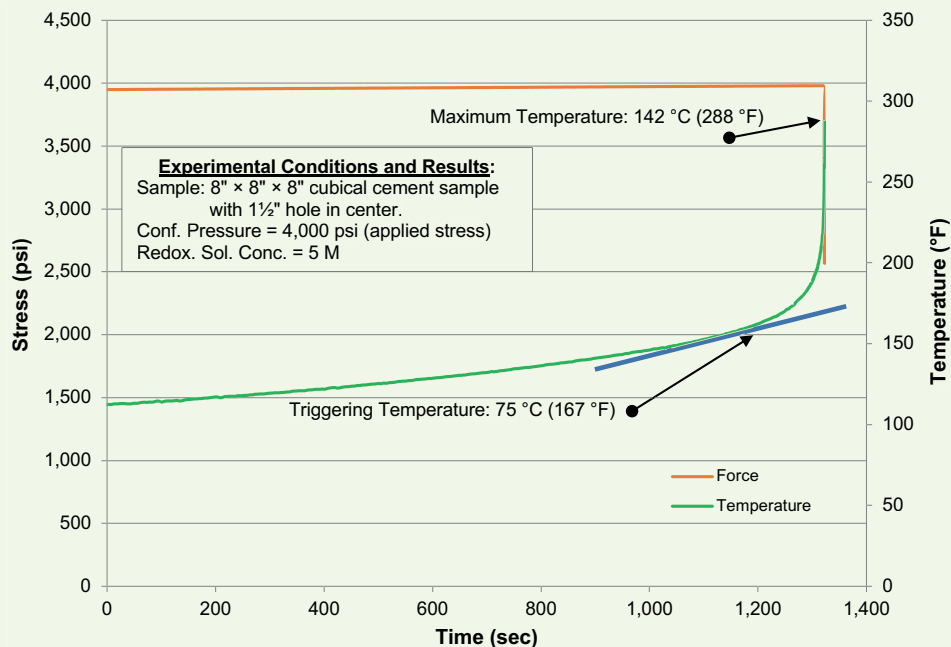
during the model, the pulse loading and rate were varied to measure the impact of these parameters on induced fractures.

Varying Pulse Load

Pressure pulse loading was varied from 1,500 psi to 22,000 psi, and the impact on created fractures were measured. Fracturing started when the pulse load was at a minimum of 2,900 psi, with one bi-wing fracture created. Below this load, there was no noticeable fractures initiated in the model. Subsequently, when the pulse load was increased to 4,400 psi, two bi-wing fractures were created, Fig. 14. At a pressure load of 7,300 psi, the length of the two induced bi-wing fractures were deeper by twofold of the fractures created

with a pulse at 2,900 psi.

When the pulse load increased to 14,500 psi, the fractures were deeper by fourfold of the initial fractures. When the pulse load was increased to 21,800 psi, three bi-wing fractures were created, however, the fracture length was only threefold of the initial fractures. Therefore, the model investigation illustrated that the higher the pulse load, the more fractures were created, and the deeper the fracture's length.

Varying Pulse Pressurization Rate

During this investigation, the pressurization rate of the pressure pulse was varied from 10 minutes to 0.01 μs, Fig. 15. It was noticed that the fracture initiation was started at a minimum pressurization rate of 1 minute,

Fig. 13 *The thermochemical pulse fracturing of the 8 × 8 × 8" cement block in a biaxial frame at 4,000 psi of stress, (a) pretest, and (b) post-test.*
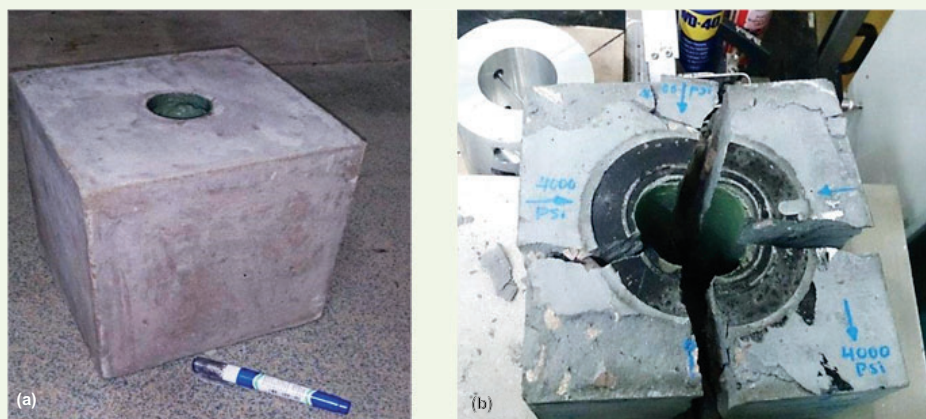
with one created bi-wing fracture. At a 6 second pressurization rate, two bi-wing fractures were created. At 100 ms, the created two bi-wing fractures were threefold deeper.

When the pressurization rate was at 10 ms, the depth of the fractures were approximately fourfold of the initial fractures created at a pressurization rate of 1 minute. Consequently, at this rate of 10 ms, two bi-wing fractures and two more random fractures were created. Therefore, the total number of created fractures were four fractures.

At 1 ms, the fracturing behavior was the same of 10 ms, however, with a deeper fracture length. At the pulse with a pressurization rate of 1 μs, intensive fracturing was created with almost three bi-wing fractures. The fracture width was almost sevenfold of the initial fractures.

Orienting Pressure Pulse

As it was demonstrated, by experimental and modeling work, thermochemical pulse-based fracturing generate multiple fractures. The higher the pulse load, the deeper and larger the number of fractures that will be developed. Pressurization time is also another critical factor of the created fractures. With the same pressure load, reducing the pressurization time will create more and deeper fractures. Therefore, it is not only the load, but also the pressurization time that will determine the expected shape of fracturing.

Subsequently, as more fractures are developed through pulsing, energy is scattered around each of the induced fractures, ending with a short fracture length. To have a longer fracture length, attempts were successfully conducted to orient the fractures to have one dominant bi-wing fracture rather than multiple fractures. When the pulse fracture is oriented, it can be hybridized efficiently with hydraulic fracturing, if it becomes necessary.

Thermochemical pulse fracturing was oriented and compared with slick water to fracture the 4 × 4 × 4" cement block. A coreflood system was used to pump

Fig. 14 *The impact of the increased pulse load on the fracturing behavior.*
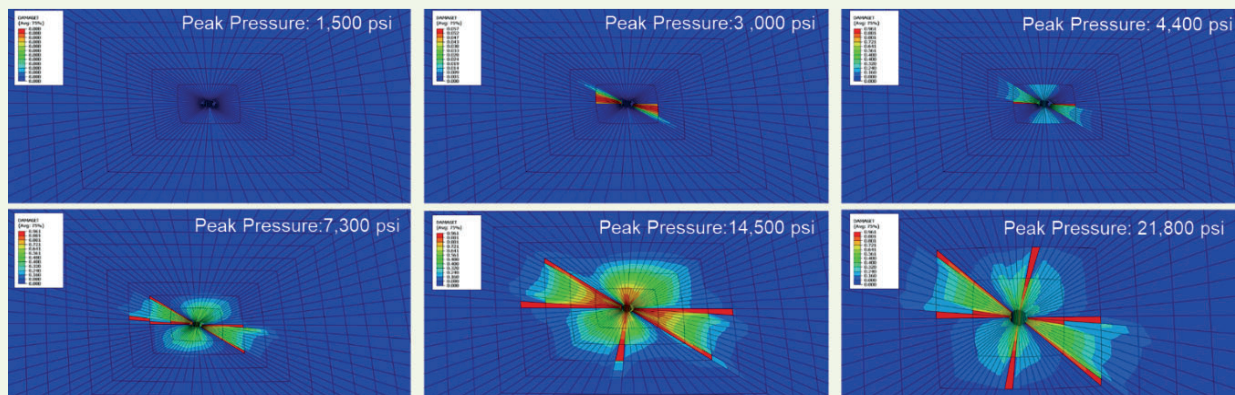
Fig. 15 *The impact of the pulse pressurization rate on the fracturing behavior.*
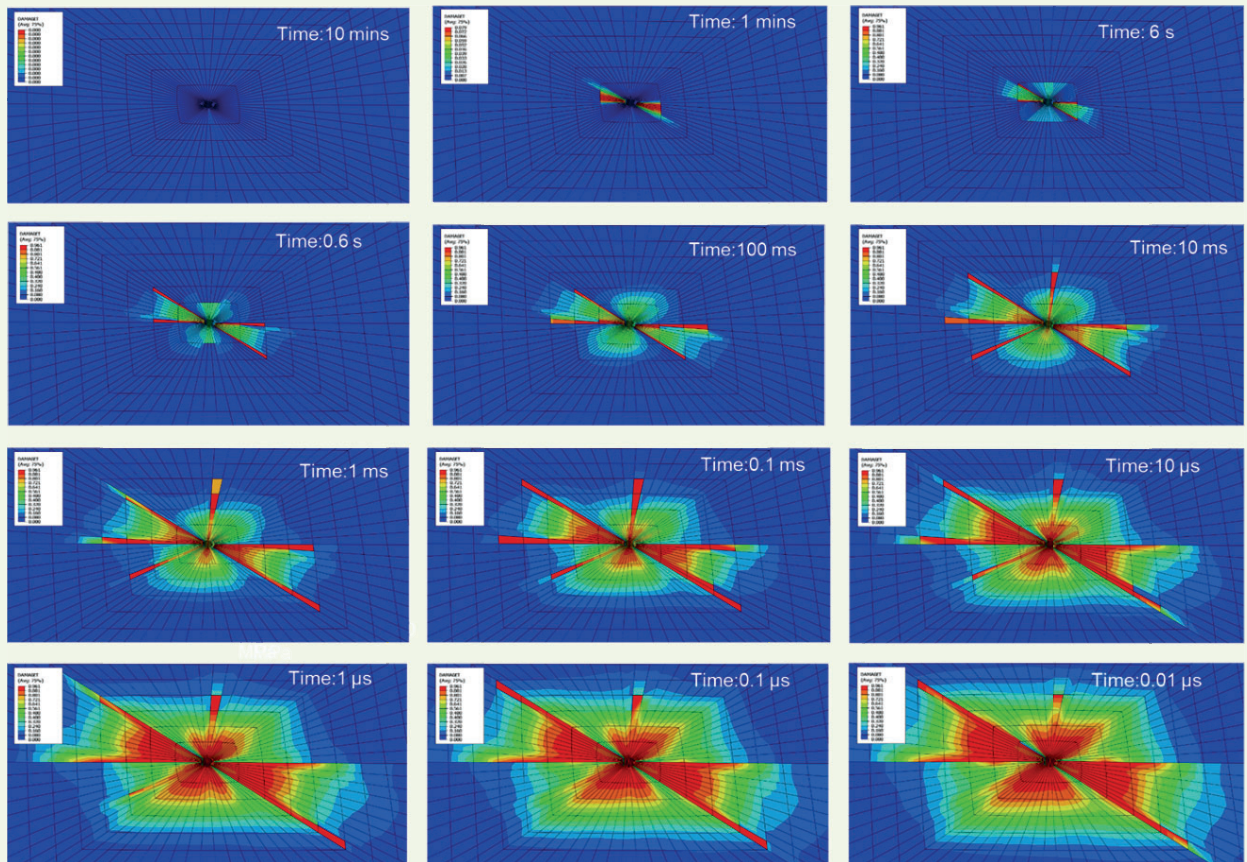
fluid and measure the breakdown pressure. When slick water was used, the measured breakdown pressure was 3,000 psi; however, when a thermochemical pulse was used, the breakdown pressure was only 700 psi, Fig. 16. With slick water, there was no clear fracture, but high leakoff, due to the generation of permeable channels. On the other hand, with the thermochemical pulse, a clear fracture was created and the rock split apart. Both tests were conducted without confining stresses.

Conclusions

In this study, the impact of the pressurization rate and the pulse load of thermochemical pulse fracturing was modeled. Based on the results achieved, the following conclusions can be drawn:

- A novel fracturing method was developed based on thermochemical reaction. Application of the thermochemical reaction can create a pressure pulse sufficient to fracture formations.
- Experimental work showed that a thermochemical induced pulse created multiple fractures in cement blocks.
- Numerical modeling was done using finite element analysis simulator ABAQUS to investigate the impact of pulse loading and the pressurization rate on

Fig. 16 *The impact of thermochemical pulse fracturing on breakdown pressure compared to slick water.*

the induced fractures' shape and depth.

- A numerical study showed that the higher the pulse load, the greater the number of induced fractures. Moreover, the shorter the pressurization rate, the more the number of induced fractures as well. Fractures vary from one bi-wing fracture to multiple bi-wing fractures.

- Successfully, pulse fracturing was oriented to contain the energy in a single bi-wing fracture, rather than multiple fractures.
- The breakdown pressure of the cement block was 76% lower when oriented thermochemical pulse fracturing is used, compared to hydraulic fracturing with slick water.

Acknowledgments

References

1. Al-Nakhli, A.R., BaTaweel, M., Mustafa, A., Tariq, Z., et al.: "Novel Methodology to Reduce the Strength of High Stress-Tight Gas Reservoirs Using Thermochemical," paper presented at the 53rd U.S. Rock Mechanics/Geomechanics Symposium, New York City, New York, June 23-26, 2019.

2. Al-Nakhli, A.R.: "Chemically Induced Pressure Pulse: A New Fracturing Technology for Unconventional Reservoirs," SPE paper 172551, presented at the SPE Middle East Oil and Gas Show and Conference, Manama, Kingdom of Bahrain, March 8-11, 2015.

3. International Energy Agency: "Shale Gas Development in China Aided by Government Investment and Decreasing Well Cost," September 2015, *www.eia.gov/todayinenergy/detail.php?id=23152*.

4. Schatz, J.F., Zeigler, B.J., Hanson, J.M., Christianson, M.C., et al.: "Laboratory, Computer Modeling, and Field Studies of the Pulse Fracturing Process," SPE paper 18866, presented at the SPE Production Operations Symposium, Oklahoma City, Oklahoma, March 13-14, 1989.

5. Mustafa, A., Tariq, Z., Abdulraheem, A., Mahmoud, M., et al.: "Increasing Stimulated Reservoir Volume (SRV) in Unconventional Reservoirs: Microstructural and Rock Mechanical Study," SPE paper 192808, presented at the Abu Dhabi International Petroleum Exhibition and Conference, Abu Dhabi, UAE, November 12-15, 2018.

6. Tariq, Z., Mahmoud, M., Abdulraheem, A., Al-Nakhli, A.R., et al.: "An Experimental Study to Reduce the Breakdown Pressure of the Unconventional Carbonate Rock by Cyclic Injection of Thermochemical Fluids," *Journal of Petroleum Science and Engineering*, Vol. 187, April 2020.

7. Tariq, Z., Mahmoud, M., Abdulraheem, A., Al-Shehri, D., et al.: "An Experimental Study and Finite Element Modeling of Thermochemical Fracturing in Ultra-Tight Cement Mortar Samples," IPTC paper 19916, presented at the International Petroleum Technology Conference, Dhahran, Kingdom of Saudi Arabia, January 13-15, 2020.

8. Lubliner, J., Oliver, J., Oller, S. and Oñate, E.: "A Plastic-Damage Model for Concrete," *International Journal of Solids and Structures*, Vol. 25, Issue 3, 1989, pp. 299-326.

About the Authors

Ayman R. Al-Nakhli

*M.S. in Entrepreneurship for
New Business Development,
Open University Malaysia*

Ayman R. Al-Nakhli is a Petroleum Scientist in Saudi Aramco's Exploration and Petroleum Engineering Center – Advanced Research Center (EXPEC ARC), where he leads the research program on thermochemicals and develops technologies related to conventional and unconventional reservoirs such as pulse fracturing, stimulation, diverting agents, and heavy oil.

Ayman has developed and field deployed several novel technologies, with four of them being commercialized with international service companies. He received the World Oil Award for Best Production Chemical in 2015.

Ayman has filed more than 20 patents, published 35 journal papers, and 40 conference papers.

He received his B.S. degree in Industrial Chemistry from King Fahd University of Petroleum and Minerals (KFUPM), Dhahran, Saudi Arabia, and an M.S. degree in Entrepreneurship for New Business Development from Open University Malaysia, Bahrain.

Dr. Zeeshan Tariq

*Ph.D. in Petroleum Engineering,
King Fahd University of Petroleum
and Minerals*

Dr. Zeeshan Tariq is an Associate Professor working at the King Fahd University of Petroleum and Minerals (KFUPM). His areas of research interests are geomechanics, hydraulic fracturing, artificial intelligence, and petrophysics.

Zeeshan has published more than 20 peer-reviewed journal articles and filed several patents.

He is an active member of various societies, such as the Society of Petroleum Engineers (SPE), the Society of Petrophysicists and Well Log Analysts (SPWLA), the Society of Exploration Geophysicists (SEG), and the American Rock Mechanics Association (ARMA).

Zeeshan received his M.S. degree in Petroleum Engineering from KFUPM, Dhahran, Saudi Arabia. He received his Ph.D. degree at the College of Petroleum Engineering and Geosciences, KFUPM.

Dr. Mohamed Mahmoud

*Ph.D. in Petroleum Engineering,
Texas A&M University*

Dr. Mohamed Mahmoud is a Professor working in the Department of Petroleum Engineering at King Fahd University of Petroleum and Minerals (KFUPM), Dhahran, Saudi Arabia. His areas of research include carbonate and sandstone stimulation, formation damage, and rock petrophysics and geomechanics.

Mohamed has authored or coauthored several journal and conference papers, in addition to more than 80 U.S. patents.

He received both his B.S. degree and M.S. degree in Petroleum Engineering from Suez Canal University, Ismailia, Egypt. Mohamed received his Ph.D. degree in Petroleum Engineering from Texas A&M University, College Station, TX, in 2011.

Dr. Abdulazeez Abdulraheem

*Ph.D. in Geotechnical
Engineering,
University of Oklahoma*

Dr. Abdulazeez Abdulraheem is an Associate Professor in the Department of Petroleum Engineering at King Fahd University of Petroleum and Minerals (KFUPM), Dhahran, Saudi Arabia. His focus is mainly on geomechanics and the applications of artificial intelligence in different areas of petroleum engineering.

Prior to joining the department, Abdulazeez worked as a Research Engineer in the Research Institute at KFUPM for almost 18 years, addressing field challenges in areas such as wellbore instability, sand production, and experimental rock mechanics.

He has published/presented almost 200 journal and conference papers in the area of geomechanics and the application of artificial intelligence in petroleum engineering.

Abdulazeez received his M.S. degree in Structural Engineering from the Indian Institute of Science, Bangalore, India. He received his Ph.D. degree in Geotechnical Engineering from the University of Oklahoma, Norman, OK.

CO$_2$ Leakage Rates Forecasting Using Optimized Deep Learning

Xupeng He, Marwah M. AlSinan, Dr. Hyung T. Kwak and Dr. Hussein Hoteit

Abstract /

Geologic carbon dioxide (CO$_2$) sequestration (GCS) has been considered a promising engineering measure to reduce global greenhouse emissions. Real-time forecasting of CO$_2$ leakage rates is an essential aspect of large-scale GCS deployment. This work introduces a data-driven, physics featuring surrogate model based on a deep learning technique for forecasting CO$_2$ leakage rates.

The workflow for the development of a data-driven, physics featuring surrogate model includes three steps: (1) Data sets generation: We first identify uncertainty parameters that affect the objective of interest, i.e., CO$_2$ leakage rates. For these identified uncertainty parameters, various realizations are then generated based on Latin Hypercube Sampling (LHS). High fidelity simulation based on a two-phase black oil solver within the MATLAB Reservoir Simulation Toolbox (MRST) is run for each of the realizations. Data sets, including inputs, i.e., the uncertainty parameters, and outputs — CO$_2$ leakage rates — are collected. (2) Surrogate development: In this step, a time series surrogate model using long short-term memory (LSTM) is constructed to map the nonlinear relationship between these uncertainty parameters as inputs and CO$_2$ leakage rates as outputs. We perform Bayesian optimization to automate the tuning of hyperparameters and network architecture instead of a traditional trial and error tuning process. (3) Uncertainty analysis: This step strives to perform Monte Carlo simulations using the successfully trained surrogate model to explore uncertainty propagation. The sampled realizations are collected in the form of distributions from which the probabilistic forecast of percentiles, P10, P50, and P50, are evaluated.

We propose a data-driven, physics featuring surrogate model based on LSTM for forecasting CO$_2$ leakage rates. We demonstrate its performance in terms of accuracy and efficiency by comparing it with ground truth solutions. The proposed deep learning workflow shows great potential and could be readily implemented in commercial-scale GCS for real-time monitoring applications.

Introduction

A promising engineering measure, geologic carbon dioxide (CO$_2$) sequestration (GCS), is considered as a way to reduce global greenhouse emissions. Various types of reservoirs have been proposed to store CO$_2$, such as geothermal reservoirs[1], depleted oil or gas reservoirs[2-4], deep ocean formations[5], and saline aquifers[6]. Leakage may occur through faults[7], or abandoned wellbores[8, 9]. Real-time forecasting of CO$_2$ leakage rates is an essential aspect of large-scale GCS deployment, e.g., quick decision making. High fidelity simulations using the multiphase black oil solver would suffer from high computation costs, making it infeasible for practical implementation.

Various analytical or semi-analytical approaches have been proposed in the literature to forecast the CO$_2$ leakage rate. Examples include Viswanathan et al. (2008)[10], who proposed a hybrid model for assessing wellbore leakage at a geologic CO$_2$ sequestration site. Nordboiten et al. (2009)[11] provided a semi-analytical model for describing CO$_2$ migration and leakage, including multiple geological layers and multiple leaky wells. Zeidouni (2012)[12] developed an analytical model to evaluate leakage rates through a leaky fault to overlying formations. Ahmadi and Chen (2019)[13] developed an analytical model for determining leakage rate and pressure response in CO$_2$ sequestration in deep saline aquifers. Qiao et al. (2021)[9] proposed a semi-analytical solution to assess CO$_2$ leakage in the subsurface through abandoned wells. All these models, however, are assumptions or specific cases, which limit their broad applicability.

Recent advances in machine learning have inspired many applications in geoscience and petroleum areas. Examples include fracture network recognition from outcrops using U-Net[14, 15], constructing an equivalent continuum model from discrete fracture characterization using a convolutional neural network[16], and well data history analysis using long short-term memory (LSTM)[17]. These three deep learning algorithms are commonly implemented, designed for image-to-image, image-to-value, and time series problems, respectively. The LSTM technique offers an alternative for time series predictions instead of the expensive high fidelity numerical model.

First, we will review problem formulation, in which the simulation model is detailed. Then, followed by the

proposed deep learning workflow, a data-driven and physics featuring surrogate model based on LSTM is developed for forecasting CO_2 leakage rates. Next, we demonstrate the performance of the proposed workflow in results and analyses. Finally, we provide the conclusions and future work of this study.

Problem Formulation

Saline aquifers offer great potential for CO_2 sequestration due to their worldwide distribution. In this study, we consider injecting supercritical CO_2 into deep saline aquifers. The corresponding physics processes are governed by the saturation equation and Darcy law. The saturation equation of phase α is given by:

$$\frac{\partial(\phi\rho_\alpha S_\alpha)}{\partial t} + \nabla\Box(\rho_\alpha \overline{u_\alpha}) = Q_\alpha \qquad \alpha = n, w \qquad \text{1}$$

where ϕ is porosity, ρ is phase density, S is phase saturation, t is time, $\overline{u}$ is phase velocity, and Q is phase sink/source term. The subscription a denotes the phase, where n is for CO_2 and w is for water.

The velocity $\overline{u_\alpha}$ is described by Darcy law as:

$$\overline{u_\alpha} = -\frac{k_{r\alpha}}{\mu_\alpha}\overline{K}\left(\nabla p_\alpha + \rho_\alpha g\nabla z\right) \qquad \text{2}$$

where $\overline{K}$ is the absolute permeability tensor, k_r, μ, and p are relative permeability, viscosity, and pressure, respectively; g is gravity acceleration, and z is the depth. The phase saturations are constrained by:

$$S_n + S_w = 1 \qquad \text{3}$$

And the two pressures are related by capillary pressure, p_c, function:

$$P_c(S_w) = p_n - p_w \qquad \text{4}$$

We use one well, placed down the flank of the model, perforated in the bottom layer. Hydrostatic boundary conditions are specified on all outer boundaries. The simulation model is solved by a two-phase black oil solver within the MATLAB Reservoir Simulation Toolbox (MRST) framework. A detailed description of the implemented solver algorithm can be found in Lie (2019)[18]. The topography of the top surface and the geological layers in the model are generated by combining the membrane function and a sinusoidal surface with random perturbations.

Figure 1 illustrates the geological model and well placement.

We consider a base case with CO_2 injected into the saline aquifer for a period of 50 years and followed by the migration of the CO_2 in a post-injection period of 450 years. Table 1 summarizes the other related data.

Figure 2 shows the simulation results for the base case CO_2 saturation distributions: (a) at 50 years, and (c) at 500 years, (b) the trapping inventory at 50 years, and (d) at 500 years — showing only 4% of the total injected CO_2 leakages through the outer boundaries during the CO_2 migration period.

We observe in Fig. 3 two cross-sections in X/Y directions through the well, showing the CO_2 tends to migrate upwards along with the structure, as the density of the CO_2 is lower than the density of water.

Proposed Deep Learning Workflow

A high fidelity simulation, based on a two-phase black oil solver, suffers from intensive computation cost, making it infeasible for practical implementation, e.g., quick decision making. This work introduces a data-driven, physics featuring surrogate model based on a deep learning technique as an alternative.

Figure 4 shows the workflow for the development of a data-driven, physics featuring surrogate model, including three steps. A detailed description of these steps follows.

Data Sets Generation

Uncertainty parameters that affect the objective of interests, i.e., CO_2 leakage rates, are first identified.

Fig. 1 *The geological model used in this study showing the well placement.*
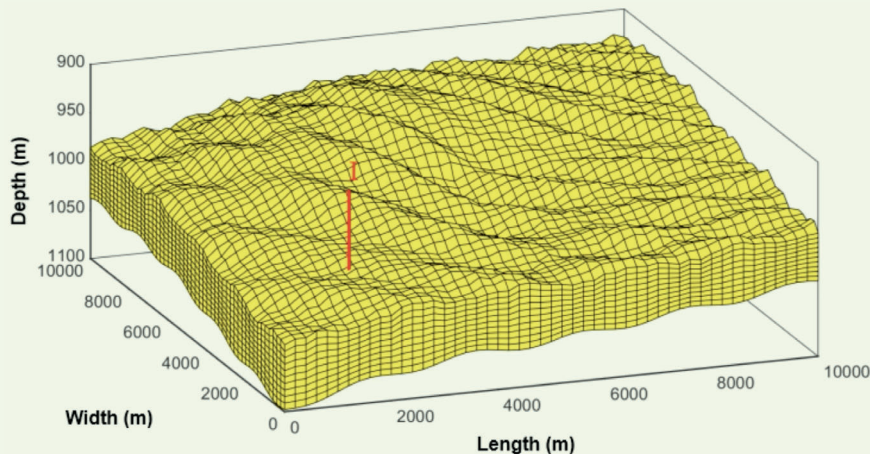
Table 1 *Relevant data for the base case.*

Permeability (K)	200 mD
CO_2 Injection Rate (Q)	6,000 m³/day
Residual CO_2 Saturation (S_r)	0.2
Residual Water Saturation (S_w)	0.1
Porosity (ϕ)	0.2
Fluid Properties	$\rho_n = 686.54$ $\rho_w = 975.86$ kg/m³ $\mu_n = 0.056641$ $\mu_w = 0.30860$ cP
Relative Permeabilities	[0.2142 0.85]
Injection Period	50 years
Post-Injection (Migration) Period	450 years

Fig. 2 *The base case simulation results: (a) CO_2 saturation at 50 years, and (c) 500 years, (b) trapping inventory at 50 years, and (d) 500 years.*
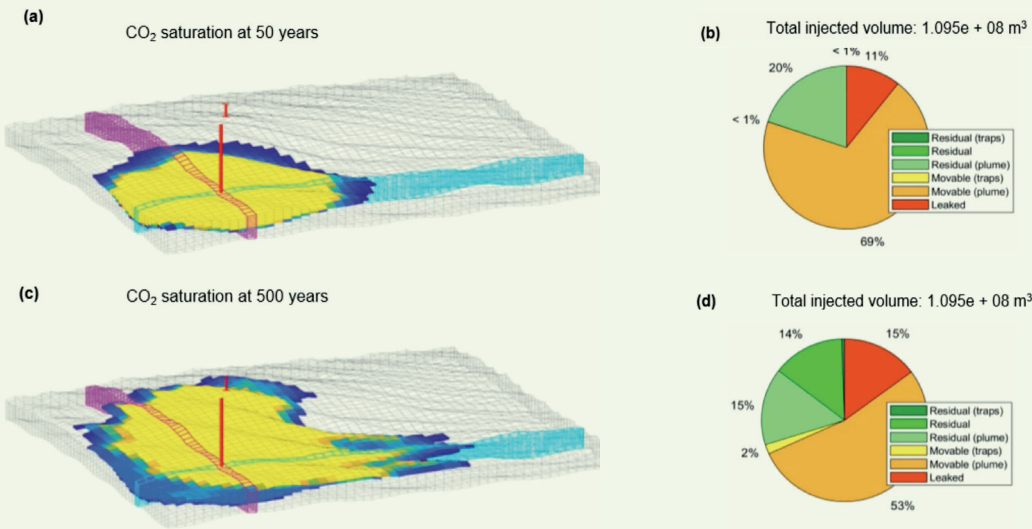
Fig. 3 *CO_2 saturation profiles (x-slice and y-slice) at (a) 50 years, and (b) 500 years.*
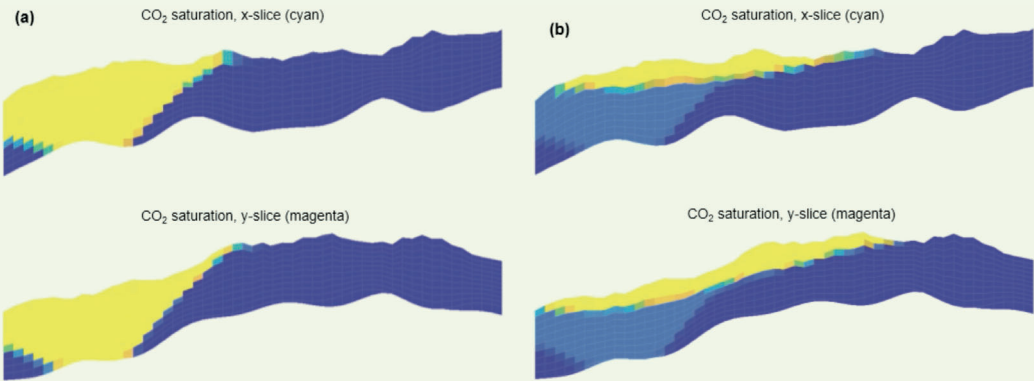
Fig. 4 *The proposed deep learning workflow, including three steps: (a) Data set generation, (b) Surrogate development, and (c) Uncertainty analysis.*
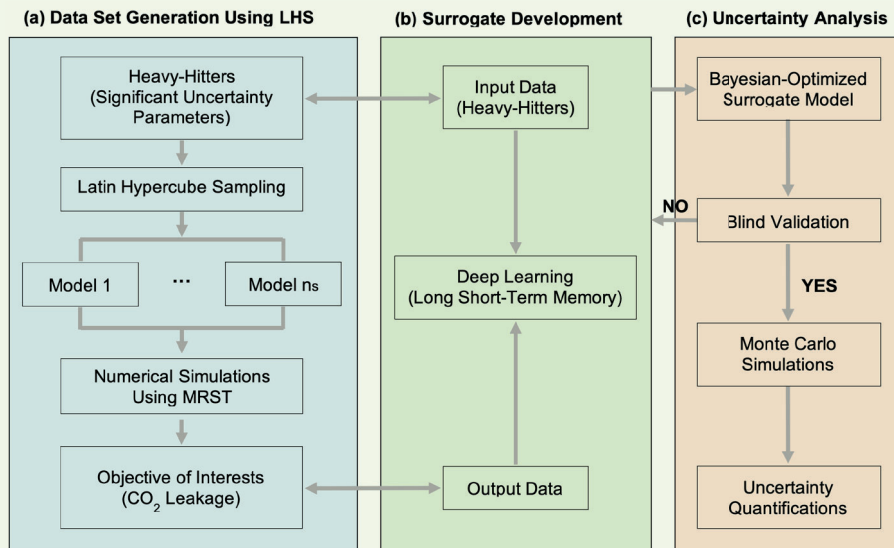
With the identified uncertainty parameters, n_s, realizations are then generated using Latin Hypercube Sampling (LHS). High fidelity simulation based on a two-phase black oil solver is run for each of the n_s realizations. These simulations are performed using open-source MRST[18]. We then collect the inputs, i.e., the uncertainty parameters, and outputs, i.e., CO_2 leakage rates, from these simulations.

In this work, the uncertainty parameters and their corresponding ranges are listed in Table 2. The first four uncertainty parameters are independent and assumed to be uniform distributions. These parameters are used to perform LHS to generate data sets. The corresponding values of porosity are computed using the correlation.

The advantage of using LHS guarantees the data sets are distributed in a space filling manner[14, 16, 21]. Figure 5 shows the LHS with two different realizations, Figs.

5a and 5c, 250, and Figs. 5b and 5d, 500. For cases with all independent parameters, data points exhibit a space filling manner within a 3D space, Figs. 5a and 5b. It becomes more obvious with the increasing number of realizations. We observe in Figs. 5c and 5d clustering effects occur in $K - \phi$ space as there exist specific correlations between permeability and porosity — more dominant clustering effects with increasing realizations. Subsequently, in the $K - Q$ space, a space filling manner still is observed because of independence between these two parameters.

Surrogate Development

In this step, a data-driven, physics featuring surrogate model based on LSTM will be established to map the nonlinear relationship between the uncertainty parameters as inputs and time series CO_2 leakage rates as outputs. LSTM, as a variant of a recurrent neural network, enables the capture of both short-term and

Table 2 *The uncertainty parameters and their corresponding ranges.*

Uncertainty Parameters	Lower Bound	Upper Bound	Distribution
Permeability (K)	1 mD	500 mD	Uniform
CO_2 Injection Rate (Q)	6,000 m³/day	12,000 m³/day	Uniform
Residual CO_2 Saturation (S_r)	0.1	0.3	Uniform
Residual Water Saturation (S_w)	0.1	0.3	Uniform
Porosity (ϕ)	0.08	0.31	$\phi = 0.082 \times K^{0.216}$

Range of K from Dai et al. (2013)[19].
Ranges of Q, S_r, and S_w from examples of MRST-CO_2 Lab[18].
Correlation between K and ϕ adopted from Chen and Pawar (2019)[20].

long-term temporal dependency.

Figure 6 is a diagram of a LSTM building block[22]. The LSTM model requires careful tuning of hyperparameters and network structure to guarantee accurate and robust applicability. The traditional trial and error tuning process, however, is exhaustive and expensive. Herein, Bayesian optimization[23] is implemented to automate the tuning process instead of traditional trial and error analysis.

Fig. 5 *(a) and (b) illustrates cases with all independent parameters, where the data points exhibit a space filling manner within a 3D space; (c) and (d) illustrates the dependent parameters showing a dominant clustering effect. (a) and (c) show the LHS with 250 realizations; (b) and (d) show the LHS with 500 realizations.*
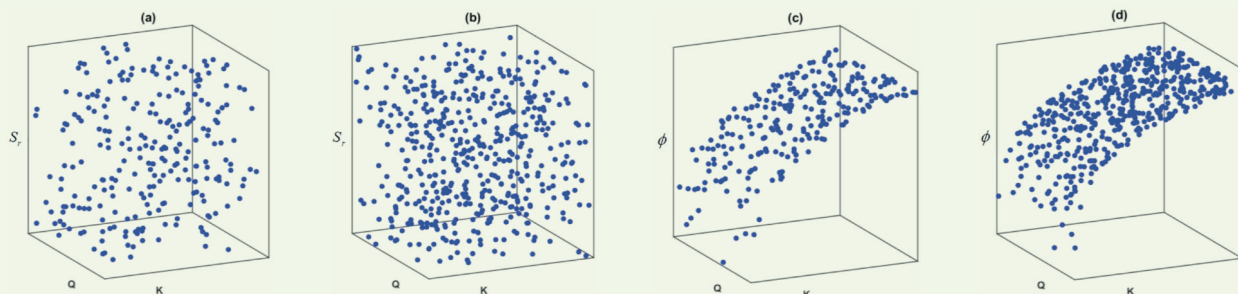
Fig. 6 *The diagram of a LSTM building block[22].*
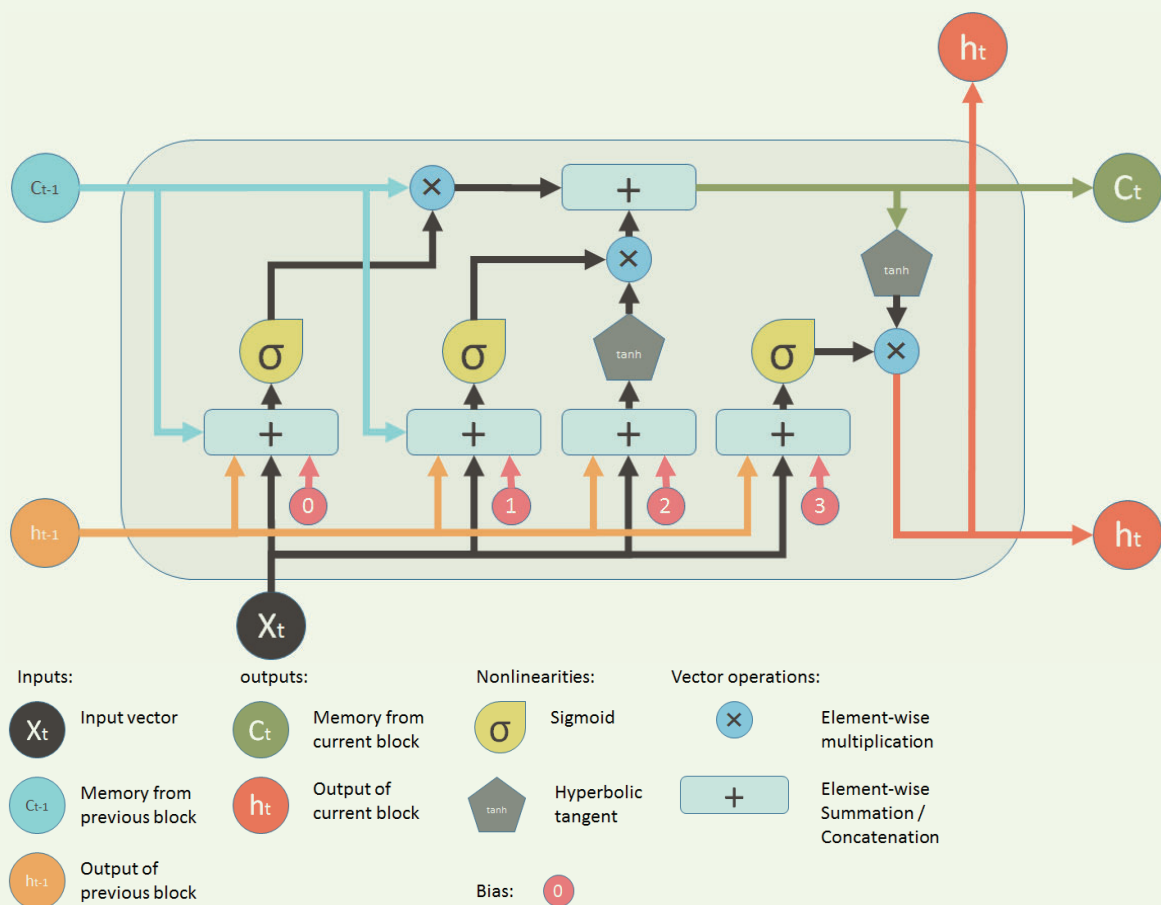
Uncertainty Analysis

This step strives to perform Monte Carlo simulations using the successfully trained surrogate model to explore uncertainty propagation. The sampled results are collected in the form of distributions from which the probabilistic forecast of percentiles, Pl0, P50, and P50, are evaluated. The specific results will be discussed next.

Before applying the Monte Carlo simulations, we conduct blind validation on the Bayesian optimized surrogate model to further assess its performance. Overfitting issues generally occur, i.e., good performance on training samples yet poor predictions on validation samples. The following parameters are used to evaluate the surrogate model performance on validation data set.

- APE: The average of prediction errors, PE, between the predicted (denoted by $Q_{Leakaged}^{Predicted}$) and ground truth ($Q_{Leakaged}^{Truth}$) CO_2 leakage rates for validation samples at each time step.

$$PE = \left| \frac{Q_{Leakaged}^{Predicted} - Q_{Leakaged}^{Truth}}{Q_{Leakaged}^{Truth}} \right| \times 100\% \qquad 5$$

$$APE = \frac{1}{N} \sum_{i=1}^{N} PE_i \qquad 6$$

- PPE: Percentage of PE within an acceptable error margin — 10% as threshold in this study.

$$PPE = \frac{N_{(where, PE \leq 10\%)}}{N} \times 100\% \qquad 7$$

- RMSE: Root-mean-square error of PE.

$$RMSE = \sqrt{\frac{\sum_{i=1}^{N} PE_i^2}{N}} \qquad 8$$

where N is the number of time steps.

Results and Analyses

We first collect inputs and outputs from high fidelity simulations based on the 250 realizations previously mentioned. LSTM coupling with Bayesian optimization is applied to obtain the optimized hyperparameter values and network architecture instead of the traditional trial and error tuning process. We next demonstrate the performance of the optimized surrogate model in terms of efficiency and accuracy by comparing it with ground truth solutions. Unlike expensive high fidelity simulation models, the optimized surrogate models significantly improve the computation efficiency, as expected.

Four new cases are selected as blind validation to demonstrate its accuracy, Fig. 7, which shows a good match between the ground truth and proposed deep learning predictions. Note: The dotted lines in Fig. 7 indicate the end of the CO_2 injection. We summarize the performance of the optimized surrogate model for these four cases in Table 3.

To explore the uncertainty propagation behavior, 5,000 Monte Carlo simulations based on the optimized

Fig. 7 *Blind validation with four new cases between the ground truth and proposed deep learning predictions.*
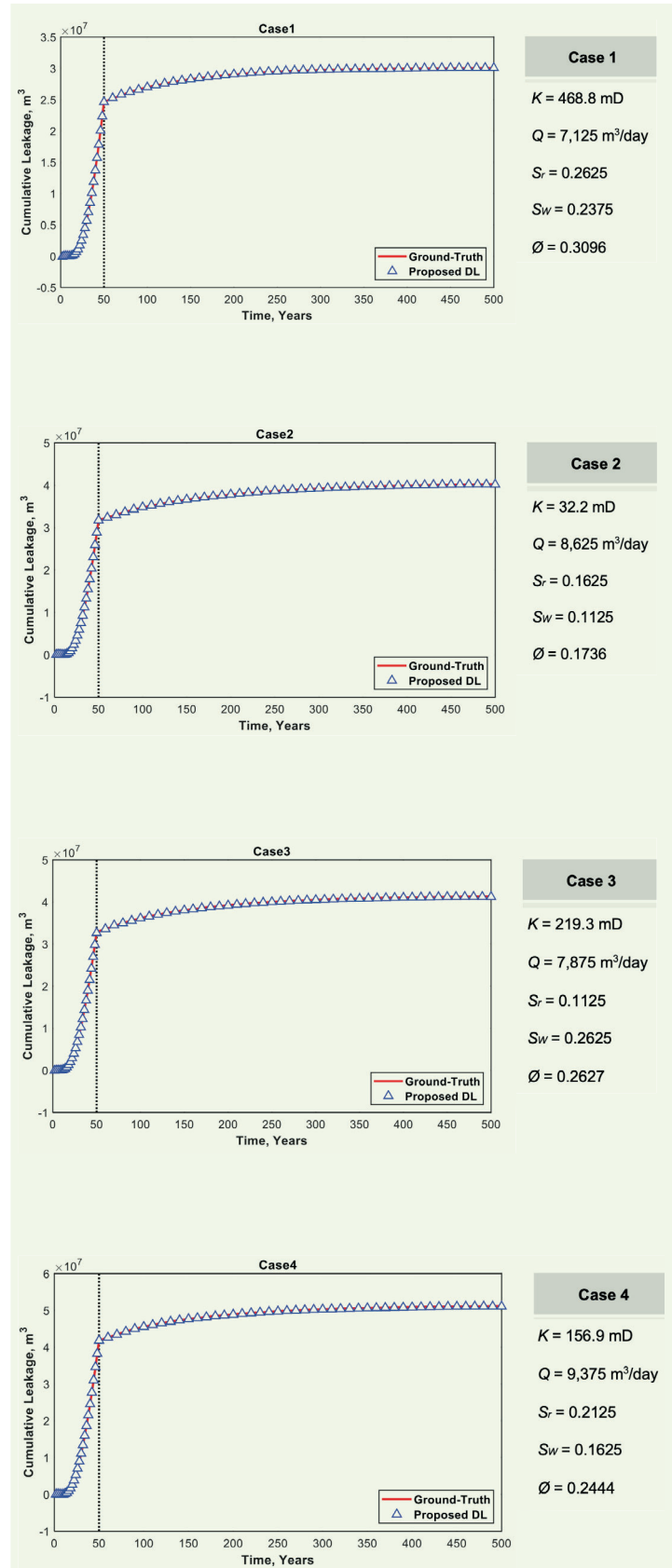
Table 3 *The performance of the optimized surrogate model for the four cases.*

	Case 1	Case 2	Case 3	Case 4
APE	5.3%	7.5%	4.2%	7.2%
PPE	94.0%	94.0%	97.0%	95.5%

Fig. 8 *Uncertainty analysis for time series cumulative CO_2 leakage using 5,000 Monte Carlo simulations applied to the successfully trained surrogate model (for illustration purposes, results illustrated every 10 years during CO_2 injection; every 50 years during CO_2 migration).*
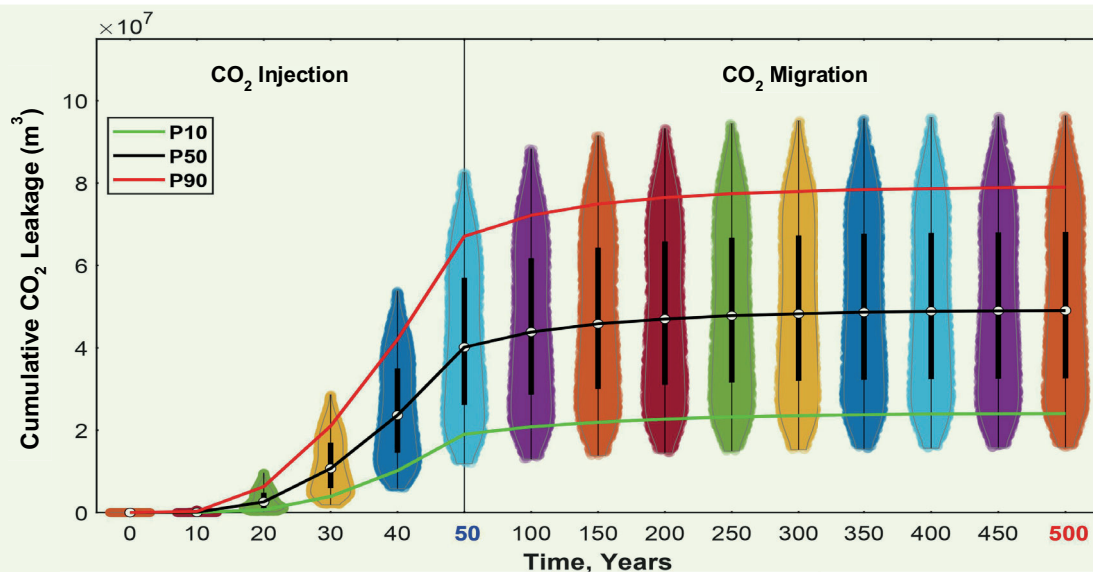
surrogate model are performed. These 5,000 sampled simulation results are collected in the form of distributions from which the probabilistic forecast of percentiles, Pl0, P50, and P50, are evaluated, Fig. 8. We observe that all Pl0, P50, and P50 curves exhibit two-segment characteristics — the cumulative CO_2 leakage increases significantly within the CO_2 injection period, yet slightly increases during the 450-year migration period. The uncertain ranges provide us a rough variability of cumulative CO_2 leakage under the ranges of the uncertainty parameters previously shown in Table 2.

Conclusions

This work introduces a data-driven, physics featuring surrogate model based on LSTM for time series CO_2 leakage rate forecasting in deep saline aquifers as an alternative to expensive high fidelity simulation models. The main conclusions are summarized as:

- The LSTM enabling to capture of short-term and long-term temporal dependency offers a good solution for time series problems. Specifically speaking, the developed data-driven, physics featuring model maps the nonlinear relation between these uncertainty parameters as the input and the objective of

interest, i.e., CO_2 leakage rates, as output.

- The advantage of using LHS enables data set points to be distributed in a space filling manner, which guarantees the general applicability of the developed surrogate model. The distribution of the data set points generated without the guidance of LHS generally exhibits clustering effects. The clustering effects always lead to unbalanced performance — working well for cases within the clustered area, yet poor predictions for other areas.

- The quality of data sets significantly impacts the quality of the developed surrogate model and further its reliability. In this study, high fidelity simulations based on a two-phase black oil solver are used to generate data sets.

- The Bayesian optimization algorithm is implemented to automate the tuning process in terms of hyperparameters and network structure, which dramatically outperforms the traditional trial and error tuning approach. Special attention is paid to the overfitting issue — high accuracy should be achieved on both training and validation samples.

- We perform 5,000 Monte Carlo simulations applied to the successfully developed model to explore the

uncertainty propagation behavior. These 5,000 sampled simulation results are collected in the form of distributions from which the probabilistic forecast of percentiles, P10, P50, and P50, are evaluated. All P10, P50, and P50 curves exhibit two segment characteristics — the cumulative CO_2 leakage increases significantly within the 50-year injection period, yet slightly increases during the 450-year migration period.

- We demonstrate the accuracy of the proposed workflow by comparing it with ground truth solutions. The proposed deep learning workflow shows great potential and could be readily implemented in commercial-scale GCS for real-time monitoring applications.

Future work could be extended to include more complex physics, such as considering capillarity and considering more uncertainty parameters that could affect the leakage rates. Realistic field cases could be adopted to further test the values of the proposed workflow. In addition, explainable and stable global sensitivity analysis could be performed to explore the impact of these uncertainty parameters on the final objective of interests.

Acknowledgments

References

1. Luo, F., Xu, R-N. and Jiang, P-X.: "Numerical Investigation of Fluid Flow and Heat Transfer in a Doublet Enhanced Geothermal System with CO_2 as the Working Fluid (CO_2-EGS)," *Energy*, Vol. 64, January 2013, pp. 307-322.

2. Hoteit, H., Fahs, M. and Soltanian, M.R.: "Assessment of CO_2 Injectivity during Sequestration in Depleted Gas Reservoirs," *Geosciences*, Vol. 9, Issue 5, 2019, pp. 1-19.

3. Ren, B., Ren, S., Zhang, L., Chen, G., et al.: "Monitoring on CO_2 Migration in a Tight Oil Reservoir during CCS-EOR in Jilin Oil Field China," *Energy*, Vol. 98, March 2016, pp. 108-121.

4. Zhang, L., Li, X., Zhang, Y., Cui, G., et al.: "CO_2 Injection for Geothermal Development Associated with EGR and Geological Storage in Depleted High Temperature Gas Reservoirs," *Energy*, Vol. 123, March 2017, pp. 139-148.

5. Herzog, H., Golomb, D. and Zemba, S.: "Feasibility, Modeling and Economics of Sequestering Power Plant CO_2 Emissions in the Deep Ocean," *Environmental Progress*, Vol. 10, Issue 1, February 1991, pp. 64-74.

6. Park, C-H., Lee, S.K., Lee, C. and Kim, S-K.: "Applicability of Thermal Response Tests for Assessing in Situ CO_2 Storage in a Saline Aquifer," *Energy*, Vol. 154, 2018, pp. 210-220.

7. Vilarrasa, V. and Carrera, J.: "Geologic Carbon Storage is Unlikely to Trigger Large Earthquakes and Reactivate Faults through which CO_2 Could Leak," *Proceedings of the National Academy of Sciences of the United States of America*, Vol. 112, Issue 19, 2015, pp. 5938-5943.

8. Harp, D.R., Pawar, R., Carey, J.W. and Gable, C.W.: "Reduced Order Models of Transient CO_2 and Brine Leakage along Abandoned Wellbores from Geologic Carbon Sequestration Reservoirs," *International Journal of Greenhouse Gas Control*, Vol. 45, Issue 1, February 2016, pp. 150-162.

9. Qiao, T., Hoteit, H. and Fahs, M.: "Semi-Analytical Solution to Assess CO_2 Leakage in the Subsurface through Abandoned Wells," *Energies*, Vol. 14, Issue 9, 2021, pp. 2452-2466.

10. Viswanathan, H.S., Pawar, R.J., Stauffer, P.H., Kaszuba, J.P., et al.: "Development of a Hybrid Process and System Model for the Assessment of Wellbore Leakage at a Geologic CO_2 Sequestration Site," *Environmental Science and Technology*, Vol. 42, Issue 19, 2008, pp. 7280-7286.

11. Nordboiten, J.M., Kavetski, D., Celia, M.A. and Bachu, S.: "Model for CO_2 Leakage Including Multiple Geological Layers and Multiple Leaky Wells," *Environmental Science and Technology*, Vol. 43, Issue 3, 2009, pp. 743-749.

12. Zeidouni, M.: "Analytical Model of Leakage through Fault to Overlying Formations," *Water Resources Research*, Vol. 48, Issue 12, 2012, pp. 1-17.

13. Ahmadi, M.A. and Chen, Z.: "Analytical Model for Leakage Detection in CO_2 Sequestration in Deep Saline Aquifers: Application to ex Situ and in Situ CO_2 Sequestration Processes," *ACS Omega*, Vol. 4, Issue 25, December 2019, pp. 21381-21394.

14. Santoso, R., He, X. and Hoteit, H.: "Application of Machine Learning to Construct Simulation Models from High-Resolution Fractured Formation," SPE paper 197459, presented at the Abu Dhabi International Petroleum Exhibition and Conference, Abu Dhabi, UAE, November 11-14, 2019.

15. Zhu, W., Khirevich, S. and Patzek, T.W.: "Fracture Recognition with U-Net and Pixel-Based Automatic Fracture Detection," paper presented at the Fourth Naturally Fractured Reservoir Workshop, Ras Al-Khaimah, UAE, February 11-13, 2020.

16. He, X., Santoso, R. and Hoteit, H.: "Application of Machine Learning to Construct Equivalent Continuum Models from High-Resolution Discrete Fracture Models," IPTC paper 20040, presented at the International Petroleum Technology Conference, Dhahran, Kingdom of Saudi Arabia, January 13-15, 2020.

17. Li, Y., Sun, R. and Horne, R.: "Deep Learning for Well Data History Analysis," SPE paper 196011, presented at the SPE Annual Technical Conference and Exhibition, Calgary, Alberta, Canada, September 30-October 2, 2019.

18. Lie, K-A.: *An Introduction to Reservoir Simulation Using MATLAB/GNU Octave: User Guide for the MATLAB Reservoir Simulation Toolbox (MRST)*, Cambridge University Press, 2019, 674 p.

19. Dai, Z., Middleton, R., Viswanathan, H., Fessenden-Rahn, J., et al.: "An Integrated Framework for Optimizing CO_2 Sequestration and Enhanced Oil Recovery," *Environmental Science and Technology Letters*, Vol. 1, Issue 1, 2014, pp. 49-54.

20. Chen, B. and Pawar, R.J.: "Characterization of CO_2 Storage and Enhanced Oil Recovery in Residual Oil Zones," *Energy*, Vol. 183, September 2019, pp. 291-304.

21. Santoso, R., Torrealba, V. and Hoteit, H.: "Investigation of an Improved Polymer Flooding Scheme by Compositionally Tuned Slugs," *Processes*, Vol. 8, Issue 2, 2020, pp. 197-216.

22. Hochreiter, S. and Schmidhuber, J.: "Long Short-Term Memory," *Neural Computation*, Vol. 9, Issue 8, November 1997, pp. 1735-1780.

23. Brochu, E., Cora, V.M. and de Freitas, N.: "A Tutorial on Bayesian Optimization of Expensive Cost Functions, with Application to Active User Modeling and Hierarchical Reinforcement Learning," *arXiv*, December 2010.

About the Authors

Xupeng He

M.S. in Petroleum Engineering, King Abdullah University of Science and Technology

Xupeng He is currently a Ph.D. student at the Ali I. Al-Naimi Petroleum Engineering Research Center, King Abdullah University of Science and Technology (KAUST), Thuwal, Saudi Arabia. His research interests include modeling naturally fractured reservoirs, machine (deep) learning applications in petroleum engineering, and uncertainty quantification and optimization in subsurface flow problems.

Xupeng is the author of 11 conference papers, and two U.S. patents.

He was the recipient of the Excellent Student Cadre and the Outstanding Undergraduate Student Awards in 2014 and 2015, respectively, at Chang'an University. Also, Xupeng received a national scholarship from the Ministry of Education of the People's Republic of China in 2012 and 2013.

He received his B.S. degree in Resource Exploration Engineering (Oil and Gas) from Chang'an University, Xi'an, China, in 2015. Xupeng received his M.S. degree in Petroleum Engineering from KAUST in 2018.

Marwah M. AlSinan

M.S. in Petroleum Engineering, Imperial College

Marwah M. AlSinan joined Saudi Aramco in 2013 as a Petroleum Engineer, working with the Reservoir Engineering Technology Division in the Exploration and Petroleum Engineering Center – Advanced Research Center (EXPEC ARC).

Her research interests include multiphase flow in fractures, carbon dioxide sequestration, and applications of nuclear magnetic resonance in porous media.

In 2013, Marwah received her B.S. degree in Petroleum and Natural Gas Engineering from Pennsylvania State University, State College, PA. She received her M.S. degree in Petroleum Engineering from Imperial College, London, U.K. in 2017.

Dr. Hyung T. Kwak

Ph.D. in Physical Chemistry, Ohio State University

Dr. Hyung T. Kwak joined Saudi Aramco in April 2010 as a Petroleum Engineer with Saudi Aramco's Exploration and Petroleum Engineering Center – Advanced Research Center (EXPEC ARC). He had been a member of the Pore Scale Physics focus area and the SmartWater Flooding focus area of the Reservoir Engineering Technology Division. Since 2014, Hyung has been a focus area champion of the Pore Scale Physics focus area. His main research focus is seeking a deeper understanding of fluid-rock interaction in pore scale of the Kingdom's reservoirs.

Since joining Saudi Aramco, Hyung has been involved with various improved oil recovery and enhanced oil recovery (EOR) research projects, such as SmartWater Flooding, carbon dioxide EOR, and chemical EOR. Currently, he is leading a suite of key EXPEC ARC Fourth Industrial Revolution technology projects. Prior to joining Saudi Aramco, Hyung was a Research Scientist at Baker Hughes, from 2001 to 2010, focused on research related to nuclear magnetic resonance (NMR)/magnetic resonance imaging technology.

In 1996, Hyung received his B.S. degree in Chemistry from the University of Pittsburgh, Pittsburgh, PA, and in 2001, he received his Ph.D. degree in Physical Chemistry from Ohio State University, Columbus, OH.

Before moving into the oil and gas industry, Hyung was involved — as a postdoctoral fellow for 2 years — in a project developing the world's largest wide bore superconducting magnet NMR spectrometer, 900 MHz, at the National High Magnetic Field Laboratory.

He has more than 300 publications, including peer-reviewed articles and patents.

Dr. Hussein Hoteit

Ph.D. in Applied Mathematics, University of Rennes 1

Dr. Hussein Hoteit is an Associate Professor in Reservoir Engineering and the Program Chair of Energy Resources and Petroleum Engineering (ERPE) at King Abdullah University of Science and Technology (KAUST), Thuwal, Saudi Arabia.

Before joining KAUST, Hussein worked for ConocoPhillips and Chevron Companies for about 12 years, where he conducted projects related to chemical enhanced oil recovery (EOR), CO_2 EOR, steam flood, EM heating, to name a few.

Hussein's current research includes chemical EOR, geological CO_2 storage, improved oil recovery optimization, data-driven machine learning, and reservoir simulation development.

He has earned several Society of Petroleum Engineers (SPE) awards, including SPE Distinguished Lecturer in 2009, and served as Associate Editor for the *SPE Journal* for more than 10 years.

Hussein received his B.S. degree in Pure Mathematics and Computer Sciences from Lebanese University, Lebanon, M.S. and Ph.D. degrees in Applied Mathematics from the University of Rennes 1, Rennes, France.

Development of Optical Gas Sensor for Well Site Geochemical Analysis and Time-lapse Monitoring

Dr. Pan Luo, Jonathan D. Harrist, Rabah Mesdour and Nathan A. StMichel

Abstract /

Natural gas is sampled or produced throughout the lifespan of a field, including the geochemical surface survey, mud gas logging, formation and well testing, and production. Detecting and measuring gas is a common practice in many upstream operations, providing gas composition and isotope data for multiple purposes, such as petroleum system analysis, fluid characterization, and production monitoring. Well site gas analysis is usually conducted within a mud gas unit, which is operationally unavailable after drilling.

Gas samples need be taken from the field and shipped back to the laboratory for gas chromatography and isotope ratio mass spectrometry (GC-IRMS) analyses. To get the results is a time-consuming process and currently lack the resolution needed to fully characterize the heterogeneity and dynamics of fluids within the reservoir and the production system. We are developing and testing advanced sensing technology to move gas composition and isotope analyses to the field for near real-time and on-site fluid characterization and monitoring.

We have developed a novel quartz-enhanced photoacoustic spectroscopy (QEPAS) sensor system, employing a single interband cascade laser, to measure concentrations of methane (C1), ethane (C2), and propane (C3) in the gas phase. The quartz fork detection module, laser driver, and interface are integrated as a small sensing box. The sensor, sample preparation enclosures, and a computer are mounted in a rack as a gas analyzer prototype for the bench testing for oil industry application. The software is designed for monitoring sample preparation, collecting data, calibration, and continuous reporting sample pressure and concentration data.

The sensor achieved an ultimate detection limit of 90 parts per billion (ppb), 7 ppb, and 3 parts per million (ppm) for C1, C2, and C3, respectively, for one second of integration time. The detection limit for C2 set a record for the QEPAS technique, and measuring C3 added a new capability to the technique. The linearity of the QEPAS sensor system was previously reported in the range of 0 ppm to 1,000 ppm, which is mainly for trace gas detection. In the study, the prototype was separately tested on standard C1, C2, and C3, with different concentrations diluted in dry nitrogen (N_2).

Good linearity was obtained for all single components and the ranges of linearity were expanded to their typical concentrations (percentage) in the natural gas samples from oil and gas fields. The testing of the C1-C2 mixtures confirms that accurate C1 and C2 concentrations in percentage levels can be achieved by the prototype. The testing results on C1-C2-C3 mixtures demonstrate the capability of simultaneous detection of three hydrocarbon components and the probability to determine their precise concentrations by QEPAS sensing.

This advancement of simultaneous measuring the C1, C2, and C3 concentrations, with previously demonstrated capability for hydrogen sulfide (H_2S) and carbon dioxide (CO_2), and the potential to analyze carbon isotopes ($^{13}C/^{12}C$), promotes QEPAS as a prominent optical technology for gas detection and chemical analysis. The capability of measuring multiple gas components and the advantages of a small sensor, the high sensitivity, quick analysis, and continuous sensing (monitoring) open the way to use the QEPAS technique for in situ and real-time gas sensing in the oil industry.

The iterations of the QEPAS sensor might be applied in a geochemical survey, on-site fluid characterization, time-lapse monitoring of production, and gas linkage detection in the oil industry.

Introduction

Gas is ubiquitous in a subsurface state, as free gas in a porous space, as adsorbed gas in a kerogen/mineral surface, or dissolved gas in water and oil. Gas is sampled or produced throughout the lifespan of a field, including the geochemical surface survey, mud gas logging, formation and well testing, and production. Detecting and measuring gas is a basic analysis in the oil industry that provides gas composition and properties for petroleum system analysis, formation evaluation, pressure-volume-temperature study, reservoir simulation, production

monitoring, safety, and economic evaluation[1, 2].

The quartz-enhanced photoacoustic spectroscopy (QEPAS) sensor system is an enhanced absorption spectrometry for gas sensing. The first QEPAS was invented at Rice University and reported in 2002[5]. The Jet Propulsion Laboratory (NASA), became involved very quickly in the development, mainly for early fire warning[4, 5]. NASA still has an active project for R&D and application of the QEPAS sensor in trace gas sensing — methane (CH_4), hydrochloric acid, nitrogen oxide, formaldehyde, sulfur dioxide, and carbon dioxide (CO_2) — relevant to spacecraft environmental monitoring and advanced life support.

QEPAS was proposed to the oil industry at the 2008 Offshore Technology Conference[6, 7] for monitoring H_2S, CO_2, and Cl inside the annulus of flexible risers, since the presence of the sour gases can dramatically influence corrosion fatigue levels and may cause the safety issue in operations. Based on our best knowledge and investigation in the market, the proposal has not been applied in the field and commercialized in the market.

In the collaboration between Bari University, Rice University, and the Aramco Houston Research Center[8-10], a new generation of QEPAS has been designed and prototyped — in the size of a cake box — as a portable gas analyzer for multiple hydrocarbon components. The sensor box demonstrated the capability of the QEPAS technique in measuring concentrations of methane (Cl) and ethane (C2) at a sensitivity level of parts per billion (ppb), and propane (C3) at a sensitivity level of parts per million (ppm) by employing a single interband cascade laser emitting at 3.345 μm, and the potential to detect $^{12}CH_4$ and $^{13}CH_4$ isotopes at a ppb level by using a quantum cascade laser operating at approximately 7.730 μm.

This article will strive to introduce the QEPAS technology to the oil industry, illustrate the realization of a QEPAS-based gas analysis and calibration system, and summarize bench testing results and performance. We will discuss the advantages and limits of the new technique and some potential applications in the laboratory and the oil and gas field.

Gas Sensing, Chemical Analysis, and QEPAS Technology

There are many types of gas sensors (detectors/monitors/analyzers), which are mainly categorized based on the detection technology into four groups: semiconductor, electrochemical, analytical (gas chromatography (GC), spectrometry), and laser optical absorption sensor[11]. In the oil industry, for operational safety, infrared point and catalytic bead (pellistor) are two major sensing techniques used for combustible (hydrocarbon) gas, and an electrochemical sensor is used for H_2S detection and warning. These sensors usually detect single gas component/species in ambient air, suffering from drift, cross-response to other gases, and changing humidity levels[12]. These semiconductor and electrochemical sensors are not made for quantification

purposes, i.e., downhole applications, in a flow line, and laboratory analytics environment.

In drilling, exploration, reservoir characterization, and production monitoring, fluid (gas) samples are taken from the drilling mud, reservoir formation, wellhead, or separator, and usually injected into GC connecting with alternative detectors for chemical composition analysis. The most commonly used detectors are a flame ionization detector (FID) for hydrocarbons, and a thermal conductivity detector (TCD) for non-hydrocarbon gases (e.g., nitrogen (N_2), CO_2, H_2S, oxygen, hydrogen, helium, and argon)[1, 13].

Recently, a quadrupole mass spectrometer (QMS) was developed for rapid and direct analysis of C1 to Cl0 hydrocarbons and common inorganic species in mud gas logging[14]. Isotope ratios, e.g., $^{13}C/^{12}C$, D/H, of each gas component — as geochemical fingerprints — commonly are determined by GC connected with isotope ratio mass spectroscopy (GC-IRMS)[15]. These are quite large and delicate instruments, requiring stable and strict laboratory conditions and sophisticated experts for operation and maintenance. Consequently, such high precision laboratory analyzers — GC/MS/IRMS — are incompatible with a tough and dynamic downhole environment and well site conditions.

Transporting field fluid samples to a laboratory provides delayed, sparse, and sometimes unrepresentative data, which does not help in near real-time and high economic value decisions during drilling, formation/well testing and on-site troubleshooting[16, 17]. In addition, the sampling, transporting, sample preparation, and routine laboratory analysis are expensive operations, which are not pragmatic to be used to generate high-resolution/time-lapse data for fluid heterogeneity and dynamics studies.

Laser-based optical absorption technology offers a non-contact, fast response, minimal drift, high specificity, low maintenance requirement, and continuous monitoring for gas detection and chemical analysis[12, 18, 19]. Several techniques, based on the Beer-Lambert Law, measuring the optical adsorption at a specific wavelength are developed, including non-dispersive infrared, spectrophotometry, tunable laser absorption spectroscopy/tunable diode laser absorption spectroscopy (TDLAS), cavity ring down spectroscopy (CRDS)/cavity enhanced absorption spectroscopy (CEAS)/integrated cavity output spectroscopy (ICOS), and photoacoustic spectroscopy (PAS). There are pros and cons associated with the optical sensors based on the different mechanisms of excitation and sensing and their applications.

PAS, based on the photoacoustic effect discovered by Alexander Graham Bell in 1880, is an indirect optical absorption technique. PAS does not require an optical detector and its responsivity is laser wavelength independent.

Figure 1 shows that when the laser output is absorbed by a target gas, the absorbed laser energy at characteristic wavelengths induces heat and expansion to create a vibration of gas molecules at the resonant

Fig. 1 *A diagram showing the principal of PAS for gas detection and the use of a QTF to enhance the photoacoustic spectroscopy. Modified from Sampaolo et al. (2019)[9] and Patimisco et al. (2014)[11].*
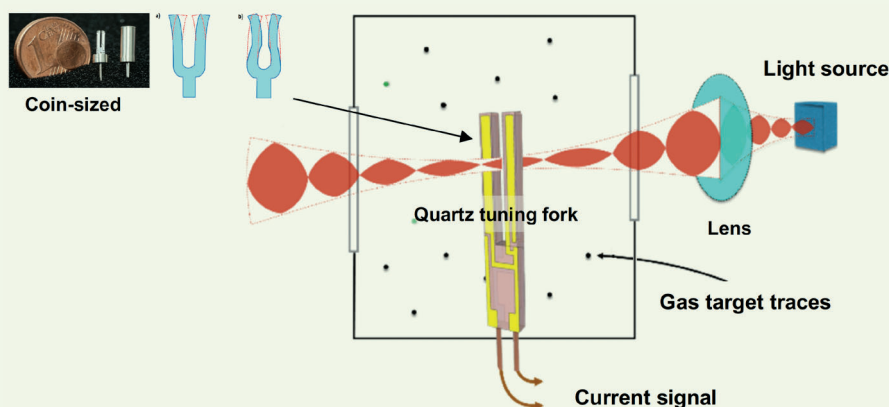
frequency, subsequently resulting in the generation of an acoustic wave. The wave can be transduced by a microphone to an electrical signal that is proportional to the concentration (mol%, vol%) of the target gas. QEPAS is an improved approach to photoacoustic detection of trace gas by replacing the microphone with a piezoelectric quartz tuning fork (QTF) as a sharply resonant acoustic transducer to detect weak photoacoustic excitation, allowing the sensor to be made in an extremely small size[11].

Among the main optical sensors, QEPAS has been proven to be a leading-edge technique for out-of-laboratory detection for trace gas, because of extremely high sensitivity, down to a ppb/ppt level of compactness, immunity to environmental noise, its proven reliability — ruggedness — and in situ operation[9, 11, 20-22]. QEPAS does not require an optical detector as it reaches high detection sensitivity within the short optical path length, and it is insensitive to the wavelength. These factors represent the main advantages with respect to other laser-based techniques, such as TDLAS, CRDS, CEAS, and other multiple pass-based spectroscopy[11, 12]. The core part of a QEPAS sensor — the QTF — is actually very small and the whole sensor could be made very compact, e.g., fitting into a 2" internal diameter pipe for downhole operations[8].

The QEPAS showed high frequency stability of the QTF's resonance with frequency shifts of ~0.04 ppm/T2 in the temperature range from -40 °C to 90 °C, suggesting the sensor may operate in a large temperature range[10]. In addition, the QEPAS can detect multiple gas species and their isotopes[10, 23], and the number of gas components that QEPAS can detect is increasing and the performance of QEPAS analysis (precision, detection limits, integration time, etc.) is continuously improving[11, 24]. Therefore, the QEPAS may overcome the disadvantages previously mentioned for conventional gas sensors and laboratory-based instruments, and be applied in the oil and gas field for in situ and real-time gas detection and chemical analysis.

QEPAS Gas Analyzer System

A QEPAS sensor with a S-QTF, using a single interband cascade laser operating in the spectral range 3.342 μm to 3.349 μm, was integrated in a portable box (5.2 × 9.8 × 9.8"), Fig. 2a. The QEPAS is very sensitive to trace hydrocarbon gas, down to the ppb level. To analyze hydrocarbon compositions — ppm to percentage level — of natural gas from the oil industry, the gas sample needs to be diluted. We developed the components for sample drying, quantitative mixing (dilution) and handling the common gas samplers (cylinder and isotube) used in the industry. All components were mounted in a rack, Fig. 2b, as a prototype of the gas analyzer for bench testing.

Figure 3 shows the diagram of the prototype system, which consists of five major components: (1) sample introduction enclosure, (2) sample mixing enclosure, (3) sample drying enclosure, (4) QEPAS and laser controller enclosure, and (5) a PC with the QEPAS specific software.

The system was designed to meet the following design parameters: (1) measuring major hydrocarbon gas components in typical concentrations in a natural gas field (C1: 70% to 100%, C2: 1% to 10%, and C3: < 2%), (2) being tolerant of N_2 in the sample, (3) handling common gas cylinders, including isotube, (4) preparing a gas sample that needs to be diluted with dry N_2 and dehumidified to the level of water vapor — less than 300 ppm; and (5) calculating and reporting the gas concentrations, ratios of hydrocarbons, and sample pressure.

Sample Introduction

The QEPAS prototype system can be connected to a gas cylinder or an isotube through the sample introduction enclosure. The gas sampler must be pressured to 80 psi to provide a driving force for a gas sample to fill the sensor chamber.

Gas Mixing Enclosure

The gas mixing enclosure takes in the gas sample

from the sample introduction panel and mixes one part with nine parts of N_2. The QEPAS needs a gas sample to be diluted to avoid too high concentrations to be out of the calibration range. This enclosure uses a commercially available gas blender to mix gas from the sample port with N_2 from an external cylinder.

Gas Drying Enclosure

The gas sample needs to be dried before entering the QEPAS chamber to minimize the effect of moisture on the detection. The drying enclosure uses a monotube dryer to dehumidify gas samples down to 300 ppm of water vapor. The monotube dryer uses a Nafion tube to transfer moisture from the sample line to a purging line surrounding the Nafion tube.

QEPAS Sensor with Laser Controller

The QEPAS measures the absorption of a gas sample using a tunable laser as a light source. The laser frequency is switched on and off on an absorption peak of the gas of interest, causing that gas to expand and contract with the switching frequency. This vibration of the gas is detected with a QTF, which has a resonance frequency equal to the switching frequency. The amplitude of the signal from the QTF is proportional to the gas concentration.

The QEPAS sensor consists of a QTF in the probe chamber for detection, a mid-infrared interband cascade laser as an excitation source, and an integrated printed circuit board to collect the data. An acoustical detection module houses the QTF and the cylindrical resonator. It is mounted on a 5° of freedom optical stage with three translation stages and two rotation stages. The laser module can also be adjusted in the vertical direction and has a collimation lens and a focusing lens; both of the lens positions can be adjusted with setscrews. The acoustical detection module must be further optimized by using the QEPAS scan feature in the QEPAS software to minimize the ratio mass spectrometry noise.

QEPAS Software

Two programs are developed for operating the QEPAS gas analyzer. The first program was developed by the Aramco Houston Research Center for monitoring the sample preparation system. The second program was developed by Bari University to control the sensing and to process data.

Fig. 2 *The realization of a QEPAS-based gas analysis system: (a) The portable QEPAS sensor box, and (b) All the components of the QEPAS assembled in a rack.*

Laboratory Testing, Calibration, and Performance

The QEPAS sensor box was previously tested with standard gases of individual components of C1, C2, and C3, diluted by N_2 into a series of concentrations — 1 ppm to ~1,000 ppm[9, 10]. The testing obtained good linearity of the QEPAS signal with the concentration of each individual component in the range, Table 1. Allan deviation analysis showed that for one second of integration time the detection limit for C1, C2, and C3 is ~90 ppb, ~7 ppb, and ~3 ppm, respectively. The detection limit achieved for C2 was a record for the QEPAS technique, and measuring C3 added a new capability to the technique. These limits are well

Fig. 3 *The enclosures and sample line for the QEPAS gas analyzer system.*
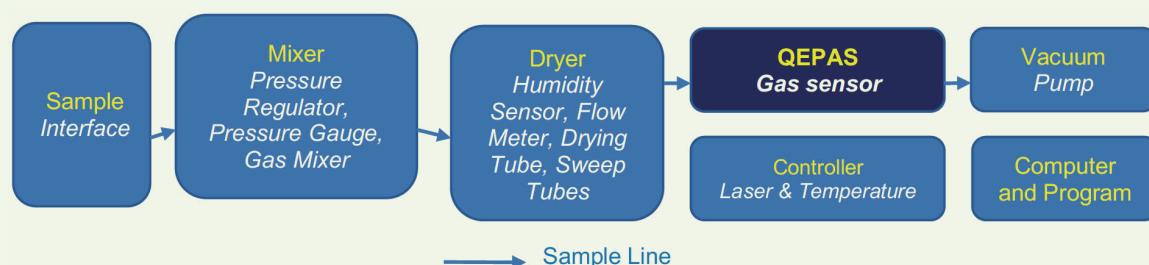
Table 1 *The performance comparison of QEPAS with representative optical sensors for hydrocarbon gas detection (after Sampaolo et al. (2020))[10].*

	CRDS[1]		TDLAS[2]		QEPAS			Reference
	C1	C2	C1	C2	C1	C2	C3	
Precision	30 ppb	10 ppb	300 ppt	50 ppt	90 ppb	7 ppb	3 ppm	
Response Time	< 1 s	< 1 s	< 1 s	< 1 s	< 1 s	< 1 s	< 1 s	
Linearity Range	1 – 5,000 ppm	0 – 500 ppm	0 – 100 ppm	0 – 50 ppm	0 – 1,000 ppm	0 – 1,000 ppm	10 – 1,000 ppm	10
Linearity Range					4 – 1,000 ppm	2 – 100 ppm	200 – 1,000 ppm	9
Linearity Range					100,000 – 1,000,000 ppm (10% – 100%)	10,000 – 100,000 ppm (1% – 10%)	2,000 – 20,000 ppm (0.2% – 2%)	This Study

[1]Picarro G4302 GasScouter
[2]Aerodyne Mini Trace Gas Monitor

below the sensitivity needed for a sensor striving for hydrocarbon detection in the petroleum exploration and engineering business, where concentrations of hydrocarbon gases are expected to be generally much above the ppm scale (usually percentage). C1-C2 and C2-C3 mixtures were also tested in the studies[9, 10] to demonstrate the capability of detecting multiple hydrocarbons by QEPAS.

In the study, we tested the QEPAS gas analyzer system, including the sensor box and new components of sampling preparation, with enlarged concentration ranges for individual C1, C2, and C3 that are typically encountered in natural gas samples from oil and gas fields for linearity assessment. Then we tested a series of C1-C2 and C1-C2-C3 mixtures and first confirmed that the QEPAS can simultaneously measure C1, C2, and C3 concentrations in the three hydrocarbon component gases.

Single Component (C1, C2, C3) Testing
Standard C1, C2, and C3 gases with certified concentrations, and high purity (99.9999%) N_2 were used to prepare artificial gas samples in the testing. Each single standard gas was diluted using the N_2 into different concentrations that may be encountered in natural gas samples from oil and gas fields. The mixing and quantitative dilution process is conducted in the gas mixing enclosure of the QEPAS system.

The C1 was diluted in a very large concentration range from 10% to 100% for the variation of C1 concentration in oil associated gas (least C1), condensate, wet gas, dry gas, or biogenetic gas (predominated C1)[2]. The C2 and C3 were diluted in the range of 1% to 10%, and 0.2% to 2%, respectively.

Testing was performed across the range of concentrations for each single gas component. Two samples taken at each target concentration were analyzed to check the reproducibility. Figures 4 to 6 show the waveforms, QEPAS signals, and linearity for the testing on C1, C2,

and C3, respectively. For C1, there are two diagnostic peaks at 55 mA and 62 mA in the waveforms, Fig. 4. The 55 mA peak is only used to determine the presence of C1, and the 62 mA peak is used to correlate the concentration of C1, because there is interaction between C1, C2, and C3 for 55 mA during the measurement when the gasses are mixed. The calibration curve of 62 mA, Fig. 4, illustrates a very good linearity for C1 in the range of typical concentrations in natural gas samples from an oil and gas field, and will be used to calculate the C1 concentration.

This process was repeated for C2 and C3 to identify the component, evaluate the linearity, and obtain calibration curves for calculating the concentrations. A linear fitting procedure used in the software to retrieve C1, C2, and C3 concentrations from the QEPAS spectra were reported[9]. The testing on single components has ensured that the system performs good linearity relations between the QEPAS response and the concentrations (percentage level) of individual C1, C2, and C3 gases.

C1-C2 and C1-C2-C3 Gas Mixtures Testing
While the detection of C1 and C2 characterized by well-defined absorption peaks in the interband cascade laser operating range is straightforward, the detection of C3 requires the extraction of the characteristic broadband absorption profiles, which merge with the C2 background signal in the interband cascade laser tuning range. Previous studies showed no cross-talk between C1 and C2 in the testing of the C1-C2 gas mixture, and developed a fitting procedure with a linear combination of reference spectra to retrieve C2 and C3 concentrations in the testing of the C2-C3 mixture[9, 10]. The QEPAS software used in our testing employed the procedure to calculate the C3 concentration.

Two component (C1-C2) and three component (C1-C2-C3) gas mixtures were used in the testing to evaluate the precision and linearity of the detection of

Fig. 4 *The sweep waveforms and calibration peaks for C1 testing.*
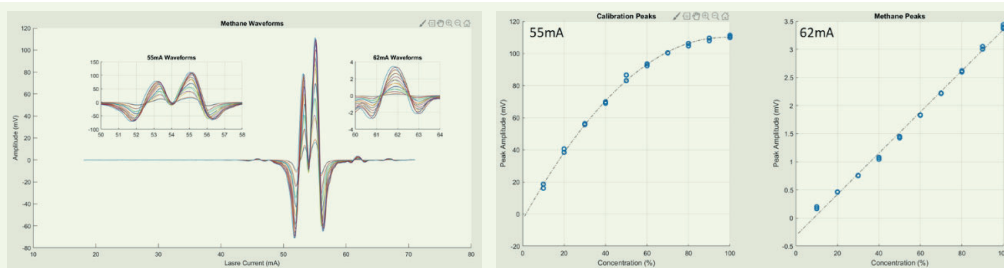
Fig. 5 *The sweep waveforms and calibration peaks for C2 testing.*
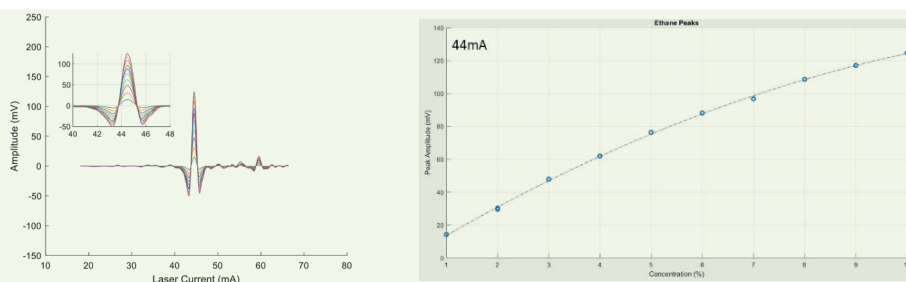
Fig. 6 *The sweep waveforms and calibration peaks for C3 testing.*
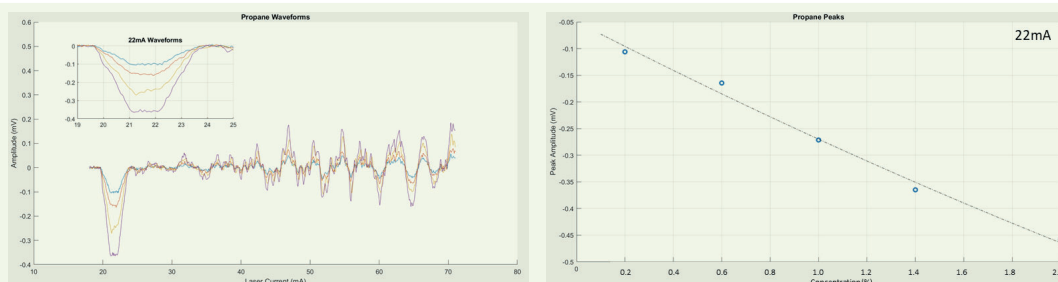
multicomponent gas by the QEPAS system. Certified C1, C2, and C3 gases, respectively, with a 10% concentration balanced to N_2, were diluted by pure N_2 in the gas mixing enclosure to make gas samples in the representative range as observed in the field — C1: 70% to ~100%, C2: 2% to ~10%, and C3: 0.4% to ~2%. Their actual concentrations and QEPAS measured values are compared and shown in Table 2 and Fig. 7 for the C1-C2 mixture, and Table 3 and Fig. 8 for the C1-C2-C3 mixture.

For the C1-C2 mixture, the measured C1 and C2 concentrations are very close to their actual values, showing good linearity with $R^2 > 0.99$, Figs 8a and 8b. The C1/C2 ratio, which is commonly used as a proxy of gas dryness and a geochemical fingerprint[2], shows good linearity as well, $R^2 > 0.99$, Fig. 8c, but with a

deviation when C1 presented the highest concentration (98%) and C2 presented the lowest concentration (2%) in the tested samples.

We first reported the results of simultaneous detection of C1, C2, and C3 in gas mixtures using the QEPAS technology. As previously shown in Fig. 8 for the C1-C2-C3 mixture, all comparisons between the actual and measured data demonstrate good linearity ($R^2 > 0.9899$), with only the C1 concentration showing a relatively big variation ($R^2 = 0.977$). There is good fitting for C2, however, an overestimate of the C1 concentration at its high concentration, e.g., measured 96% vs. actual 93%, and a shift for C3 — underestimated in the whole tested range — in the measurement. Obtaining accurate concentrations for individuals in a gas mixture consisting of a homologous series, e.g.,

Table 2 *The gas concentrations (%) and ratios of the C1-C2 mixture in the bench testing.*

Mixture #	C1 (%)		C2 (%)		C1/C2 (%)	
	Actual	**Measured**	**Actual**	**Measured**	**Actual**	**Measured**
1	98	98.0	2	1.8	49	54.4
2	95	94.7	5	4.6	19	20.6
3	90	88.2	10	10.0	9	8.8
4	90	90.4	5	4.6	18	19.7
5	80	81.5	10	10.0	8	8.2
6	80	81.9	5	5.1	16	16.1
7	70	70.4	10	10.0	7	7.0
8	70	70.6	5	5.2	14	13.6

Fig. 7 *A comparison of the actual and measured gas concentrations and ratios in the bench testing of the C1-C2 mixture.*
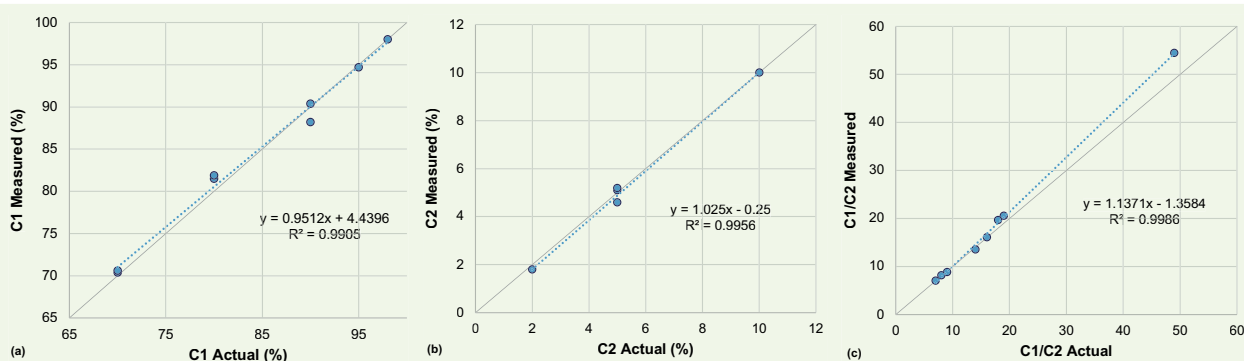
hydrocarbons, is much more challenging than dealing with single or double components[10, 25].

The good correlation and linearity between all measured gas concentrations and ratios, and their actual values, suggest that an improved algorithm and fitting procedure may generate more accurate results. Several aspects will be pursued to enhance the performance of the QEPAS system: (1) Quantitative control in the gas mixing enclosure, (2) Selective waveform features for better defining C3 in the background with C1 and C2, (3) Testing in a larger concentration range for C2 and C3 to have a more dynamic calibration curve, and (4) Trying multivariate analysis and machine learning methods to optimize the procedure to calculate gas concentrations in the mixture.

Currently, we suggest using the ratios of C1/(C1+C2+C3) as a dryness parameter/geochemical fingerprint in the application of the QEPAS system; because the gas ratio as a procedure of normalization eliminates the error and demonstrates better results than direct use of the concentrations, Figs. 8d and 8f.

Conclusions and the Way Forward

QEPAS is a novel laser-based optical absorption technology for gas sensing and chemical analysis. The technology is versatile in detecting trace gas and measuring concentrations and isotopic compositions of multiple gas components[8, 25, 26]. Recent advances has demonstrated the features of the QEPAS sensor[11, 20-22, 24], including a high-level of compactness, extreme high sensitivity (down to ppb/ppt), immunity to environmental noise, insensitivity to wavelength, the potential for continuous monitoring, overall reliability, and ruggedness for in situ operations.

QEPAS's main advantage is as a multicomponent gas detection and quantitative analyzer over semiconductor and electrochemical sensors. Currently, QEPAS cannot measure the extensive gas species for their concentrations and isotopic compositions in natural gas samples like the analytic instruments, e.g., GC-FID/TCD, QMS, and IRMS. The optical sensor is much smaller and relatively cheaper, requiring less maintenance and offering quicker analysis with higher sensitivity than the laboratory-based instruments.

Table 3 *The gas concentrations (%) and ratios of the C1-C2-C3 mixture in the bench testing.*

Mixture #	C1%		C2%		C3%	
	Actual	Measured	Actual	Measured	Actual	Measured
1	93	96.0	2	2.0	1	0.7
2	90	91.6	8	8.1	0.4	0.2
3	90	92.5	5	4.5	1	0.6
4	85	84.3	10	10.0	1	0.7
5	80	80.6	10	10.0	2	1.6

Mixture #	C1/C2		C1/(C2 + C3)		C1/C1+C2+C3)	
	Actual	Measured	Actual	Measured	Actual	Measured
1	46.5	48.0	31.0	35.6	0.97	0.97
2	11.3	11.3	10.7	11.0	0.91	0.92
3	18.0	20.6	15.0	18.1	0.94	0.95
4	8.5	8.4	7.7	7.9	0.89	0.89
5	8.0	8.1	6.7	6.9	0.87	0.87

Fig. 8 *The comparison of the actual and measured gas concentrations and ratios in the bench testing of the C1-C2-C3 mixture.*
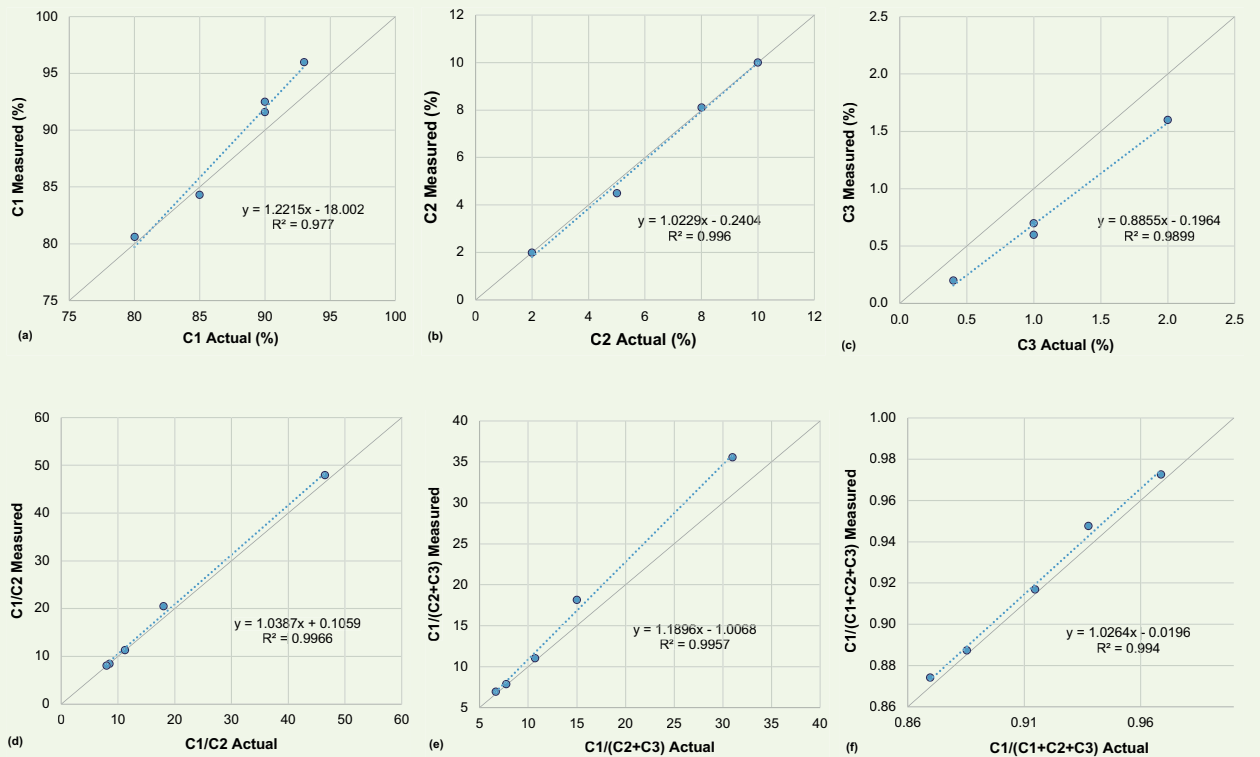
There are pros and cons for QEPAS in contrast to other optical absorption techniques, e.g., CRDS, ICOS, and TDLAS. Comparing technical specifications and performance is beyond the theme of the article. There are two advantages presented by QEPAS among the optical sensing techniques: (1) The capability to measure C3 concentrations as shown in the study, and (2) extremely high sensitivity in short optical pathlengths[11].

With its beneficial features and advantages, QEPAS has been proposed for field applications in monitoring sour gases (H_2S, CO_2) in offshore risers[6], downhole gas analysis[8,10], early fire[5], leak detection, and health, safety, environment monitoring[26]. A typical QEPAS sensor system can be compacted in a small lightweight size, supporting the deployment of the sensor in a portable analyzer, a downhole tool, and an unmanned aerial vehicle (UAV)[21, 27]. Several applications of QEPAS in real-world use have already been reported[28], including carbon monoxide detection in urban areas, monitoring of CH_4 in landfills, and leak detection of sulfur hexafluoride in a vacuum-seal test station for diesel engine injectors.

In the study, we developed and tested a QEPAS-based hydrocarbon gas analysis system. The QEPAS sensor is very sensitive for hydrocarbon gas detection — ppb to 10 ppm level. The sensor is not suitable for direct analyzing of a natural gas sample with hydrocarbon components in the ppm to percentage level. We integrated enclosures for introducing gas, mixing, and drying with a novel QEPAS sensor reported recently[9, 10] in a rack, and developed the software for monitoring the sample preparation. We have developed a new QEPAS prototype for detecting trace hydrocarbon gas — C1, C2, and C3 — and measuring their concentrations for oil industry samples by quantitative dilution and optical sensing.

The prototype system was tested with C1, C2, and C3 single components and C1-C2 and C1-C2-C3 mixtures, with a series of concentration gradients that are typically encountered in natural gas samples from oil and gas fields. The testing on the single components show that the system performs good linearity relations between QEPAS response and concentrations of individual C1, C2, and C3 gases in percentage levels, which expands the linearity range of the QEPAS detection from ppm to percentage range. The testing on the C1-C2 mixtures confirms that accurate C1 and C2 concentrations in percentage level can be achieved by the system.

We report here the testing results on C1-C2-C3 mixtures for the first time, demonstrating the capability of simultaneous detection of three hydrocarbon components and the probability to determine their precise concentrations by QEPAS sensing. Although there are some deviations of the measured C1%, C3%, and C1/(C2+C3) ratio compared to actual values, all measured concentrations and gas ratios illustrate good linear correlation with actual values, suggesting that it is highly possible to generate more accurate results by improving calibration curves and the fitting procedure.

The steps for the development and applications of QEPAS technology in the oil industry will be: (1) Testing natural gas samples and developing the fitting procedure to determine gas concentrations and isotopic compositions in the real samples (complex mixture), (2) Integrating a CO_2 and H_2S sensor with the hydrocarbon gas sensor in a compact device, (3) Reducing the size and increasing the robustness for field deployment, and (4) Developing the applications of on-site gas analysis while drilling, testing and production, offered by the advanced sensing, to support real-time decision making and time-lapse operation.

Acknowledgments

References

1. Rojey, A. and Jaffret, C.: *Natural Gas: Production, Processing, Transport*, Technip Editions, 1997, 429 p.

2. Prinzhofer, A. and Battani, A.: "Gas Isotopes Tracing: An Important Tool for Hydrocarbons Exploration," *Oil & Gas Science and Technology*, Vol. 58, Issue 2, March 2003, pp. 299-311.

3. Kosterev, A.A., Bakhirkin, Y.A., Curl, R.F. and Tittel, F.K.: "Quartz-Enhanced Photoacoustic Spectroscopy," *Optics Letters*, Vol. 27, Issue 21, 2002, pp. 1902-1904.

4. Miller, J.H., Awtry, A.R., McAndrew, B., Tittel, F.K., et al.: "Development of Optical Trace Gas Monitoring Technology for NASA Human Space Flight," *SAE Transactions*, Vol. 113, Section 1, 2004, pp. 297-304.

5. Kosterev, A.A., Tittel, F.K. and Bearman, G.: "Advanced Quartz-Enhanced Photoacoustic Trace Gas Sensor for Early Fire Detection," S*AE International Journal of Aerospace*, Vol. 1, Issue 1, April 2008, pp. 331-336.

6. Weppenaar, N., Kosterev, A., Dong, L., Tomazy, D., et al.: "Fiber Optic Gas Monitoring of Flexible Risers," paper presented at the Offshore Technology Conference, Houston, Texas, May 4-7, 2009.

7. Bybee, K.: "Fiber Optic Gas Monitoring for Flexible Risers," *Journal of Petroleum Technology*, Vol. 61, Issue 12, December 2009, pp. 73-74.

8. Csutak, S., Li, W., Sampaolo, A., et al.: "Photoacoustic Gas Detection," U.S. Patent 10,429,350, 2019.

9. Sampaolo, A., Csutak, S., Patimisco, P., Giglio, M., et al.: "Methane, Ethane and Propane Detection Using a Compact Quartz-Enhanced Photoacoustic Sensor and a Single Interband Cascade Laser," *Sensors and Actuators B: Chemical*, Vol. 282, March 2019, pp. 952-960.

10. Sampaolo, A., Menduni, G., Patimisco, P., Giglio, M., et al.: "Quartz-Enhanced Photoacoustic Spectroscopy for Hydrocarbon Trace Gas Detection and Petroleum Exploration," *Fuel*, Vol. 277, October 2020.

11. Patimisco, P., Scamarcio, G., Tittel, F.K. and Spagnolo, V.: "Quartz-Enhanced Photoacoustic Spectroscopy: A Review," *Sensors*, Vol. 14, Issue 4, April 2014, pp.

6165-6206.

12. Hodgkinson, J. and Tatam, R.P.: "Optical Gas Sensing: A Review," *Measurement Science and Technology*, Vol. 24, Issue 1, November 2012.

13. Erzinger, J., Wiersberg, T. and Zimmer, M.: "Real-Time Mud Gas Logging and Sampling during Drilling," *Geofluids*, Vol. 6, Issue 3, August 2006, pp. 225-233.

14. Field, S. and Hall, D.: "Direct Quadrupole Mass Spectrometry Advanced Borehole Gas and Cuttings Volatile Analysis for Oil and Gas Wells," *Outcrop,* Vol. 62, Issue 2, February 2013, pp. 9-14.

15. Philp, R.P. and Monaco, G.L.: "Applications of Stable Isotopes in Hydrocarbon Exploration and Environmental Forensics," in Baskaran, M. (ed.) *Handbook of Environmental Isotope Geochemistry. Advances in Isotope Geochemistry,* Springer, 2012, pp. 639-677.

16. Elshahawi, H., Hashem, M.N., McKinney, D., Ardila, M., et al.: "The Power of Real-Time Monitoring and Interpretation in Wireline Formation Testing — Case Studies," *SPE Reservoir Evaluation & Engineering*, Vol. 10, Issue 3, June 2007, pp. 241-250.

17. Jones, C., Gao, L., Perkins, D., Chen, D., et al.: "Field Test of the Integrated Computational Elements: A New Optical Sensor for Downhole Fluid Analysis," paper presented at the SPWLA 54th Annual Logging Symposium, New Orleans, Louisiana, June 22-26, 2013.

18. Jin, W., Ho, H.L., Cao, Y.C., Ju, J., et al.: "Gas Detection with Micro- and Nano-Engineered Optical Fibers," *Optical Fiber Technology*, Vol. 19, Issue 6, Part B, December 2013, pp. 741-759.

19. Du, Z., Zhang, S., Li, J. and Gao, N.: "Mid-Infrared Tunable Laser-Based Broadband Fingerprint Absorption Spectroscopy for Trace Gas Sensing: A Review," *Applied Sciences*, Vol. 9, Issue 2, January 2019, pp. 338-370.

20. Patimisco, P., Sampaolo, A., Dong, L., Tittel, F.K., et al.: "Recent Advances in Quartz Enhanced-Photoacoustic Sensing," *Applied Physics Reviews*, Vol. 5, Issue 1, March 2018.

21. Ma, Y.: "Review of Recent Advances in QEPAS-Based Trace Gas Sensing," *Applied Sciences*, Vol. 8, Issue 10, October 2018.

22. Palzer, S.: "Photoacoustic-Based Gas Sensing: A Review," *Sensors*, Vol. 20, Issue 9, May 2020.

23. Kosterev, A.A., Dong, L., Thomazy, D. and Tittel, F.K.: "QEPAS for Chemical Analysis of Multicomponent Gas Mixtures," *Applied Physics B*, Vol. 101, Issue 3, November 2010, pp. 649-659.

24. Spagnolo, V., Patimisco, P. and Tittel, F.K.: "Quartz-Enhanced Photoacoustic Spectroscopy for Gas Sensing Applications," Chapter 15 in *Mid-Infrared Optoelectronics, Materials, Devices and Applications*, Woodhead Publishing, 2020, pp. 597-659.

25. Wang, Z., Wang, Q., Ching, J.Y-L., Wu, J.C-Y., et al.: "A Portable Low Power QEPAS-Based CO_2 Isotope Sensor Using a Fiber Coupled Interband Cascade Laser," *Sensors and Actuators B: Chemical*, Vol. 246, July 2017, pp. 710-715.

26. Spagnolo, V., Dong, L., Kosterev, A.A. and Tittel, F.K.: "Modulation Cancelation Method for Isotope $^{18}O/^{16}O$ Ratio Measurements in Water," *Optics Express*, Vol. 20, Issue 4, 2012, pp. 3401-3407.

27. Menduni, G., Sgobba, F., Russo, S.D., Ranieri, A.C., et al.: "Fiber-Coupled Quartz-Enhanced Photoacoustic Spectroscopy System for Methane and Ethane Monitoring in the Near-Infrared Spectral Range," *Molecules*, Vol. 25, Issue 23, November 2020.

28. Giglio, M., Patimisco, P., Sampaolo, A., Wu, H., et al.: "New Developments in Quartz-Enhanced Photoacoustic Sensing Real-World Applications," paper presented at the 22nd International Conference on Transparent Optical Networks (ICTON), Bari, Italy, July 19-23, 2020.

About the Authors

Dr. Pan Luo

Ph.D. in Geology,
Chinese Academy of Sciences

Dr. Pan Luo joined Saudi Aramco in 2013 as a Research Geologist, working with the Geology Technology Division in the Exploration and Petroleum Engineering Center – Advanced Research Center (EXPEC ARC).

He works on the development of geochemical tools for petroleum system analysis, unconventional resource assessment, real-time and time-lapse geochemistry applications in the upstream oil business. Pan is leading multiple projects in regional charge assessment and the

application of advanced gas sensors. His work has been published not only in academic journals, in the domains of geology and petroleum geochemistry; but he was also recognized by the industry as a 2017 World Oil Award Finalist for Best Exploration Technology.

In 2010, Pan received his Ph.D. degree in Geology from the Institute of Geology and Geophysics, Chinese Academy of Sciences, Beijing, China, and then started his career in PetroChina as a postdoctoral researcher.

Jonathan D. Harrist

B.S. in Electrical Engineering,
University of Louisiana at
Lafayette

Jonathan D. Harrist joined the Aramco Americas' Houston Research Center in September 2018 as a Product Development Engineer with a firmware engineering background. His research areas include using acoustics for flow metering and cement

bonding applications, developing downhole wireline tools, and data acquisition hardware and firmware.

Jonathan received his B.S. degree in Electrical Engineering from the University of Louisiana at Lafayette, Lafayette, LA.

Rabah Mesdour

B.S. in Petroleum Engineering,
Algerian Petroleum Institute

Rabah Mesdour joined Saudi Aramco in November 2011 as a Petroleum Specialist with the Gas Reservoir Management Department, working on offshore gas fields, northwest gas and Red Sea projects. In 2017, he moved to Saudi Aramco's Unconventional Resources Group, working as a Consultant Reservoir Engineer overlooking the Jafurah source rock,

the south Ghawar and north Arabian fields.

Rabah has authored and coauthored 20 plus technical papers and journals papers, and published two patents.

He received his B.S. degree in Petroleum Engineering from the Algerian Petroleum Institute, Boumerdas, Algeria.

Nathan A. StMichel

M.S. in Mechanical Engineering,
Massachusetts Institute of
Technology

Nathan A. StMichel joined the Aramco Americas' Houston Research Center in January 2019 as a Research Engineer. He is currently working with the Sensors Development Team where he supports the design and testing of novel sensing ideas that are optimized for

Aramco's specific needs.

Nathan received his B.S. and M.S. degrees, both in Mechanical Engineering, from the Massachusetts Institute of Technology, Cambridge, MA.

A Framework for Coupled Physics Deep Learning Inversion and Multiparameter Joint Inversion

Dr. Daniele Colombo, Dr. Ersan Turkoglu, Dr. Weichang Li and Dr. Diego Rovetta

Abstract /

A new approach to the inversion and joint inversion of geophysical data is described. We take advantage of the domains of local optimization and of the machine learning or deep learning technique to generate efficient optimization schemes to reduce uncertainties in the model parameter estimations, exploit the image segmentation capability of deep learning techniques, and guarantee compliance with the requirement of physics for the wave propagation.

The domains of physics-driven optimization, based on data misfit functionals, and of deep learning optimization, based on model misfit (loss), are coupled by multiple penalty functions imposed on the common model term of the physical domain such as performed in a joint inversion approach. The procedure is complemented by network retraining with partial inversion results to augment the network knowledge base and enable more physics oriented deep learning predictions.

After several iterations, the procedure tends to converge to models satisfying both physics and deep learning optimization schemes by providing at the same time better resolution and accuracy in parameter estimation. The developed method is demonstrated on synthetic and field transient electromagnetic (EM) data.

Introduction

Machine learning or deep learning applied to inverse problems is a growing area of interest. The expectations are for quickly mapping the data domain into the model space by adopting purely data-driven approaches, avoiding typical simplifications of the problem such as linearization, and obtaining robust and higher resolution descriptions of the model parameters. Such expectations, based on initial demonstrations performed on statistically well-behaved distributions of synthetic models and associated data, have quickly shown limitations when applied to field data.

Several authors[1-3] reported disappointing results when deep learning predicted resistivity models were used for simulating the propagation of electromagnetic (EM) wavefields for time-domain or frequency-domain applications such as logging while drilling or near surface characterization with transient electromagnetics (TEM). Such observations have induced various researchers to invoke the introduction of physics in the training and derivation of the neural network (NN) models[2, 4]. Recent and ongoing research is in the direction of introducing physics in the derivation of machine learning surrogate inversion schemes.

Physics informed NN schemes[1, 5, 6] introduce physics constraints in composite loss functions to act as regularization mechanisms toward nonphysical solutions for the derivation of the network parameters. Such schemes, while steering the NN predictions in a physics compliant direction, are bounded by the initial choice of the model space used for training and do not enable the network to evolve and adapt toward different data distributions previously unseen by the network.

To overcome typical limitations in the application of machine learning techniques to real world geophysical inversion applications, the adopted machine learning/deep learning schemes should become compliant to the physics requirements, and should enable automatic expansion of the network knowledge base. This would allow the refinement of the corresponding predictions for model distributions different from those used in the initial training. The latter requirement will in turn enable the use of small training sets, an important requirement in geoscience and engineering applications where the collection of vast training sets is typically costly, time-consuming, or intensive from the computing side.

The scheme proposed by Colombo et al. (2021)[3], described and expanded in the present contribution, is addressing the above problems through an iterative and coupled physics deep learning inversion (PhyDLI) scheme involving dynamic network retraining for expanding its knowledge base.

Method

Figure 1 shows the general framework of a coupled PhyDLI for single or multiple parameters subject to regularization by means of penalty functions applied to the model term. Considering a multiparameter model

Fig. 1 *General framework of a coupled PhyDLI for single or multiple parameters.*
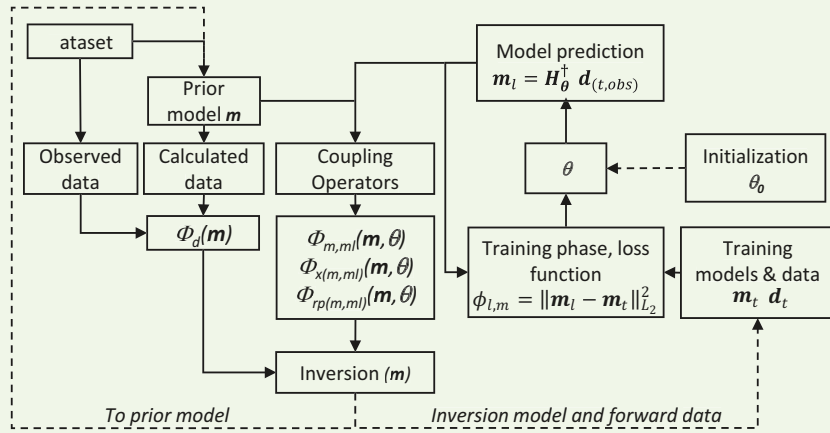
space, the model vector is described by $\boldsymbol{m} = [\boldsymbol{m}_1, \boldsymbol{m}_2, \ldots, \boldsymbol{m}_M]$ where for the geophysical domain we may consider, e.g., P-wave velocity, resistivity, and density, among other possible parameters. The corresponding data space is defined by the vector $\boldsymbol{d} = [\boldsymbol{d}_1, \boldsymbol{d}_2, \ldots, \boldsymbol{d}_N]$, containing the observed data, e.g., traveltimes/waveforms, TEM dBz/dt magnetic field responses, gravity acceleration, etc. The PhyDLI composite objective function contains data misfit and model misfit with penalty terms that can be written as:

$$\phi_t(\boldsymbol{m}, \boldsymbol{\theta}) = \phi_d(\boldsymbol{m}) + \phi_{l,m}(\boldsymbol{\theta}) + \mu_1\,\phi_{m,ml}(\boldsymbol{m}, \boldsymbol{\theta}) + \mu_2\phi_{x(m,ml)}(\boldsymbol{m}, \boldsymbol{\theta}) + \mu_3\phi_{rp(m,ml)}(\boldsymbol{m}, \boldsymbol{\theta}) ,$$

<div align="right">1</div>

where $\phi_d(\boldsymbol{m})$ is defined as:

$$\phi_d(\boldsymbol{m}) = (\boldsymbol{Gm} - \boldsymbol{d}_{obs})^T \boldsymbol{W}_d^T \boldsymbol{W}_d(\boldsymbol{Gm} - \boldsymbol{d}_{obs}) = \|\boldsymbol{W}_d(\boldsymbol{Gm} - \boldsymbol{d}_{obs})\|_{L_2}^2$$

<div align="right">2</div>

where $\boldsymbol{d}_{abs}$ is the vector of the observed data, $\boldsymbol{G}$ is the Jacobian, and $\boldsymbol{W}_d$ is a data weighting matrix (and $\boldsymbol{W}_d^T\boldsymbol{W}_d$ the equivalent inverse covariance). The deep learning objective, i.e., loss, function $\phi_{l,m}$ is defined as:

$$\phi_{l,m} = \left\|\boldsymbol{H}_\theta^\dagger \boldsymbol{d}_t - \boldsymbol{m}_t\right\|_{L_2}^2 ,$$

<div align="right">3</div>

where the pseudoinverse operator $\boldsymbol{H}_\theta^\dagger$ is parameterized by $\boldsymbol{\theta}$. The optimization of the network parameters, $\boldsymbol{\theta}$, is performed offline during the training phase using training models, $\boldsymbol{m}_t$, and predicted models associated to the data responses, $\boldsymbol{d}_t$. The optimized network is then applied during the testing phase to observed data, $\boldsymbol{d}_{obs}$, for predicting the physical domain model parameter distributions and obtaining $\boldsymbol{m}_l$ (online phase):

$$\boldsymbol{m}_l = \boldsymbol{H}_\theta^\dagger \boldsymbol{d}_{obs} .$$

<div align="right">4</div>

A penalty term linking the two inversion domains and based on the common (physical) model term, $\boldsymbol{m}$, can be written as:

$$\phi_{m,ml}(\boldsymbol{m}, \boldsymbol{\theta}) = \|\boldsymbol{W}_m(\boldsymbol{m} - \boldsymbol{m}_l(\boldsymbol{\theta}))\|_{L_2}^2 ,$$

<div align="right">5</div>

where $\boldsymbol{m}_l$ represents the model prediction (Eqn. 4) obtained during the online phase and $\boldsymbol{W}_m$ is the model covariance matrix. Additional penalty terms can be borrowed from joint inversion schemes to be based on structure ϕ_x or compositional ϕ_{rp}, e.g., rock physics, operators[7]. Structure operators for two models (i, j) are based on cross-gradients[8]:

$$x(\boldsymbol{m}_i, \boldsymbol{m}_j) = \nabla \boldsymbol{m}_i \times \nabla \boldsymbol{m}_j ,$$

<div align="right">6</div>

or summative gradients[9]:

$$x(\boldsymbol{m}_i, \boldsymbol{m}_j) = \frac{\nabla \boldsymbol{m}_i}{\sqrt{|\nabla \boldsymbol{m}_i|^2 + \varepsilon^2}} + h \frac{\nabla \boldsymbol{m}_j}{\sqrt{|\nabla \boldsymbol{m}_j|^2 + \varepsilon^2}}$$

<div align="right">7</div>

where $h = \pm 1$ is the correlation sign, and ε is a damping parameter. The difference between the structure coupling terms is that cross-gradients, Eqn. 6, constrain the general direction of the gradients regardless of the respective polarity, i.e., sign, while summative gradients, Eqn. 7, consider the polarity, i.e., correlated vs. anticorrelated distributions, allowing the injection of more constraints into the solution. The compositional operator, ϕ_{rp}, is a generic nonlinear function, f_{rp}, relating the parameters of two models (i, j), such as:

$$\hat{\boldsymbol{m}}_j = f_{rp}(\boldsymbol{m}_i)$$

<div align="right">8</div>

where $\hat{\boldsymbol{m}}_j$ is an estimate of the model $\boldsymbol{m}_j$. Structure operators can be used to exploit the image segmentation capability of deep learning, thereby encouraging the resemblance of the shape of the model parameter distributions while compositional operators are expected to become valuable for multiple physical parameter optimizations. Finally, weights, μ, are used to balance the contributions of the different terms in the composite objective function. As per typical joint inversion schemes, the setting of weights is facilitated by the application of appropriate normalizations to the objective function terms[10].

The objective function in Eqn. 1 is solved by alternate minimizations, yielding:

$$m^k = arg \min_{m} \phi_t(m, \theta^{k-1}) =$$

$$\phi_d(m) + \mu_1 \phi_{m,ml}(m, \theta^{k-1}) +$$

$$\mu_2 \phi_{x(m,ml)}(m, \theta^{k-1}) + \mu_3 \phi_{rp(m,ml)}(m, \theta^{k-1}) \qquad 9$$

for the physics domain, and:

$$\theta^k = arg \min_{\theta} \left\| H_\theta^\dagger d_t - m^k \right\|_{L_2}^2, \qquad 10$$

for the deep learning domain. The optimization of the physics procedure is performed with second order differential operators and the deep learning inversion with second order or first order stochastic gradient descent methods depending on the number of parameters involved in the backpropagation process. The procedure is complemented by network base augmentation utilizing the inversion models and corresponding forward responses. An optional aspect is the use of deep learning predictions as prior models for physics inversion other than for penalty.

Synthetic Test

The procedure is demonstrated with a synthetic test using TEM data and a feedforward network consisting of an input layer, a single hidden layer of 30 neurons, and an output layer. Use of a deeper NN model provided equivalent results. Two sets of 1D models are randomly generated to represent statistically different distributions in the model space, Table 1 and Fig. 2, which are called Training, a data set used for training

and optimizing the network parameters, and Alien, a data set for testing the network prediction capability on previously "unseen" data. The goal is to combine results from the Alien inversion using the scheme in Fig. 1 to iteratively augment the initial Training set, retrain the NN model and steer new predictions toward physics compliant models. We applied the schemes where the NN prediction is used as prior and penalty at the same time.

The results of the PhyDLI process (cycles) are displayed in Table 2 and Fig. 3. The prediction from the initial Training set shows slightly higher model root mean square (RMS) and better data RMS than starting the inversion from a half space of 10 Ωm. The Training set inversion results are slightly worse than the half space inversion and representation of the density cross plot of the true and predicted parameters, Figs. 3a and 3b, show that the results are still far from the diagonal.

After the repetition of the PhyDLI procedure where the partial inversion data, i.e., 10th iteration, are used to retrain the NN, the corresponding predictions and inversion results provide much smaller residuals for both model and data and the corresponding density cross plots align better along the diagonal value. Figure 4 shows the evolution of the model space during the PhyDLI process.

Field Data

A test of the PhyDLI scheme is performed on field TEM data acquired in an arid environment with dry fluvial channels (*wadi*). The TEM soundings were acquired with a grid of 240 × 240 m for characterizing the near surface and enhancing the shallow velocity for seismic imaging. The same Training distribution was used for the initial NN predictions and progressively augmented with additional inversion results after each PhyDLI cycle. In this case, we tested a scheme where the NN predictions are used only as penalty terms, Fig. 1, and not as prior models at each cycle.

A half space inversion was performed and used as a benchmark while the PhyDLI procedure was run five times to achieve a large data RMS misfit improvement corresponding to 90% from the initial RMS and a

Table 1 *Characteristics of the Training and Alien data sets.*

Data Set	NN Models	Resistivity Mean (Ωm)	Resistivity Standard Deviation (Ωm)
Training	5,000	31.6	2.5
Alien	5,000	5.6	1.8

Fig. 2 *The Training and Alien data sets: (a) Model space distribution, and (b) data responses represented as apparent resistivity.*
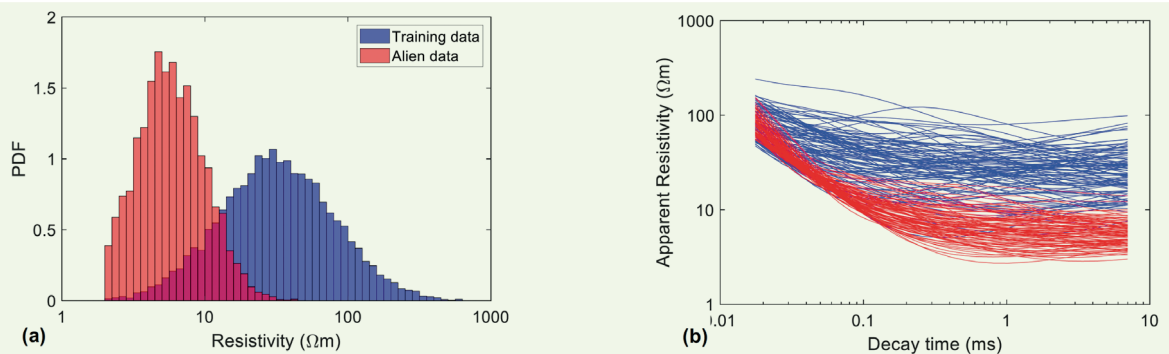
Table 2 *The PhyDLI performance on the Alien data set (HS = half space; TR = initial Training set; Bi, Ci, etc. = partial inversion results from a previous cycle).*

	Predictions Prior and Penalty	Modified RMS Prediction	Data RMS Prediction	Modified RMS Inversion	Data RMS Inversion
0	HS	0.32	11.23	0.230	0.590
A	TR	0.39	7.83	0.340	0.660
B	TR + HS	0.20	2.62	0.192	0.299
C	TR + HS + Bi	0.179	1.56	0.175	0.213
D	TR + HS + Bi + Ci	0.174	1.02	0.171	0.172
E	TR + HS + Bi + Ci + Di	0.177	0.86	0.174	0.184
F	TR + HS + Bi + Ci + Di + Ei	0.174	0.74	0.171	0.175

Fig. 3 *The prediction and inversion performances over different cycles of PhyDLI (40th iteration): (a) and (b) "A" cycle, and (c) and (d) "F" cycle (see Table 2).*
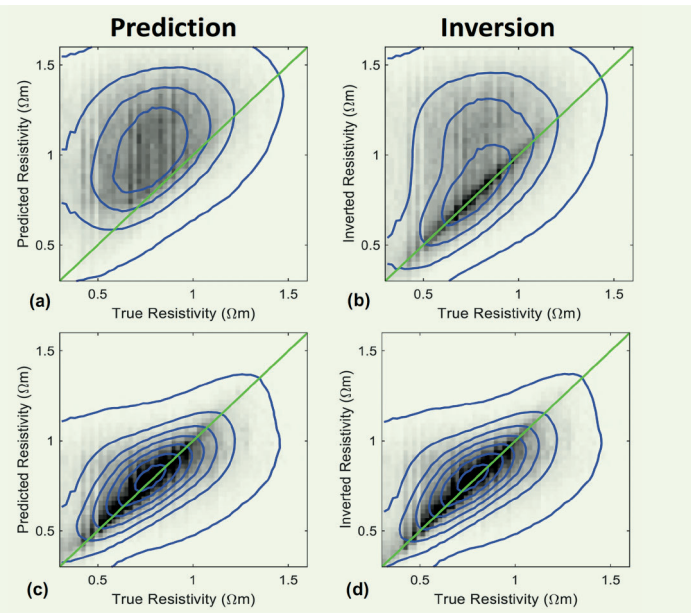
Fig. 4 *The model space evolution from the PhyDLI process: (a) Evolution of the network predictions with reference to the true distributions, and (b) parameter distributions from the inversion process.*
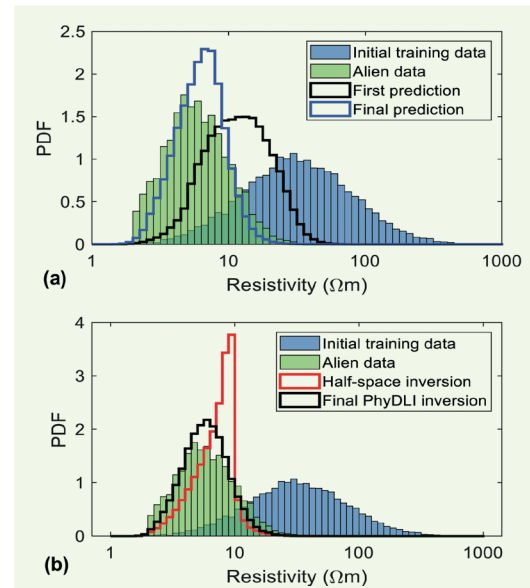
smaller data RMS residual when compared to the half space inversion.

Figure 5 displays the final resistivity prediction from the NN model compared to the geomorphological features shown by the elevation map. The cross section in Fig. 6 displays a standard half space inversion with the final PhyDLI results, displaying a sharper definition of the expected geological layering.

Conclusions

We have demonstrated a novel scheme for coupled PhyDLI. Such an approach combines the benefits of highly accurate and physics-driven second order local optimization schemes with the pseudo-stochastic and nonlinear machine learning/deep learning inversion schemes. The approach is addressing a common problem in geophysical applications represented by the scarcity of labeled data to be used for training NN, which in turn, prevents the derivation of highly accurate pseudo-inverse operators.

The PhyDLI schemes compete and collaborate at the same time to obtain a range of models that could be potentially used to infer parameter error estimates and reduce the risk of ending the inversion in local minima. After several iterations, the two procedures embedded in PhyDLI converge to commonly agreeable models that outperform individual inversion schemes. The extension to multiparameter joint inversion is

Fig. 5 *The field TEM data: (a) Geomorphological features (wadi channels 1, 2, and 3) shown by the elevation map and acquisition grid, and (b) NN prediction of shallow resistivity at the last PhyDLI cycle.*
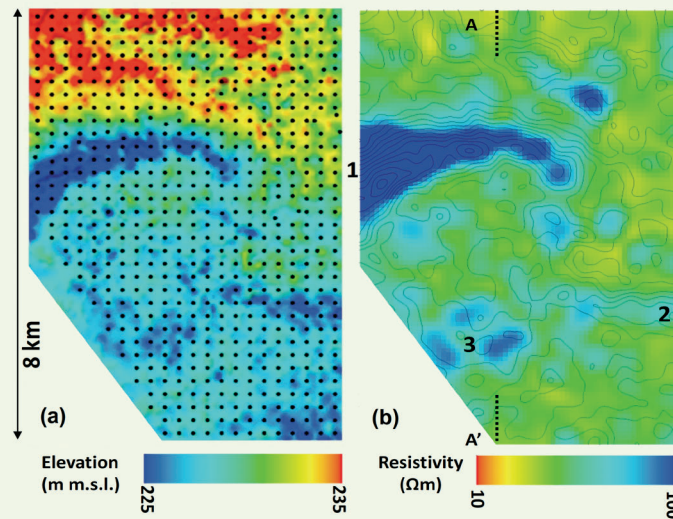
Fig. 6 *The inversion results for the TEM field data where the final prediction and inversion from the PhyDLI scheme is compared to the half space, stand-alone, inversion. The PhyDLI process obtains a lower data RMS when compared to the half space inversion, as well as a better reconstruction of shallow wadi channels (arrows) and of the underlying layered geology.*
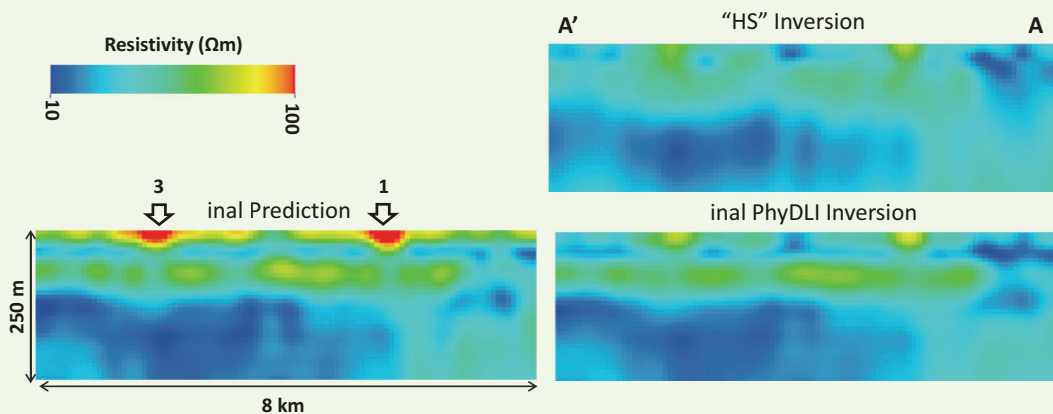
straightforward, a domain we plan to analyze in future studies. The devised procedure has a general validity that can be extended to the solution of general inverse problems for a variety of disciplines.

References

1. Jin, Y., Wu, X., Chen, J. and Huang, Y.: "Using a Physics-Driven Deep Neural Network to Solve Inverse Problems for LWD Azimuthal Resistivity Measurements," SPWLA paper, presented at the SPWLA 60th Annual Logging Symposium, The Woodlands, Texas, June 15-19, 2019.

2. Shahriari, M., Pardo, D., Picon, A., Galdran, A., et al.: "A Deep Learning Approach to the Inversion of Borehole Resistivity Measurements," *Computational Geosciences*, Vol. 24, Issue 2, June 2020, pp. 971-994.

3. Colombo, D., Turkoglu, E., Li, W., Sandoval-Curiel, E., et al.: "Physics-Driven Deep Learning Inversion with Application to Transient Electromagnetics," *Geophysics*, Vol. 86, Issue 3, May-June 2021, pp. E209-E224.

4. Russel, B.: "Machine Learning and Geophysical Inversion — A Numerical Study," *The Leading Edge*, Vol. 38, Issue 7, July 2019, pp. 498-576.

5. Raissi, M., Perdikaris, P. and Karniadakis, G.E.: "Physics Informed Neural Networks: A Deep Learning Framework for Solving Forward and Inverse Problems Involving Nonlinear Partial Differential Equations," *Journal of Computational Physics*, Vol. 378, February 2019, pp. 686-707.

6. Fuks, O. and Tchelepi, H.A.: "Limitations of Physics Informed Machine Learning for Nonlinear Two-Phase Transport in Porous Media," *Journal of Machine Learning*

for Modeling and Computing, Vol. 1, Issue 1, 2020, pp. 19-37.

7. Colombo, D. and Rovetta, D.: "Coupling Strategies in Multiparameter Geophysical Joint Inversion," *Geophysical Journal International*, Vol. 215, Issue 2, November 2018, pp. 1171-1184.

8. Gallardo, L.A. and Meju, M.A.: "Joint Two-Dimensional DC Resistivity and Seismic Travel Time Inversion with Cross Gradient Constraints," *Journal of Geophysical Research Atmospheres*, Vol. 109, Issue B3, 2004.

9. Molodtsov, D.M., Colombo, D., Roslov, Y.V., Troyan, V.N., et al.: "Comparison of Structural Constraints for Seismic-MT Joint Inversion in a Subsalt Imaging Problem," *Saint Petersburg State University Bulletin*, Vol. 4, 2015, pp. 230-236.

10. Rovetta, D. and Colombo, D.: "Analysis of Inter-Domain Coupling Constraints for Multi-Physics Joint Inversion," *Inverse Problems*, Vol. 34, Issue 12, August 2018, pp. 1-31.

About the Authors

Dr. Daniele Colombo

Ph.D. in Geophysics, Milan University

Dr. Daniele Colombo is a Senior Geophysical Consultant and the Champion of Reservoir Multiphysics Technology working in the Geophysics Technology Division of Saudi Aramco's Exploration and Petroleum Engineering Center – Advanced Research Center (EXPEC ARC). His research interests include seismic and electromagnetic imaging, and physics-coupled deep learning inversion with application to exploration and reservoir monitoring.

Prior to joining Saudi Aramco in 2009, Daniele held various positions in service companies such as the Technical and R&D Manager for seismic imaging in complex geology, and as the Data Processing Manager for Schlumberger in Milan and Calgary, respectively. He was at the forefront of the development of multiphysics imaging and joint inversion methods for integrated seismic electromagnetic gravity velocity modeling applied to seismic depth imaging.

This research activity gained Daniele several industry recognitions and awards, including a

Society of Exploration Geophysicists Honorable Mention for Best Paper in *The Leading Edge* in 2016, and also (with a team) the Saudi Aramco CEO Excellence Award in 2018 for Disruptive Technology Creation. In 2020, he received the American Association of Petroleum Geologists Robert R. Berg Outstanding Research Award.

Daniele has published more than 100 peer-reviewed papers on a variety of subjects, including microseismic monitoring during reservoir stimulation, multiphysics joint inversion, depth imaging in complex geology, near surface full waveform inversion and surface consistent modeling, electromagnetic applications for reservoir fluid monitoring, and deep learning applied to the solution of inverse problems.

In 1991, Daniele received his M.S. degree, and in 1994, he received his Ph.D. degree, both in Geophysics from Milan University, Milan, Italy. This was followed by a postdoctoral position at the National Institute for Geophysics and Volcanology in Rome.

Dr. Ersan Turkoglu

*Ph.D. in Geophysics,
University of Alberta*

Dr. Ersan Turkoglu is a Research Geophysicist working in the Geophysics Technology Division of Saudi Aramco's Exploration and Petroleum Engineering Center – Advanced Research Center (EXPEC ARC). Since joining Saudi Aramco in 2013, Ersan has worked on land, marine, and airborne electromagnetic (EM) data acquisition, inversion and integration with other disciplines.

He previously worked for Quantec Geoscience of Toronto from 2011 to 2013, and WesternGeco Canada from 2008 to 2011, focusing on mineral and geothermal exploration using land-based EM and potential field methods.

In 1999, Ersan received his B.S. degree from Istanbul University, Istanbul, Turkey, followed by an M.S. degree from Istanbul Technical University, Istanbul, Turkey, both in Geophysical Engineering. In 2009, he received his Ph.D. degree in Geophysics from the University of Alberta, Edmonton, Canada. Ersan studied the tectonics of active continental margins and primarily focused on understanding the Arabia-Eurasia collision by use of magnetotellurics (MT) during his Ph.D. He used long period MT resistivity images to show that the Anatolian high plateau might be elevated by an upwelling hot asthenosphere similar to the Tibetan high plateau.

Dr. Weichang Li

Ph.D. in Electrical and Oceanographic Engineering, Massachusetts Institute of Technology

Dr. Weichang Li leads the AI Technology Team at Aramco Americas' Houston Research Center, Houston, TX. His current research is focused on developing machine learning and signal processing algorithms/models for geophysics, geoscience and petroleum engineering applications.

Prior to joining Aramco in 2015, Weichang had been with ExxonMobil's Corporate Strategic Research Lab since 2008, where he led the machine learning team from 2011 to 2014.

Weichang co-organized the Society of Exploration Geophysicists (SEG) machine learning post-convention workshop from 2018 to 2021, and the Society for Industrial and Applied Mathematics Data Mining workshop in Geoscience Applications in 2018. He is the Associate Editor for the *Geophysics* special section on Machine Learning, and recently, the *IEEE Transactions on Neural Network and Learning Systems* special issue on Deep Learning for Earth Sciences and Planetary Geosciences.

Weichang is a member of the SEG research committee and the National Science Foundation's Institute for Research on Innovation and Science working group on machine learning for fiber optic distributed acoustic sensing. He has published over 90 papers and 15 patents.

Weichang obtained his M.S. degree (dual) in Electrical Engineering and Computer Sciences, and Ocean Engineering in 2002, and his Ph.D. degree in Electrical and Oceanographic Engineering in 2006, all from the Massachusetts Institute of Technology, Cambridge, MA. Following this, he was an Office of Naval Research postdoctoral fellow at Woods Hole Oceanographic Institution from 2006 to 2007.

Dr. Diego Rovetta

Ph.D. in Information Engineering, Polytechnic University of Milan

Dr. Diego Rovetta is a Research Geophysicist working at Aramco's Overseas Company on multi-geophysics integration and joint inversion. He previously worked as a Researcher for Politecnico di Milano, collaborating with different companies (Eni, Saipem, Schlumberger, etc.), and as a Geophysicist at the WesternGeco Electromagnetics Center of Excellence.

In 2002, Diego received his M.S. degree in Telecommunications Engineering from Polytechnic University of Milan, Milan, Italy, studying nonlinear inverse problem applications using simulated annealing. In 2006, he received his Ph.D. degree in Information Engineering, from the same institute, focusing on geophysical inverse problems.

Diego is currently the president of the European Association of Geoscientists and Engineers' local chapter in the Netherlands.

Simulation of Advanced Waterflooding in Carbonates Using a Surface Complexation-Based Multiphase Transport Model

Dr. Moataz O. Abu-AlSaud, Salah H. Al-Saleh, Dr. Subhash C. Ayirala and Dr. Ali A. Yousef

Abstract /

Understanding the injection water chemistry effect, in terms of both salinity and ionic composition, is becoming crucial to increase oil recovery from waterflooding in carbonate reservoirs. Various studies have shown that surface charge alteration is the main mechanism behind favorable wettability changes toward water-wet conditions observed during the injection of controlled ionic composition water in carbonates. Therefore, the synergistic coupling between multiphase transport and electrokinetics of brine/calcite and brine/crude oil interfaces becomes important to optimize injection water compositions for enhanced oil recovery in carbonates.

In this investigation, the electrokinetic interactions of brine and crude oil in carbonates are accounted for and coupled with the multiphase Darcy flow model. The electrokinetic interactions are parametrized by the zeta potential values of brine/calcite and crude oil/brine interfaces, which are determined using a surface complexation model (SCM). The SCM zeta potential parameters are computed based on the local concentration of aqueous ions that follow the transport equation. The relative permeability and capillary pressure curves are altered based on zeta potential shifts, which resembles the wettability alteration process. The SCM zeta potentials are compared with the experimental zeta potential measurements, while the multiphase transport model coupled with geochemistry is validated through a comparative coreflood experimental data reported in the literature.

The SCM results governed by specified surface geochemical reactions agreed well with zeta potential measurements obtained at both calcite/brine and crude oil/brine interfaces. The coupled geochemical SCM with multiphase transport model accurately matched both recovery and pressure drop data from forced imbibition tests reported[1] in both secondary and tertiary modes. The generated relative permeability curves followed Craig's rules in shifting the wettability from oil-wet toward water-wet conditions for advanced waterflooding processes in carbonates. These results confirm the robustness of the proposed model based on validated SCM electrokinetic interactions. The development of such a coupled geochemistry-based multiphase transport model is an important step to simulate advanced waterflooding processes in carbonates at reservoir scale by considering the more representative physicochemical effects.

The novelty of this work is that it validates the SCM results with experimental zeta potential data for different injection water compositions. Also, the applicability of coupled SCM with a multiphase transport model is successfully demonstrated by history matching the experimental coreflood data. The developed model and new findings will focus on the importance of lower salinity and potential determining ions during fluid flow and oil recovery in complex carbonate formations.

Introduction

Waterflooding is one of the most successful and widely used methods in oil recovery for both carbonate and sandstone formations. Yet, the physicochemical interactions associated with the water injection process for oil recovery are not fully understood, especially for carbonates[2]. The practice of tuning the injected water's ionic composition to improve and optimize the oil recovery process is called advanced waterflooding, low salinity, or SmartWater[3, 4].

Many studies have observed that the injected water chemistry impacts the oil recovery, while several other experiments have not observed such an effect on oil recovery[5]. The conflicting results observed on the effect of water salinity are due to a lack of fundamental understanding about the root causes of wettability alteration associated with manipulating the brine's ionic composition, which takes place at the microscale level. Various microscopic mechanisms have been hypothesized to delineate the physicochemical interactions of wettability alteration in carbonates.

Such pore-scale mechanisms include electric double layer[6], the saponification effect[7], multi-ion exchange[8],

and fine migration[9]. In each of these proposed hypotheses, the carbonate/brine and crude oil/brine surface charges are altered. Therefore, the associated electric zeta potential are affected, which is an important parameter for the wettability alteration process in carbonates[10].

There has been multiple studies that couple a transport model with physicochemical interactions to study the wettability alteration in an advanced waterflooding process, both at the microscopic[11, 12] and macroscopic scales[13]. In this work, we focus on wettability alteration in advanced waterflooding from a macroscopic point of view, where the wettability alteration is generally incorporated as a manipulating parameter in the relative permeability and capillary pressure curves in the multiphase Darcy model. The work of Jerauld et al. (2008)[14] has modeled low salinity flooding by including salinity dependent fluid and flow parameters that are linearly interpolated between high salinity and low salinity injected brines. The salinity adsorption has also been used as an interpolating parameter to model the low salinity effect in spontaneous imbibition[15].

In the work of Evje and Hiorth (2010)[16], brine/chalk interactions — mainly calcite dissolution — have been used as a wettability alteration parameter to couple with multiphase transport equations. Besides the brine/calcite interactions, the crude oil/brine interactions have been recently included in the wettability alteration parameter through the zeta potential values[17]. The brine/carbonate and crude oil/brine zeta potentials have been correlated to different wettability parameters based on the Derjaguin, Landau, Verwey, and Overbeek theory. Such wettability interpolating parameters include contact angle[18], wetting stability number[19], oil-wetting adsorbed surface concentration[20], and available adsorption sights[21]. A recent review of low salinity modeling can be found in the work of Al-Shalabi and Sepehrnoori (2016)[13].

In this work, we attempt to model the coupling of brine/carbonate and crude oil/brine electrokinetics with multiphase transport equations using the Matlab Reservoir Simulation Toolbox (MRST)[22]. First, the zeta potentials of brine/carbonate and crude oil/brine for different brines are computed using a surface complexation model (SCM) embedded in the MRST geochemistry module[23]. The SCM geochemical reactions of a calcite surface are based on the work of Song et al. (2019)[24]. For the crude oil/brine, the surface reactions are similar to the work of Brady et al. (2012)[25].

The MRST geochemical model is validated with both experimental measurements[26] and recent computed results on zeta potentials obtained using PHREEQC software[27]. Then, the geochemistry MRST-based SCM is extended to couple with multiphase transport. The coupled model is validated by history matching the advanced waterflooding recovery and pressure drop data reported[1] in carbonate cores at reservoir conditions.

Methods and Procedures

This section describes the methods used to measure and model the electrokinetics of the calcite/brine/crude oil system.

Rock, Brine and Crude Oil Properties

The rock sample is based on a pure calcite disk with a 99 wt% of calcium carbonate. The considered brine recipes are prepared by adding different salts to deionized water. Table 1 lists the considered brine ionic compositions, and Table 2 lists the key properties of the crude oil sample used in this study. The crude oil sample is obtained and collected from a carbonate reservoir in the field.

Table 1 *The composition of different brine ionic compositions used in this study.*

	Brine Samples (Concentration mg/L)			
	High Salinity Water	**SmartWater**	**NaCl**	**Na_2SO_4**
Na^+	18,300	1,824	2,266	1,865
Cl^-	32,200	3,220	3,495	—
Ca^{2+}	650	65	—	—
Mg^{2+}	2,110	211	—	—
SO_4^{-2}	4,290	429	—	3,896
HCO^{3-}	120	—	—	—
Total Dissolved Solids (ppm)	57,670	5,761	5,761	5,761
Ionic Strength (mol/l)	1.15	0.115	0.098	0.123
pH	7.45	7.4	6.3	6.11

Table 2 *Key properties of the crude oil sample.*

API	27.1
Acid Number, mg (KOH/g)	0.47
Base Number, mg (KOH/g)	0.04
Saturates (%)	50.6
Asphaltenes (%)	1.6
Resins (%)	20.7
Aromatics (%)	27.1

Zeta Potential Measurement

The zeta potential is measured using the phase analysis light scattering technique, where an electric field is applied between two electrodes that contain the dispersed and bulk phases. The magnitude and charge polarity of the zeta potential dictates the direction and velocity of the dispersed phase (calcite particles for calcite/brine interface or crude oil emulsion for crude oil/brine interface), which is determined using the Smoluchowski approximation.

Additional details on the zeta potential measurement procedure can be found in the work of Alghambi et al. (2019)[26] and Alotaibi and Yousef (2017)[28].

SCM

The SCM is used to predict the adsorption of ions based on specified surface reactions at equilibrium state. The adsorbed ions dictate the surface electric charge based on their concentration, charge magnitude, and charge polarity. The determined surface electric charge corresponds to a zeta potential parameter for each calcite/brine and crude oil/brine interface. The SCM has been utilized to gain insights on electrokinetics and the wettability of a carbonate/brine/crude oil system[29].

Several SCM surface reactions have been proposed to predict the zeta potentials of calcite/brine and crude oil/brine interfaces. Brady et al. (2012)[25] used SCM based on surface reactions proposed by other researchers[30, 31] to predict zeta potentials for both rock/brine and brine/crude oil interfaces in sandstone and carbonate rocks. Consequently, the SCM has not been validated with experimental zeta potential measurements in this study. Mahani et al. (2017)[32] studied the electrokinetics of carbonate-based rocks with different water salinities using SCM. The SCM results were qualitatively validated with different carbonate/brine zeta potential measurements.

Song et al. (2017)[24] applied SCM and reported quantitative agreement with experimental zeta potential measurements of synthetic calcite in multiple brine recipes. These authors used SCM surface reactions based on the model proposed by Heberling et al. (2011)[53]. In this work, we use the SCM with surface reactions similar to the approach of Song et al. (2017)[24] to predict zeta potentials for pure calcite and different brine recipes. In addition, we determine brine/crude oil zeta potentials by modeling the SCM reactions at the brine/crude oil interface using a similar model presented in the work of Takeya et al. (2019)[54].

Tables 3 and 4 list the surface reactions and the equilibrium constants for both calcite and crude oil surfaces. The SCM equations are solved using the MRST geochemistry module[23].

The double layer model is specified to model the surface structure of crude oil and calcite surfaces. In the model, the concentration of adsorbed surface complexes (adsorbed ions) determines the total surface charge as:

$$\sigma = \frac{F}{SA} \Sigma z_i c_i \,, \qquad \boxed{1}$$

where σ is the surface charge density (C/m²), F is the Faraday constant (96493.5 C/mol), S is the surface material mass (g), A is the specific surface area (m²/g), z_i is the ionic electric charge, and c_i is the adsorbed ion concentration (mol). The surface charge and surface potential are related through the Gouy-Chapman model:

Table 3 *The surface complexation reactions and parameters for the calcite surface.*

Calcite Surface Reaction	Equilibrium Constant ($\log_{10} K_{int}$)
$> CaOH^{-0.75} + H^+ \leftrightarrow > CaOH_2^{+0.25}$	0.4
$> CO_3H^{+0.75} + OH^- \leftrightarrow > CO_3^{-0.25} + H_2O$	0.5
$> CaOH^{-0.75} + Ca^{2+} \leftrightarrow > CaOH..Ca^{+1.25}$	1.53
$> CaOH^{-0.75} + Mg^{2+} \leftrightarrow > CaOH..Mg^{+1.25}$	1.15
$> CO_3H^{+0.75} + SO_4^{2-} \leftrightarrow > CO_3H..SO_4^{-1.25}$	1.5
$> CO_3H^{+0.75} + HCO^{-3} \leftrightarrow > CO_3H..HCO_3^{-0.25}$	0.09
$> CaOH^{-0.75} + Na^+ \leftrightarrow > CaOH..Na^{+0.25}$	0.22
$> CO_3H^{+0.75} + Cl^- \leftrightarrow > CO_3H..Cl^{-0.25}$	0.65

Table 4 *The surface complexation reactions and parameters for the crude oil surface.*

Crude Oil Surface Reaction	Equilibrium Constant ($log_{10} K_{int}$)
$-COOH \leftrightarrow -COO^- + H^+$	6.0
$-N + H^+ \leftrightarrow -NH^+$	4.0
$-COOH + Ca^{+2} \leftrightarrow -COOCa^+ + H^+$	-4.0
$-COOH + Mg^{+2} \leftrightarrow -COOMg^+ + H^+$	-4.3
$-COOH + Na^+ \leftrightarrow -COONa + H^+$	-4.0

$$\sigma = (8000\epsilon_o\epsilon_w RTI)^{1/2} \sinh\left(\frac{vF\Psi}{2RT}\right), \qquad (2)$$

where ϵ_0 is the vacuum permittivity $\left(\frac{C^2}{mJ}\right)$, ϵ_w is the water relative permittivity Ψ is the surface potential (V), R is the gas constant $\left(\frac{J}{mol\,K}\right)$, T is the temperature (K), I is the brine ionic strength (mol/l), and v is the electrolyte ionic charge, which is assumed to be unity. The bulk concentration of ions interacts with the adsorbed ions at the surface due to coulombic forces. Therefore, the apparent equilibrium constants are considered to include the effect of bulk concentration of the ions. The apparent and intrinsic equilibrium constants, Tables 3 and 4, are described through the Boltzmann distribution:

$$K_{app} = K_{int} \exp\left(\frac{Z_c F\Psi}{RT}\right), \qquad (3)$$

where Z_c is the net change of the surface charge at the surface due to surface reaction. The zeta potential, ζ, can be approximated from the surface potential based on the linearized Debye-Huckel theory[24], which is valid for $|\Psi| \leq 25$ mV[35]:

$$\zeta = \psi \exp(-\kappa d_s) \qquad (4)$$

where $_K$ is the inverse Debye length-scale, and d_s is the slipping plane distance from the outer Helmholtz plane.

For brines with an ionic strength of around 0.1 mol/l (all the considered brine recipes except for high salinity water), the d_s is 0.33 nm[24], while the Debye length $_K^{-1}$ is 0.97 nm. For the high salinity water case (ionic strength of 1.1 mol/l), d_s is 0.1 nm ($d_s = 0.1/c^{0.5}$), while K_{sw}^{-1} is 0.29 nm[35]. The site density for the calcite surface is 4.95 sites/nm² [25], while the crude oil surface has a site density of 0.47 sites/nm² [34]. The calcite specific surface area is 1 m²/g[25], while the crude oil specific area is 0.5 m²/g[34]. Additional details of the above SCM equations are elaborated in the MRST geochemistry module[23] and PHREEQC user guide[27].

Multiphase Transport Equations

The transport equation is modeled using the multiphase Darcy equations. Assuming that the rock and fluids are incompressible, the mass conservation for each fluid phase is written as:

$$\phi\frac{\partial S_\alpha}{\partial t} + \nabla \cdot u_\alpha = 0, \qquad (5)$$

where the subscript α denotes the average fluid phase

(w for water or o for oil), ϕ is the rock porosity, S_a is the phase saturation, and u_a is the fluid phase velocity (m/s). The multiphase Darcy velocity is expressed as:

$$u_\alpha = -\frac{kk_{r\alpha}}{\mu_\alpha}\nabla p_\alpha, \qquad (6)$$

where k is the rock absolute permeability (m²), $k_{ra}(S_a)$ is the fluid phase relative permeability, μ_a is the fluid viscosity (Pas), and ∇p_α is the fluid phase pressure gradient (Pa). The saturation and pressure for each phase is related as:

$$S_w + S_o = 1 \qquad (7)$$

$$p_c = p_o - p_w, \qquad (8)$$

where $p_c(S_a)$ is the capillary pressure (Pa). The individual ions are transported in the aqueous phase (water) according to Eqn. 9:

$$\phi\frac{\partial c_i}{\partial t} + (1-\phi)\rho_s a_s \frac{\partial c_{i,ad}}{\partial t} + \nabla \cdot u_w = 0, \qquad (9)$$

where ρ_s is the rock density (kg/m^5) and $c_{i,ad}$ is the adsorbed ion concentration. The first term on the left side corresponds to the transported dissolved ions in water, and the second term is the ion adsorption term.

The multiphase flow equations are solved using the two-phase oil water model in MRST[22], while the ion transport equation is solved using the geochemistry module in MRST[23]. This work couples these two modules through a linear interpolating parameter that considers the zeta potentials of the calcite/brine and crude oil/brine interfaces.

The interpolating parameter that captures the wettability alteration process follows the approach of Korrani and Jerauld (2019)[19], where a stability number relevant to wetting water thin films is defined. This stability number compares the electrostatic forces with the attractive Van der Waals forces as suggested by Hirasaki (1991)[36] to predict the crude oil adhesion map of Buckley et al. (1989)[37]. The dimensionless stability number is the ratio of electrostatic over the Van der Waals, which can be expressed for a brine/oil/rock system as:

$$SN = 0.09\epsilon_w^{1.5}\psi_{b/r}\psi_{b/o}\sqrt{\frac{T}{I}}, \qquad (10)$$

where $\psi_{b/r}$ is the brine/rock surface potential, and $\psi_{b/o}$ is the brine/crude oil surface potential. The interpolant associated with the stability number is defined as:

$$\theta = \max\left(\min\left(\frac{SN - SN_{ow}}{SN_{ww} - SN_{ow}}, 1\right), 0\right),$$ 11

where SN is the stability number corresponding to a computational grid cell with a given concentration of ions, SN_{ww} is the water-wet stability number, and SN_{ow} is the oil-wet stability number. Equation 11 is defined to ensure the bounding interval to range between 0 and 1 for the interpolant θ. The relative permeability and capillary pressure curves are written as:

$$k_{r\alpha} = (1 - \theta)k_{r\alpha}^{OW} + \theta k_{r\alpha}^{ww},$$ 12

$$p_c = (1 - \theta)p_c^{OW} + \theta p_c^{ww}.$$ 13

When the interpolant θ is equal to zero, the relative permeability curves correspond to the water chemistry with the more oil-wet state. When the wettability is altered toward a more water-wet state, the interpolant value approaches 1, which is usually the ionically controlled water salinity. The relative permeability curves follow the empirical Brooks-Corey correlation:

$$k_{rw}(S_w) = k_{rw}^O (S_{wn})^{n_w},$$ 14

$$k_{ro}(S_w) = (1 - S_{wn})^{n_o},$$ 15

where k_{rw}^O is the water relative permeability end point, n_w is the water phase exponent, n_o is the crude oil phase exponent, and S_{wn} is the normalized water saturation, expressed as:

$$S_{wn} = \frac{S_w - S_{wi}}{1 - S_{wi} - S_{or}}$$ 16

where S_{wi} is the irreducible water saturation, and S_{or} is the residual oil saturation. In our study, the coupling between the SCM geochemical model and multiphase transport equations is mainly achieved through Eqns. 9, 12, and 13. Equation 9 is the transport equation for each individual ion, while the interpolant associated with electrokinetics of the brine/crude oil/carbonate system manipulates the relative permeability and capillary pressure curves.

These equations are solved sequentially using Matlab geochemistry and multiphase transport MRST modules. First, the multiphase transport equations are solved fully implicitly. Then, the transported ion concentrations are passed to the Matlab geochemistry to compute the electrokinetic parameters, which mainly include surface potential, ψ, and ionic strength, I.

Results and Discussion

Here, the results of electrokinetic and multiphase transport modeling are shown. First, the SCM is validated by comparing with experimental zeta potential measurements. Then, the results obtained from coupling of the SCM with multiphase transport equations are compared with advanced waterflooding coreflood experimental data reported[1] to validate the proposed SCM-based multiphase transport model.

SCM

Figures 1 and 2 compare the SCM and experimental measurements of zeta potential values for different

Fig. 1 *The experimental and SCM zeta potential values at the calcite/brine interface.*
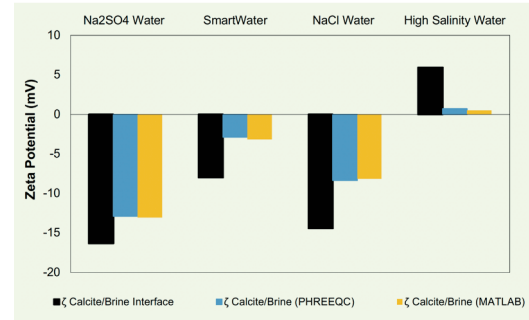
Fig. 2 *The experimental and SCM zeta potential values at the crude oil/brine interface.*
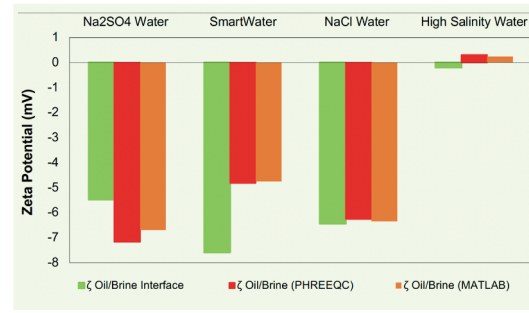
brine recipes. First, the zeta potentials for the brine/calcite interface are analyzed, followed by the brine/crude oil interface. The intrinsic equilibrium constants are varied in the SCM to match the measured zeta potentials. The number of fitting parameters is equal to the number of surface reaction equations — eight equations for the calcite/brine interface, and five equations for the crude oil/brine interface.

The site density and specific surface area of the considered surfaces are fixed. For the brine/calcite interface, the SCM results follow the trends observed in experimental data, and quantitatively agree with the laboratory zeta potential measurements especially for NaCl, SmartWater, and Na_2SO_4 brines. For the high salinity water case, the SCM underestimates the zeta potential, Fig. 1. Calcite precipitation/dissolution has not been considered in the SCM, which is likely to contribute to the slight discrepancy observed in the high salinity water case. The computed results from the PHREEQC and MRST geochemistry of the SCM approaches are almost identical. The verification with PHREEQC and the experimental validation of the zeta potential values provide confidence in the MRST geochemistry of the SCM. Also, the intrinsic equilibrium constants (fitting parameters) in Table 3 agree with the work of Song et al. (2017)[24]. The SCM results (both PHREEQC and MRST geochemistry) confirm that

the total surface charge and zeta potential of calcite/brine interface strongly depend on the divalent ions (Ca^{2+}, Mg^{2+}, and SO_4^{2-}) due to larger surface charge and intrinsic equilibrium values.

For the crude oil/brine interface cases, the SCM zeta potential results qualitatively matched the experimental observations. Figure 2 shows the predicted zeta potentials are in general negatively charged, which is consistent with the experimental results. The equilibrium constants in Table 4 are also similar to the values reported in the works of Brady et al. (2012)[25] and Takeya et al. (2019)[34] — the discrepancy in the equilibrium constants are within a value of one for each reaction.

When the pH level is around 7 (above the crude oil/brine isoelectric point), the carboxylic acids in crude oil are not completely protonated (reaction 1 in Table 4). In addition, the protonation of nitrogen bases (reaction 2 in Table 4) is not sufficient to switch the crude oil surface to a positive charge, which agrees well with the previously reported experimental observations[37, 38].

SCM-Based Multiphase Transport Model

A comparison between the developed SCM-based multiphase flow simulation results and experimental data of Yousef et al. (2011)[1] is presented for both secondary (high salinity water) and tertiary (SmartWater) coreflooding processes. First, high salinity water (first brine composition in Table 1) is injected for about 10 pore volumes (PVs) to displace oil inside a carbonate composite. Then, high salinity water is diluted twice (moderate salinity water) and injected for another 10 PVs, where the experimental data showed an increase of 7% in the oil recovery. Finally, an additional 10 PVs of SmartWater (10-times diluted high salinity water shown as second brine composition in Table 1) are injected, which resulted in a 10% incremental oil recovery.

Figures 3 and 4 show the oil recovery and pressure drop history matches obtained for the considered advanced waterflooding coreflood experiment at reservoir conditions. The blue line indicates the simulation results, while the red stars are the coreflood data. The details on the composite carbonate reservoir core petrophysical properties can be found in Yousef et al. (2011)[1]. The fluid flow is assumed to be 1D, where the number of grid blocks is 20 in the direction of the water injection. In this study, the capillary pressure is neglected, which means the brine and crude oil pressures are equal. Also, the ion adsorption is small and assumed to be negligible.

The simulation results based on the coupled electrokinetics with multiphase transport are in good agreement with the experimental data for both oil recovery and pressure drop. The oil recovery increases from about 75% to 85% when the high salinity water is diluted twice. In the proposed model, this increase in oil recovery is captured by shifting the high salinity relative permeability curves to those of moderate salinity water through the stability number, *SN*, interpolant (electrokinetic interpolating parameter in Eqn. 11). The interpolating parameter increases from 0 to 1 for each grid block as the diluted water salinity is injected, and

the wettability becomes more water-wet as illustrated in Eqn. 12. A similar methodology is followed when the moderate salinity water is altered to SmartWater, where the oil recovery increased to 93%. The pressure drop slightly decreases with SmartWater due to a decrease in residual oil as well as brine viscosity.

Figure 5 illustrates the two sets of oil/water relative permeability curves used for coreflood history matching, which correspond to high salinity water and SmartWater recipes. Based on the transported ions and computed zeta potentials, the oil/water relative permeability curves gradually shift to the right side as the two brine compositions get mixed. Due to this shift, the crossover point between the oil and water relative permeability curves changes from 0.5 to about 0.6. This increase in the crossover point agrees with

Fig. 3 *The oil recovery vs. injected PVs for advanced waterflooding coreflood process. The blue line indicates the simulation results, and the red stars are the coreflood data of Yousef et al. (2011)[1].*

Fig. 4 *The pressure drop vs. injected PVs for advanced waterflooding coreflood process. The blue line indicates the simulation results, and the red stars are the coreflood data of Yousef et al. (2011)[1].*
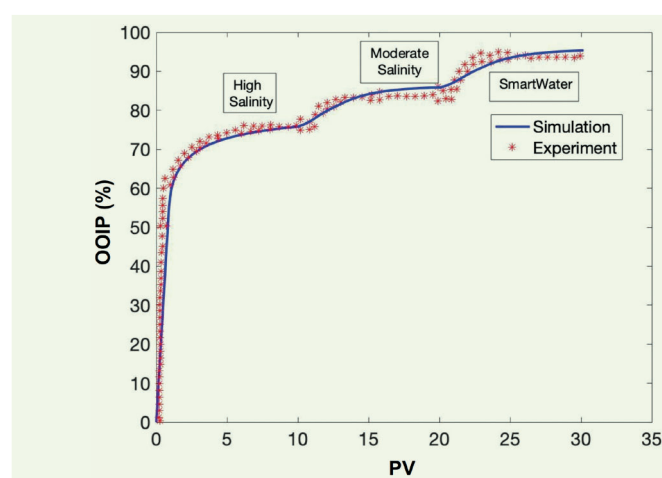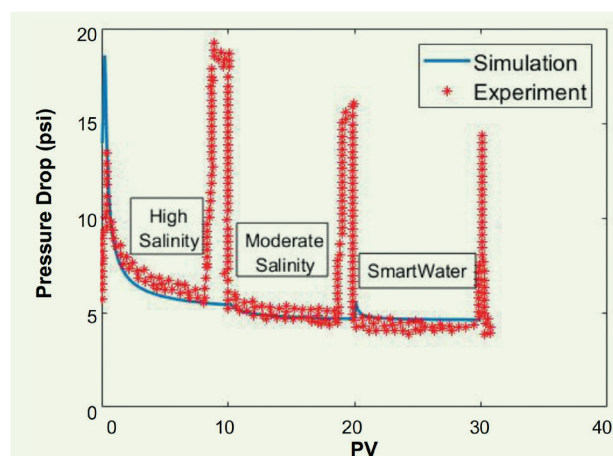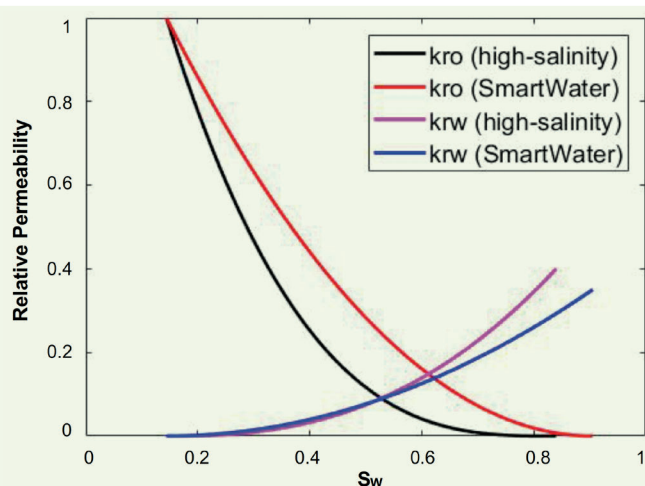
SCM zeta potentials become parameters of both the relative permeability and capillary pressure curves. The proposed model is shown to successfully history match the oil recovery and pressure drop data on advanced waterflooding[1] from reservoir condition coreflood tests.

The generated relative permeability curves demonstrated the favorable shifts in relative permeability curves to capture the wettability alterations from oil-wet toward water-wet conditions associated with advanced waterflooding in carbonates. These promising results confirmed the robustness of the proposed model based on validated SCM electrokinetic interactions. The development of such a coupled geochemistry-based multiphase transport model is an important step to simulate advanced waterflooding processes in carbonate reservoirs by considering more representative physicochemical effects. The efforts are currently ongoing to enhance the predictive capabilities of the proposed model by including ion adsorption/diffusion mechanisms and fluid-fluid interaction effects in terms of interface viscosity/viscoelasticity.

Acknowledgments

Craig's rule of thumb on wettability interpretation[39], wherein the crossover point below 0.5 implies oil-wet conditions and above 0.5 represents a water-wet state.

Therefore, the proposed model, through coupling of electrokinetics with multiphase transport equations, has been shown to successfully simulate the core-scale wettability alteration associated with advanced waterflooding in carbonates. Although the simulation results reasonably matched experimental coreflood data, further refinements in the proposed model will be considered in the future. These include incorporating ion adsorption and diffusion effects, since these mechanisms are especially important to promote spontaneous imbibition in low permeability carbonates. It should be further considered to include fluid-fluid interaction effects in the tuning parameter such as the surface viscosity/viscoelasticity of crude oil/brine interface for improving the model accuracy.

These effects are important as several recent studies have shown that interface viscosity/viscoelasticity has a strong effect to impact oil mobilization in advanced waterflooding through reducing snap-off[40] and enhancing oil blob coalescence[41, 42]. More validations should also be performed against additional experimental data such as effluent ion concentrations obtained from a chromatographic test to increase the confidence and enhance the robustness of the proposed electrokinetics-based multiphase transport model.

Summary and Conclusions

In this work, a multiphase transport model coupled with electrokinetics is developed to simulate an advanced waterflooding coreflood process in carbonates. The SCM results are validated through comparison with zeta potential measurements of calcite/brine and crude oil/brine interfaces for different brine recipes. The validated SCM geochemical model is then coupled with a multiphase Darcy model, where the computed

References

1. Yousef, A.A., Al-Saleh, S., Al-Kaabi, A. and Al-Jawfi, M.: "Laboratory Investigation of the Impact of Injection Water Salinity and Ionic Content on Oil Recovery from Carbonate Reservoirs," *SPE Reservoir Evaluation & Engineering*, Vol. 14, Issue 5, October 2011, pp. 578-593.

2. Mahani, H., Keya, A.L., Berg, S., Bartels, W-B., et al.: "Insights into the Mechanism of Wettability Alteration by Low-Salinity Flooding (LSF) in Carbonates," *Energy & Fuels*, Vol. 29, Issue 3, 2015, pp. 1352-1367.

3. Austad, T., Strand, S., Høgnesen, E.J. and Zhang, P.: "Seawater as IOR Fluid in Fractured Chalk," SPE paper 93000, presented at the SPE International Symposium on Oil Field Chemistry, Houston, Texas, February 2-4, 2005.

4. Morrow, N. and Buckley, J.: "Improved Oil Recovery by Low-Salinity Waterflooding," *Journal of Petroleum Technology*, Vol. 63, Issue 5, May 2011, pp. 106-112.

5. Jackson, M.D., Vinogradov, J., Hamon, G. and Chamerois, M.: "Evidence, Mechanisms and Improved Understanding of Controlled Salinity Waterflooding Part 1: Sandstones," *Fuel*, Vol. 185, December 2016, pp. 772-793.

6. Ligthelm, D.J., Gronsveld, J., Hofman, J., Brussee, N., et al.: "Novel Waterflooding Strategy by Manipulation of Injection Brine Composition," SPE paper presented at the EUROPEC/EAGE Conference and Exhibition, Amsterdam, the Netherlands, June 8-11, 2009.

7. McGuire, P.L., Chatham, J.R., Paskvan, F.K., Sommer, D.M., et al.: "Low Salinity Oil Recovery: An Exciting New EOR Opportunity for Alaska's North Slope," SPE paper 93903, presented at the SPE Western Regional

Meeting, Irvine, California, March 30-April 1, 2005.

8. Lager, A., Webb, K.J., Black, C.J.J., Singleton, M. and Sorbie, K.S.: "Low Salinity Oil Recovery — An Experimental Investigation 1," *Petrophysics*, Vol. 49, Issue 1, February 2008.

9. Tang, G-Q. and Morrow, N.R.: "Influence of Brine Composition and Fines Migration on Crude Oil/Brine/Rock Interactions and Oil Recovery," *Journal of Petroleum Science and Engineering*, Vol. 24, Issues 2-4, December 1999, pp. 99-111.

10. Al Mahrouqi, D., Vinogradov, J. and Jackson, M.D.: "Zeta Potential of Artificial and Natural Calcite in Aqueous Solution," *Advances in Colloid and Interface Science*, Vol. 240, February 2017, pp. 60-76.

11. Maes, J. and Geiger, S.: "Direct Pore-Scale Reactive Transport Modeling of Dynamic Wettability Changes Induced by Surface Complexation," *Advances in Water Resources*, Vol. 111, January 2018, pp. 6-19.

12. Abu-AlSaud, M.O., Esmaeilzadeh, S. and Tchelepi, H.: "Insights into the Impact of Water Salinity on Multiphase Flow at the Pore-Scale in Carbonate Formations," SPE paper 194985, presented at the SPE Middle East Oil and Gas Show and Conference, Manama, Kingdom of Bahrain, March 18-21, 2019.

13. Al-Shalabi, E.W. and Sepehrnoori, K.: "A Comprehensive Review of Low Salinity/Engineered Water Injections and their Applications in Sandstone and Carbonate Rocks," *Journal of Petroleum Science and Engineering*, Vol. 139, March 2016, pp. 137-161.

14. Jerauld, G.R., Webb, K.J., Lin, C-Y. and Seccombe, J.C.: "Modeling Low-Salinity Waterflooding," *SPE Reservoir Evaluation & Engineering*, Vol. 11, Issue 6, December 2008, pp. 1000-1012.

15. Yu, L., Evje, S., Kleppe, H., Kårstad, T., et al.: "Spontaneous Imbibition of Seawater into Preferentially Oil-Wet Chalk Cores — Experiments and Simulations," *Journal of Petroleum Science and Engineering*, Vol. 66, Issue 3, June 2009, pp. 171-179.

16. Evje, S. and Hiorth, A.: "A Mathematical Model for Dynamic Wettability Alteration Controlled by Water-Rock Chemistry," *Networks & Heterogeneous Media*, Vol. 5, Issue 2, June 2010, pp. 217-256.

17. Sharma, H. and Mohanty, K.K.: "An Experimental and Modeling Study to Investigate Brine-Rock Interactions during Low Salinity Water Flooding in Carbonates," *Journal of Petroleum Science and Engineering*, Vol. 165, June 2018, pp. 1021-1039.

18. Sanaei, A., Tavassoli, S. and Sepehrnoori, K.: "Investigation of Modified Water Chemistry for Improved Oil Recovery: Application of DLVO Theory and Surface Complexation Model," *Colloids and Surfaces A: Physicochemical and Engineering Aspects*, Vol. 574, April 2019, pp. 131-145.

19. Korrani, A.K.N. and Jerauld, G.R.: "Modeling Wettability Change in Sandstones and Carbonates Using a Surface-Complexation-Based Method," *Journal of Petroleum Science and Engineering*, Vol. 174, March 2019, pp. 1093-1112.

20. Qiao, C., Johns, R. and Li, L.: "Modeling Low-Salinity Waterflooding in Chalk and Limestone Reservoirs," *Energy & Fuels*, Vol. 30, Issue 2, 2016, pp. 884-895.

21. Bonto, M., Eftekhari, A.A. and Nick, H.: "A Calibrated Model for the Carbonate-Brine-Crude Oil Surface Chemistry and its Effect on the Rock Wettability, Dissolution, and Mechanical Properties," SPE paper 193865, presented at the SPE Reservoir Simulation Conference, Galveston, Texas, April 10-11, 2019.

22. Lie, K.A.: *An Introduction to Reservoir Simulation Using MATLAB/GNU Octave: User Guide for the MATLAB Reservoir Simulation Toolbox (MRST)*, Cambridge University Press, 2019, 674 p.

23. McNeece, C.J., Raynaud, X., Nilsen, H. and Hesse, M.A.: "Matlab Geochemistry: An Open Source Geochemistry Solver Based on MRST," paper presented at the American Geophysical Union Fall Meeting, New Orleans, Louisiana, December 11-15, 2017.

24. Song, J., Zeng, Y., Wang, L., Duan, X., et al.: "Surface Complexation Modeling of Calcite Zeta Potential Measurements in Brines with Mixed Potential Determining Ions (Ca^{2+}, CO_3^{2-}, Mg^{2+}, SO_4^{2-}) for Characterizing Carbonate Wettability," *Journal of Colloid and Interface Science*, Vol. 506, July 2017, pp. 169-179.

25. Brady, P.V., Krumhansl, J.L. and Mariner, P.E.: "Surface Complexation Modeling for Improved Oil Recovery," SPE paper 153744, presented at the SPE Improved Oil Recovery Symposium, Tulsa, Oklahoma, April 14-18, 2012.

26. Alghamdi, A.O., Abu-AlSaud, M.O., Al-Otaibi, M.B., Ayirala, S.C., et al.: "Electro-Kinetic Induced Wettability Alteration in Carbonates: Tailored Water Chemistry and Alkali Effects," *Colloids and Surfaces A: Physicochemical and Engineering Aspects*, Vol. 583, Issue 1, August 2019.

27. Parkhurst, D.L. and Appelo, C.A.J.: "Description of Input and Examples for PHREEQC Version 3 — A Computer Program for Speciation, Batch-Reaction, One Dimensional Transport, and Inverse Geochemical Calculations," *U.S. Geological Survey Techniques and Methods*, Book 6, Chapter A43, 2013, 497 p.

28. Alotaibi, M.B. and Yousef, A.A.: "The Role of Individual and Combined Ions in Waterflooding Carbonate Reservoirs: Electrokinetic Study," *SPE Reservoir Evaluation & Engineering*, Vol. 20, Issue 1, February 2017, pp. 77-86.

29. Xie, Q., Sari, A., Pu, W., Chen, Y., et al.: "pH Effect on Wettability of Oil/Brine/Carbonate System: Implications for Low Salinity Water Flooding," *Journal of Petroleum Science and Engineering*, Vol. 168, September 2018, pp. 419-425.

30. Van Cappellen, P., Charlet, L., Stumm, W. and Wersin, P.: "A Surface Complexation Model of the Carbonate Mineral-Aqueous Solution Interface," *Geochimica et Cosmochimica Acta*, Vol. 57, Issue 15, August 1993, pp. 3505-3518.

31. Pokrovsky, O.S., Schott, J. and Thomas, F.: "Dolomite Surface Speciation and Reactivity in Aquatic Systems," *Geochimica et Cosmochimica Acta*, Vol. 63, Issues 19-20, October 1999, pp. 3133-3143.

32. Mahani, H., Keya, A.L., Berg, S. and Nasralla, R.: "Electrokinetics of Carbonate/Brine Interface in Low-Salinity Waterflooding: Effect of Brine Salinity, Composition, Rock Type, and pH on ζ-Potential and a Surface Complexation Model," *SPE Journal*, Vol. 22, Issue 1, August 2018, pp. 53-68.

33. Heberling, F., Trainor, T.P., Lützenkirchen, J., Eng, P., et al.: "Structure and Reactivity of the Calcite-Water Interface," *Journal of Colloid and Interface Science*, Vol. 354, Issue 2, February 2011, pp. 843-857.

34. Takeya, M., Shimokawara, M., Elakneswaran, Y., Nawa, T., et al.: "Predicting the Electrokinetic Properties of the Crude Oil/Brine Interface for Enhanced Oil Recovery in Low Salinity Water Flooding," *Fuel*, Vol. 235, January 2019, pp. 822-831.

35. Israelachvili, J.N.: *Intermolecular and Surface Forces*, Academic Press, 2015, 710 p.

36. Hirasaki, G.J.: "Wettability: Fundamentals and Surface Forces," *SPE Formation Evaluation*, Vol. 6, Issue 2, June 1991, pp. 217-226.

37. Buckley, J.S., Takamura, K. and Morrow, N.R.: "Influence of Electrical Surface Charges on the Wetting Properties of Crude Oils," *SPE Reservoir Engineering*, Vol. 4, Issue 3, August 1989, pp. 332-340.

38. Hirasaki, G. and Zhang, D.L.: "Surface Chemistry of Oil Recovery from Fractured, Oil-Wet, Carbonate Formation," *SPE Journal*, Vol. 9, Issue 2, June 2004, pp. 151-162.

39. Craig Jr., F.F.: *The Reservoir Engineering Aspects of Waterflooding*, SPE Monograph Series, Vol. 3, Society of Petroleum Engineers, 1971, 134 p.

40. Alvarado, V., Moradi Bidhendi, M., Garcia-Olvera, G., Morin, B., et al.: "Interfacial Visco-Elasticity of Crude Oil Brine: An Alternative EOR Mechanism in Smart Waterflooding," SPE paper 169127, presented at the SPE Improved Oil Recovery Symposium, Tulsa, Oklahoma, April 12-16, 2014.

41. Ayirala, S.C., Yousef, A.A., Li, Z. and Xu, Z.: "Coalescence of Crude Oil Droplets in Brine Systems: Effect of Individual Electrolytes," *Energy & Fuels*, Vol. 32, Issue 5, 2018, pp. 5763-5771.

42. Ayirala, S.C., Li, Z., Saleh, S.H., Xu, Z., et al.: "Effects of Salinity and Individual Ions on Crude Oil/Water Interface Physicochemical Interactions at Elevated Temperature," *SPE Reservoir Evaluation & Engineering*, Vol. 22, Issue 3, August 2019, pp. 897-910.

About the Authors

Dr. Moataz O. Abu-AlSaud

Ph.D. in Energy Resources Engineering,
Stanford University

Dr. Moataz O. Abu-AlSaud joined Saudi Aramco in 2004, and is currently a member of the SmartWater Flooding team in Reservoir Engineering Technology Division, of Saudi Aramco's Exploration and Petroleum Engineering Center – Advanced Research Center (EXPEC ARC). His research interests focus on the fundamental understanding of multiphase flow inside carbonates from the nanoscale to the reservoir scale, as well as digital rock physics.

Moataz has been published in several highly cited journals, and is the author of numerous conference papers. He serves as a Technical Reviewer for the *Journal of Computational Physics*, the *Journal of Energy and Fuels*, and the *Journal of Petroleum Science and Engineering*.

In 2009, Moataz received two B.S. degrees, in Mechanical Engineering and Mathematics, from Rice University, Houston, TX. In 2012, he received an M.S. degree in Mechanical Engineering from King Abdullah University of Science and Technology (KAUST), Thuwal, Saudi Arabia, and in 2017, Moataz received his Ph.D. degree in Energy Resources Engineering from Stanford University, Stanford, CA.

Salah H. Al Saleh

B.S. in Geochemistry,
King Abdulaziz University

Salah H. Al Saleh is a Petroleum Scientist with the Reservoir Engineering Technology Division of Saudi Aramco's Exploration and Petroleum Engineering Center – Advanced Research Center (EXPEC ARC). He has more than 30 years of specialized and research experience in conventional and special core analysis, capillary pressure and relative permeability by centrifuge, electrical properties, improved oil recovery/enhanced oil recovery, including SmartWater flooding, chemical, thermal, and CO_2 techniques, assisted by imaging technologies such as X-ray computer tomography and nuclear magnetic resonance imaging.

Salah has received several awards during his career, including the King Salman prize for Innovation Award.

He has authored and coauthored 45 technical papers, 22 journal articles, and holds 12 U.S. patents and several pending patent applications.

Salah received his B.S. degree in Geochemistry from King Abdulaziz University, Jiddah, Saudi Arabia.

Dr. Subhash C. Ayirala

Ph.D. in Petroleum Engineering,
Louisiana State University

Dr. Subhash C. Ayirala is an Improved/Enhanced Oil Recovery (IOR/EOR) Specialist and is currently leading the SmartWater Flooding team in the Reservoir Engineering Technology Division of Saudi Aramco's Exploration and Petroleum Engineering Center – Advanced Research Center (EXPEC ARC), as the Focus Area Champion. He has more than 15 years of experience in the oil and gas industry.

Subhash played a major role in the successful execution of the SmartWater flooding multiscale research program, in addition to unraveling the importance of injection water chemistry in the EOR portfolio to develop several novel hybrid recovery technologies.

Prior to joining Saudi Aramco, he worked as a Reservoir Engineer in Shell International Exploration & Production, Houston, Texas. Subhash has authored or coauthored more than 70 technical papers, 50 journal publications, and holds 25 granted U.S. patents, and 10 pending patent applications.

He is a Society of Petroleum Engineers (SPE) distinguished member, and serves as co-executive editor for the SPE *Reservoir Evaluation & Engineering Journal*. Subhash also serves as one of the Executive Editors for the *Journal of Petroleum Science and Engineering* (JPSE), an Elsevier international journal. He received the SPE Outstanding Technical Editor recognition nine times in 2008, 2013, 2016, 2017, 2018, 2019, and 2020, and is the recipient of the 2017 SPE "A Peer Apart Award." Subhash also received the 2019 SPE Middle East and North Africa Regional Service Award.

Subhash received both his M.S. and Ph.D. degrees in Petroleum Engineering from Louisiana State University, Baton Rouge, LA. He also holds a B.Tech and an M.Tech degree in Chemical Engineering from Sri Venkateswara University, Titupati, and the Indian Institute of Technology, Kharagpur, India, respectively.

Dr. Ali A. Al-Yousef

Ph.D. in Petroleum Engineering,
University of Texas at Austin

Dr. Ali A. Yousef is a Senior Petroleum Engineering Consultant and Chief Technologist at the Reservoir Engineering Technology Division in Saudi Aramco's Exploration and Petroleum Engineering Center – Advanced Research Center (EXPEC ARC). He has more than 26 years of experience in upstream research and technology. Since joining Saudi Aramco, Ali has been involved in applied research projects on improved oil recovery (IOR), waterflooding, enhanced oil recovery (EOR), and advanced reservoir evaluation/monitoring. He played a pivotal role in planning, developing and implementing the EOR roadmap for the company.

Ali is currently leading more than 50 scientists, engineers, and technicians. Those researchers are dedicated to the development of various IOR/EOR processes, including SmartWater, CO_2, and chemical EOR technologies as well as other novel technologies focusing on nanotechnology and advanced reservoir evaluation/monitoring.

He has written over 100 technical papers, and has 32 granted patents and more than 30 pending patent applications. Ali is currently an active member of the Society of Petroleum Engineers (SPE) and has chaired several SPE workshops and forums, helped organize several petroleum engineering related conferences, and taught courses on IOR/EOR and waterflooding.

He is considered as a worldwide authority in the field of IOR/EOR. Ali was the recipient of SPE's prestigious IOR Pioneer Award at the 2016 IOR Conference in Tulsa for his significant contributions made to the advancement of recovery technologies.

He was recognized by The Custodian of the Two Holy Mosques in 2018 for his pioneering invention on SmartWater flooding technology. More recently, the technology on the zero liquid discharge water management solution that Ali co-invented has received the World Oil's 2020 Best Water Management Technology Award. He has also been elected as a 2021 Fellow of Energy Institute.

Ali received his B.S. degree in Chemical Engineering from King Fahd University of Petroleum and Minerals (KFUPM), Dhahran, Saudi Arabia, and his M.S. and Ph.D. degrees, both in Petroleum Engineering, from the University of Texas at Austin, Austin, TX.

Magnetic Permeability Sensor Array Prototype to Evaluate Reservoir Phase Permeability in Situ Downhole

Robert W. Adams, Jesus M. Felix Servin, Dr. Wei Wang and Dr. Max Deffenbaugh

Abstract / A measurement system capable of in situ measurements of formation permeability is described. The measurement method relies upon imaging the distribution of magnetic permeability fluid injected into a wellbore system through mutual inductance measurements between a pair of coils, and relating the change in distribution of this fluid over time to a direct measurement of formation phase permeability.

Analysis of the mutual inductance measurement method shows a unique response to distributions of magnetic permeability for various coil spacings, and insensitivity to other confounding electrical parameters. The lower bound of measurement variance for this system is modeled for a continuum of coil spacings and radii of investigation for a perturbation in magnetic permeability.

Introduction

Oil field reservoir models rely upon accurate measurements of formation absolute and phase permeability to predict the movement of hydrocarbon and brines through the reservoir during production. The phase permeability relates to the flow of fluid through a formation to the pressure difference driving the flow:

$$q_i = \frac{k_i}{\eta_i}\Delta P \qquad \qquad 1$$

where q_i is the flux of fluid through the formation, k_i is the phase permeability for fluid phase, i = oil, gas, water, η_i is the dynamic viscosity for the fluid phase, and ΔP is the pressure drop across the formation through which the fluid is flowing[1]. Phase permeability is an important unique aspect to specific types of formations and specific conditions of the reservoir. The accuracy of fluid flow models through a reservoir require an accurate quantification of phase permeability across the reservoir. Production simulation results from oil field reservoir models establish where injection and production wells should be located in the reservoir, and the rate at which to inject into and produce fluid from these wells to maximize the hydrocarbon production from the reservoir.

Existing methods to measure formation permeability include: ex-situ core analysis, empirically derived correlations with other formation measurements such as porosity, and inference from system level pressure measurements[1]. Ex-situ methods face difficulties replicating the conditions that the formation experiences downhole, and often include permanent changes to the physical structure of the sample as it is removed from the subsurface. Empirically derived correlations are often unique for each reservoir, implying formation permeability measurements are acquired ex post facto, and are therefore not useful for initial reservoir modeling. Inferred measurements from system level testing are average measurements of absolute permeability over the depth of the well, with no specificity in the formation's absolute permeability at selected depths.

A novel system, which measures the formation's absolute and phase permeability in situ downhole is presented, Fig. 1. Colloidal magnetite fluid with ultra-high magnetic permeability[2-4] fluid is injected from the surface into the downhole formation. The high magnetic permeability fluid permeates through the formation some radial distance over a period of time, which is directly related to the formation phase permeability. A sensor array measures the radial distribution of surrounding magnetic permeability during the injection process. The phase permeability is proportional to the integrated difference in radial distribution of magnetic permeability, such that:

$$k_i \sim \frac{2\pi}{\Delta T}\int_{\rho_w}^{\rho_{max}} \frac{\mu_2(\rho)-\mu_1(\rho)}{\mu_{fluid}-\mu_1(\rho)}\rho \, d\rho \qquad \qquad 2$$

where ρ is the radial distance from the measurement system into the surrounding formation, ρ_{max} is the maximum radius of investigation of the system into the surrounding formation, ρ_w is the radial distance from the measurement system to the borehole wall, μ_{fluid} is the known magnetic permeability of the injected fluid, μ_1 is the baseline radial magnetic permeability distribution measured at time T_1, μ_2 is the radial magnetic permeability distribution measured at time T_2, and $\Delta T = T_2 - T_1$ is the time difference between radial magnetic permeability distribution measurements.

By comparing the magnetic permeability radial distribution surrounding the sensor array before/during/after

the magnetic permeability fluid injection, the system is able to directly measure the phase permeability of the surrounding formation in situ downhole.

In this work, the analytical description of the measurement sensor's measurement is described. Sensitivity to the formation's magnetic permeability radial measurements is investigated, along with other confounding measurement parameters, e.g., formation conductivity. The Cramer-Rao lower bound of magnetic permeability estimation as a function of radial depth and sensor array spacing is quantified.

Methods

The sensor array measures the radial magnetic permeability distribution of the formation via mutual inductance between pairs of solenoid coils axially distributed along the downhole tool. The mutual inductance between the pairs of coils is altered by the magnetic permeability of the surrounding formation, as the magnetic field lines are distorted by the distribution of magnetic permeability. Additionally, the alteration of these field lines has a radial sensitivity related to the axial spacing between coil pairs[5]. Measuring the mutual inductance across the array of solenoid coils distributed axially along the tool with unique spacing enables the system to map the radial distribution of the magnetic permeability surrounding the sensor.

Any eddy current effects on mutual inductance measurements can be minimized by reducing the interrogation frequency of the measurement, such that electrical conductivity and permittivity changes have no effect on the measurement of interest. This implies the measurement can be made insensitive to the displacement of brine and hydrocarbon fluids within the formation as the high magnetic permeability fluid permeates the subsurface. This is a unique advantage for this measurement system, as it is sensitive only to the movement of the high magnetic permeability fluid.

The radial sensitivity of the mutual inductance measurements for pairs that this system is modeled by are a pair of induction coils in a cylindrically symmetric system, Fig. 2. A transmitting induction coil with N_T turns and coil radius, a, is located at the origin, with a receiver coil having N_R turns and a that is spaced axially from the transmitting coil a distance, L. The coils are surrounded by three cylindrical shells having permittivity, ε_m, conductivity, σ_m, and magnetic permeability, μ_m, where the subscript $m = 1,2,3$ denotes the index of the cylindrical shell. The innermost shell, $m = 1$, extends from the origin to a first interface radius, ρ_1. The outermost shell, $m = 3$, extends infinitely from interface radius, ρ_2. The shell, $m = 2$, extends from interface radius, ρ_1, to ρ_2 with some thickness, $\Delta\rho$, and contains a perturbation in the electrical parameters that define the material.

For this analysis, it is assumed that the interrogation frequency of the measurement is low, such that the electromagnetic behavior of the system is defined by the magneto-quasistatic regime. In general, the axial vector potential of a cylindrically symmetric magneto-quasistatic system, $A_{z,m}^*$, is:

Fig. 1 *The formation phase permeability measurement system, including a sensor array to image the radial profile of magnetic permeability surrounding the tool, injection of ultra-high magnetic permeability fluid from the surface to the downhole subsurface, and the surrounding formation with altered magnetic permeability due to the injected fluid.*
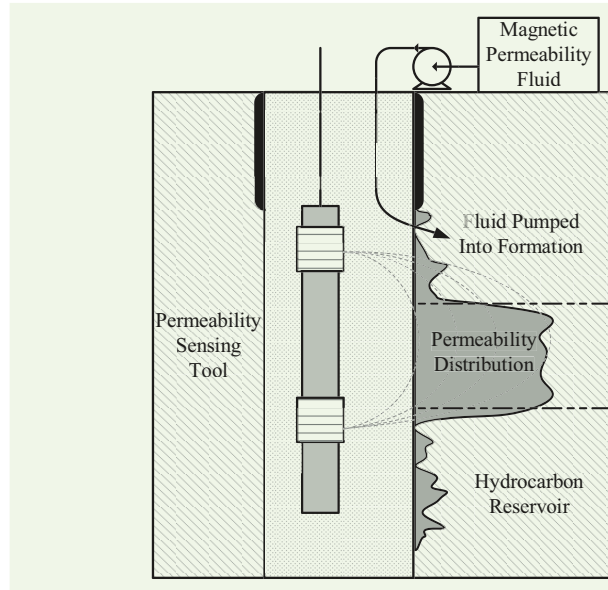
Fig. 2 *The mutual inductance measurement array modeled as a two coil system in a cylindrically symmetric medium. A cylindrical shell of perturbed magnetic permeability is located some radial distance away from the coils.*
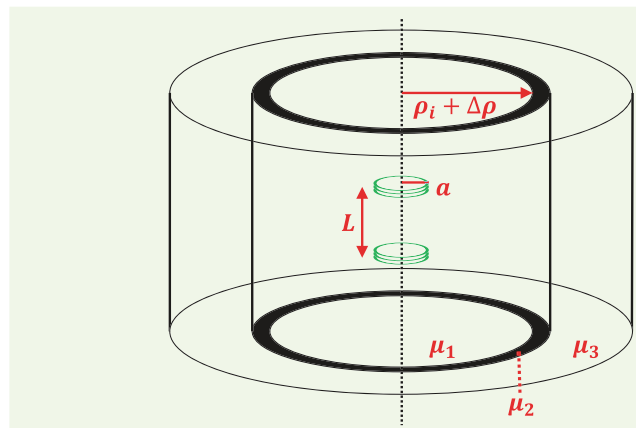
$$A_{z,m}^* = \frac{M_T}{2\pi^2}\int_0^\infty [C_m I_0(\lambda_m\rho) +$$

$$D_m K_0(\lambda_m\rho)]cos(\lambda z)d\lambda \qquad \boxed{3}$$

where I_0 and K_0 are zero order modified Bessel functions of the first and second kind, C_m and D_m are continuity coefficients for shell m derived from the boundary conditions at each shell interface, z is the axial separation distance from the transmitting coil, $M_T = N_T I_T \pi a_T^2$ is the moment of the transmitter coil, I_T

is the magnitude of the current driving the transmitter coil, $\lambda_m \approx \sqrt{\lambda^2 + i\sigma_m \mu_m \cdot 2\pi f_0}$ is the wavelength of the quasi-stationary mode in cylindrical shell m where the $\varepsilon_m \cdot 2\pi f_o$ term is removed as it is assumed the system is operating in a lower frequency regime, λ is a separation constant for the continuum of propagating modes, and f_o is the operating frequency of the transmitter coil.

In this cylindrically symmetric system, tangential components of the electric and magnetic field are continuous functions at each shell interface, and as such the boundary conditions at the interface between the shells are:

$$\mu_m \frac{\partial A_{z,m}^*}{\partial r} = \mu_{m+1} \frac{\partial A_{z,m+1}^*}{\partial r} \qquad 4$$

$$-i\sigma_m \mu_m 2\pi f_0 \cdot A_{z,m}^* + \frac{\partial^2 A_{z,m}^*}{\partial z^2} = \\ -i\sigma_{m+1}\mu_{m+1} 2\pi f_0 \cdot A_{z,m+1}^* + \frac{\partial^2 A_{z,m+1}^*}{\partial z^2} \qquad 5$$

The unknown continuity coefficients, C_m and D_m, for each shell can be solved using a series of equations from these boundary condition relations, such that:

$$\mu_m \lambda_m [C_m I_1(\lambda_m \rho_m) - C_m K_1(\lambda_m \rho_m)] = \\ \mu_{m+1}\lambda_{m+1}[C_{m+1}I_1(\lambda_{m+1}\rho_m) - C_{m+1}K_1(\lambda_{m+1}\rho_m)] \qquad 6$$

$$\lambda_m^2 [C_m I_0(\lambda_m \rho_m) + C_m K_0(\lambda_m \rho_m)] = \\ \lambda_{m+1}^2[C_{m+1}I_0(\lambda_{m+1}\rho_m) + C_{m+1}K_0(\lambda_{m+1}\rho_m)] \qquad 7$$

where I_l and K_l are first order modified Bessel functions of the first and second kind[5]. In the innermost shell containing the transmitter, the coefficient $D_l = 1$ as the source excitation takes the form of $\frac{2}{\pi}\int_0^\infty K_0(\lambda_1\rho)\cos(\lambda z)d\lambda$. In the outermost shell, the coefficient $C_3 = 0$ since function $I_0(\lambda_3\rho) \to \infty$ as the radial distance $\rho \to \infty$. The axial component of the magnetic field, $H_{z,m}$, is then computed from the vector potential, $A_{z,m}^*$, as:

$$H_{z,m} = -i\sigma_m \mu_m \cdot 2\pi f_0 \cdot A_{z,m}^* + \frac{\partial^2 A_{z,m}^*}{\partial z^2} \qquad 8$$

Along the borehole axis, the radial components of the magnetic field, H_r, and the rotational field, E_ϕ, reduce to $H_r = E_\phi = 0$. The axial magnetic field at the receiver coil simplifies to:

$$H_z = \frac{M_T}{2\pi}\left[\frac{1}{L^3}(1 - ik_1L)e^{ik_1L} - \frac{1}{\pi}\int_0^\infty \lambda_1^2 C_1 \cos(\lambda L)d\lambda\right] \qquad 9$$

In Eqn. 9, the left hand side represents the primary magnetic field along the z-axis and the right hand side of the equation represents the magnetic field due to induced currents in the surrounding medium, e.g., $H_z = h_{source} + h_{formation}$. The mutual inductance, M_{12}, between the transmitter and receiver coil is then:

$$M_{12} = \frac{1}{I_T}\oint_S \mu_1 H_z = \frac{\mu_1 \pi a^2 N_R H_z}{I_T} \qquad 10$$

Figure 3 shows the mutual inductance between a transmitting and receiving coil with radius $a = 0.0318$ meters, $N_T = N_R = 1$, and axial spacings ranging from $L = 1$ to 10 meters at an interrogation frequency of $f_o = 1$ kHz. The interior and exterior shells are assumed to be

air, e.g., $\sigma_{1,3} \approx 0$ and $\mu_{1,3} = \mu_0$. The middle shell $m = 2$, with a thickness of $\Delta\rho = 0.01$ meters, has conductivity, $\sigma_2 \approx 0$, and a perturbed magnetic permeability, $\mu_2 = 1.1 \cdot \mu_0$. The inner radial interface of the perturbed shell, ρ_I, ranges from 0.06 to 5 meters, and the mutual inductance between coils is calculated at each location. The normalized mutual inductance, $\widehat{M}_{12}$, is the ratio of the total mutual inductance to the mutual inductance contribution from the source term, such that the effects of the formation is highlighted, where:

$$\widehat{M}_{12} = \frac{\mu_1 \pi a^2 N_R}{I_T} \cdot \frac{(h_{source} + h_{formation})}{h_{source}} \qquad 11$$

From Fig. 3, it is evident that the unique sensitivity profiles of $\widehat{M}_{12}$ exist for each unique coil spacing for alterations in the magnetic permeability of the system. Note that the sensitivity to perturbations in magnetic permeability decreases when the extents of the shell radius increase. This follows from the density of the field lines traversing this perturbed shell, which rapidly decreases at the radii further from the coil pair. Given the uniqueness of each mutual inductance sensitivity profile for a fixed spacing of transmitter and receiver coil, an image of the radial distribution of magnetic permeability can be constructed from mutual inductance measurements across an array of coils with varying spacings.

A similar analysis is performed with a perturbation in conductivity. The geometries and coils are the same as in the analysis for Fig. 3. The interior and exterior shells are assumed to be brine saturated subsurface formations, e.g., $\sigma_{1,3} \approx 0.1$ S/meter and $\mu_{1,3} = \mu_0$. The middle shell, $m = 2$, with a thickness of $\Delta\rho = 0.01$ meters, has magnetic permeability, $\mu_2 = \mu_0$, and a perturbation in conductivity such that $\sigma_2 \approx 1$ S/meter. Figure 4 shows the normalized mutual inductance of this cylindrically symmetric system with a conductivity perturbation. In this case, there is little sensitivity to the perturbations in formation electrical characteristics

Fig. 3 *The mutual inductance normalized by the transmitter moment and source field contribution between two induction coils for axial spacings, L = 1 to 10 meters, as a perturbation of magnetic permeability in a thin shell of material is moved radially away from the coil system.*
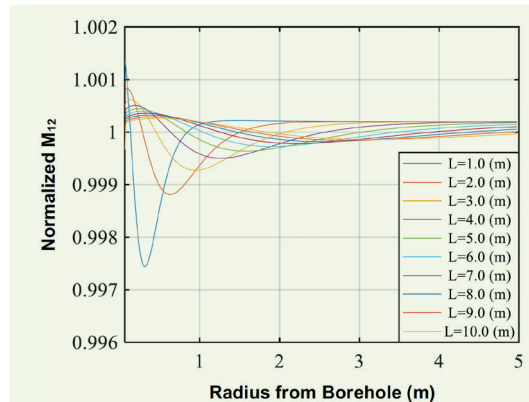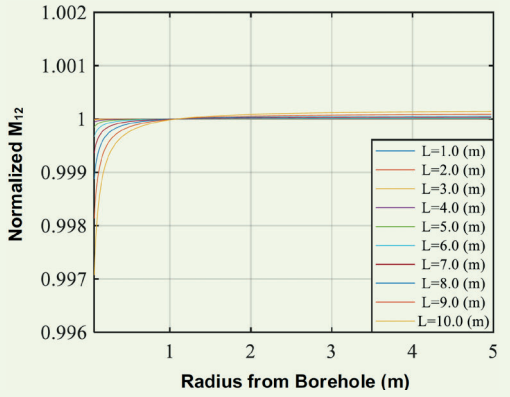
beyond 0.5 meters. Additionally, the response from each coil spacing does not have a unique sensitivity response vs. the perturbation radius.

Figure 5 shows the mutual inductance response of the sensor system to a variety of magnetic permeability profiles. Similar to the analysis for Fig. 3, transmitting and receiving coils with a radius of $a = 0.0318$ meters are arranged axially along a tool and probe the formation at an interrogation frequency of $f_0 = 1\ kHz$. A continuum of cylindrical shells with a thickness of $\Delta\rho = 0.01$ meters is constructed with conductivity $\sigma_m \approx 0$ and a relative magnetic permeability profile, μ_m, that corresponds to the profiles in Fig. 5a. Figure 5b shows the response from the system.

The mutual inductance due to the formation, $M_{12,formation} = M_{12}(H_z - h_{source})$, is the measurement response with the source term effects removed. From these figures, it is evident that extending the length of a higher

magnetic permeability region radially outwards into the surrounding formation provides an easily discernable difference in mutual inductance response of the system. The lensing effect of the higher magnetic permeability region provides a sharp response in mutual inductance at specific coil separations, and an effect in the amplitude envelope of the mutual inductance as a function of coil separation. The magnitude of the measured mutual inductance, due to the formation response, is in the sub-nH range. Consequently, this response scales proportionally with the number of turns of the transmitting and receiving coil.

Although the formation-only mutual inductance shows a strong response to changes in magnetic permeability of the surrounding formation, the small measurement magnitude brings into question the feasibility of the measurement in a physical system. The lower bound of variance in this measurement can be quantified by the Cramer-Rao lower bound. The system estimates relative magnetic permeability from a set of N mutual inductance measurements:

$$x[n] = M_{12}[n; \mu_R] + w[n] \qquad \text{12}$$

where $n = 1, \ldots, N$ is the sample index, $x[n]$ are discrete measurements taken with the system, $M_{12}[n; \mu_R]$ is the actual value of mutual inductance at sample n, which is a function of the relative magnetic permeability, μ_R, and $w[n]$ is white Gaussian noise with a mean of zero and a variance of σ^2. The minimum variance of an estimate of the scalar parameter, μ_R, $\hat{\mu}_R$, is given by the Cramer-Rao lower bound of this sampling process, such that:

$$var(\hat{\mu}_R) \geq \mathcal{I}(\mu_R)^{-1} \qquad \text{13}$$

As the Gaussian noise component of these measurements are independent of the parameter, μ_R, the covariance matrix of this data set is $C = \sigma^2 I$, where I is an $N \times N$ identity matrix[6]. The Fisher information matrix, $\mathcal{I}(\mu_R)$, is then computed as:
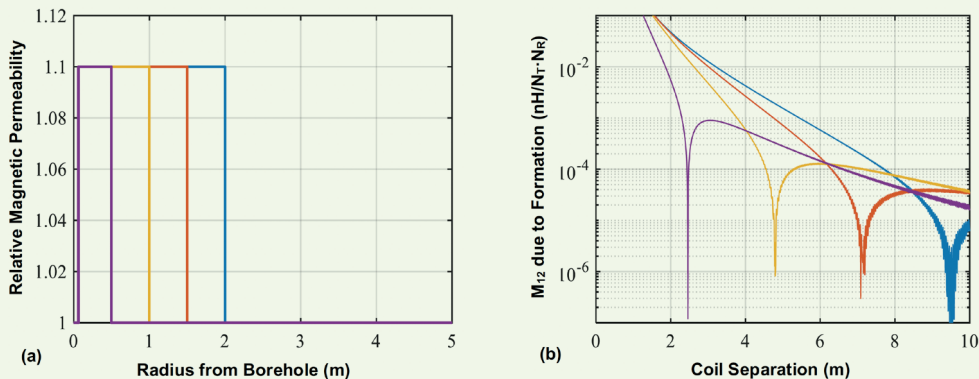
$$\mathcal{I}(\mu_R) = \frac{1}{\sigma^2} \sum_{n=1}^{N} \left(\frac{\partial M_{12}[n;\mu_R]}{\partial \mu_R} \right)^2 \qquad \text{14}$$

The minimum standard deviation of an estimate of $\hat{\mu}_R$, and therefore, the smallest value of μ_R detectable by this system, is then:

$$std(\hat{\mu}_R) \geq \frac{\sigma}{\sqrt{N}} \left(\frac{\partial M_{12}[n;\mu_R]}{\partial \mu_R} \right)^{-1} \qquad \text{15}$$

Figure 6 shows the minimum standard deviation of magnetic permeability estimates from a two coil mutual inductance measurement system. In this analysis, the geometry and coil configuration is the same as the analysis for Fig. 3, with air for the interior and exterior shells such that $\sigma_{1,3} \approx 0$ and $\mu_{1,3} = \mu_0$, and a perturbation shell, $m = 2$, with a thickness of $\Delta\rho = 0.01$ meters, $\sigma_2 \approx 0$, and $\mu_2 = 1.1 \cdot \mu_0$. The transmitter and receiver coils have $N_T = N_R = 100$ turns. It is assumed that the white Gaussian noise standard deviation of the measurement system is $\sigma = 1 \times 10^{-10}\,H$. This corresponds to $\sim 60\,\mu A$ of measurement noise in impedance measurement of inductance at a frequency of $1\,kHz$ at an amplitude of $1\,V$, which is well within the specifications of modern impedance analyzers.

The number of samples is $N = 1 \times 10^4$, which corresponds to 10 s of integration time for a system sampling frequency of $1\,kHz$. Results are displayed for a continuum of axial coil spacings, and radial depth of investigation for a perturbation in magnetic permeability. In this example, estimates of a change in magnetic permeability, $\Delta\mu_R \leq 0.1 \cdot \mu_0$, are feasible within ~ 1 meter from the borehole and coil spacings up to ~ 2 meters in separation. To increase the bounds of this $\Delta\mu_R \leq 0.1 \cdot \mu_0$ measurement region, the designer of such a system could: increase the number of turns in the transmitter and/or receiver coil, increase the number of samples in the data set, or decrease the magnitude of the measurement noise in the system.

Conclusions

Radial imaging of magnetic permeability with an array of induction coils arranged axially along a tool is feasible. The multiple coil system is sensitive to perturbations in magnetic permeability, and insensitive to other confounding electrical parameters, e.g., conductivity and permittivity. The unique response to radial distributions of magnetic permeability for fixed coil spacings provides a basis upon which radial images can be constructed. The lower bound of magnetic permeability estimation variance demonstrates the need for a precision measurement system, but this is within the capability of modern impedance measurement systems.

References

1. Tiab, D. and Donaldson, E.C.: *Petrophysics: Theory and Practice of Measuring Reservoir Rock and Fluid Transport Properties*, 4th edition, Gulf Professional Publishing, 2015, 918 p.

2. Al-Shehri, A.A., Ellis, E.S., Felix Servin, J.M., Kosynkin, D.V., et al.: "Illuminating the Reservoir: Magnetic Nanomappers," SPE paper 164461, presented at the SPE Middle East Oil and Gas Show and Conference, Manama, Kingdom of Bahrain, March 10-13, 2013.

3. Felix Servin, J.M., Deffenbaugh, M., Adams, R. and Riachentsev, V.: "Can We Propagate MHz EM Signals for 1 km through the Subsurface in the Presence of Conductive Media?" SEG paper 3215992, presented at the SEG International Exposition and Annual Meeting, San Antonio, Texas, September 15-20, 2019.

4. Felix Servin, J.M., Schmidt, H.K. and Ellis, E.S.: "Improved Saturation Mapping Using Planar Tranmission Lines and Magnetic Agents," SPE paper 181343, presented at the SPE Annual Technical Conference and Exhibition, Dubai, UAE, September 26-28, 2016.

5. Kaufman, A.A. and Dashevsky, Y.A.: *Principles of Induction Logging*, Elsevier, 2003, 656 p.

6. Kay, S.M.: *Fundamentals of Statistical Signal Processing: Estimation Theory*, Prentice-Hall Inc., 1993, 595 p.

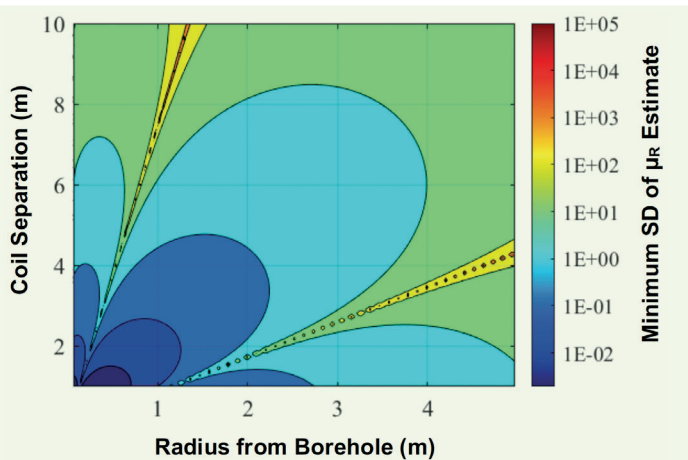**Fig. 6** *The minimum standard deviation of an estimate of relative magnetic permeability for a two coil mutual inductance measurement array for a continuum of axial coil spacings and radial depth of investigation into the subsurface formation.*

About the Authors

Robert W. Adams

M.S. in Electrical Engineering, University of Texas at Austin

Robert W. Adams is a Research Engineer within the Sensors Development Team at the Aramco Americas' Houston Research Center. Prior to joining Aramco Americas in 2015, he was a Research Engineer in the Emerging Technologies Group at Baker Hughes.

Robert's research interests include: statistical signal processing, electromagnetic imaging, acoustic imaging, sensor front-end system design, and optoelectronic devices.

In 2011, he received his M.S. degree in Electrical Engineering from the University of Texas at Austin, Austin, TX.

Jesus M. Felix Servin

M.S. in Chemical and Biological Engineering, King Abdullah University of Science and Technology

Jesus M. Felix Servin joined the Reservoir Engineering Technology Division of Saudi Aramco's Exploration and Petroleum Engineering Center – Advanced Research Center (EXPEC ARC) in February 2012. His focus is on the development of electromagnetic methods and nanoparticle-based contrast agents for reservoir characterization and monitoring. Jesus's role has been instrumental in the development and deployment of the Magnetic Nano-Mappers project, including hardware design and in-house fabrication, instrumentation, computer programming, and data processing.

Jesus' interests include the development of nanoscale strategies for reservoir illumination and electromagnetic methods for reservoir description and monitoring.

He received his B.S. degree in Engineering Physics from Instituto Tecnologico y de Estudios Superiores de Monterrey, Monterrey, Mexico, and an M.S. degree in Chemical and Biological Engineering from King Abdullah University of Science and Technology, Thuwal, Saudi Arabia.

Dr. Wei Wang

Ph.D. in Physical Chemistry, Chinese Academy of Sciences

Dr. Wei Wang is a Research Science Consultant on the Reservoir Engineering and Technology Team, Aramco Americas, Aramco Research Center-Boston. Since he joined the Aramco Research Center-Boston as one of the founding members in 2012, Wei's research has been focused on the application of advanced materials and nanotechnology for reservoir engineering.

Prior to joining Aramco, he was a Staff R&D Scientist at the Oak Ridge National Laboratory (ORNL), where he was the PI or co-PI for 17 research projects funded by the U.S. Department of Energy and ORNL. Wei received the Stanley I. Auerbach Award for Excellence in Environmental Sciences in 2009.

He has published more than 160 peer-reviewed research papers, four book chapters, and 12 patents. Wei is a Fellow of the Industrial and Engineering Chemistry Division of the American Chemical Society (ACS), and serves as a Program Chair at Energy and Fuel Division of ACS and a Program Committee Member of the Society of Petroleum Engineers (SPE) Annual Technical Conference and Exhibition. He is also an Editorial Board Member of *Nature Scientific Reports*.

In 1993, Wei received his Ph.D. degree in Physical Chemistry from the Chinese Academy of Sciences, Changchun, China, with the honors.

Dr. Max Deffenbaugh

Ph.D. in Electrical Engineering, Massachusetts Institute of Technology

Dr. Max Deffenbaugh joined the Aramco Americas' Houston Research Center in 2013 as a Research Engineer. He founded and leads the Sensors Development Team, who create new measurement techniques and instruments for the oil field.

Previously, Max worked for 16 years at ExxonMobil on seismic signal processing, inverse problems related to geological processes, computational rock physics, and development of downhole sensor networks.

In 1991, he received his B.S.E. degree in Electrical Engineering from Princeton University, Princeton, NJ. Max then received his M.S. degree in 1994, and his Ph.D. degree in 1997, both in Electrical Engineering, in a joint program of the Massachusetts Institute of Technology, Cambridge, MA, and the Woods Hole Oceanographic Institution, Falmouth, MA.

Sensor Ball: Field Deployment of Autonomous and Untethered Surveillance

Mohamed Larbi Zeghlache, Dr. Ahmed Y. Bukhamseen, Husain A. Muailu and Ahmed J. Abdulghani

Abstract /

With the evolving sensor technologies and advances in integrated solutions, routine surveys and interventions in oil and gas fields are going through a major revamp. The most recent developments in autonomous and untethered devices set a new paradigm shift in such crucial and frequent well operations. In this article, field implementation and deployment of the novel Sensor Ball technology is discussed to highlight success, challenges, and lessons learned.

The Sensor Ball is a small device, approximately the size of a tennis ball, which enables autonomous and untethered logging of pressure, temperature, and triaxial magnetic field amplitude. This intelligent device is self-powered using a battery pack with a battery life that suffices logging a dozen wells, including logging time and data transfer time. The internal memory is designed for large and high definition data rates for high-resolution and extended recording. The Sensor Ball is encapsulated in a ruggedized housing that can withstand downhole conditions as the device travels on a free-fall down to the programmed depth, as well as while floating back to the surface. This housing is light enough to enable an efficient and flawless return of the Sensor Ball exclusively under a bouncy effect once the attached weight is dropped off.

For the deployment of this innovative technology, new procedures and guidelines are developed to ensure a successful journey of the Sensor Ball. Despite the fail-safe features, pre-job planning and risk assessment procedures complement this user-friendly technology and make it reliable, efficient, and easy to use.

The results of the field trial of the Sensor Ball in water supply wells revealed a superior data quality of in both down log and log up modes. In fact, during the mission time of three hours only, thousands of feet of high-resolution data were collected. This operation would have taken double the time and a much more significant well site footprint, in addition to increased health, safety, and environment risk, if a standard wireline/slick line unit was mobilized for this routine operation. The Sensor Ball is a reliable and more advanced alternative to traditional well surveillance methods considering the operational efficiency and comparison with benchmark data. In fact, the footprint, cost, and time savings are substantial, especially in an offshore environment where barges are mobilized and operations depend on weather conditions.

This technology is a major breakthrough in the surveillance and logging world as it enables a fully autonomous and untethered acquisition of high-resolution data. The Sensor Ball offers more with less, and will ultimately replace traditional surveillance and intervention methods.

Introduction

In the oil and gas industry, data acquisitions of downhole pressure and temperature are considered one of the fundamental and routine responsibilities in any field's life cycle. Since early hydrocarbon exploration, the urgency of collecting bottom-hole pressure (BHP) and bottom-hole temperature (BHT) measurements has expanded, due to its direct contribution to understanding reservoir health, performance, and behavior. Static BHP (SBHP) and static BHT (SBHT) are obtained from wells to depict knowledge of local and average reservoir pressures and temperatures, which can help reservoir management study and optimize fluid movements, reservoir interference, and the driving mechanism. Consequently, as physical and chemical properties in a reservoir change over time, routine monitoring — monthly, quarterly, biannually, or annually — is essential to capture these dynamic changes.

Evaluation of well integrity is a priority and represents a key element of the well integrity management system. In fact, temperature and pressure surveys play a major role in evaluating and preventing casing leaks in the wells and any potential flow behind casings. Usually, these surveys are the first line of defense in evaluating immediate risks related to downhole flow anomalies in a well. There are several patterns for such anomalies that may indicate potential leaks, fluid dumping, up flow or flow behind the casing. Frequent surveillance and time-lapse analysis of such data are useful to maintain asset integrity and promptly recommend remedial

actions as needed.

There are several methods to obtain pressure and temperature surveys, such as from drillstem test strings, slick line gauges, wireline logging, coiled tubing sensors, a permanent downhole monitoring system (PDHMS), and electric submersible pump (ESP) sensors. In wells without ESPs or a PDHMS, a conventional well intervention is required to record these surveys. One of the cost-effective intervention methods is the use of a slick line unit with electronic gauges, Fig. 1.

This operation requires a vessel and ideal weather conditions in case of an offshore environment. The procedure involves rigging up safety equipment, a lubricator, and a pressure memory gauge. Then, the slick line cable with the pressure gauge is run in hole (RIH) to the desired depth with multiple stationary points throughout the survey to calculate the pressure gradient (psi/ft). Consequently, the average pressure will be calculated and referenced to the original oil-water contact.

As for the temperature surveys, the data is downloaded and analyzed by production engineers to evaluate potential leaks or downhole fluids communication. Intelligent field equipment, such as the PDHMS and ESP sensors, usually includes two gauges installed in the completion string by a rig near the reservoir's depth. These sensors are useful to estimate the reservoir pressure and gradient. In all cases where the sensors are permanent or retrievable, the collected data are stationary point measurements.

Well Surveillance Solutions

In most cases, more than 60% of a field's annual data acquisition and surveillance programs require pressure and temperature surveys. Conventional well intervention techniques, such as wireline and slick line, are considered a cost-effective conveyance and acquisition method. With relatively extensive logistical and operational procedures, they produce a good quality data with depth references. This data adds to the other solutions from downhole permanent and retrievable systems for a comprehensive integration and analysis at well and field scales.

Ultimately, equipping all wells with intelligent field monitoring systems can bring a major benefit to generalize and automate downhole surveillance. Research and development of new solutions to address field challenges and further optimize operations led to a miniaturized and self-deployable device for such applications[1]. The new autonomous and untethered well logging device, such as the Sensor Ball, brings numerous benefits:

- Small operational footprint. For offshore operations, this means a small transportation boat can be used. This solution brings a considerable cost saving as there is no need for big barges and cranes.

- Saves time and is cost-effective, due to a shorter job duration and manpower requirement.

- Improved health, safety, and environmental aspects as operators are not exposed to high pressure or gas release.

Fig. 1 *An illustration of a typical slick line rig up with its associated safety equipment. (Courtesy of Schlumberger)*
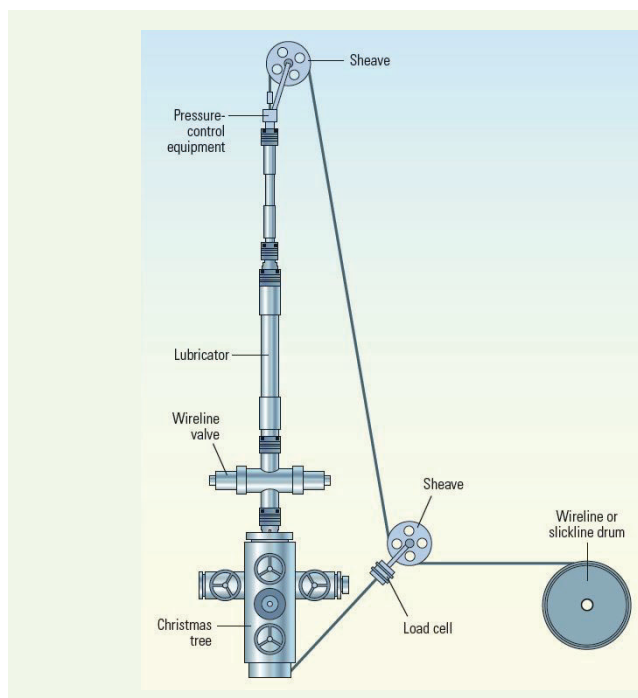
- Less risk of getting stuck in the well and leaving a fish, due to miniaturized design and multiple built-in safety features.

- No requirement for additional equipment to run the job, such as wireline and slick line rig-up equipment.

- The ability to get continuous pressure/temperature profile instead of selecting a handful of points in regular conveyance logging jobs.

- The ability to deploy several Sensor Balls simultaneously and independently for batch logging of several wells. This technique potentially enables batch surveillance of an eight-well platform in a single day as opposed to taking several days with conventional techniques.

- Provides superior data quality and validation from both acquisitions while descending and ascending in a well. Data repeatability and accuracy can be further analyzed.

- The Sensor Ball is a reliable conveyance platform. It has a modular design that can easily integrate more sensors in the future as needed.

## Sensor Ball Design

The Sensor Ball was designed as a fit-for-purpose tool to address field challenges. Here, the main design features are described[2] and aligned with the project's objectives.

Mechanical Housing

The main tool body is made of syntactic foam housing on top of a 3D printed polycarbonate chassis, Fig. 2. A perfect seal between these two elements is achieved
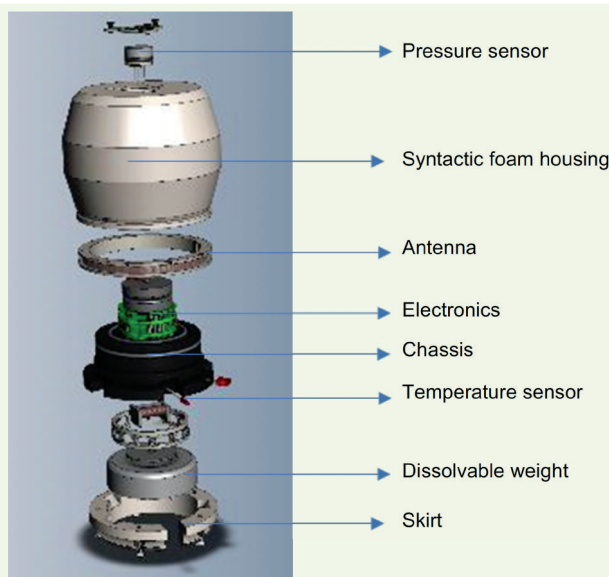
using two radial seal O-rings. The chassis contains the temperature and a three-axis magnetometer while the pressure sensor is mounted on top of the syntactic foam housing. The magnetometer is used as a casing collar locator (CCL), which is also used for depth correlation.

This engineered solution ensures that all internal components fit tightly in place while adhering to size constraints — a diameter of approximately 2.5" to be easily deployable in most well completions and restrictions. The material was carefully selected to have an effective overall density for the tool — approximately 0.9 g/cc — to allow it to float back to the surface in a water well when the down log is complete.

The housing has a unique hydrodynamic design to reduce drag forces along the well tubing and ensure minimal wiggling while descending and ascending.

Weight Assembly

To allow the Sensor Ball to navigate to the target well depth by gravity, a dissolvable weight made of composite material is attached magnetically to the bottom of the tool. With the weight attached, the effective tool density increases to 1.1 g/cc. The Sensor Ball can be programmed to demagnetize the electromagnet and release the weight when a predetermined criterion is met[3].

Currently, triggers include time, pressure, or temperature setpoints to initiate the release. Once the weight is released, it is left to dissolve on the bottom of the well and the Sensor Ball floats back to the surface using buoyancy.

Electrical Circuitry

Figure 3 shows the electrical architecture of the Sensor Ball. The four main printed circuit boards (PCBs) are stacked on top of each other using connectors and mounted on top of the chassis. The function of each PCB is described as follows:

- The first PCB provides power to other system components through two 3.3 V batteries rated up to 250 °C. The power PCB is responsible for releasing the dissolvable weight when the release criteria is met. The weight release actuator is composed of two magnets that can be magnetized or demagnetized by applying a short current pulse into the coil around it. Before Sensor Ball deployment, the magnets are polarized on the same direction to pull the magnetic weight toward the Sensor Ball body. When the weight release is triggered, the two magnets are polarized in opposite directions.

Fig. 3 *The electrical architecture for the Sensor Ball.*
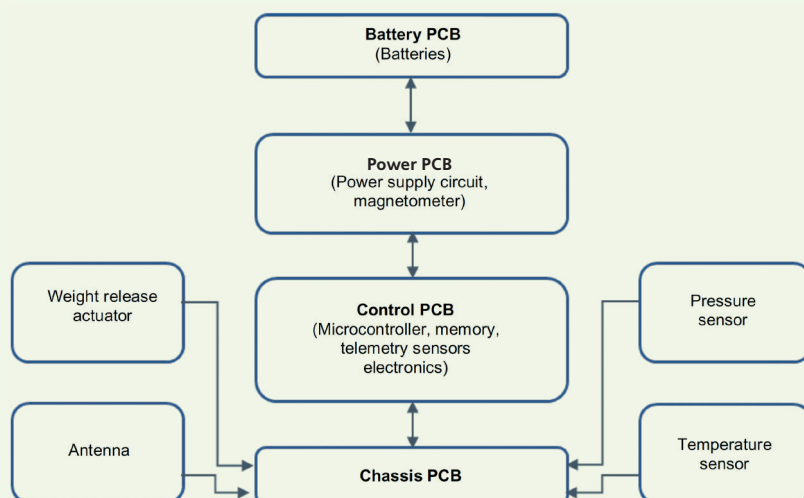
- The second PCB contains the control circuit and sensors, including a microcontroller, an external memory block, and the sensor's electronics. Wireless communication for both programming and retrieving data is achieved through an antenna coil and the telemetry circuit[4].
- The last PCB physically connects the sensors to the Sensor Ball chassis.

Field Deployments of Sensor Ball

The untethered logging, surveillance, and intervention services will revolutionize the oil and gas industry. Many aspects around this new technique are established to accommodate logistical and operational procedures. To ensure safe and efficient execution, a fit-for-purpose program was established and communicated with stakeholders, Fig. 4.

The deployment program is tailored to both a single well survey as well as campaign surveys. In this latter one, few options are discussed depending on the number of wells to be logged and the number of devices to be used. The first and straightforward deployment is the series technique, Fig. 5. This technique enables the survey of multiple wells with the same device.

The second technique is the parallel deployment where multitasking takes place offline during the logging time. Once the Sensor Ball is below the master valve, the operator can move to the next well and repeat the same deployment procedure. This process can be repeated until the last well to be surveyed or the last available Sensor Ball. Once the deployment is completed, the operator attends the wells in the same sequence to retrieve the Sensor Ball in the first well and so on. Figure 6 represents the sequence of events

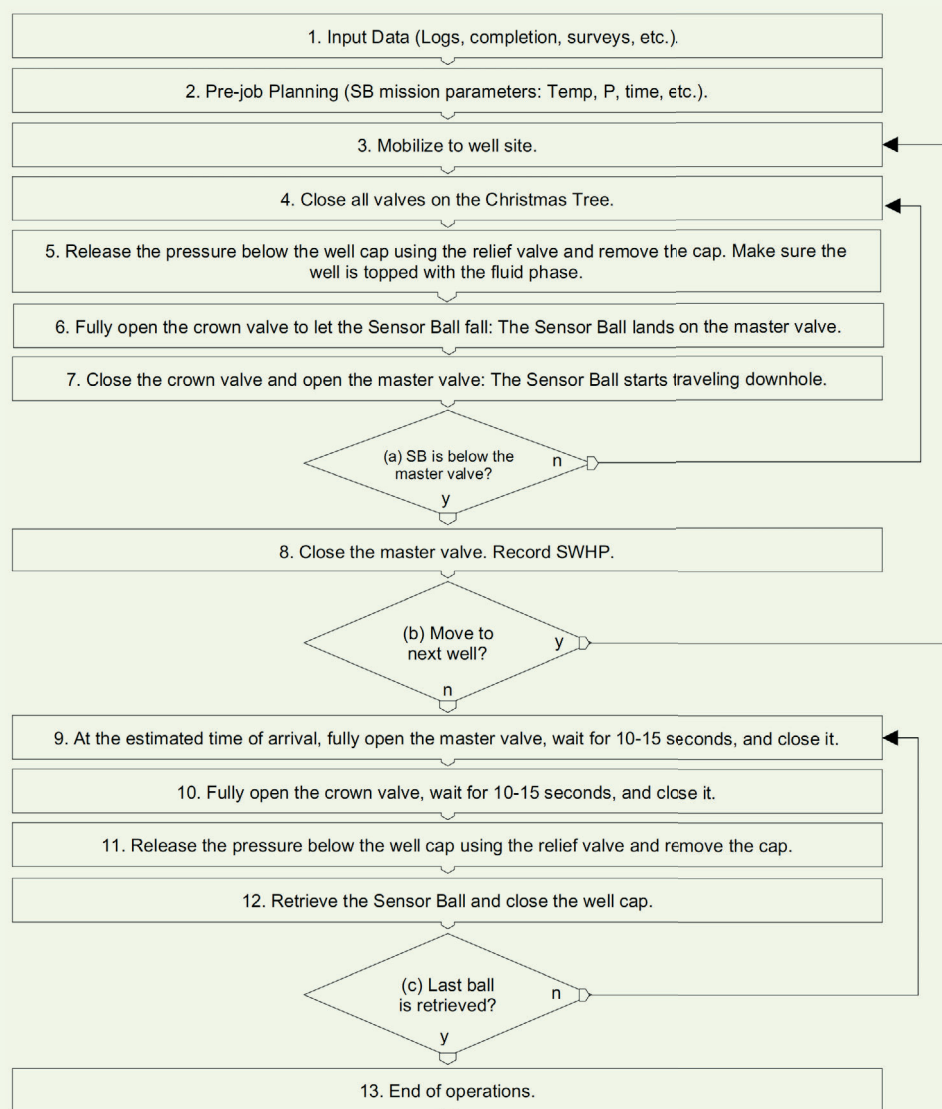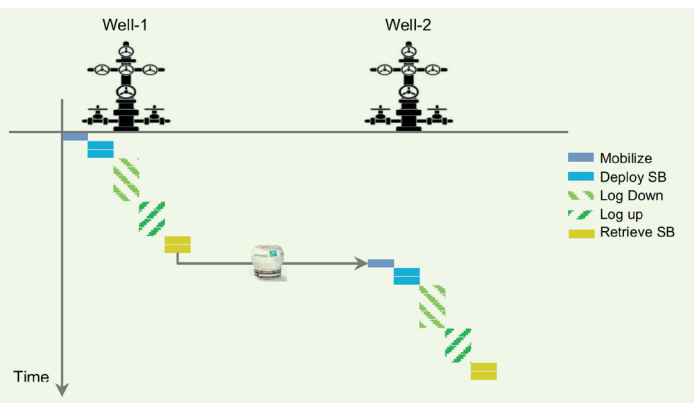***Fig. 4*** *The untethered surveillance program.*

Fig. 5 *The series deployment in multiple wells using one device.*

to illustrate the parallel deployment of Sensor Balls.

Obviously, this means that retrieval of the Sensor Ball and the number of available Sensor Balls are not a concern. Otherwise, the number of wells to assess before returning to the first one is roughly equal to the truncated ratio of the Sensor Ball's average mission time to the cumulative time of mobilizing and deploying the Sensor Ball in the next well. This technique ensures minimal time for the Sensor Ball to wait below the master valve before retrieval, and helps to save battery life as well as to anticipate any operational or technical issues.

The combination of series and parallel deployment can further optimize operations and increase the number of surveyed wells; thereby further reducing time and cost associated with well surveillance. The resulting deployment scheme, referred to as batch surveillance, is a large-scale deployment of multiple

devices for simultaneous multiple well surveillance. Figure 7 illustrates the batch surveillance of 12 wells using four Sensor Balls.

Technology Validation

The testing protocol of each manufactured Sensor Ball includes deployment in the Houston Research Center (HRC2) test well[5]. In this shallow depth well, the expected BHT and BHP are 600 psi and 70 °F, respectively. In addition to these two important parameters, the mission time is programmed to ensure that the weight release mechanism is activated if pressure and temperature limits are not reached within the mission's estimated time. This is critical in case of any operational concern during deployment or premature mission failure due to stack, for example. The safety measures that are included in the Sensor Ball design ensures safe deployment and retrieval of the device with the primary mechanism or secondary measures such as flow back.

As illustrated in step 2 of Fig. 4, the parameters of the Sensor Ball's mission depends on the surveillance objectives and the well information. The temperature and pressure set points for the weight release trigger are usually taken from the previous well surveys when available[6]. Otherwise, a known temperature and pressure gradients can be used to estimate these parameters. For the mission time, multiple runs of the Sensor Ball in a known environment helped to establish a good model to estimate the RIH and pull out of hole speeds.

Test Well Results

In the field trial, pre-job checks of the Sensor Ball were completed, including release parameters before the dissolvable weight was attached in place, Fig. 8. At this stage, it is important to ensure the integrity of the weight and verifying both the ferromagnetic plate and screw. Partial magnetization or rugous magnet

Fig. 6 *The parallel deployment in multiple wells using multiple Sensor Balls.*
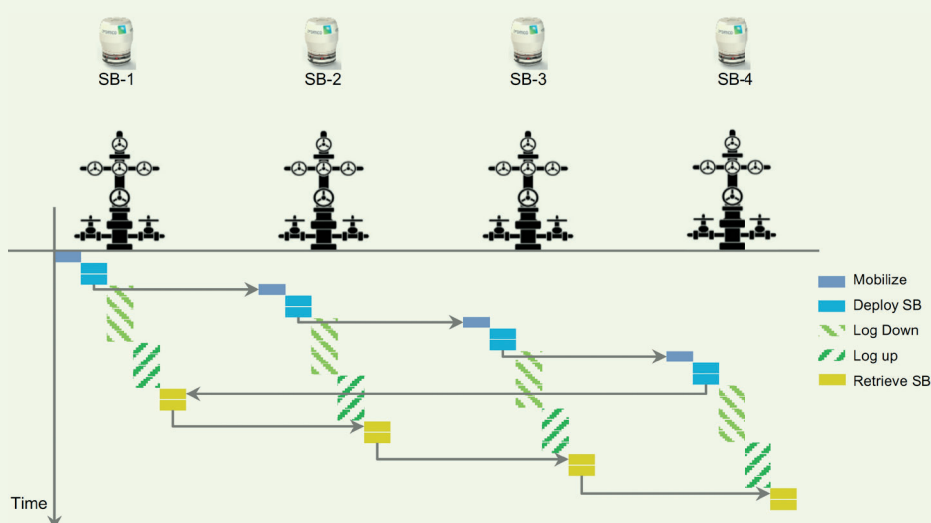
Fig. 7 *A batch deployment in multiple wells using multiple Sensor Balls.*
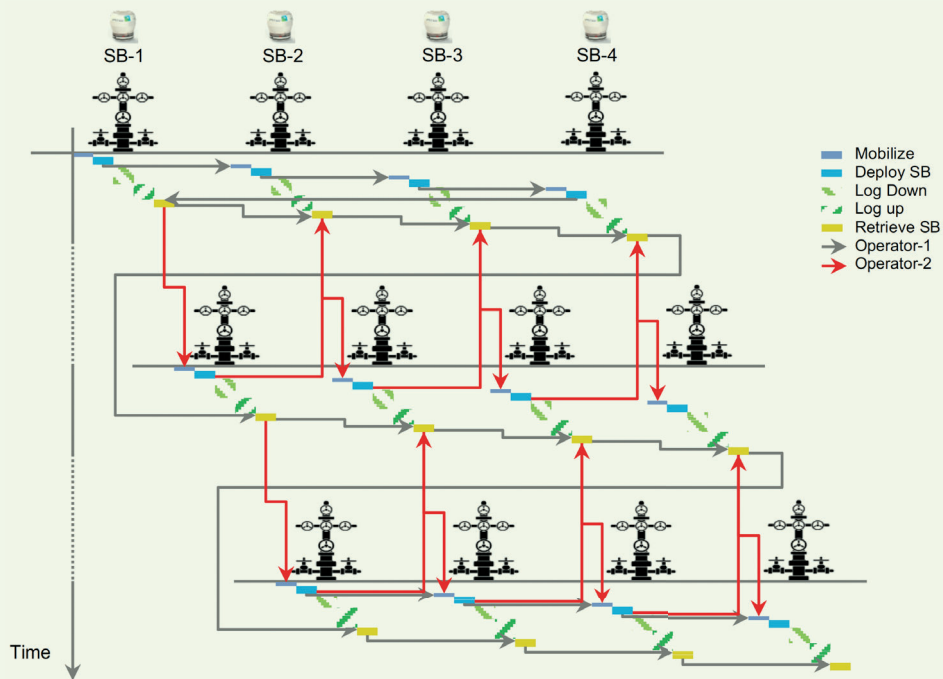
Fig. 8 *The field deployment of a Sensor Ball in a land rigless well: (a) Sensor Ball pre-job check, (b) dropped in the well, and (c) returned back.*
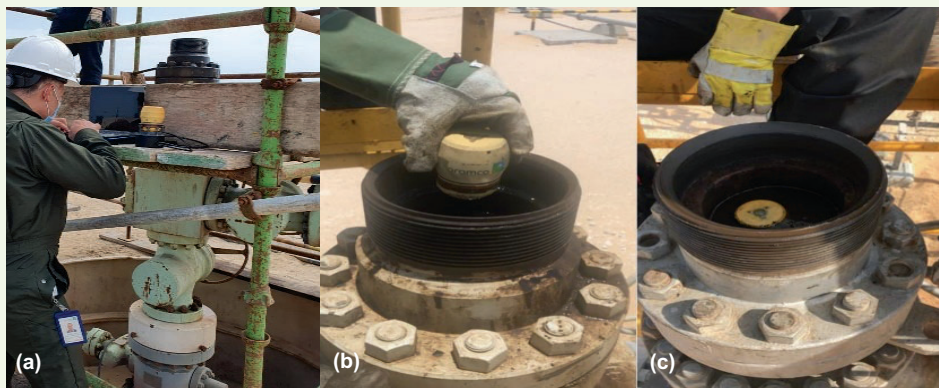
poles due to accumulated debris can cause premature release of the weight material; thereby leading to an incomplete surveillance.

A good practice is to clean the surface of the magnetic poles and physically test the weight adherence. Once the well is ready and the cap is opened, dropping the ball has to be done gently in a full fluid column. Due to some difficulties opening the tree cap, lubricants and other spray chemicals might be used to facilitate and accelerate this process. Contaminated fluids have to be purged prior to contact with the Sensor Ball.

The collected raw data comprising temperature,

pressure, and triaxle magnetic field is retrieved from the Sensor Ball using a docking station. To visualize and analyze the data, commercial logging software can be used to import the data into a table, either in ASCI or any convenient format.

The major events captured by the Sensor Ball in Fig. 9 are quality control points and summarized as follows:

1. The Sensor Ball is powered up, parameters are checked, and the weight is loaded. The sensors read atmospheric pressure and surface temperature. The magnetometers show the initial activity during testing and weight loading, which usually

Fig. 9 *The Sensor Ball's quality control points for raw data and major events.*
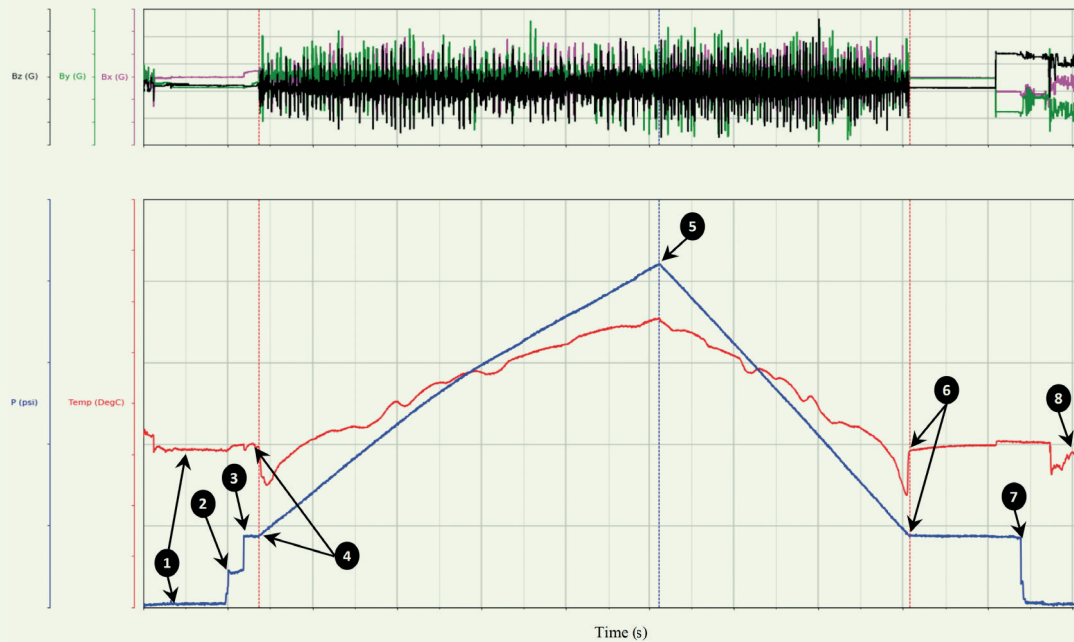
happens away from the wellhead.

2. The Sensor Ball is dropped and the well cap is sealed. There is a slight increase in pressure due to opening the crown valve.

3. The pressure increases the surface wellhead pressure (SWHP) as soon as the master valve is opened. There is a standby time (between event 3 and event 4), during which the Sensor Ball pressure sensor is exposed to well conditions; however, temperature and magnetometer sensors indicate that the device is stationary. This corresponds to the required valve operation to allow enough room for the Sensor Ball to start the downward journey.

4. All sensors respond as the Sensor Ball starts its down movement. The magnetometer is one of the precise sensors used to identify wellhead and casing collars, and respond in a timely manner to this event. The temperature sensor shows a typical response of surface variations, whereas pressure buildup vs. time reflects increased depth. The pressure data is an important quality control to the overall mission as well as to identify fluid gradient and compare it to the expected/known fluid properties.

5. As one of the set conditions is met to trigger the weight release, the mirror profile begins. In this candidate well, the temperature set parameter was met, and so the Sensor Ball successfully released the weight and started to float back to the surface. This position is what is commonly known in the logging world as the bottom log interval. It can be the total depth of the well or any desired depth to start the log up.

If the Sensor Ball is programmed to reach the bottom of the well, then the pressure and temperature at this event represents the SBHP and SBHT, respectively. This is quite important to consider in the pre-job planning as it can determine the success of the mission and data acquisition.

6. After the completed log up, the Sensor Ball is standing by below the master valve, waiting to be retrieved. The magnetometer shows no movement of the Sensor Ball. In addition, pressure and temperature return to the initial values before RIH. The difference in logging speed is clearly noticeable in time between down log and log up. The down movement is relatively slower due to buoyancy and friction. This feature is an important quality control of sensor data repeatability at different speeds and potential sensor positions in the wellbore.

Event 6 also marks the total mission time that is used in pre-job planning. Therefore, it is a good practice to compare the expected values with respect to the actual ones. A safety factor should be applied to the timed weight release to account for any intermittent stick and slip, or stuck situation. Methods to detect the Sensor Ball below the master valve before departure and after arrival can be added for more operational optimization and they are not discussed in this article.

7. The master valve is opened to let the Sensor Ball go below the crown valve. Once the master valve is closed and the crown valve is opened, pressure is relieved from the bleed nose on the cap; therefore, the recorded pressure drops to atmospheric levels. This movement is captured by the magnetometers

and reflected in the triaxle responses.

8. As soon as the Sensor Ball is retrieved and cleaned, the power is switched off to save the battery life, waiting for data retrieval.

During any operation or intervention downhole in the oil and gas well, depth is the primary measurement. For tethered intervention, depth measurement relies on surface and/or downhole devices such as drillpipes' tally, depth marks, magnetic marks, depth wheels, etc. For the case of untethered devices (or robots) that are not equipped with the previously mentioned devices or techniques for direct or indirect depth measurement, the sensor data is recorded vs. time. The challenge is to properly and accurately convert the time stamp into depth for meaningful and useable data.

In the depth calculation workflow, a data set is created using two subsets of the recorded data. If a well is logged multiple times, each run data can be handled separately for processing purposes and then compared for better QA/QC. The outcome of this workflow is two subsets of data corresponding to different resolutions. These logs are depth matched to each other at

a first step and then correlated to the reference depth measurement. Log stretching and compression due to uneven motion of the Sensor Ball can be corrected using the predefined collars' location. This effect can be greatly minimized with the use of an accelerometer sensor. This will allow proper speed correction of the data prior to depth matching.

The automated workflow using data analytics and machine learning addresses depth measurement challenges. The example of data used in this article can be applied to any other data package where recording starts and ends at the surface with either manual switch (on/off) or based on a built-in sensor to satisfy a specific condition (temperature, pressure, time, etc.). Once data acquisition is successfully completed, the automated depth correlation process will sequentially and intuitively generate parameters to clean and prepare the data, e.g., SWHP, SBHP, and SBHT.

This is mainly used for clipping the nonrequired portion of the data such as surface idle condition. This will also detect the time index of the bottom position where the untethered device has reached the total depth based on recorded data such as pressure,

Fig. 10 *The Sensor Ball's processed and separated time driven data; (a) down log, and (b) log up.*
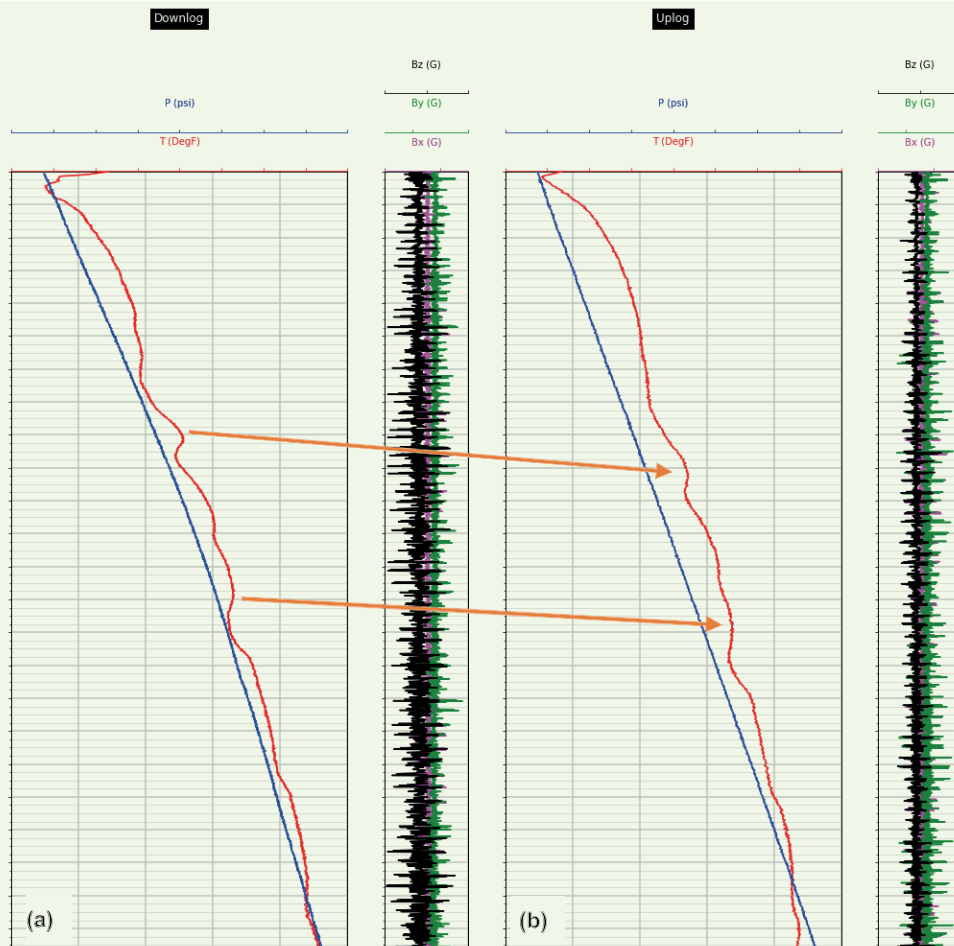
temperature, magnetometer, and accelerometer data, etc. Once data is clean and the time of the total depth position is marked, data is separated into two sets: down log and log up. To properly present both subsets, a time stamp of the fast data (log up) data is corrected and re-indexed.

The results of this process are presented in Fig. 10. Both down log and log up are processed and synchronized to the down log. The time logs will be converted to a depth log using one or a combination of the following techniques:

1. Pressure gradient: In this technique, the pressure gradient from both logs is used to convert time to depth using the known well fluid density. This qualitative approach can help for quick-look analysis of the data prior to full processing and proper depth conversion. In addition, it is a good quality control to assess the Sensor Ball mission success. Anomalies can be spotted quite easily across zones where pressure gradient comes off the expected range of the fluid column.

The derived depth, D, is calculated using the SWHP and SBHP shown in event 4 and event 5, respectively:

$$SBHP = SWHP + HP \tag{1}$$

$$HP = p \times g \times h \tag{2}$$

Therefore,

$$h = \frac{SBHP - SWHP}{\rho \times g} \tag{3}$$

where $SBHP$ is the static bottom-hole pressure, $SWHP$ is the surface wellhead pressure, HP is the hydrostatic pressure, ρ is the fluid density, g is the gravity acceleration, and h is the true vertical depth.

The main challenge with this technique is borehole fluid heterogeneity, well deviation and sensor motion.

2. Tubing tally: It is quite efficient to correlate down log and log up data to the reference tally using the magnetometer data. The collar location is further improved using all six channels from the triaxle magnetometer in both the down and up directions.

Fig. 11 *The Sensor Ball's final depth driven data.*
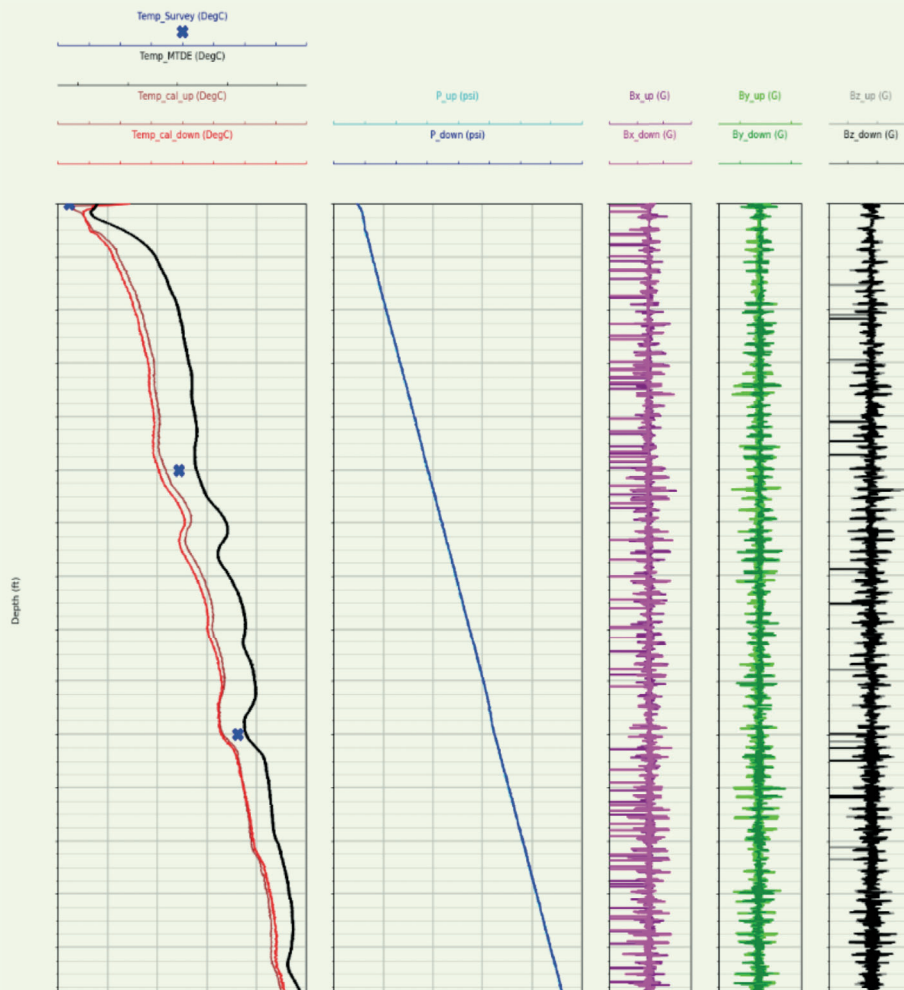
Obviously, this technique will work in a cased hole environment with good tally or CCL log.

3. Log correlation: Time driven data can be correlated to previous temperature and pressure surveys. The depth reference of the original conveyance is used for the untethered sensor data.

As illustrated in Fig. 10, data follows similar responses and trends from both the down log and log up path. Despite the fact that both logs can be "on time" by stretching and compressing the logs, it is clear that additional speed correction and correlations are needed to properly put the data "on depth." This crucial step is performed to produce the final data with a wireline quality and display.

Sensor Ball Solution

The final product in Fig. 11 represents a paradigm shift in the logging and intervention business. In fact, the correlation validation of the processed data used benchmarks from previous wireline surveys as well as stationary measurements. This approach is used to qualitatively and quantitatively assess the Sensor Ball response in downhole conditions.

The temperature data tracks the response from the previous wireline run, and the calibrated temperature values show a consistent response to well history and downhole conditions. The depth matching has eliminated the apparent discrepancy in the pressure profiles and produced a perfect match between the two data sets. The resultant gradients match the fluid sample analysis and calculated gradient from other pressure sensors.

Concerning the triaxle magnetometer data, the casing collar detection is a key enabler to multiple quality control points as well as for the depth correlation with reference to the completion tally. Having such large data with six channels increases detection accuracy and collar location confidence, which results in a reliable alternative to CCL. The Sensor Ball can help attend wells where the accessibility of standard wireline and slick line tools might be challenging due to sophisticated well completion.

The algorithms used to derive this answer are developed using python open source libraries to clean and process the data. The software capabilities adds another dimension to data acquisition and processing by adding further process optimization and service automation. Such an example is demonstrated in the correlation between different data as well as channels of the same data set. Classification algorithms are also used in collar detection to discriminate noise peaks and confidently allocate coherent peaks to the corresponding collar in the completion tally. For data plotting and display, the pyplot module from the matplotlib library enabled great flexibility and features to deal with log data.

Conclusions

With the ever evolving sensor technologies, in terms of miniaturization and capabilities, the Fourth Industrial Revolution adds the algorithms and techniques to further optimize and automate downhole data acquisition and interpretation. This major advance in the oil and gas industry is demonstrated through the Sensor Ball technology that brings the intervention and surveillance of wells to a new era. In fact, the Sensor Ball enables untethered and autonomous acquisition of pressure, temperature, and triaxial magnetic field data. This revolutionary small device paves the way to eliminate routine wireline and slick line surveys in both land and offshore environments.

The field trials of this technology helped to tailor a unique solution and facilitate field operations. The lessons learned from these trials played a major role in the continuous development of the Sensor Ball. The technology value realization relies on the reduced footprint, logistics, and personnel involved in well surveillance, which leads to a major health, safety, and environmental improvement in cost and time savings. In addition, remote offshore locations will no longer wait for barges and ideal weather.

The flexibility that the Sensor Ball offers also enabled optimization of logging and surveillance campaigns through simultaneous multiwell operations. This major step cannot be achieved with traditional wireline or slick line units and crews. In the future, more sensors will be integrated and the design will be upgraded to extend capabilities to other well types and well conditions.

Acknowledgments

References

1. Deffenbaugh, M., Ham, G.D., Alvarez, J.O., Bernero, G., et al.: "Method and Device for Obtaining Measurements of Downhole Properties in a Subterranean Well," U.S. Patent No. 10,900,351, January 2021.

2. Buzi, E.S., Seren, H.R., Deffenbaugh, M., Turner, R., et al.: "Sensor Ball: An Autonomous Untethered Logging Platform," OTC paper 30538, presented at the Offshore Technology Conference, Houston, Texas, May 4-7, 2020.

3. Seren, H.R., Buzi, E. and Deffenbaugh, M.: "Electro-Permanent Magnetic Weight Release Mechanism for Buoyancy Control of an Autonomous Well Logging Tool," *AIP Advances*, Vol. 11, Issue 2, February 2021.

4. Seren, H.R., Buzi, E., Powell, C. and Deffenbaugh, M.: "Wireless Communication and Charging for an Untethered Downhole Logging Tool," *2019 IEEE Sensors*, 2019, pp. 1-3.

5. Buzi, E., Seren, H.R., Deffenbaugh, M., Bukhamseen, A., et al.: "Sensor Ball: Autonomous, Intelligent Logging Platform," OTC paper 31149, presented at the Offshore Technology Conference, Houston, Texas, August 16-19, 2021.

6. Seren, H.R., Buzi, E., Al-Maghrabi, L., Ham, G., et al.: "An Untethered Sensor Platform for Logging Vertical Wells," *IEEE Transactions on Instrumentation and Measurement*, Vol. 67, Issue 4, 2018, pp. 798-803.

About the Authors

Mohamed Larbi Zeghlache

M.S. in Reservoir Engineering and Field Development, French Petroleum Institute

Mohamed Larbi Zeghlache is a Senior Researcher and the well integrity logging subject matter expert working with the Production Technology Team of Saudi Aramco's Exploration and Petroleum Engineering Center – Advanced Research Center (EXPEC ARC). He previously led the well integrity logging team in the Reservoir Description and Simulation Department.

Since joining Saudi Aramco, Mohamed has been responsible for formation evaluation and well placement in Ghawar carbonates and Central Arabia clastics.

He has 19 years of experience in the oil and gas industry, and previously worked with both Schlumberger and Halliburton where he held various positions, including Wireline Field Engineer, Log Analyst, Business Development, and Technical Advisor.

Mohamed is the author of several publications and patents.

He received his M.S. degree in Reservoir Engineering and Field Development from the French Petroleum Institute (IFP), Paris, France.

Dr. Ahmed Y. Bukhamseen

Ph.D. in Petroleum Engineering, Stanford University

Dr. Ahmed Y. Bukhamseen is a Petroleum Engineer working with the Production Technology Team of Saudi Aramco's Exploration and Petroleum Engineering Center – Advanced Research Center (EXPEC ARC). His extensive experience includes reservoir engineering, production operations and completions research and development. Ahmed's current research activities cover smart well completions,

production optimization, fiber optic sensing and multiphase flow metering.

He has published several technical papers and holds three patents.

Ahmed received his B.S. degree from the Colorado School of Mines, Golden, CO, and both his M.S. and Ph.D. degrees from Stanford University, Stanford, CA, all in Petroleum Engineering.

Husain A. Muailu

M.S. in Petroleum Engineering, University of New South Wales

Husain A. Muailu is a Production Engineering Unit Supervisor for the Berri field. He oversees the production, well integrity, and surveillance programs of Berri field, and supports the field's ongoing expansion program to double the production capacity. Husain started his career in 2009 as a Production Engineer working in the Safaniyah Production Engineering Division. Then, he worked in several development assignments between operations and engineering departments, including reservoir engineering, workover, and offshore well services.

In 2019, Husain was promoted to a Unit Supervisor of the Technical Support Unit, then he moved to his current position.

He is the author or coauthor of more than 10 technical and journal papers.

In 2009, Husain received his B.S. degree from King Fahd University of Petroleum and Minerals (KFUPM), Dhahran, Saudi Arabia, and then received his M.S. degree in 2016 from the University of New South Wales, Sydney, New South Wales, Australia, both in Petroleum Engineering.

Ahmed J. Alabdulghani

M.S. in Petroleum Engineering, King Abdullah University of Science and Technology

Ahmed J. Alabdulghani is a Production Engineer working in the Ras Tanura Production Engineering Division of Saudi Aramco's Northern Area Production Engineering Department. He has more than 10 years of experience in production optimization, well intervention, well integrity management, and technology deployment.

Ahmed has worked in several assignments throughout his career, including Workover, Reservoir Management, and the Production Technology Division of the Exploration and Petroleum Engineering Center – Advanced Research Center (EXPEC ARC). He is currently a

candidate in the Production Engineering Specialist Program (PESP) in Well Completion and Wellhead Equipment.

Ahmed completed Saudi Aramco's College Degree Program for Non-Employees. He then received a scholarship to study for his B.S. degree in Petroleum Engineering at the University of Manchester, Manchester, U.K., graduating in 2010. In 2019, Ahmed received his M.S. degree in Petroleum Engineering from the King Abdullah University of Science and Technology, Thuwal, Saudi Arabia.

Produced Water Reuse for Drilling and Completion Fluids Using a Novel Ion Exchange Unit

Dr. Fahd I. Alghunaimi, Dr. Young C. Choi and Hind S. Aldossary

Abstract /

Produced water is considered one of the largest by volume waste streams and one of the most challenging effluents in the oil and gas industry. This is due to the variety of contaminants that make up produced water. A variety of treatment methods have been studied and implemented. These methods strive to reduce the hydrocarbon content and the number of contaminants in produced water to meet the disposal, reuse, and environmental regulations. These contaminants can include dispersed oil droplets, suspended solids, dissolved solids, heavy metals, and other production chemicals.

Some of those contaminates have value and can be a commodity in different applications such as bromine (Br). Br ions (Br^-) can be used to form calcium bromide ($CaBr_2$), which is considered one of the most effective drilling agents and is used extensively in drilling and completion operations.

This article will strive to highlight the utilization and the new extraction method of Br^- from produced water to form $CaBr_2$. The conventional preparation of $CaBr_2$ drilling and completion fluids involves adding solid $CaBr_2$ salts to the water, which can be relatively expensive. Another method can involve the handling of strong oxidants and toxic gas to form solid $CaBr_2$.

The novel method outlined in this article is a cost-effective and environmentally friendly way of generating $CaBr_2$ from produced water. The method includes processing the produced water to recover Br^-. This is done by first passing the produced water through a resin bed, including Br specific ion exchange resin, where the Br^- will adsorb/absorb onto the resin.

The second step involves regenerating the resin with regenerant having calcium cations and water to form $CaBr_2$. The final stage is generating the $CaBr_2$ in the water from the bed of resin by introducing concentrated calcium chloride ($CaCl_2$), forming a concentrated solution of water and $CaBr_2$. The developed solution will be further processed to provide drilling and completion fluids.

This novel method constitutes a good example of produced water utilization in different applications to minimize waste and reduce the costs of forming highly consumable materials.

Introduction

Produced water treatment is a major process in the petroleum field, and adsorption is one of the effective ways to remove oil/ions from produced water to meet the disposal, reuse, and environmental regulations[1, 2]. The conventional way of treating produced water is mainly physical separation of oil and water using gravity; however, this technology could not produce high quality water for reuse in applications like fracturing.

Currently, there is a need to develop novel methods and materials targeting the removal of oil/ions from produced water. Br ions (Br^-) are available in oil field produced water. Br^- can be used to form calcium bromide ($CaBr_2$), which is considered one of the most effective drilling agents and is typically used extensively in drilling and completion operations.

This article strives to highlight the utilization and the new extraction method of Br^- from produced water to form $CaBr_2$. As previously mentioned, $CaBr_2$ can be used as a drilling fluid based on its high specific gravity. The conventional preparation of $CaBr_2$ drilling and completion fluids involves adding solid $CaBr_2$ salts to the water, which can be relatively expensive. Subsequently, this novel process is using Br specific ion exchange resins and calcium chloride ($CaCl_2$) as a regenerant to recover and generate $CaBr_2$ from waste material (produced water) with less cost.

Some oil field produced water contains high levels of Br, which is used in drilling operations for various purposes. It would be beneficial to generate and obtain drilling fluid ($CaBr_2$) from a location that is in close proximity to where it will be consumed. During the drilling, the drilling fluid helps to cool and lubricate the drill bit and carry and remove rock cuttings from the hole. The drilling fluid also provides hydrostatic pressure to prevent or reduce formation fluids from the subterranean formation entering into the hole during drilling. These drilling fluids include the completion fluids and workover fluids.

Completion fluid is placed into the well (wellbore) for completion activities, including final operations prior to

hydrocarbon production. Such final operations include setting screens or production liners, setting tubing, installing packers, and perforating the wellbore casing (in productions zones). Completion fluids also help to improve well productivity by reducing damage to the producing zone, and prepare, repair, clean out, and complete the wellbore during the completion phase.

Water-based drilling fluids have a base fluid that is freshwater, seawater, brine, saturated brine, or a formation brine. Drilling fluid with $CaBr_2$ is a beneficial drilling fluid utilized to cool and lubricate the drill bit and to remove rock cuttings from the hole. The $CaBr_2$ drilling fluid will increase the density to overcome formation pressures and thereby maintain oil, gas, and water in place in the formation during drilling or well completion operations.

The current practice of extracting Br from brine is to use chlorine (Cl_2), a strong oxidant, to convert Br^- to Br_2 gas under high temperature. Then, a solvent is used to extract Br_2, which is later used to produce $CaBr_2$. This traditional method involves many toxic gaseous processes that are not suitable for oil field operations[3, 4].

Here, this work utilizes the ionic affinity of resins to capture Br and then release it with $CaCl_2$, which will produce $CaBr_2$ in a single step instead of multiple steps that are highly energy intensive and costly. This idea will allow the production of $CaBr_2$ in the oil production sites from produced water and prevent the production of dangerous chemicals and gases. Using only aqueous and ionic processes makes this work naturally safer and compatible with current oil operations. Also, it will provide more value from the current production sites.

Field/Lab Work

Collected Data for Produced Water

Several produced water samples were collected from the field and analyzed in the lab for Br concentration and total dissolved solids (TDS). This is to reuse produced water and generate valuable materials such as $CaBr_2$ for oil and gas well drilling operations. Hydrocarbon production operations use high quantities of Br as part of a drilling fluid formulation and this is currently a significant cost for oil and gas companies.

Table 1 lists the Br concentration data of the collected produced water samples. These concentrations are significantly sufficient for Br extraction and generate valuable material. Also, the Br concentrations in the selected seven fields are higher than Br seawater concentration, which is around 65 ppm and is usually used for a source of Br.

Conventional Method for Br Production

The preparation of $CaBr_2$ drilling fluids — including $CaBr_2$ completion fluids — that are aqueous-based typically involves adding solid $CaBr_2$ salt to the water. Consequently, solid $CaBr_2$ salt is relatively expensive, and the manufacture of $CaBr_2$ salt can include the handling of strong oxidants and toxic gas. Also, the current method of producing $CaBr_2$ salt involves dedicated facilities and operations for oxidation and recovery of Br, which makes it costly[5, 6].

Briefly, Br is generated at an industrial scale using the following methods:

1. Use Cl gas and a strong acid (sulfuric acid (H_2SO_4)) to oxidize Br^- into Br gas.

2. Production of Br gas and its removal by large fans.

3. Production of hydrogen Br in an aqueous solution by dissolving Br gas in the water with sulfur dioxide (SO_2).

4. Oxidation of hydrogen Br with steam and Cl to Br.

Most of these steps require handling of highly hazardous material at a high temperature and in a vapor state. Using such a method at oil production sites is not favorable, which has many hazardous operations already.

In this work, we propose to use Br specific ion exchange resins for the capture of Br^- from water and then generate $CaBr_2$ in solution in water by using $CaBr_2$ salt. Prior articles on ion exchange resin for Br recovery dates back to 1963[7, 8].

Novel Method to Form $CaBr_2$

The novel method in this article can generate $CaBr_2$ in solution in water without requiring the addition of the costly solid $CaBr_2$ salt and generally without handling of strong oxidants or toxic gas. The method includes processing the produced water to recover Br^- from the produced water to give the $CaBr_2$ in solution in water, wherein the produced water is discharged from oil or gas wells. Also, the method includes concentrating the $CaBr_2$ and forming the drilling fluid.

Specifically, the method flows the produced water through a bed of resin, including Br specific ion exchange resin, that are specific to Br for the capture of Br^- and absorbs Br^- from the produced water onto the resin, wherein the produced water includes produced water discharged from a subterranean formation. When the resin is fully loaded (or approaching fully loaded) with Br^-, $CaCl_2$ in water will be used as a regenerant

Table 1 *Br concentration data in produced water.*

Oil/Gas Field	A	B	C	D	E	F	G
TDS (ppm)	97,869	188,034	196,952	86,427	146,238	131,793	124,124
Br (ppm)	435.2	589.0	674.3	680.1	857.5	818.6	749.2

to replace the Br⁻ in the resin with chloride ion (Cl⁻). Therefore, a solution of $CaBr_2$ in the water will be discharged from the ion exchange vessel. The $CaBr_2$ water solution will be further processed to concentrate the $CaBr_2$ to apply the $CaBr_2$ solution as a drilling fluid due to its relatively high specific gravity.

Ion exchange resin is a resin medium or support structure for ion exchange and is typically small beads. The beads are generally spherical, with a diameter of 0.25 millimeters (mm) to 1.0 mm. The ion exchange resin (beads) can be from an organic polymer substrate such as polystyrene, acrylic polymers, or other polymers. The beads are porous to provide a relatively large surface area on and in the beads. The sorption of ions "onto" the ion exchange resin can be sorption "on" surfaces of the ion exchange resin, including "in" the ion exchange resin matrix.

Examples of the resin that can be used for this purpose include but are not limited to Purolite® Br Plus/9218. At the initial state, the resin is loaded with Cl⁻. When the produced water is passed through the bed of ion exchange resins in a column reactor, Br⁻ will replace Cl⁻. Once the binding sites on the resin is fully loaded with Br⁻, a typical regeneration method is to use highly concentrated sodium chloride (NaCl) to replace Br⁻ with Cl⁻ again. This process will generate a NaBr solution, which is not as desirable as a $CaBr_2$ solution for use as a drilling fluid. Therefore, we plan to use a saturated $CaCl_2$ solution as a method of regeneration, instead of NaCl. This way, the $CaBr_2$ solution will be obtained, which is desirable as a drilling fluid. Figure 1 illustrates the overall process, and it is a time-sequence diagram.

The overall mass balance can be expressed as: R–Cl + Br⁻ ↔ R–Br + Cl⁻, where R is the ion exchange resin.

The forward reaction occurs until the saturation of the resin and the reverse reaction indicates the regeneration process.

The overall regeneration can be expressed as: R–Br + $CaCl_2$ ↔ R–Cl + $CaBr_2$.

This method is significantly simpler compared to the conventional method that uses Cl, which also requires a high amount of energy for steam and other chemicals such as SO_2 and H_2SO_4. In addition, this method would not cause exposure of the produced water to the atmosphere, which can cause further issues when the final wastewater needs to be disposed of underground.

Conclusions

Produced water with valuable impurities, such as Br_2, can be wasted by injecting it into deep wells. At the same time, there is an increase in drilling activities and consumption of a significant amount of the costly $CaBr_2$ as part of the drilling operation, which increases the overall cost of drilling. This work will add value from wasted produced water by extracting Br and forming $CaBr_2$, and thereby generate valuable materials from waste, reducing the cost of chemical purchase for high consumable material in the oil and gas industry.

Currently, generating drilling fluid using conventional technology includes using very high risk plants with deadly gases and material handling, which needs to be addressed. Even if this can be done, the produced water will be oxidized from the oxygen in the atmosphere, and it will make it impossible to inject the produced

Fig. 1 *A schematic representation of the new process to form the $CaBr_2$ solution from produced water.*
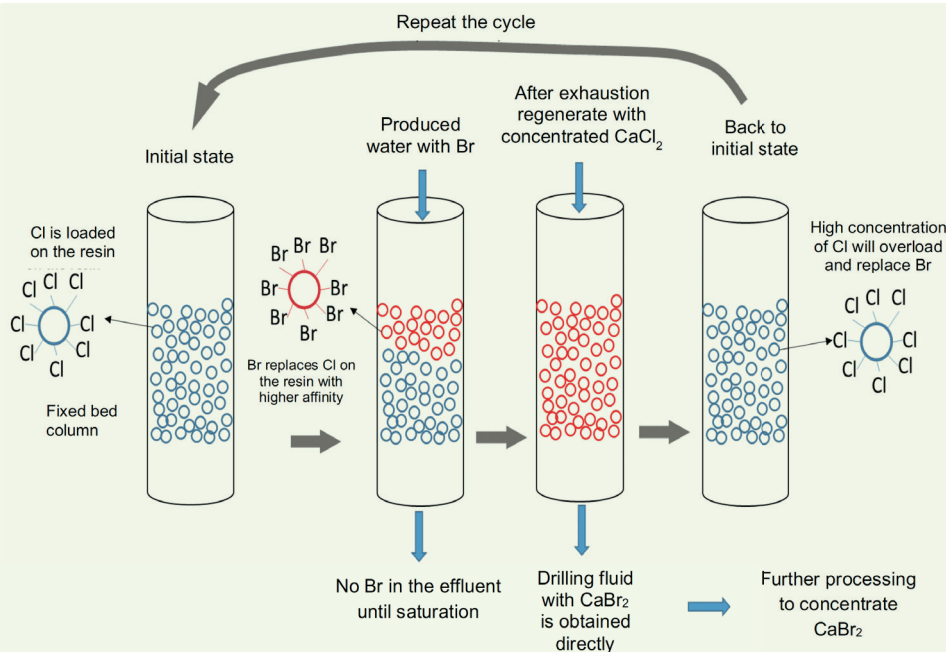
water for pressure maintenance or final disposal in deep wells. This will require a high cost to reduce the oxygen, or a new method of handling and utilizing the produced water. This work explains an ion exchange method that is inherently safe and low in cost, and the produced water will not come in contact with oxygen, so that after Br extraction, the produced water can be utilized and disposed of as planned before adding the new Br extraction process.

A portable unit can be designed with simple feed and collection tanks connected with a resin bed for Br extraction and $CaBr_2$ generation. This new unit could recover Br from the produced water for utilization in oil and gas well drilling, completion, and workover operations.

References

1. Lai, H.Y., de Leon, A., Pangilinan, K. and Advincula, R.: "Superoleophilic and Under Oil Superhydrophobic Organogel Coatings for Oil and Water Separation," *Progress in Organic Coatings*, Vol. 115, February 2018, pp. 122-129.

2. Munirasu, S., Abu Haija, M. and Banat, F.: "Use of Membrane Technology for Oil Field and Refinery Produced Water Treatment — A Review," *Process Safety and Environmental Protection*, Vol. 100, March 2016, pp. 183-202.

3. Schoenbeck, L.C.: "Process for Sorption of Bromide Ion on Anion Exchange Resins," U.S. Patent 3,101,250, August 1963.

4. Hein, R.F.: "Sorption of Bromine on Anion Exchange Resins in the Presence of Excess Chlorine," U.S. Patent 3,174,828, March 1965.

5. Soyluoglu, M., Ersan, M.S., Ateia, M. and Karanfil, T.: "Removal of Bromide from Natural Waters: Bromide Selective vs. Conventional Ion Exchange Resins," *Chemosphere*, Vol. 238, January 2020.

6. Gradishar, F.J. and Hein, R.F.: "Recovery of Bromine from Solution Thereof," U.S. Patent 3,098,716, July 1963.

7. Marinsky, J.A. and Yizhak, M. (eds): *Ion Exchange and Solvent Extraction: A Series of Advances,* Vol. 12, CRC Press, 1995, 472 p.

8. Singare, P.U. and Patange, A.N.: "Study on Halide Ions Selectivity of Industrial Grade Anion Exchange Resin Auchlite A-378," *International Letters of Chemistry, Physics and Astronomy*, Vol. 30, 2014, pp. 44-50.

About the Authors

Dr. Fahd I. Alghunaimi

Ph.D. in Chemical Engineering, King Abdullah University of Science and Technology

Dr. Fahd I. Alghunaimi is currently the Water Treatment Program Lead with the Production Technology Division of Saudi Aramco's Exploration and Petroleum Engineering Center – Advanced Research Center (EXPEC ARC). His area of expertise is crude oil separation and water treatment.

Fahd's recent work in oil removal from produced water was selected by the Institution of Chemical Engineers (IChemE) as a finalist in the Oil and Gas Category of the 2021 Global Energy Show Awards.

He has published more than 25 technical papers, disclosed more than 15 patents, deployed several technologies, received eight international awards, presented several conference papers, and has more than 650 citations.

Fahd received his Ph.D. degree in Chemical Engineering from the King Abdullah University of Science and Technology, Thuwal, Saudi Arabia.

Dr. Young C. Choi

Ph.D. in Environmental Engineering, University of Illinois at Urbana-Champaign

Dr. Young C. Choi is a Research Science Consultant working on the Produced Water Treatment Team at the Oil and Gas Treatment Division in Saudi Aramco's Research & Development Center since 2019.

His current work includes pretreatment and membrane processes for the treatment and reuse of produced water, aimed at reducing the consumption of groundwater.

Young has more than 20 years of experience in the industry and research institutes working on water and wastewater treatment processes as well as desalination and industrial water reuse.

He received his Ph.D. degree in Environmental Engineering from the University of Illinois at Urbana-Champaign, Champaign, IL.

Hind S. Aldossary

B.S. in Chemical Engineering, University College London

Hind S. Aldossary joined Saudi Aramco in 2017 as a Chemical Engineer, and works in the Production Technology Division of Saudi Aramco's Exploration and Petroleum Engineering Center – Advanced Research Center (EXPEC ARC). Currently, Hind is working on several projects in the area of underwater treatment research.

She has submitted several articles for publication, and patents. Her conference presentation on Novel Adsorbent Materials for Oil Removal from Produced Water was selected as the best presentation of the Fifth International Conference on Innovative Engineering Materials in 2021.

Hind received her B.S. degree in Chemical Engineering from University College London, London, U.K.

Reservoir Characterization for Isolated Porosity from Multifrequency Dielectric Measurements

Dr. Guodong Jin, Dr. Shouxiang M. Ma, Ryan Antle and Salah M. Al-Ofi

Abstract /

Due to processes of geological diagenesis, pores in rocks can be isolated from the rest of the connected pore networks. The amount and spatial distribution of isolated pores can have a direct effect on petrophysical properties and performance of the reservoir.

This article introduces a new methodology to quantify the isolated porosity of heterogeneous reservoirs from multifrequency (dispersion) dielectric measurements. Based on numerical simulation studies, digital rock physics techniques are used to generate rock models with different isolated porosities. 3D dielectric dispersion modeling is then performed on the models to obtain the dispersion of the rock's dielectric constant. Dielectric dispersion behaves differently as the pore connectivity changes due to an increase in isolated porosity. The dielectric constant is sensitive to frequency when pores are isolated, while insensitive to the frequency when pores are connected.

Variation of the dielectric constant is strongly related to the number of isolated pores. For rocks having the same total porosity, their dielectric constant increases as the isolated porosity increases. This enhancement of dielectric constant is attributed to the increase in pore network tortuosity, resulting in increased accumulations of electric charges at the interfaces between the solid and pores. Analytical relationships are developed to correlate isolated porosity with the rate of permittivity change and/or the permittivity ratio, derived from the dispersion of dielectric constants.

The validity and applicability of the established method are demonstrated by the agreement of predicted isolated porosity with the true values used in building the rock models. Potentially, this method can be used for enhancing reservoir characterization with modern multifrequency dielectric logs.

Introduction

Characterization of carbonate reservoirs can be very challenging due to the intrinsic heterogeneities that occur at all scales of observations and measurements. Heterogeneity in carbonates can be attributed to pores with different shapes, origin, and sizes, and more importantly the degree of pore connectivity. Due to the processes of geological diagenesis, pores in carbonates can be completely isolated or connected via very narrow pore throats. A pore (or a cluster of pores) is defined as the isolated pore if the size of its pore throats, d_{PT}, connecting to the neighboring pores, is smaller than a critical size of $d_{PT,c}$, i.e., $d_{PT} < d_{PT,c}$. In this study, $d_{PT,c} = 0$, that is, isolated pores are completely disconnected. The number of isolated pores is then the isolated porosity, ϕ_i. Connected porosity, ϕ_c, is the difference between total, ϕ_t, and isolated porosities.

Isolated pores in carbonate rocks can be in the forms of vugular, moldic, and intra-particle porosities. Depending on the number of such pores, petrophysical properties of carbonate reservoirs can vary dramatically, even if they have similar total porosities. For example, the permeability of carbonate rocks with similar total porosities can vary over several orders of magnitude. Isolated porosity is an important reservoir property that needs to be characterized because it contributes little to reservoir fluid flow, but is directly related to total reservoir pore volume[1]. Currently there are no practical methods available to characterize isolated porosity in the laboratory or downhole, without cutting rocks open for petrographical studies. One of the methods is to characterize total and connected porosities separately[2], the isolated porosity is then derived from the difference between the total and connected porosity, Eqn. 1.

$$\emptyset_t = \phi_i + \phi_c$$

<div align="right">1</div>

Imaging techniques such as micro-computed tomography (micro-CT) and focused ion beam scanning electron microscopy can be used to directly characterize connected and isolated pores as well as the interconnectivity of the pore system from the reconstructed pore morphology[3]. The accuracy of these properties are affected by the image resolution[4, 5]. Based on various physical principles, downhole logging tools, including density, neutron, and nuclear magnetic resonance (NMR), can be used to infer formation porosity without differentiating the connected and isolated porosities, though various methods of integrating these porosity logs with acoustic log for formation porosity characterization have been published.

Chang et al. (1997)[6] considered the vugs be isolated if their NMR T_2 relaxation times are larger than 750 ms. Chen et al. (2008)[7] assumed that all pores in carbonate rocks are connected, but they differ in pore connectivity, a variable difficult to quantify from the measurements. Kwak et al. (2019)[8] derived the pore connectivity factor from the volume comparison of NMR invisible D_2O replacement with NMR visible H_2O in the pore systems. Chi et al. (2016)[9] and Cheng and Heidari (2017)[10] estimated the isolated porosity and connected porosity from the difference of NMR T_2 distributions acquired before and after the injection of a nanoparticle contrast agent or manganese-bearing solution into the rock samples.

The amount and spatial distribution of isolated pores have a strong effect on the dielectric responses of a porous medium. When pores are isolated from the network of pore space, they reduce the interconnectivity of the pore system and increase the tortuous paths of both viscous fluid flow and electric current flow[11-13]. The tortuous flow channels will enhance the interfacial polarization due to the accumulations of electric changes at the solid-void space interface, when the medium is under an external electric field.

When a pore throat connecting two large pores is narrow, e.g., < 1 µm, positive electric charges (cations) will accumulate at one end of the narrow throat and be deficit at the other side, resulting in an electrically neural concentration gradient. This concentration gradient imposes an electric dipole moment across the narrow pore throat, and therefore, gives rise to an enhancement of the dielectric permittivity of the medium[14]. Such an enhancement of dielectric permittivity can be used to characterize pore connectivity of a porous medium. Toumelin and Torres-Verdín (2007)[15] and (2009)[16] observed a significant effect of pore connectivity on dielectric dispersion in their 2D pore-scale simulations. Consequently, it is challenging, if not impossible, to quantify the effect of the isolated porosity on the dielectric dispersion from reservoir rocks because samples with known isolated porosity are usually unavailable.

This article details an innovative technique and methodology[17] to quantify isolated porosity of heterogeneous reservoirs from multifrequency dielectric measurements. Digital rock models with a various number of isolated porosities are created using advanced digital rock physics techniques. 3D dielectric dispersion modeling is then performed on the models to obtain the dispersion of dielectric constant and electrical conductivity. From the simulated data, analytical models are derived to determine the isolated porosity from the dielectric measurements. For validation of the established models, new digital rock models are created and the predicted isolated porosity from the established analytical models is compared to the true values used in the rock model generations.

Methodology

Digital Rock Models

It is extremely difficult, if not impossible, to obtain natural rock samples that have a similar total porosity, but with a different amount of isolated porosities. Digital rock physics techniques provide an alternative way to generate models of a various number of isolated porosities while keeping their pore morphology, as well as total porosity, almost the same or similar. The 3D digital rock models used in this dielectric dispersion simulation study are created either based on the random sphere packs or from the micro-CT images.

Figure 1 displays three types of base models used in this study. Model type A is extracted from a random pack of uniform spheres, in which the grain size is 149 µm. Models B and C are micro-CT images from two different types of rock samples. Table 1 lists the properties of three base models and the variants that are created directly from the base models.

The fraction of isolated porosity (f_i) is defined in Eqn. 2 as the ratio of the ϕ_i to the ϕ_t:

$$f_i = \frac{\phi_i}{\phi_t} \qquad \qquad 2$$

When all pores in the sample are well connected, f_i = 0.0. If all pores are disconnected, f_i = 1.0. The base model is used to create its derived models (or variants) that can have a various number of isolated porosities. The connected pore network of the base model was first partitioned into individual pores, and the connectivity of each individual pore is determined. After partition, individual pores are selectively isolated to tune the final connected and isolated porosity fractions. It is critical for the pore network to remain fully connected from one end to the other for the dielectric simulation to work properly.

Five models are created for each type of A and B. They have similar total porosity of approximately 20%, but a different number of connected porosities, Table 1. These models are used to establish relationships between the isolated porosities and the dielectric responses. For comparison and validation, five type C models with different fractions of connected porosities are created.

Fig. 1 *The three types of base models used in the dielectric dispersion simulations: A is created from a random sphere pack of uniform grain size, while types B and C are micro-CT images of two types of rock samples.*
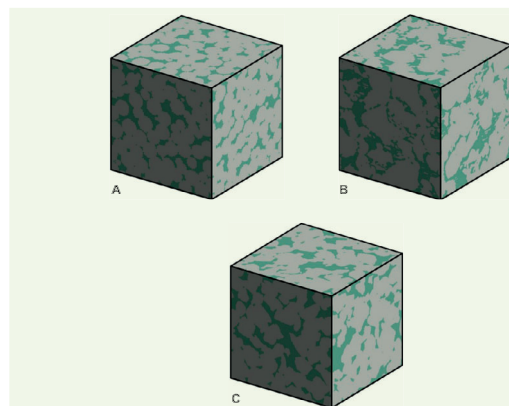
Table 1 *The properties of digital rock models used in this dielectric dispersion simulation study, where fi represents the fraction of porosity that is disconnected.*

Type of Model	Dimensions (# of Voxels)	Voxel Resolution (microns)	Total Porosity of Models (%)				
			$f_i = 0.0$	$f_i = 0.25$	$f_i = 0.5$	$f_i = 0.75$	$f_i = 1.0$
A	101^3	10.0	19.76	19.58	19.38	19.25	19.05
B	202^3	4.50	20.03	19.95	19.84	19.76	19.68
			$f_i = 0.0$	$f_i = 0.1$	$f_i = 0.2$	$f_i = 0.25$	$f_i = 0.30$
C	202^3	5.68	20.11	20.00	19.87	19.75	19.63

Dielectric Dispersion Simulation

Dielectric constant is a measure of the electric polarizability of a material under an external electric field. A material with high permittivity polarizes more in response to an applied electric field than a material with low permittivity, thereby storing more energy in the material. The relative permittivity, $\varepsilon_r(\omega)$, defined as the permittivity of a given material relative to the permittivity of a vacuum, is in general a complex function having the real and imaginary components:

$$\varepsilon_r(\omega) = \varepsilon_r'(\omega) - i\frac{\sigma(\omega)}{\omega\varepsilon_0} \qquad \boxed{3}$$

where i is the imaginary number, $\sigma(\omega)$ is the electrical conductivity (S/m, Siemens per meter), ε_0 is the vacuum permittivity, ω is the angular frequency $\omega = 2\pi F$, where F is the frequency of the external electric field.

The real component $\varepsilon_r'(\omega)$ of relative permittivity, Eqn. 3, generally decreases with the increasing frequency, while the imaginary component usually expressed as dielectric loss increases with the increasing frequency. The dielectric loss is negligible if the conductivity of a solid material is low, less than ~10 m S/m, as it is for many geologic materials[18]. Therefore, the dielectric constant is typically the real component of the dielectric permittivity. For simplicity hereafter, the dielectric permittivity or the dielectric constant represents the real component of the relative dielectric permittivity.

In this study, dielectric dispersion simulations are conducted on the digital models, Table 1, to obtain the dielectric constant, $\varepsilon_r'(\omega)$. The theoretical methodology of dielectric simulations is described in detail in Chen and Heidari (2016)[19], Garcia and Heidari (2018)[20], and Azizoglu and Heidari (2021)[21]. Simulations are performed only along the z-direction. A constant potential difference is applied on the two opposing faces in the z-direction, and no current flow across other faces. The simulation frequency ranges from 0.2 MHz to 10 GHz, covering frequencies used in both logging while drilling electromagnetic, 0.4 to 2 MHz, and wireline dielectric logging tools, 20 MHz to 1 GHz[22, 25]. All rock models are fully brine saturated. The brine salinity is 50 kppm NaCl, simulating seawater, and the temperature is 175 °F. The rock composition is assumed to be pure calcite. The relative permittivity and conductivity of the calcite used are 7 and 1/2,000 S/m, respectively.

Results and Analysis

There are many factors that may affect dielectric constant measurements, including rock mineralogy, pore structure and porosity, saturating water salinity and saturation, and measurement temperature and frequency (dielectric dispersion). The most important factors in determining a rock's dielectric constant are water filled porosity, i.e., porosity and water saturation, and pore structure. In the following discussions, all factors are kept the same except pore structure, more specifically, the amount of isolated porosity, which is the focus of this study.

The dielectric constant generally decreases with increasing frequency, while electric conductivity increases with the increasing frequency. Figure 2 displays the simulated dispersion of the dielectric constant for model A with all pores disconnected or isolated, $f_i = 1.0$. Two parameters are defined from the dispersion curve: the rate of permittivity change, S_{rpc}, and the permittivity ratio, R_p.

The rate of permittivity change is the slope of the best fit line to the dispersion curve at a given frequency interval in the log-log plot (dashed line in Fig. 2):

$$\varepsilon_r' = C \cdot F^{S_{rpc}} \qquad \boxed{4}$$

where ε_r' is the dielectric constant, F is the frequency, and C is the fitting coefficient. Two frequency intervals

Fig. 2 *Simulated dielectric constant dispersion for model A with $f_i = 1.0$, in which all pores are isolated with each other. The dashed line is the curve fitting on the results at the frequency range of 30 MHz to 1 GHz.*
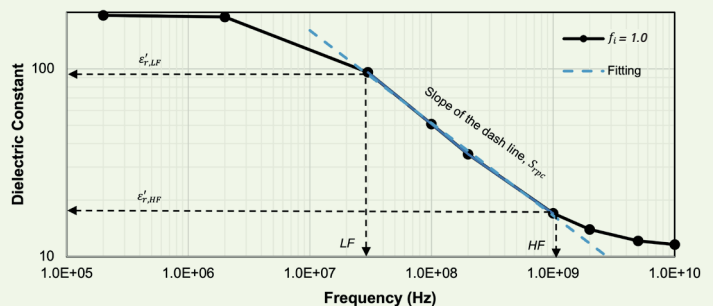
are used to fit the dispersion curve: one is from 30 MHz to 1 GHz, and the other from 100 MHz to 2 GHz; both within the frequency range of modern multifrequency dielectric logging tools[22, 25].

The permittivity ratio is defined as the permittivity difference between two given frequencies divided by the permittivity at the higher frequency:

$$R_p = \frac{\varepsilon'_{r,LF} - \varepsilon'_{r,HF}}{\varepsilon'_{r,HF}} \qquad \boxed{5}$$

where $\varepsilon'_{r,LF}$ is the dielectric constant at the low frequency (30 MHz or 100 MHz in this study) and $\varepsilon'_{r,HF}$ is the dielectric constant at the high frequency, such as 1 GHz.

Figure 3 compares the dielectric constant's dispersion of five type A models, in which their fractions of isolated porosities are 0, 0.25, 0.5, 0.75, and 1.0, respectively. It is observed that the dielectric constant increases as the fraction of isolated porosity increases, indicating the strong effect of the isolated porosity on the dielectric responses. In addition, the dispersion effect is relatively weak when all pores are connected, $f_i = 0.0$, while it becomes strong when all pores are isolated, $f_i = 1.0$, indicating the enhancement of the interfacial polarization (Maxwell-Wagner effect).

As expected, the dielectric constant starts to converge from the frequency of 2 GHz for these five models, because their total porosities are almost the same,
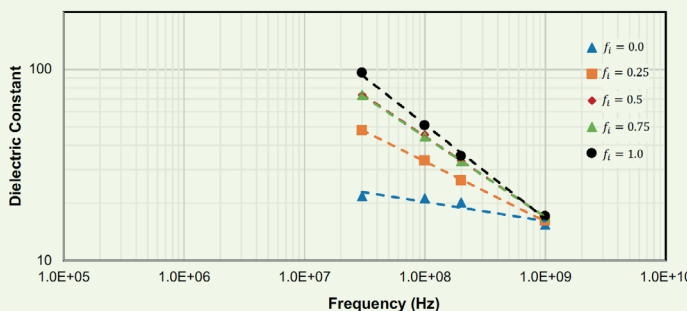
Table 1. In the high frequency range ($F > 1$ GHz), the interfacial polarization is largely attenuated or becomes negligible, while the dipolar polarization of water molecules becomes dominant, which depends on the total porosity. Figure 4 illustrates the best fit lines of the dielectric constant dispersion at the frequency interval of 30 MHz to 1 GHz (dashed rectangle area in Fig. 3).

Figure 5 shows the relationship between the fraction of isolated porosity (f_i) and the rate of the S_{rpc} as well as the R_p for the type A models. A second degree polynomial function can be used to best fit the data:

$$f_i = A_1 (S_{rpc})^2 + A_2 S_{rpc} + A_3 \qquad \boxed{6}$$

and

$$f_i = B_1 (R_p)^2 + B_2 R_p + B_3 \qquad \boxed{7}$$

where A_1, A_2, A_3, B_1, B_2, and B_3 are the fitting coefficients, Table 2.

The high determination coefficient indicates the existence of the correlation between the fraction of isolated porosity and the rate of permittivity change (or the permittivity ratio), i.e., the dielectric dispersion measurements can be used to characterize isolated porosities of porous media.

Similar types of correlations are also observed in type B and C models. Results from type A and B models are used as training data to derive a general analytical model for predicting the fraction of the isolated porosity from the rate of permittivity change or the permittivity ratio, while results from type C models are used as the test and validation data to compare the prediction performance of the analytical models.

Figures 6 and 7 show the comparison of the fraction of isolated porosity between the prediction, Eqns. 6 and 7, and the design (true value). The analytical models are the second degree polynomial functions that best fit the data of models of type A and B at the frequency intervals of 30 MHz to 1 GHz and 100 MHz to 2 GHz, respectively. The fitting coefficients are given in Table 2. The rate of permittivity change and permittivity ratio are the model inputs. The predicted fractions of the isolated porosity match well with the true values, Figs. 6 and 7, especially in the frequency range of 100 MHz to 2 GHz, Fig. 7.

Discussion and Conclusions

This article presented a new methodology for the determination of isolated porosity, or connected porosity, of porous media from multifrequency dielectric measurements. The 3D dielectric dispersion modeling demonstrated the significant effect of the isolated porosity on dielectric constant dispersion. When pores are disconnected, the dielectric constant variation is very sensitive to measurement frequency, while it is insensitive to frequency when the pores are well connected.

Two parameters were introduced to characterize the variation of dielectric constants at specific frequency intervals — the rate of permittivity change and permittivity ratio. Analytical functions were derived

Fig. 3 *The dielectric constant dispersion for the five type A models, with different isolated porosities.*
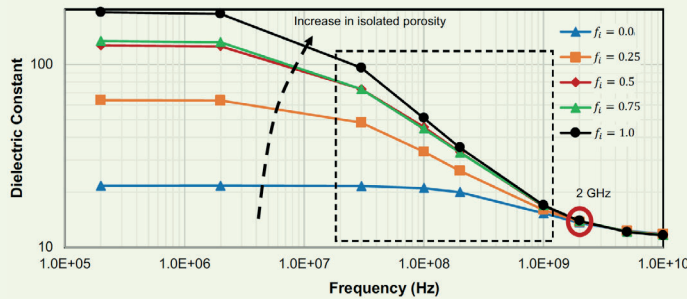

Fig. 4 *A comparison of the rate of permittivity change among the five type A models. The dashed lines are the best fitting to the results at the frequency interval of 30 MHz to 1 GHz.*

Fig. 5 *The relationships of the fraction of isolated porosity vs. the rate of permittivity change (a) and the permittivity ratio (b), for type A models.*
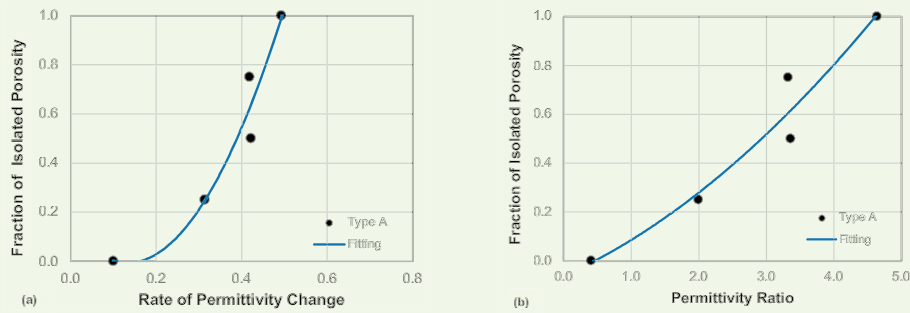

Table 2 *Values of the fitting coefficients and the coefficient of determination, R^2.*

Type of Model	A_1	A_2	A_3	R^2	B_1	B_2	B_3	R^2
Frequency Interval of 30 MHz to 1 GHz								
A	7.65	-2.01	0.13	0.94	0.02	0.13	-0.06	0.94
A + B	5.30	-0.94	0.04	0.81	0.005	0.18	-0.09	0.80
Frequency Interval of 100 MHz to 2 GHz								
A	13.02	-4.41	0.38	0.91	0.17	-0.07	-0.002	0.92
A + B	7.86	-1.85	0.11	0.85	0.08	0.13	-0.08	0.85

Fig. 6 *A comparison of the fraction of isolated porosity between the design (diamond — true value) and the prediction (solid curve — fitting) from: (a) the rate of permittivity change, and (b) the permittivity ratio. Data are derived from the frequency interval of 30 MHz to 1 GHz.*
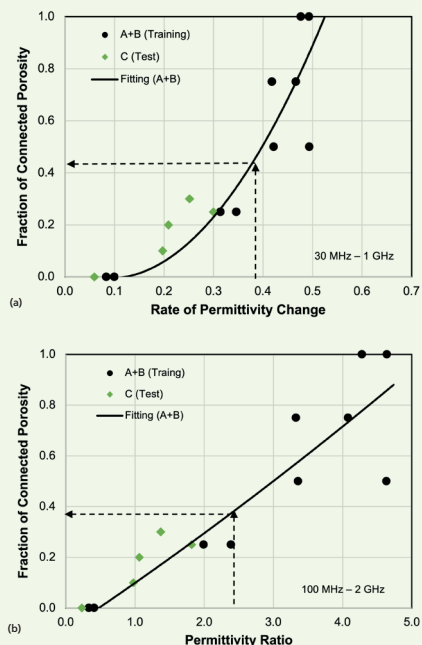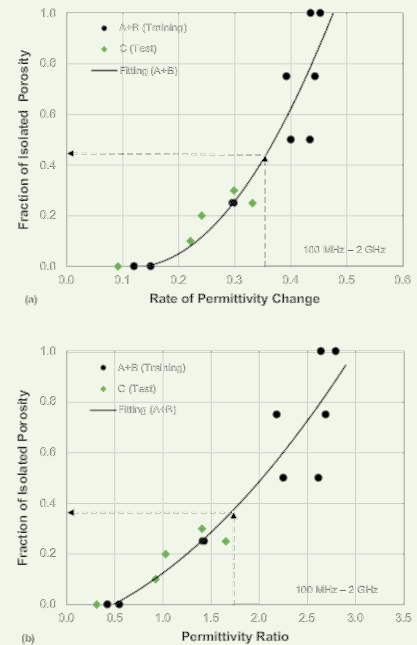
Fig. 7 *A comparison of the fraction of isolated porosity between the design (diamond — true value) and the prediction (solid curve — fitting) from: (a) the rate of permittivity change, and (b) the permittivity ratio. Data are derived from the frequency interval of 100 MHz to 2 GHz.*

from the simulation results to correlate the fraction of isolated porosity with the rate of permittivity change and the permittivity ratio, which enabled the prediction of isolated porosity from the dielectric measurements.

The dielectric constant depends on many factors, including rock and fluid properties and measurement conditions. In this study, all factors except pore structure were kept constant. Generalization of the derived analytical functions for other conditions requires further investigation and validation. The spatial distribution of the isolated pores may also affect the dielectric constant dispersion, and studies are required to test and validate its effect.

Acknowledgments

References

1. Bernabé, Y., Li, M. and Maineult, A.: "Permeability and Pore Connectivity: A New Model Based on Network Simulations," *Journal of Geophysical Research: Solid Earth*, Vol. 115, Issue B10, October 2010.

2. Anovitz, L.M. and Cole, D.R.: "Characterization and Analysis of Porosity and Pore Structures," *Reviews in Mineralogy and Geochemistry*, Vol. 80, Issue 1, January 2015, pp. 61-164.

3. Smodej, J., Lemmens, L., Reuning, L., Hiller, T., et al.: "Nano- to Millimeter Scale Morphology of Connected and Isolated Porosity in the Permo-Triassic Khuff Formation of Oman," *Geosciences*, Vol. 10, Issue 1, 2020.

4. Bazaikin, Y., Gurevich, B., Iglauer, S., Khachkova, T., et al.: "Effect of CT Image Size and Resolution on the Accuracy of Rock Property Estimates," *Journal of Geophysical Research: Solid Earth*, Vol. 122, Issue 5, May 2017, pp. 3635-3647.

5. Guan, K.M., Nazarova, M., Guo, B., Tchelepi, H., et al.: "Effects of Image Resolution on Sandstone Porosity and Permeability as Obtained from X-ray Microscopy," *Transport in Porous Media*, Vol. 127, Issue 1, March 2019, pp. 233-245.

6. Chang, D., Vinegar, H.J., Morriss, C. and Straley, C.: "Effective Porosity, Producible Fluid and Permeability in Carbonates from NMR Logging," paper presented at the SPWLA 35th Annual Logging Symposium, Tulsa, Oklahoma, June 19-22, 1994.

7. Chen, S., Jacobi, D., Kwak, H.T., Altunbay, M., et al.: "Pore Connectivity-Based Permeability Model for Complex Carbonate Formations," paper presented at the 49th Annual Logging Symposium, Austin, Texas, May 25-28, 2008.

8. Kwak, H.T., Gao, J. and Harbi, A.: "Improving the Permeability Derivation from NMR Data for Reservoir Rocks with Complicated Pore Connectivity," SPE paper 195113, presented at the SPE Middle East Oil and Gas Show and Conference, Manama, Kingdom of Bahrain, March 18-21, 2019.

9. Chi, L., Cheng, K. and Heidari, Z.: "Improved Assessment of Interconnected Porosity in Multiple Porosity Rocks by Use of Nanoparticle Contrast Agents and Nuclear Magnetic Resonance Relaxation Measurements," *SPE Reservoir Evaluation & Engineering*, Vol. 19, Issue 1, January 2016, pp. 95-107.

10. Cheng, K. and Heidari, Z.: "Pore-Network Connectivity and Permeability Assessment by Use of Nuclear Magnetic Resonance Log-Inject-Log Method," *SPE Reservoir Evaluation & Engineering*, Vol. 20, Issue 4, November 2017, pp. 831-838.

11. Amyx, J.W., Bass, D.M. and Whiting, R.L.: *Petroleum Reservoir Engineering: Physical Properties*, McGraw-Hill Book Company Inc., 1960, 610 p.

12. Colombier, M., Wadsworth, F.B., Gurioli, L., Scheu, B., et al.: "The Evolution of Pore Connectivity in Volcanic Rocks," *Earth and Planetary Science Letters*, Vol. 462, March 2017, pp. 99-109.

13. Cunha, A.R., Fernandes, C.P., Emeric dos Santos, L.O., Kronbauer, D.P., et al.: "A Phenomenological Connectivity Measure for the Pore Space of Rocks," *arXiv:2012.00835v1*, 2020.

14. Niu, Q., Zhang, C. and Prasad, M.: "A Framework for Pore-Scale Simulation of Effective Electrical Conductivity and Permittivity of Porous Media in the Frequency Range from 1 MHz to 1 GHz," *Journal of Geophysical Research: Solid Earth*, Vol. 125, Issue 10, October 2020.

15. Toumelin, E. and Torres-Verdin, C.: "2D Pore-Scale Simulation of Wide-Band Electromagnetic Dispersion of Saturated Rocks," *Geophysics*, Vol. 72, Issue 5, May 2007, pp. F97-F110.

16. Toumelin, E. and Torres-Verdin, C.: "Pore-Scale Simulation of KHz-GHz Electromagnetic Dispersion of Rocks: Effects of Rock Morphology, Pore Connectivity, and Electrical Double Layers," paper presented at the SPWLA 50th Annual Logging Symposium, The Woodlands, Texas, June 21-24, 2009.

17. Ma, S., Jin, G., Antle, R., Le, F., et al.: "System and Method for Estimating Porosity of Porous Formations Using Permittivity Measurements," U.S. Patent Application 63/250,435, September 30, 2021.

18. Martinez, A. and Byrnes, A.P.: "Modeling Dielectric-Constant Values of Geologic Materials: An Aid to Ground-Penetrating Radar Data Collection and Interpretation," *Current Research in Earth Sciences*, Vol. 247, Issue 1, January 2002, pp. 1-16.

19. Chen, H. and Heidari, Z.: "Pore-Scale Joint Evaluation of Dielectric Permittivity and Electrical Resistivity for Assessment of Hydrocarbon Saturation Using Numerical Simulations," *SPE Journal*, Vol. 21, Issue 6, December 2016, pp. 1930-1942.

20. Garcia, A.P. and Heidari, Z.: "Quantifying the Influence of Rock Fabric, Composition, and Electrical Double Layer on the Broadband Dielectric Dispersion of Organic-Rich Mud Rocks," URTEC paper 2867679, presented at the SPE/AAPG/SEG Unconventional Resources Technology Conference, Houston, Texas, July 23-25, 2018.

21. Azizoglu, Z. and Heidari, Z.: "Interpretation of Multifrequency Dielectric Permittivity Measurements for Assessment of Water Saturation in Carbonate Formations with Complex Pore Structure," paper presented at the SPWLA 62nd Annual Logging Symposium, Virtual, May 17-20, 2021.

22. Hizem, M., Budan, H., Deville, B., Faivre, O., et al.: "Dielectric Dispersion: A New Wireline Petrophysical Measurement," SPE paper 116150, presented at the SPE Annual Technical Conference and Exhibition, Denver, Colorado, September 21-24, 2008.

23. Forgang, S., Corley, B., Garcia, A., Hanif, A., et al.: "A New Multifrequency Array-Dielectric Logging Service: Tool Physics, Field Testing, and Case Studies in the Permian Basin Wolfcamp Shale," paper presented at the SPWLA 60th Annual Logging Symposium, The Woodlands, Texas, June 15-19, 2019.

About the Authors

Dr. Guodong Jin

Ph.D. in Reservoir Engineering and Petrophysics, University of California at Berkeley

Dr. Guodong Jin is a Senior Engineer at the Baker Hughes Energy Innovation Center in Oklahoma. He has been actively involved in underground gas storage, reservoir characterization and evaluation, geomechanics, and data analytics applications in well logging.

Prior to his current position, Guodong was a Petrophysics Advisor at the Dhahran Technology Center in Saudi Arabia, and a Research Scientist

at the Houston Technology Center for Baker Hughes.

He received his B.Eng. degree in Petroleum Engineering from the China University of Petroleum, Beijing, China. Guodong then received his M.S. degree in Geomechanics, and his Ph.D. degree in Reservoir Engineering and Petrophysics, both from the University of California at Berkeley, Berkeley, CA.

Dr. Shouxiang M. Ma

Ph.D. in Petroleum Engineering, New Mexico Institute of Mining and Technology

Dr. Shouxiang M. "Mark" Ma is a Senior Petroleum Engineer Consultant overseeing research and development, subject matter technical support, and professional development in the Advanced Petrophysical Modeling Group of Saudi Aramco's Reservoir Description and Simulation Department. Prior to this, he was Supervisor of the Petrophysical Support & Study Unit, advisor at the Upstream Professional Development Center, and Lead Petrophysicist for logging operations.

Before joining Saudi Aramco in 2000, Mark worked at the Exxon Production Research Company, Wyoming Western Research Institute, New Mexico Petroleum Recovery Research Center, and China Yangtze University.

He served as a chairperson of the 2013 Society of Petroleum Engineers (SPE) Formation Evaluation Award Committee, the 2018 SPE Annual Technical Conference and Exhibition

Formation Evaluation Committee, and on the 2019 International Petroleum Technology Conference Education Week Conference.

Mark was awarded the 2019 SPE MENA Formation Evaluation Award.

From 2015 to 2020, he served on the *JPT* Editorial Board where he was responsible for formation evaluation content. Mark is a Society of Petrophysicists and Well Log Analysts (SPWLA) Saudi Arabia Chapter vice president for technical events, and from 2018 to 2020, he was a SPWLA Director representing the Middle East and Africa region. Mark is also an Associate Editor for the *Journal of Petrophysics*, and Vice President of the SPWLA Saudi Arabia Chapter.

He received his B.S. degree from the China University of Petroleum, Shandong, China, and his M.S. and Ph.D. degrees from the New Mexico Institute of Mining and Technology, Socorro, NM, all in Petroleum Engineering.

Ryan Antle

M.S. in Geology, University of South Carolina

Ryan Antle joined Baker Hughes Energy Innovation Center in 2014. His research interest is related to computed tomography for pore-scale imaging and analysis.

Ryan is a member of the Society of Petroleum Engineers (SPE) and the Society of Petrophysi-

cists and Well Log Analysts (SPWLA). He has published several papers on core analysis.

In 2011, Ryan received his B.S. degree in Marine Science, and in 2013, his M.S. degree in Geology, both from the University of South Carolina, Columbia, SC.

Salah M. Al-Ofi

M.S. in Electromagnetics, King Fahd University of Petroleum and Minerals

Salah M. Al-Ofi joined Baker Hughes' Dhahran Technology Center 4.0 as a Physics Team Lead in 2018. Prior to this, he had worked as a Research Engineer with Schlumberger for more than 8 years.

Salah's current focus is on developing new applications for formation evaluation through laboratory applied research on emerging logging techniques, mainly on multifrequency dielectric and resistivity.

He is member of the Institute of Electrical and

Electronics Engineers (IEEE), the Society of Petroleum Engineers (SPE) and the Society of Petrophysicists and Well Log Analysts (SPWLA). Salah is the author of several papers and patents on formation evaluation and core analysis.

In 2010, he received his B.S. degree in Electrical Engineering, and in 2015, Salah received his M.S. degree in Electromagnetics, both from King Fahd University of Petroleum and Minerals (KFUPM), Dhahran, Saudi Arabia.

Have an article you would like to publish?
Here are our guidelines.

These guidelines are designed to simplify and help standardize submissions. They need not be followed rigorously. If you have any questions, please call us.

Length

Average of 2,500-4,000 words, plus illustrations/photos and captions. Maximum length should be 5,000 words. Articles in excess will be shortened.

What to send

Send text in Microsoft Word format via email. Illustrations/photos should be clear and sharp. Editable files are requested for graphs, i.e., editable in Excel.

Procedure

Notification of acceptance is usually within three weeks after the submission deadline. The article will be edited for style and clarity and returned to the author for review. All articles are subject to the company's normal review. No paper can be published without a signature at the manager level or above.

Format

No single article need include all of the following parts. The type of article and subject covered will determine which parts to include.

Working Title
Lorem Ipsum here.

Abstract
Usually 150-300 words to summarize the main points.

Introduction
Different from the abstract in that it sets the stage for the content of the article, rather than telling the reader what it is about.

Main body
May incorporate subtitles, artwork, photos, etc.

Conclusion/Summary
Assessment of results or restatement of points in introduction.

Endnotes/References/Bibliography
Use only when essential. Use author/date citation method in the main body. Numbered footnotes or endnotes will be converted. Include complete publication information. Standard is *The Associated Press Stylebook*, 52nd ed. and *Wesbter's New World College Dictionary*, 5th ed.

Acknowledgments
Use to thank those who helped make the article possible.

Illustration/Tables/Photos and explanatory text

If the files are large, these can be submitted separately, due to email size limits. Initial submission may include copies of originals; however, publication will require the originals. When possible, submit original images. Color is preferable.

File Format

Illustration files with .EPS extensions work best. Other acceptable extensions are .TIFF/.JPEG/.PICT.

Permission(s) to reprint, if appropriate

Previously published articles are acceptable but can be published only with written permission from the copyright holder.

Author(s)/Contibutor(s)

Please include a brief biographical statement.

Submission/Acceptance Procedures

Papers are submitted on a competitive basis and are evaluated by an editorial review board comprised of various department managers and subject matter experts. Following initial selection, authors whose papers have been accepted for publication will be notified by email.

Papers submitted for a particular issue but not accepted for that issue may be carried forward as submissions for subsequent issues, unless the author specifically requests in writing that there be no further consideration.

Submit articles to:

Editor
The Saudi Aramco Journal of Technology
C-10B, Room AN-1080
North Admin Building #175
Dhahran 31311, Saudi Arabia
Tel: +966-013-876-0498
Email: *william.bradshaw.1@aramco.com.sa*

Submission deadlines

Issue	Paper submission deadline	Release date
Winter 2022	August 4, 2022	December 30, 2022
Spring 2023	November 7, 2022	March 31, 2023
Summer 2023	February 1, 2023	June 30, 2023
Fall 2022	May 9, 2023	September 30, 2023

There is more.

GeoDIN — Geoscience-Based Deep Interaction Networks for Predicting Flow Dynamics in Reservoir Simulation Models

Dr. Marko Maucec and Ridwan S. Jalali

Abstract /   Network graphs represent a general language for describing complex systems and a framework for knowledge discovery. Graph learning is a new concept with applications emerging in biomedicine, pharmacology, smart mobility, and physical reasoning. When applied to petroleum systems, such as reservoir models, graphs provide unique differentiators for the abstraction of reservoir connectivity to facilitate "reservoir centric" machine learning applications.

In this article, we demonstrate, for the first time, the application of Geoscience-based Deep Interaction Networks (GeoDIN) to learn complex physics relationships from 3D reservoir models for fast and accurate prediction of subsurface spatiotemporal flow dynamics. We build the network graph with embedded subsurface and physics representations and train the machine learning model to "act like the reservoir simulator."

Imaging Subsurface Targets Using Cross-Borehole GPR: A Field and Modeling Approach

Jesus M. Felix Servin and Hussain A. Shateeb

Abstract /   Cross-borehole ground penetrating radar (XBGPR) is a geophysical technique that allows for high-resolution characterization of the interwell region. This method relies on the propagation of electromagnetic (EM) waves — typically in the MHz region — that are analyzed to generate subsurface maps of EM properties, which can be interpreted into fluid saturation maps. We present the results of a large-scale field experiment complemented by 3D numerical simulations evaluating the feasibility of locating small fluid targets of different compositions in the subsurface.

An array of 33 target wells and six observation wells completed with nonconductive, nonmagnetic pipe were used to conduct the experiments. The target wells were filled with different fluids, including dielectrically and magnetically tagged fluids, such as polymer solutions and polymer solutions with magnetite. Time-domain EM measurements were acquired using a 100 MHz XBGPR system in a semi-reciprocal tomographic setup. The acquired waveforms were filtered and processed using bh_tomo, an open source platform for XBGPR analysis. Traveltime and amplitude inversions were performed to obtain velocity and attenuation maps of the surveyed area. In parallel, 3D numerical simulations were conducted using a commercially available finite element modeling package. The simulation results were compared and validated with the experimental results.

أرامكو السعودية
saudi aramco

Aramco
Journal
of **Technology**

Liked this issue?
Sign up. It's free.

To begin receiving the *Aramco Journal of Technology*
please complete this form, scan and send by email to
william.bradshaw.1@aramco.com.

Got questions?

Just give us a call at +966-013-876-0498
and we'll be happy to help!

Scan the QR code to go straight
to your email and attach the form!

Subscription Form

Name

Title

Organization

Address

City

State/Province

Postal code

Country

Email address

Phone number

Number of copies

GeoDIN — Geoscience-Based Deep Interaction Networks for Predicting Flow Dynamics in Reservoir Simulation Models

Dr. Marko Maucec and Ridwan S. Jalali

Abstract /

Network graphs represent a general language for describing complex systems and a framework for knowledge discovery. Graph learning is a new concept with applications emerging in biomedicine, pharmacology, smart mobility, and physical reasoning. When applied to petroleum systems, such as reservoir models, graphs provide unique differentiators for the abstraction of reservoir connectivity to facilitate "reservoir centric" machine learning applications.

In this article, we demonstrate, for the first time, the application of Geoscience-based Deep Interaction Networks (GeoDIN) to learn complex physics relationships from 3D reservoir models for fast and accurate prediction of subsurface spatiotemporal flow dynamics. We build the network graph with embedded subsurface and physics representations and train the machine learning model to "act like the reservoir simulator."

We use a simulation benchmark model for two-phase incompressible flow, with an approximate 1.1 million grid size, one central injector and four corner producers. Static 3D grid properties include porosity and permeability. We use a full physics simulation output to construct the interaction network graph, where graph node objects (nodes) represent reservoir grid cells. We embed the feature vector combining pore, oil, and water volumes, pressure, and relative permeability. The graph objects representing wells are connected with well completion factors. The producing wells have embedded oil and water production rates, while the objects representing injecting wells have embedded water injection rates. We represent graph relations (edges) with bidirectional transmissibility of the source cell. To preprocess the data for machine learning, we scale the graph object attributes using "min-max" normalization and we normalize the graph relation attributes using Box-Cox transformation.

We train the GeoDIN framework to predict oil and water saturation dynamics in space and time. When benchmarked with full physics simulation, the interaction networks ran on two V100 GPUs and substantially accelerated the prediction phase compared to a physics-based simulator running on 70 Intel Xeon E5 CPU cores. On average, the error in GeoDIN predicted spatiotemporal distribution of oil saturation remains within 5% of full physics simulation for 90% of the model grid cells, while the error in water saturation remains within 2.5% of full physics simulation.

The spatiotemporal propagation of pressure is more sensitive to local embeddings of interaction networks, which communicate on node-to-node information transfer. This results in a larger prediction error of the GeoDIN model when benchmarked to full physics simulation. On average, the error distribution suggests that a great majority (90% to 95%) of grid cells fall within 10% to 30% error bound, relative to the full physics simulation.

The presented GeoDIN approach to network learning carries a game changing potential for prediction of subsurface flow dynamics. As the way forward, we will investigate implementation of graph neural networks (NN) with automated feature learning, generalization, and scale up.

Introduction

Accurate numerical simulation of flow dynamics in subsurface reservoir systems lies at the heart of petroleum engineering and science. Reservoir simulation has become a standard tool for hydrocarbon reserve assessment, field development planning, and optimization and for strategic decision making purposes. The state-of-the-art simulation models of mature, real-life hydrocarbon assets can exceed hundreds of millions in grid-size, integrate thousands of wells and span decades of production history under various operational scenarios. Despite the wide expansion and deployment of massively parallelized high performance computing (HPC) clusters, novel GPU-based architectures and cloud computing, advanced reservoir simulation still poses extreme computational challenges to dynamic model calibration and optimization, long-term forecasting, and rigorous uncertainty and risk analysis.

Driven by advances in machine learning and deep learning, alternative approaches to predictive modeling and

simulations of complex petroleum systems' behavior have been proposed in the form of physics informed, referred to as scientific machine learning, or SciML. By incorporating physical knowledge, constraints and conservation laws into machine learning and deep learning, one can potentially reduce the data requirements and dependency, significantly improve the predictive accuracy, statistical efficiency, interpretability and generalizability of the model, eliminate physically implausible predictions from the search space and reduce the computational cost of models[1].

Recently, the amalgamation of data and physics governed machine learning and deep learning modeling in the energy and oil and gas domains has gained significant momentum in research and development. Zhao and Sarma (2018)[2] introduce the data physics technology that combines the reservoir physics with machine learning and benchmark it against the conventional simulator for thermal recovery problems while dramatically reducing the computational run time. Klie et al. (2020)[3] introduce the application of integrated transfer learning from previously learned full physics development scenarios to accelerate and optimize the execution of the forthcoming field development plan.

Zhang et al. (2019)[4] used the deep learning concepts combined with model reduction schemes to predict multiphase flow dynamics, while Jin et al. (2019)[5] and Al-Sulaimani and Wheeler (2021)[6] deploy physics-based reduced order modeling with Embed-to-Control framework[7] for multiphase surface flow simulation. Fraces et al. (2020)[8] used physics informed neural networks (PINN) and apply transfer learning and generative methods to solve an inference problem for two-phase immiscible transport, while Wang et al. (2020)[9], (2021)[10] introduced the concept of the theory guided NNs to incorporate governing equations, boundary conditions and practical experience into multiphase flow prediction.

In another approach, Thavarajah et al. (2021)[11] trained a deep learning-based proxy model by full physics simulation output using the encoder-decoder NNs (convolutional long short-term memory (LSTM)) to simulate fluid dynamics. While Cai et al. (2021)[12] and references therein provide a review of PINNs for solving inverse problems in fluid mechanics, Fuks and Tchelepi (2020)[13] demonstrated that physics informed machine learning approaches fail to approximate the fluid flow dynamics governed by nonlinear partial differential equations (PDEs) in the presence of sharp variations of saturation and propose the solution by adding a small amount of diffusion to the conservation equation.

In our article, we approach the training of the machine learning and deep learning model with subsurface physics and solve the forward predictive problem by encoding the reservoir simulation model as a network graph. Network graphs represent a general language for describing complex systems and a framework for knowledge discovery. Representation learning on graphs is a new concept with applications in biomedicine[14], pharmacology and drug discovery[15], smart mobility[16] and physical reasoning and inference[17]. Recently, the applications of network graph

modeling and learning were introduced for subsurface modeling and optimization[18] using a hybrid artificial intelligence framework, and for learning to simulate complex physical[19] and chemical processes[20].

When applied to reservoir models, graphs provide unique functionality for the abstraction of reservoir connectivity and enable generalization from well centric to reservoir centric machine learning and deep learning applications. We leverage the concept of an interaction network framework[21] and build the network graph with embedded subsurface and physics representations, and train the deep learning model to act like the reservoir simulator.

Models and Methods

Reservoir Simulation Model

We use the SPE10[23] as a reference reservoir simulation model. The geological model represents a part of a Brent sequence described on a regular Cartesian grid with $60 \times 220 \times 85$ (1,122,000) cells. The model consists of two formations: a shallow marine Tarbert formation in the top 35 layers, where the permeability is relatively smooth, and a fluvial Upper-Ness permeability in the bottom 50 layers. Both formations are characterized by large permeability variations, with eight to 12 orders of magnitude, but are qualitatively different, Fig. 1. The porosity field is strongly correlated to the permeability, and about 2.5% of the blocks have zero porosity assigned as inactive.

The reservoir is produced using a water drive from a vertical well in the center of the reservoir with a constant injection rate of 5,000 stock tank barrels per day and produced from four vertical wells at the corners, each at a bottom-hole pressure of 4,000 psi. We simulated 1,827 days of production assuming incompressible flow, running on 70 Intel Xeon E5 CPU cores of a highly parallelized HPC cluster.

Interaction Networks

The concept of modeling an interaction network was introduced[21] to reason how objects in complex dynamic systems interact, to infer the abstract system properties and relations, and to enable dynamical predictions. The

---

Fig. 1 *The SPE10 reservoir simulation model: 3D model renderings of X-permeability (left) and Z-permeability (right) with a vertical central injector and the four corner producers, completed top to bottom.*
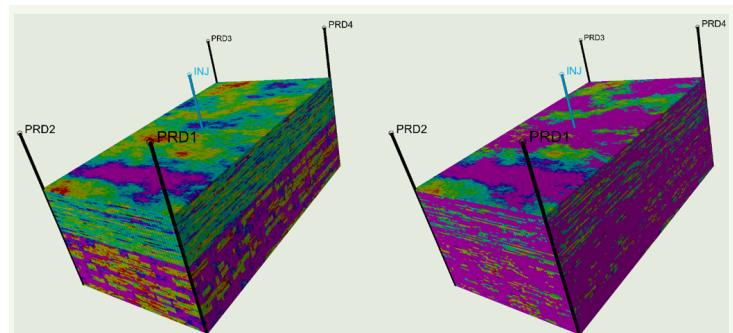
interaction network model represents the first, general purpose, learnable physics engine and was evaluated with experiments in several challenging physical domains: n-body problems, rigid-body collision, and nonrigid dynamics.

In the simplified example to predict the dynamics of a single object, one may use an object centric function, f_O, which takes the objects' state, o_t, as the input at time, t, and outputs the new states of the object, o_{t+1}, at future time, $t+1$. Moreover, if the two or more objects are governed by the same dynamics, f_O could be applied independently to predict the future states of such objects.

Consequently, if several objects interact with each other, the f_O is insufficient because it does not capture the inter-object relationships. For example, when the first object, o_1, defined as the sender, influences the second object, o_2, defined as the receiver via directed interaction, the interaction network model introduces a relation centric function, f_R, to predict the effect of this interaction, e_{t+1}, on the receiving object o_2. The f_R takes as input the objects o_1 and o_2, as well the properties of their relationship, r:

$$e_{t+1} = f_R(o_{1,t}, o_{2,t}, r) \hspace{2cm} \text{1}$$

The f_O is modified so it can input both, the effect of interaction e_{t+1} caused by r and the current state of the receiving object, $o_{2,t}$, to predict the future (dynamic) state of the receiving object, $o_{2,t+1}$:

$$o_{2,t+1} = f_O(o_{2,t}, e_{t+1}) \hspace{2cm} \text{2}$$

For larger and more complex systems, Battaglia et al. (2016)[21] generalizes Eqn. 2 by introducing the model input in the form of a graph, $G = \langle O, R \rangle$ [21]. They assume an attributed, directed multigraph as the relations have attributes and there can be multiple distinct relations between two objects. For a system with N_O objects and N_R relations, Battaglia et al. (2016)[21] defines the inputs to the interaction network as $O = \{o_j\}_{j=1\ldots N_O}$, $R = \{\langle i, j, r_k \rangle_k\}_{k=1\ldots N_R}$ where $i \neq j, 1 \leq i, j \leq N_O$ and $X = \{x_j\}_{j=1\ldots N_O}$. The O represents the states of each object while the triplet $\langle i, j, r_k \rangle_k$ represents the k-th relation in the system, from sender o_i, to receiver o_j, with relation attribute, r_k. The X represents the external effects, such as active control inputs or constraints that manipulate objects and can be applied to each object separately. The basic interaction network is defined as:

$$IN(G) = \emptyset_O(a(G, X, \emptyset_R(m(G)))) \hspace{1cm} \text{3}$$

where

$$m(G) = B = \{b_k\}_{k=1\ldots N_R} \hspace{1cm} a(G, X, E) = C = \{c_j\}_{j=1\ldots N_O}$$

$$f_R(b_k) = e_k \hspace{2cm} f_O(c_j) = p_j$$

$$\emptyset_R(B) = E = \{e_k\}_{k=1\ldots N_R} \hspace{1cm} \emptyset_O(C) = P = \{p_j\}_{j=1\ldots N_O} \hspace{0.3cm} \text{4}$$

The marshalling function m, rearranges the objects and relations into pair-wise interaction terms and compute their effects, e_k, via relational model, Φ_R, using the relation centric function, $f_R(\cdot)$. The aggregation function a, aggregates the e_k and combines them with o_j and x_j, to generate the input for an object model, Φ_O, using the object-centric function, $f_O(\cdot)$. The $f_O(\cdot)$ predicts how the object's interactions, dynamics, and external effects influence the behavior of objects. This basic interaction network can predict the evolution of the states in a dynamic system, and for physical simulation, P may equal to the future (predicted) states of the objects, O_{t+1}. For further details on mathematical frameworks and notations related to interaction network modeling, refer to Battaglia et al. (2016)[21].

Geoscience-Based Deep Interaction Networks (GeoDIN)

The concept of an interaction network is … agnostic to the choice of functions and algorithms …, for a learnable implementation capable of reasoning about complex systems with nonlinear relations and dynamics[21]. In our work, we formalize and expand the implementation to the domain of petroleum systems and develop Geoscience-based Deep Interaction Networks (GeoDIN) to predict complex fluid-flow dynamics in reservoir simulation models. In Fig. 2, we partially reproduce Fig. 1 from Battaglia et al. (2016)[21] to schematize the architecture of the GeoDIN with an annotated forward calculation.

Data Abstraction: We parse the output of the simulation run from an in-house, full physics, massively parallelized reservoir simulator[24]. The data format of the simulation output is a customized format for reading and writing the result files from the Eclipse reservoir simulator[25]. We build a network graph with object/node and relation/edge attributes and types, Table 1. To preprocess the data for machine learning, we scale the graph object attributes using "min-max" normalization and we normalize the graph relation attributes, i.e., cell transmissibility ($TRANS$), using Box-Cox transformation. Relation/edge types were one-hot encoded into a vector of size 3.

In Fig. 3, we show examples of network graph representations for the reservoir simulation grid, Nx = 3, Ny = 3, Nz = 1 (left), and Nx = 10, Ny = 10, Nz = 3 (right), where graph edges are color-coded with source $TRANS$ and graph nodes are color-coded with cell oil saturation, $SOIL$.

The dimensionality of the relations vector (the number of graph edges, N_R) is a dynamic, simulation case dependent variable: as indicated in Fig. 3, the $3 \times 3 \times 1$ simulation grid (with only lateral grid communication via x- and y-transmissibility) results in a graph representation with 24 relations/edges. The $10 \times 10 \times 3$ simulation grid on the other hand, renders 1,480 relations/edges that account for both, the lateral and vertical (multilayer) grid communication, embedded with full, 3D transmissibility tensor. The network graph representations of reservoir simulation grids become significantly more complex when additional abstractions of grid connectivity are integrated, such as sealing faults or fracture networks or models with unstructured grids and the presence of nonneighbor connections.

Implementation: We define an array of objects (O) as the $N_O \times D_s$ array. The columns correspond to the number
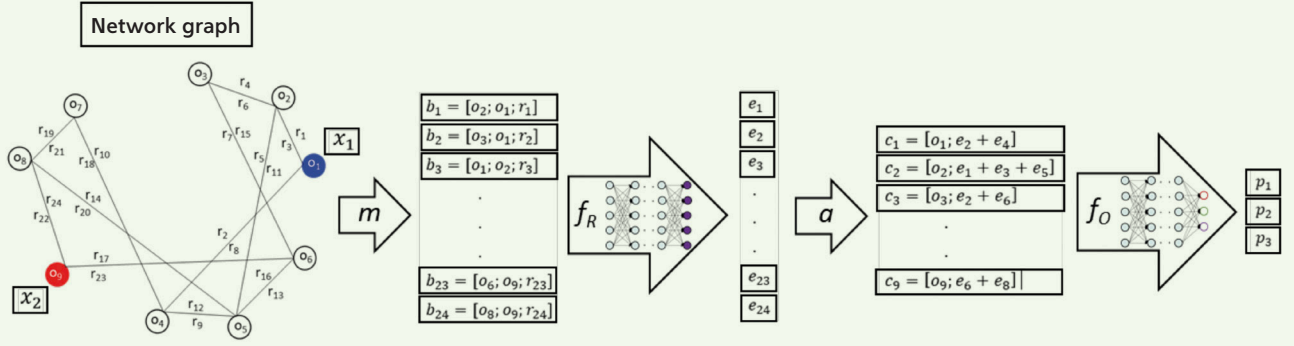
Table 1 *Features and encodings of a GeoDIN graph.*

|				
Object/Node (object state variables: D_S)	Attribute	Oil saturation	$\boldsymbol{D_{SDyn}}$	SOIL
		Water saturation		SWAT
		Pressure		PRESS
		Pore volume		PORVOL
		Porosity		POROS
		Permeability tensor	$\boldsymbol{D_{SStat}}$	PERM
		Connate water saturation (0.2; constant)		SWC
		Oil-water relative permeability endpoints		KRW, KROW
		Oil Production Rate (Producer)		WOPR
		Water Production Rate (Producer)	$\boldsymbol{X}$	WWPR
		Water Injection Rate (Injector)		WWIR
Relation/Edge (relation variables: D_R)	Attribute	Transmissibility tensor of source cell		TRANS
		Well completion factor		CF
	Type	Simulation Grid Cells		DIFFUSE
		Producing Wells		PRODUCE
		Injecting Wells		INJECT

of graph objects, $N_O = N_{gc} + N_{pw} + N_{iw}$, where N_{gc}, N_{pw}, and N_{iw} represent the number of simulation grid cells, the number of producing, and the number of injecting wells, respectively. The rows correspond to the objects' D_S length state vector and $D_S = D_{SDyn} + D_{SStat} + X$. In the GeoDIN model, the elements of the state vector are categorized as:

- Dynamic state variables, D_{SDyn}, that combine cell attributes such as *SOIL*, water saturation, *SWAT*, and

reservoir pressure, *PRESS*, subject to a spatiotemporal update in each time step of the GeoDIN prediction.
- Static state variables, D_{SStat}, that combine cell attributes like porosity, *POROS*, and permeability, *PERM*, tensors as well as pore volume, *PORVOL*, which was used to constrain the NN while training with simulation data and limit error accumulation in predicted barrels of fluid. The object's model was augmented with relative permeability to capture

Fig. 3 *The network graph representations for the reservoir simulation grid (3 × 3 × 1; left) and (10 × 10 × 3; right).*
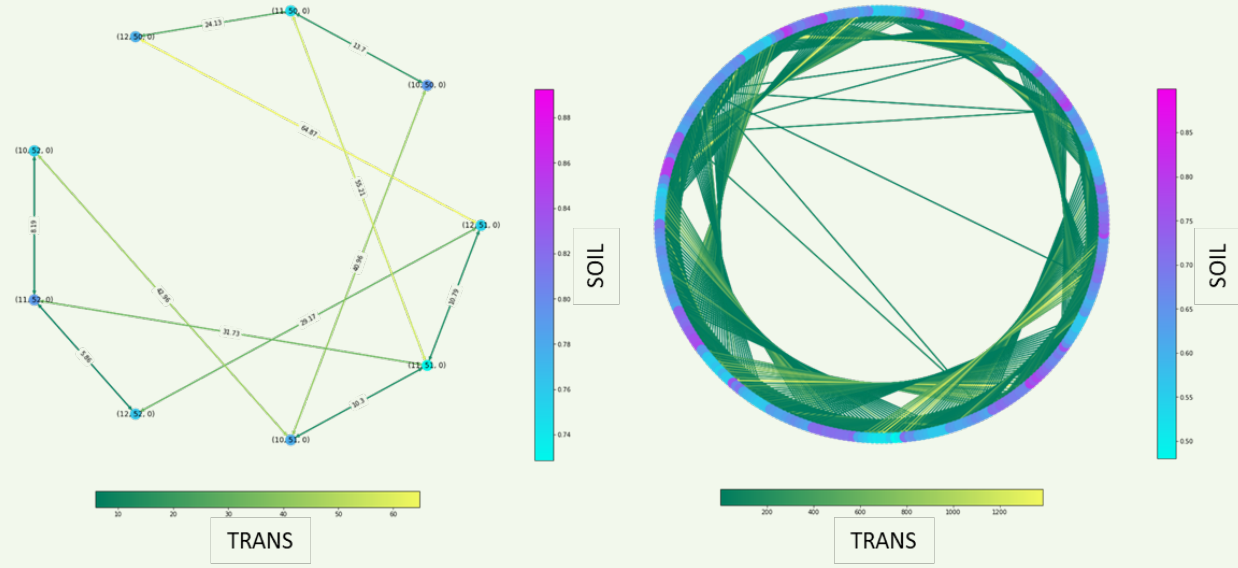
correct two-phase flow dynamics and note-to-node information transfer of spatiotemporal fluid propagation in the training phase. Encoding the relative permeability parameters, i.e., connate water saturation, SWC, and oil-water endpoints, KRW, $KROW$, as a Corey function, Fig. 4, instead in its tabular form, accelerates the deep NN training.

- Operational state variables, X, that combine well attributes such as the oil production rate, $WOPR$, and water production rate, $WWPR$, for producers and water injection rate, $WWIR$, for injectors, encoded as control variables, representing well operational constraints per each time step.

The relations (R) are represented as a triplet $R = \langle R_R, R_S, R_I \rangle$, where:

- R_R and R_S are $N_O \times N_g$ arrays, which index the receiver and sender objects, respectively.

- R_I represents the $D_R \times N_R$ array where D_R sums over the number or relation attributes and types. In GeoDIN, we encode two relation types: bidirectional $TRANS$ and well completion factor, CF. Both, the $TRANS$ and CF are continuous variables. The relation type is one-hot encoded into a vector of size 3 with categorical representation of how interacting objects in the triplet R exchange the information ($DIFFUSE$ for grid cell-to-cell communication and $PRODUCE/INJECT$ for well-to-cell communication), which makes D_R a vector of size 5. In the GeoDIN experiments, where all the wells were top-to-bottom vertical wells, the corresponding well CFs are set to $CF = 1$. The generalization of the GeoDIN model to incorporate, e.g., slanted wells, would encode $CF \neq 1$ values.

The j-th columns of the R_R and R_S arrays represent one-hot encoding vectors that indicate the receiver and

sender object's indices, respectively.

The m computes[21] the matrix products $O^T R_R$ ($\dim(O^T R_R) = D_S \times N_R$) and $O^T R_S$ ($\dim(O^T R_S) = D_S \times N_R$) and concatenates them vertically with R_I:

$$m(G) = [O^T R_R; O^T R_S; R_I] = B \qquad 5$$

The resulting B is a $(2D_S + D_R) \times N_R$ array, whose columns represent the interaction terms b_k for the N_R relations or edges in graph G. As indicated in Fig. 2, in GeoDIN implementation the X are encoded as well object attributes into m.

B represents an input to Φ_R, which applies $f_R(\cdot)$, a NN, to each array column. In such manner, the Φ_R predicts

Fig. 4 *The encoded relative permeability function used to augment the GeoDIN object's model.*
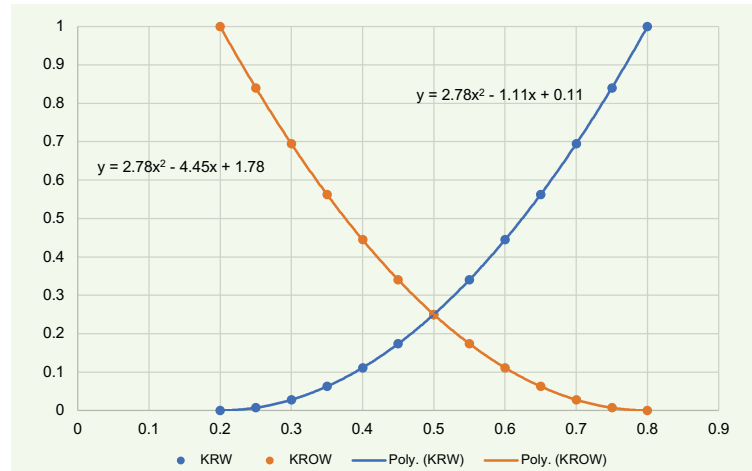
the effect of each interaction e_k by applying $f_R(\cdot)$ to each b_k. The output of $f_R(\cdot)$ is a D_E length effect vector, e_k, which represents an embedded distribution of calculated effects on objects (O). The role of Φ_R is to concatenate the N_R effects to form the $D_E \times N_R$ effect array, E.

G and E are input to aggregation function a, which computes the $D_E \times N_O$ matrix product, $\bar{E} = ER_R^T$, whose j-th column equals to element-wise summation over all e_k whose corresponding relation has a receiver object, o_j.

$$a(G, E) = [O^T; \bar{E}] = C \qquad 6$$

The resulting C is a $(D_{SDyn} + D_E) \times N_O$ array whose N_O columns are the object states and per object aggregated interaction effects.

To clarify, the GeoDIN model is applied to solve a forward problem, to predict the evolution of dynamic state variables, i.e., the future $t{+}1$ states of $SOIL$, and $SWAT$, and $PRESS$, while the state updates are not applied to D_{SStat}. Should the application of GeoDIN be reformulated to solve the inverse problem, e.g., static model reconciliation with dynamic data, referred to as history matching, then the array C of the aggregated interaction effects would combine both, D_{SDyn} and D_{SStat}.

C is input to Φ_O, which applies $f_O(\cdot)$, another NN, to each N_O column. The output of $f_O(\cdot)$ is a D_P length vector, p_j, and Φ_O concatenates them to form the output array P ($\dim(P) = 3 \times N_O$) of which components are predicted vectors of $SOIL$, $SWAT$, and $PRESS$ per simulated time step.

We train the GeoDIN using multiple hidden layers with various numbers of neurons, gated by the ReLU activation function and optimized with a stochastic gradient-based optimizer (ADAM)[26]. The GeoDIN is comprised of two FFNNs: the first FFNN, the Φ_R, calculates the e_k, and the second FFNN, the object model, learns to apply this e_k on the o_j. During training, the objective is to minimize the loss of the object model, defined as a mean square error (MSE) between the model's prediction and the full physics simulation, per simulation time step, across all the objects:

$$loss = MSE\left(f_O(o_{j,t}, e_k), (o_{j,t+1})\right) \qquad 7$$

At this point it is worth clarifying that GeoDIN does not incorporate an explicit time integration as perceived for and implemented in the PINN frameworks[8]. In GeoDIN, the flow physics is captured from simulation models by learning object-to-object interaction terms and computing their effects to predict the next object states. As such, the GeoDIN loss function only incorporates data-driven terms. In PINNs, however, the flow physics is emulated, and loss function combines the terms for solving flow governing PDEs, the terms with associated initial and boundary conditions as well as data-driven terms. In Maucec and Jalali (2021)[27] we further demonstrate the assembly of the O and R arrays with implementation on a simplified example of $3 \times 3 \times 1$ simulation grid with a corner injector and producer.

Experiments: We use the data for 800 days out of 1,827 days of simulated production for training. The FFNN was trained for 500 epochs. Figure 5 shows the convergence

of model loss function and the convergence of the mean cell error as a contribution from the individual predicted response terms, $SOIL$, $SWAT$, and $PRESS$.

In Table 2 we list the GeoDIN model training time, for models presented in Fig. 6. The timing values correspond

Fig. 5 *The training error convergence of the GeoDIN model: (a) the model loss as MSE between the model's prediction and the full physics simulation, and (b) contribution of individual predicted response terms, SOIL, SWAT, and PRESS, to the cell mean error.*
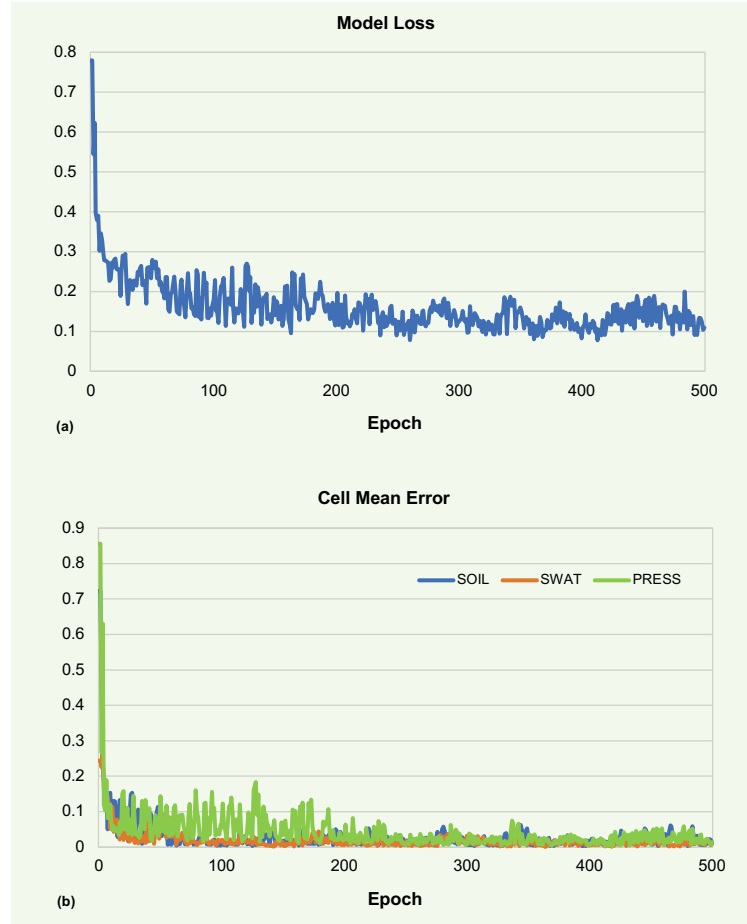

Table 2 *The GeoDIN model training time for models presented in Fig. 6.*

No. of Layers	Training (min)
3	4.4
5	3.3
10	7.7
20	15.4
40	30.3
80	N/A

to the use of a single GPU for all the models. The 80-layer model was not used for training to avoid memory allocation problems. Note that the training time values, as listed do not correspond to run time. They are only reported for evaluation purposes, but not used for prediction.

The prediction performance of the GeoDIN model was benchmarked against the full physics simulation run. The full physics simulation runs were performed on 70 Intel Xeon E5 CPU cores. The prediction period was 1,827 days. In Fig. 6, we show the run time performance as a function of the model size, by increasing the number of vertical layers from 3, 5, 10, 20, and 40, to 80. For the model sizes with a number of layers up to 40, a single V100 GPU was used to run the GeoDIN model predictions, for the model with 80 vertical layers, two GPUs were used to meet the memory requirements. Herewith, the run time corresponds to the rollout of 1,827 daily time steps in prediction mode.

While the predictive run time performance of full physics and GeoDIN model is comparable for the smallest model size (after discounting for the difference in hardware), the later model demonstrates significantly faster prediction for larger size models. In particular, when using the two GPUs vs. 70 CPUs, the GeoDIN prediction is almost five times faster.

In Fig. 7 we compare the number of relations (graph edges in the GeoDIN model) and the size of underlying simulation grid model as a function of the number of K-layers in the represented SPE10 model. The annotated trendlines indicate a linear dependence on the number of K-layers for both, the simulation grid size and the number of graph relationships. Consequently, the size of the graph increases approximately six times faster than the size of the grid. In practical terms, this suggests that with model scale up, the expansion of the network graph, as a representation of the reservoir simulation grid, potentially poses a challenge for interaction network training, due to the GPU memory limitations.

We have performed three prediction experiments with GeoDIN while benchmarking against a full physics reservoir simulator. It is important to note that the same full physics simulation model with three top layers from the upper shallow marine formation, was used to train all three GeoDIN predictive models.

1. **Experiment 1:** Perform prediction of spatiotemporal dynamics of *SOIL*, *SWAT*, and *PRESS* in the same three model layers as used for training. *SOIL* and *SWAT* were predicted independently and not constrained by the mass conservation equation for two-phase flow, i.e., $SOIL + SWAT = 1$. We have considered such an approach to investigate the predictive capability of the GeoDIN framework when generalized to three-phase gas/oil/water systems. The derivation of a gaseous component from three-phase mass conservation equation as $SGAS = 1 - SOIL - SWAT$, requires the independent prediction of oil and water components.

2. **Experiment 2:** Do not retrain the GeoDIN model, relocate the water injector to a different position in the

Fig. 6 *The run time performance of the GeoDIN model (orange) against the full physics simulation model (blue) as a function of the model size for the rollout of 1,827 daily time steps in prediction mode.*
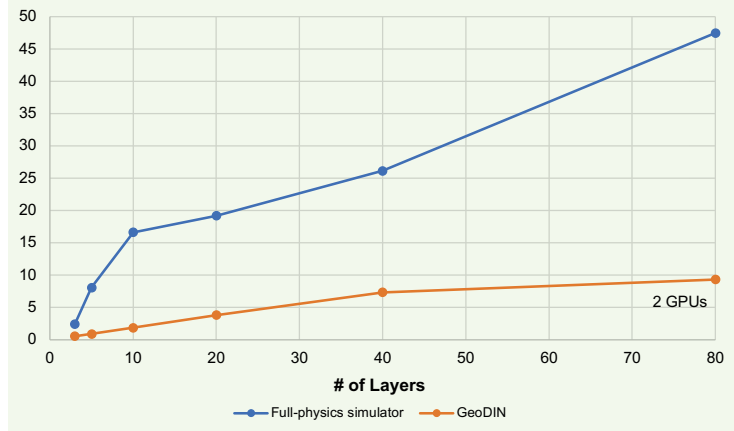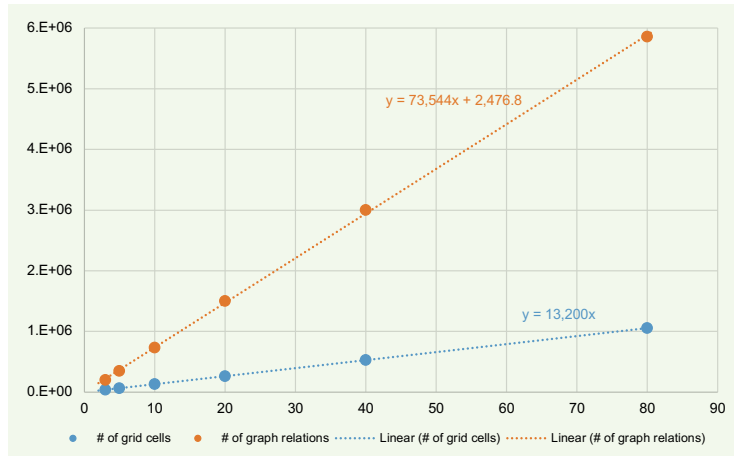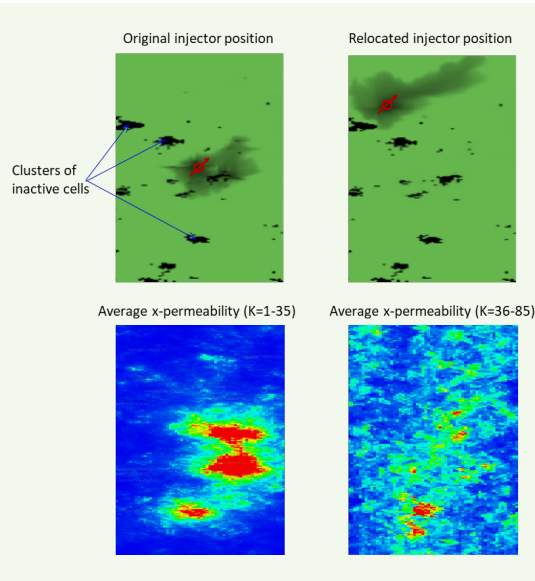

Fig. 7 *The number of relations (graph edges in GeoDIN model; orange) and grid cells in the underlying full physics simulation model (blue) vs. number of K-layers.*

simulation grid (Fig. 8; top row) and perform prediction of spatiotemporal dynamics of *SOIL*, *SWAT*, and *PRESS* in the same three-layer model. The objective of this experiment was to investigate how accurately the GeoDIN model can capture spatiotemporal flow dynamics with perturbed injector location, mimicking a stage of simplified infill drilling plan.

3. **Experiment 3:** As previously outlined, the SPE10 reservoir model under study consists of two distinctive formations, where in the top 35 shallow marine layers the permeability is relatively smooth, while in the bottom 50 layers follows a fluvial channel spatial distribution (Fig. 8; bottom row). Both formations are characterized by large permeability variations between eight to 12 orders or magnitude. The objectives of this experiment were to:

• Learn the representative fluid flow dynamics in

Fig. 8 *The visualization of information complimentary to a specific GeoDIN prediction experiment: relocation of the water injector in the simulation grid in Experiment 2 (top) and visualization of X-permeability in distinctive formations, corresponding to top shallow marine formation and bottom fluvial channel formation in Experiment 3 (bottom). In the top panel, the appearance of dark-colored clusters of points, corresponding to inactive cells is marked for clarification.*

three-layer simulation model. The represented fluid flow dynamics corresponds to a centrally located injector.

The presentation format is as follows:

- The top panel shows the snapshots of dynamic flow property predicted with the GeoDIN model at four time steps: 3 days, 500 days, 1,000 days, and 1,600 days.
- The central panel shows the snapshots of dynamic flow property predicted with a full physics simulator at the same time steps.
- The bottom panel shows the spatial map of a logarithm (for visualization purposes) square error per cell between the GeoDIN predicted and full physics simulated dynamic flow property at the same time steps.
- The unified color scales used are green for oil, blue for water, magenta for pressure, and red for square error.

Figure 12 outlines the boxplots of per cell error distribution for the GeoDIN prediction relative to full physics simulation for *SOIL*, *SWAT*, and *PRESS*, respectively, as a function of the simulation/prediction time step. The statistical error analysis corresponding to the final time step — end of simulation/prediction — indicates that the mean absolute error in *SOIL* is approximately 2%. The error distribution suggests that 50% of grid cells fall within a 4% error bound, while 90% of the grid cells fall within a 5% error bound. For *SWAT*, the mean absolute error is approximately 0.5%. The error distribution suggests that 50% of the grid cells fall within a 1.5% error bound, while 90% of the grid cells fall within a 2.5% error bound. For the *PRESS*, while the mean absolute error is approximately 5%, the error distribution suggests that 90% of grid cells fall within a 20% error bound, indicating that the GeoDIN model prediction overestimates the simulated pressure.

The spatiotemporal propagation of pressure is more sensitive to local embeddings of interaction networks, which communicate on node-to-node information transfer. The representation of reservoir pressure dynamics in the SPE10 model is governed by initial pore fluid distribution. This characterizes pressure as a global physics property, establishing several orders of magnitude faster than the fluid convection speed[11]. The external pressure support comes in the form of a single water injector, and in training, the GeoDIN framework fails to capture meaningful small variability in induced pressure dynamics, which results in a larger prediction error when benchmarked with full physics simulation.

Experiment 2: Prediction of Fluid Flow Dynamics in Three-Layer Model with Relocated Water Injector

Figures 13 to 15 provide a comparison between the GeoDIN prediction conducted in Experiment 2, and full physics simulation for *SOIL*, *SWAT*, and *PRESS*, respectively. We visualize the property maps for a selected layer (K = 2) of the three-layer simulation model. The represented fluid flow dynamics corresponds to a relocated water injector, as previously discussed.

Figure 16 outlines the boxplots of per cell error distribution for the GeoDIN prediction relative to full physics

shallow marine subsurface depositions and predict the spatiotemporal flow dynamics in the 85-layer model.

- Compare GeoDIN predicted spatiotemporal flow dynamics in a layer, selected from the bottom formation with the full physics simulation model.

The SPE10 simulation grid contains approximately 2.5% of inactive cells. In the simulation model, the inactive cells are assigned zero porosity and are not considered in flow calculations with full physics PDE solvers. In GeoDIN, we remove inactive cells from the graph, i.e., we ignore inactive cells when we convert the simulation model grid to a graph. Subsequently, we maintain one-on-one correspondence or mapping between the simulation grid and the generated graph by preserving the exact spatial location of inactive cells when the graph is converted back to the grid. In visualization of pressure and saturation maps, the inactive cells appear as dark-color clusters or ghost regions of points, Fig. 8. The same correspondence applies to pressure and saturation maps, previously noted.

Results

Experiment 1: Prediction of Fluid Flow Dynamics in Three-Layer Model

Figures 9 to 11 provide a comparison between the GeoDIN prediction and full physics simulation for the *SOIL*, *SWAT*, and *PRESS*, respectively. We visualize the property maps for a selected layer (K = 2) of the

Fig. 9 *A comparison of* SOIL *maps between the GeoDIN prediction and full physics simulation for a selected layer (K = 2) of the three-layer simulation model (Experiment 1) over time. The dark-colored clusters of points correspond to inactive cells.*
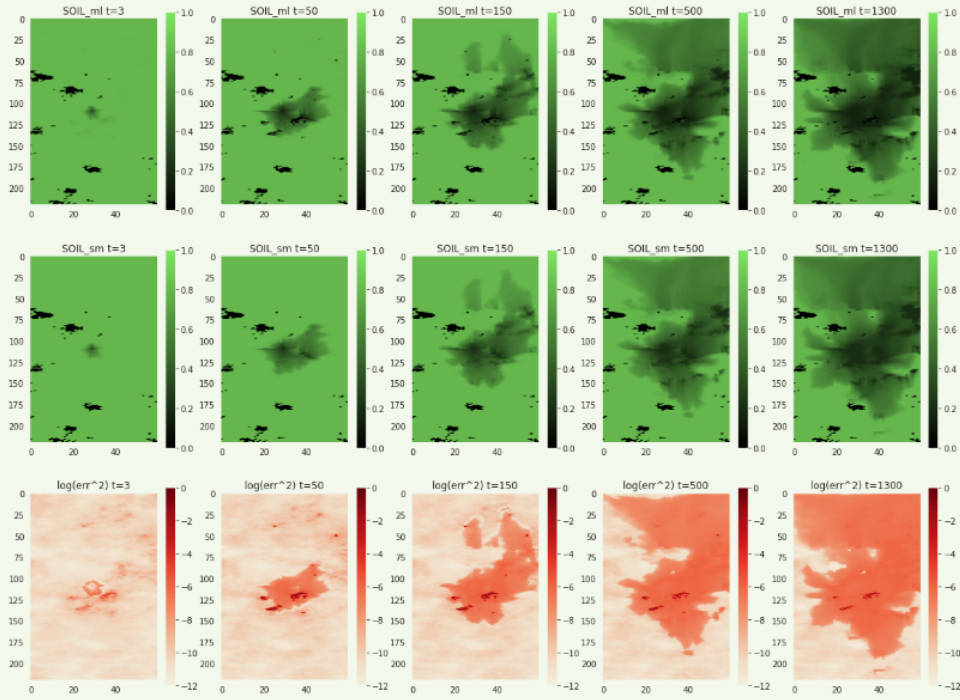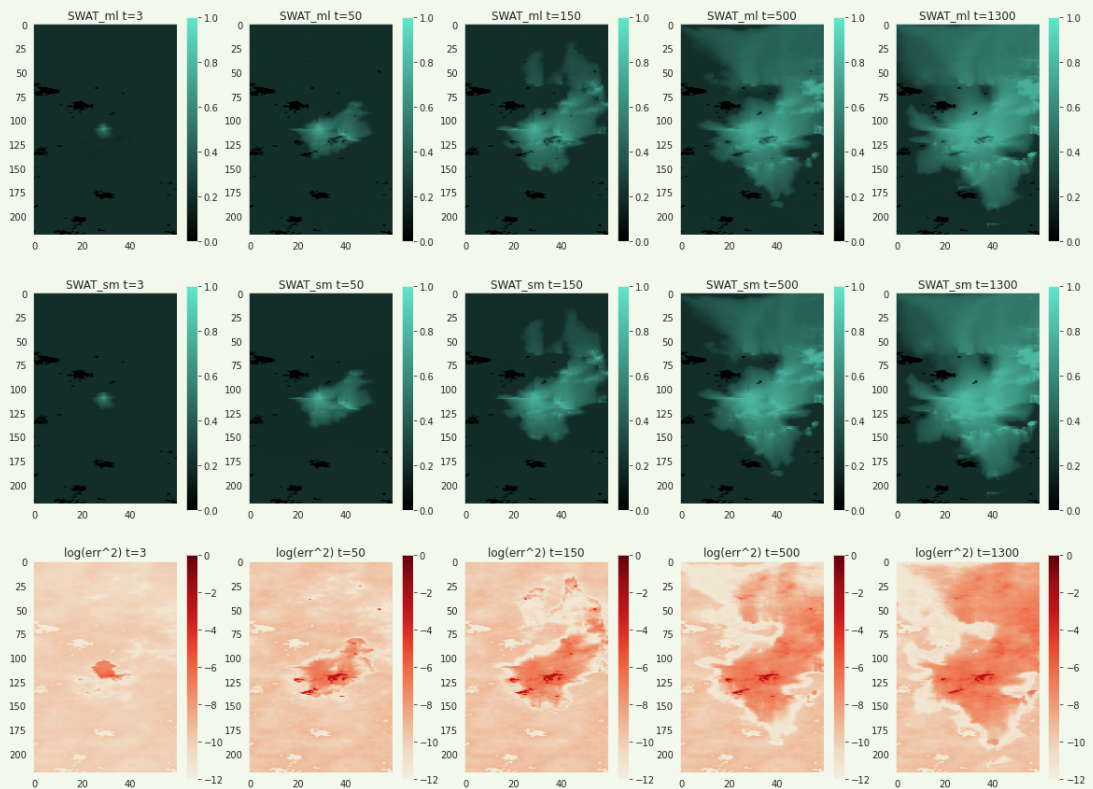

Fig. 10 *A comparison of* SWAT *maps between the GeoDIN prediction and full physics simulation for a selected layer (K = 2) of the three-layer simulation model (Experiment 1) over time. The dark-colored clusters of points correspond to inactive cells.*

Fig. 11 *A comparison of normalized PRESS maps between the GeoDIN prediction and full physics simulation for a selected layer (K = 2) of the three-layer simulation model (Experiment 1) over time. The dark-colored clusters of points correspond to inactive cells.*
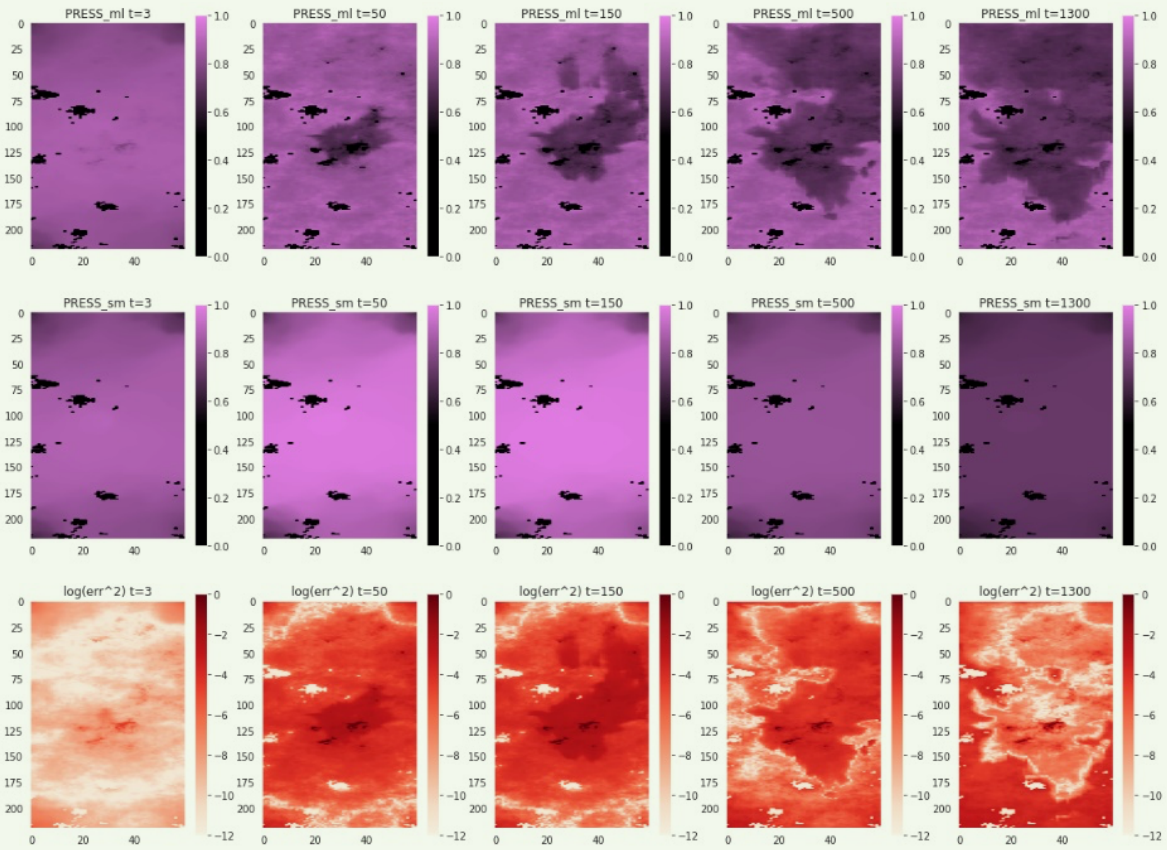

Fig. 12 *The per cell error distribution for the GeoDIN prediction relative to full physics simulation for SOIL, SWAT, and PRESS, respectively, in a three-layer simulation model (Experiment 1), over time.*

Fig. 13 *A comparison of SOIL maps between the GeoDIN prediction and full physics simulation for a selected layer (K = 2) of the three-layer simulation model with relocated injector (Experiment 2), over time. The dark-colored clusters of points correspond to inactive cells.*
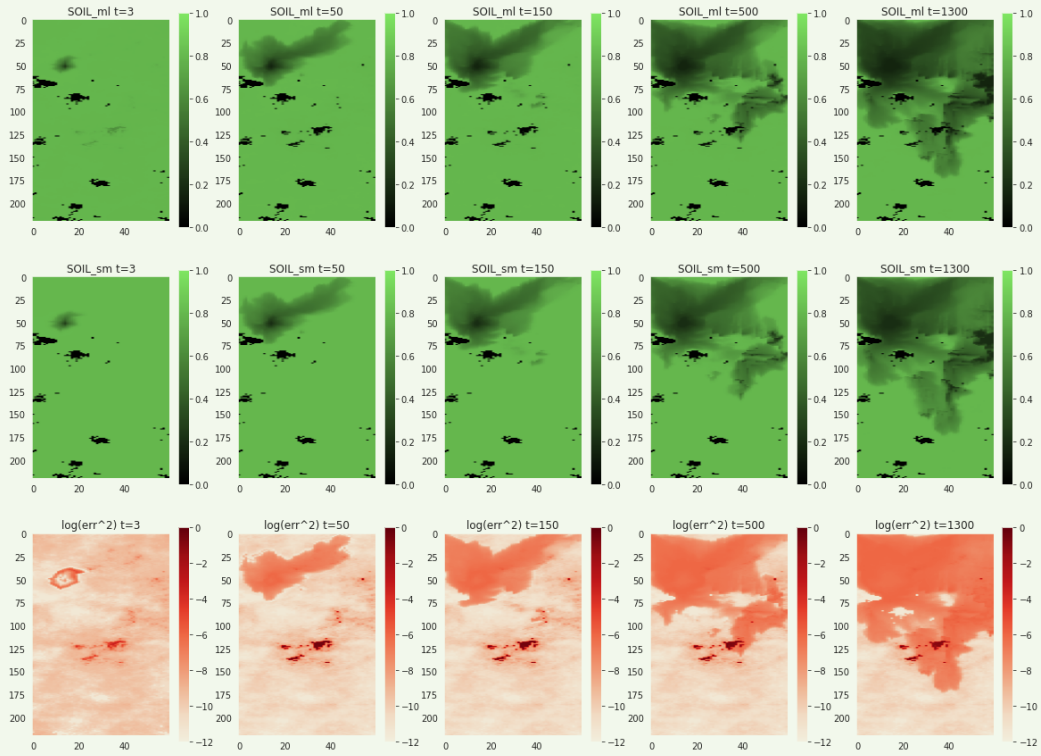

Fig. 14 *A comparison of* SWAT *maps between the GeoDIN prediction and full physics simulation for a selected layer (K = 2) of the three-layer simulation model with relocated injector (Experiment 2), over time. The dark-colored clusters of points correspond to inactive cells.*

Fig. 15 A comparison of PRESS maps between the GeoDIN prediction and full physics simulation for a selected layer (K = 2) of the three-layer simulation model with relocated injector (Experiment 2), over time. The dark-colored clusters of points correspond to inactive cells.
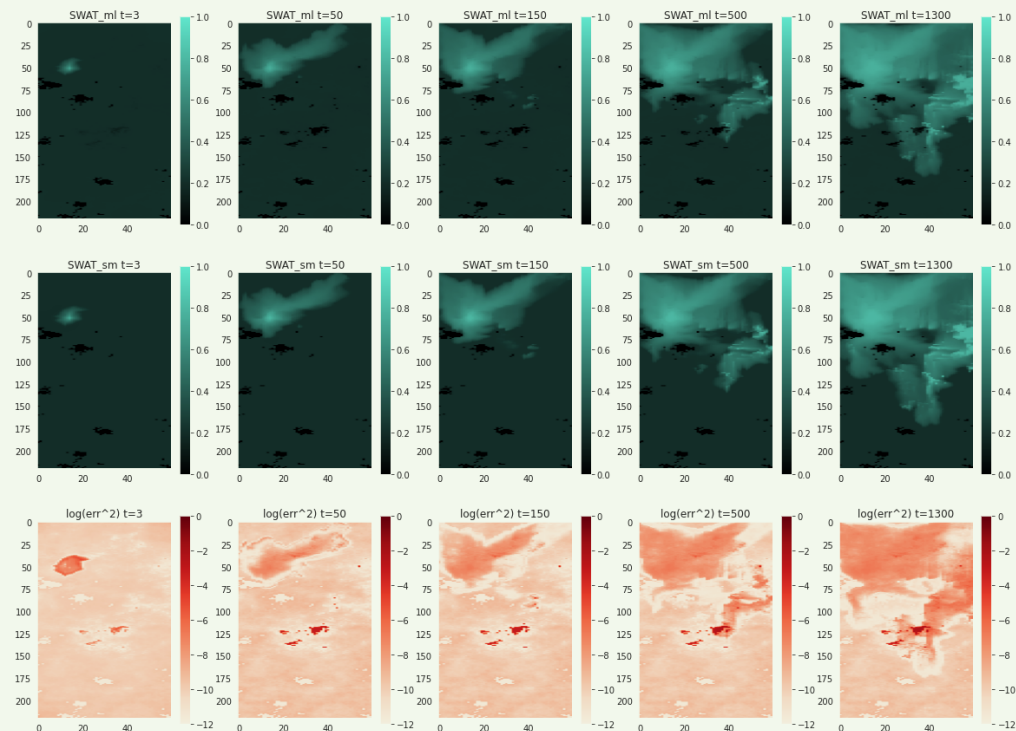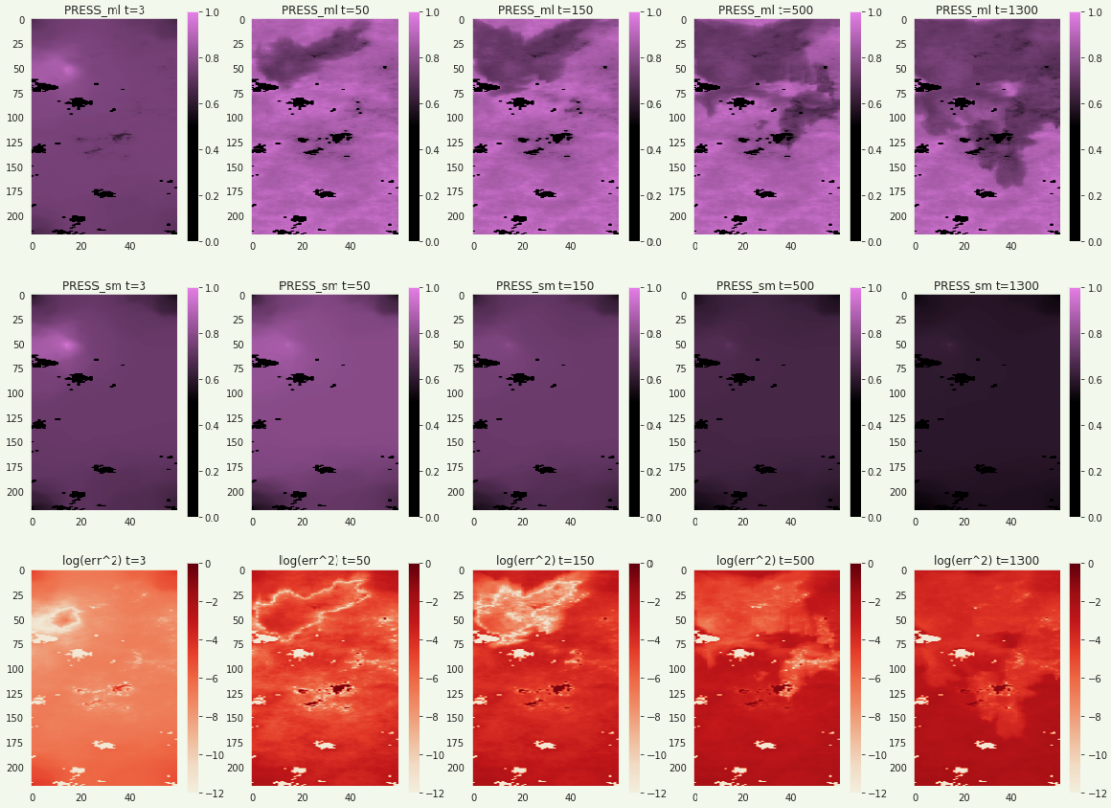

Fig. 16 The per cell error distribution for the GeoDIN prediction relative to full physics simulation for SOIL, SWAT, and PRESS, respectively, in a three-layer simulation model with relocated injector (Experiment 2), over time.
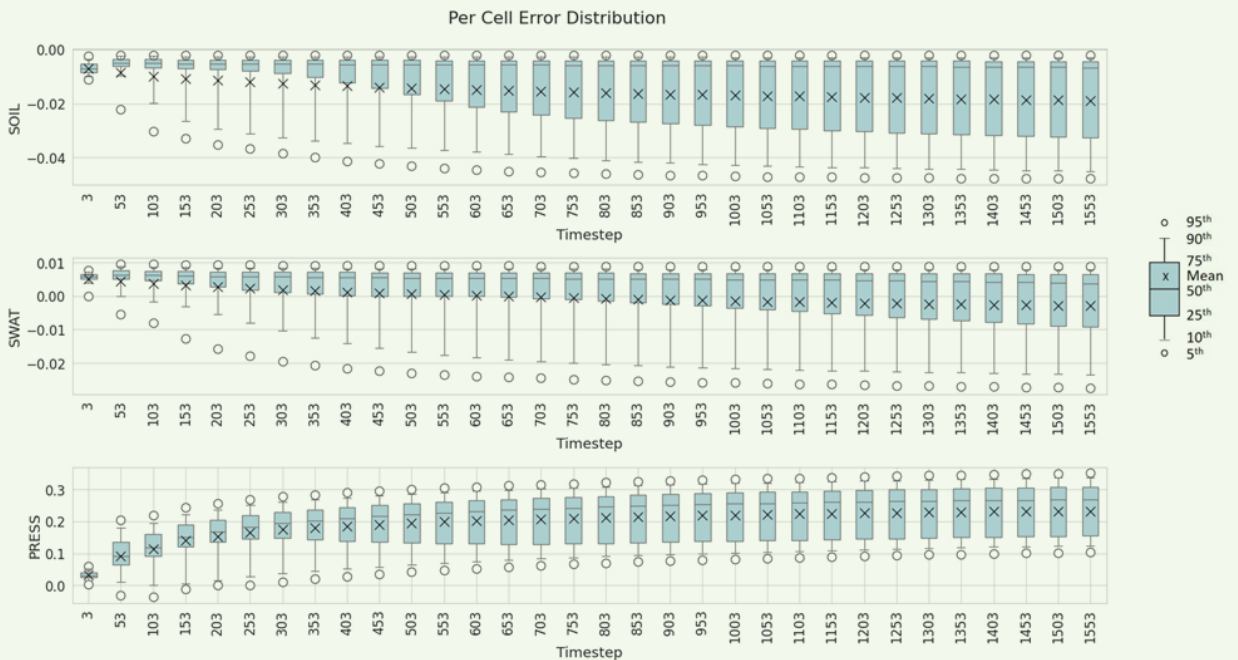
Fig. 17 *A comparison of* SOIL *maps between the GeoDIN prediction and full physics simulation for a selected layer (K = 55) of the 85-layer simulation model (Experiment 3), over time. The dark-colored clusters of points correspond to inactive cells.*

Fig. 18 *A comparison of* SWAT *maps between the GeoDIN prediction and full physics simulation for a selected layer (K = 55) of the 85-layer simulation model (Experiment 3), over time. The dark-colored clusters of points correspond to inactive cells.*

Fig. 19 *A comparison of PRESS maps between the GeoDIN prediction and full physics simulation for a selected layer (K = 55) of the 85-layer simulation model (Experiment 3), over time. The dark-colored clusters of points correspond to inactive cells.*
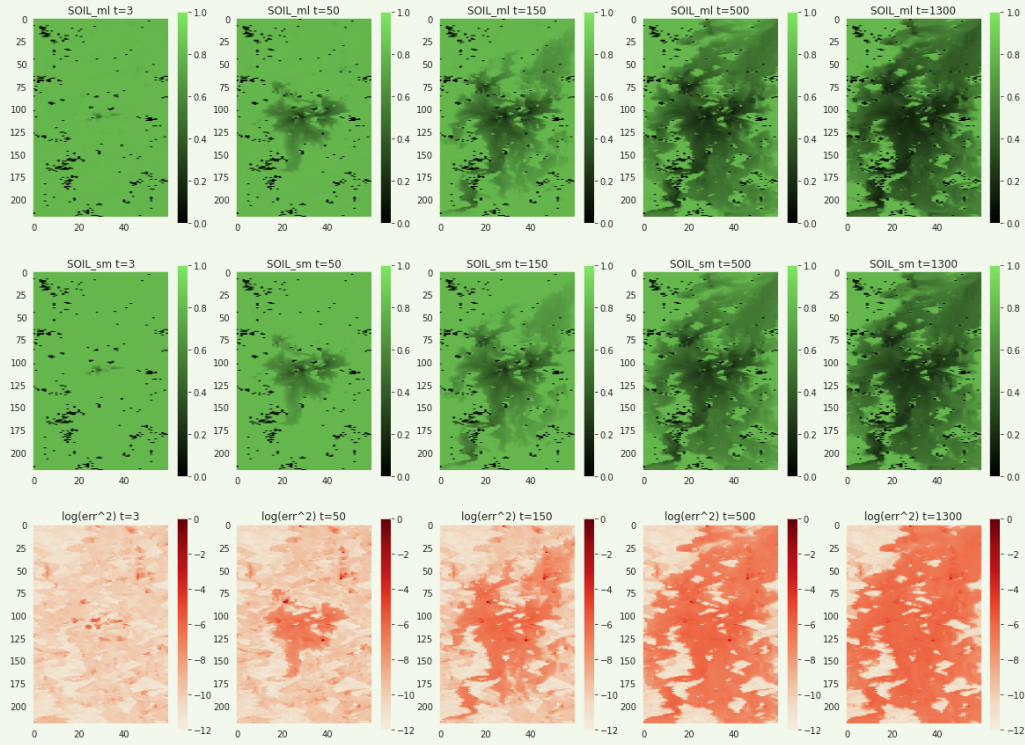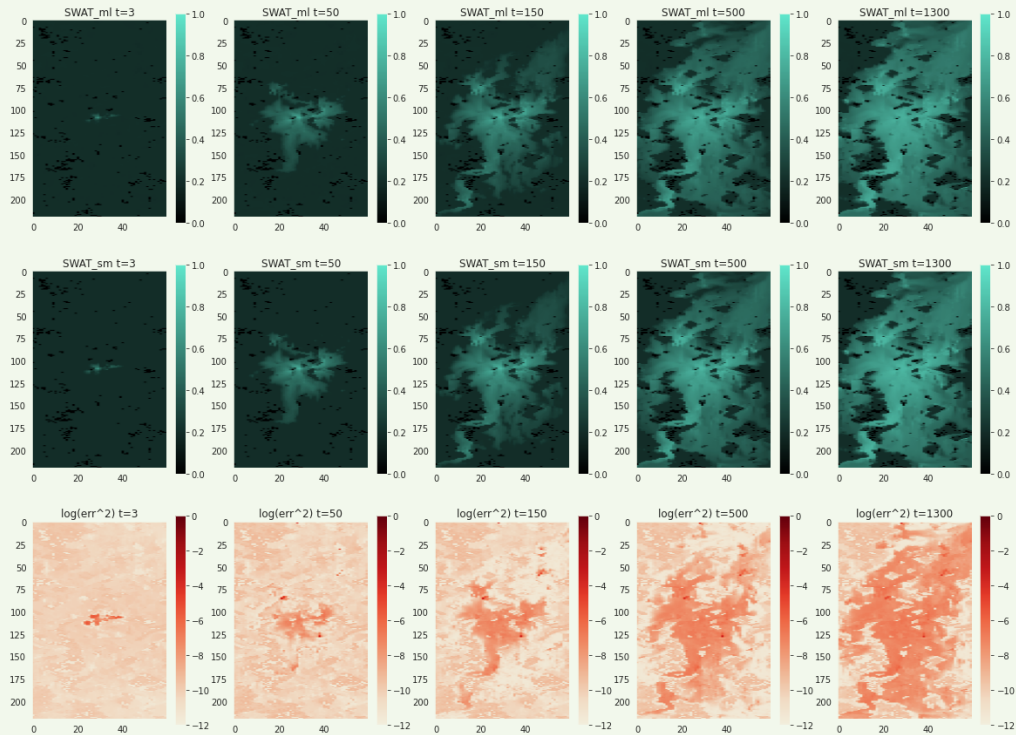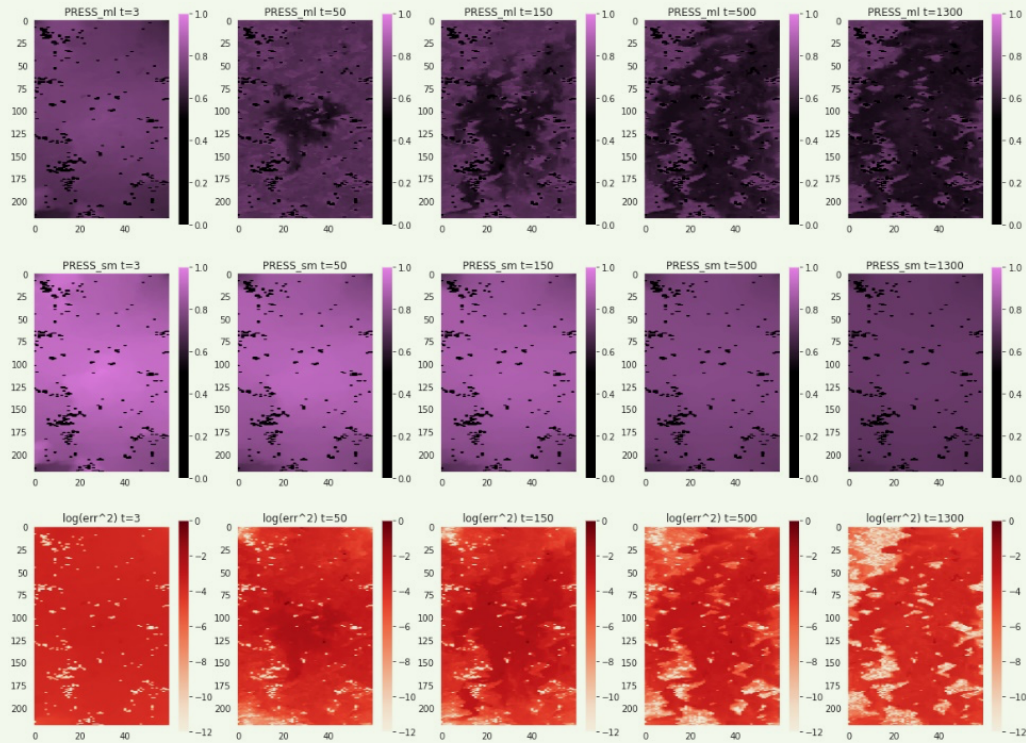

simulation for *SOIL*, *SWAT*, and *PRESS*, respectively, as a function of simulation/prediction time step. The statistical error analysis corresponding to the final time step — end of simulation/prediction — indicates the mean absolute error in *SOIL* is approximately 2%. The error distribution suggests that 50% of the grid cells fall within a 3% error bound, while 90% of the grid cells fall within a 4.5% error bound. For *SWAT*, the mean absolute error is approximately 0.5%. The error distribution suggests that 50% of the grid cells fall within a 1% error bound, while 90% of the grid cells fall within a 2.5% error bound. For *PRESS*, the mean absolute error is approximately 23%, while the error distribution suggests that 90% of the grid cells fall within a 10% to 30% error bound, indicating that the GeoDIN model prediction overestimates the simulated reservoir pressure. The physical reasoning behind the phenomenon refers to the explanation previously discussed.

Experiment 3: Prediction of Fluid Flow Dynamics in Distinctively Different Formation of 85-Layer Model

In experiment 3, the GeoDIN model was trained with the three-layer full physics simulation model of the upper formation and learned the representative fluid flow dynamics in the upper shallow marine subsurface depositions. The model was then used to predict the spatiotemporal flow dynamics in the 85-layer model. We visualize the fluid distribution maps in a selected layer (K = 55) corresponding to the lower fluvial channel formation of the 85-layer simulation model. Figures 17 to 19, respectively, correspond to *SOIL*, *SWAT*, and *PRESS*.

The results demonstrate the ability of the GeoDIN model to learn the fluid dynamics from the three-layer model and accurately generalize the interaction effects on a larger — 85-layer — simulation grid model with distinctively different distribution of matrix permeability, spatially, and by magnitude. We augment the outcome by interpreting Fig. 20, which shows the results of *TRANS* normalization for data points corresponding to active cells, using Box-Cox transformation. The upper row corresponds to the transmissibility from three-layer simulation model used for GeoDIN training, while the bottom row corresponds to transmissibility of the 85-layer model used for prediction.

The *TRANS*, extracted from the full physics simulation output, is severely right-skewed and resembles power law distribution with extreme values reaching up to 600,000. The transformation of the *TRANS* into a distribution that resembles normality is essential because in general, for the NNs, the learning from highly imbalanced data with power-law-like distributions can be quite challenging. Moreover, since transmissibility represents the main relation/edge attribute in the network graph model that controls cell-to-cell communication via diffusivity, the outlier removal is not recommended.

It is interesting to observe that the Box-Cox transformation of model transmissibility renders a multimodal

distribution for the 85-layer model, which clearly indicates the presence of distinctive formations as well as flow units in a subsurface model. Moreover, as shown by the boxplots in the right column of Fig. 20, the shapes of transformed density distributions of three-layer and 85-layer models are statistically sufficiently similar for GeoDIN to learn spatial fluid dynamics in the three-layer model and accurately predict in the 85-layer model.

Figure 21 outlines the boxplots of per cell error distribution for the GeoDIN prediction relative to full physics simulation for the *SOIL*, *SWAT*, and *PRESS*, respectively, as a function of simulation/prediction time step. The statistical error analysis corresponding to the final time step — end of simulation/prediction — indicates the mean absolute error in *SOIL* is approximately 2%. The error distribution suggests that 50% of the grid cells fall within a 3.8% error bound, while 90% of the grid cells fall within a 4.5% error bound. For the *SWAT*, the mean absolute error is approximately 0.5%. The error distribution suggests that 50% of the grid cells fall within a 1.5% error bound, while 90% of the grid cells fall within a 2.5% error bound. For *PRESS*, the mean absolute error is approximately 8%, while the error distribution suggests that 95% of the grid cells fall within a 20% error bound, indicating that the GeoDIN model prediction underestimates the simulated reservoir pressure. The physical reasoning behind the phenomenon refers to the explanation previously discussed.

Discussion

We introduced the GeoDIN framework that learns complex representations of subsurface from reservoir simulation models and predicts 3D flow dynamics. We conducted various experiments and demonstrated that, on average, the error in GeoDIN predicted spatiotemporal distribution of *SOIL* remains within 5% of full physics simulation for 90% of the model grid cells, while the error in *SWAT* remains within 2.5% of the full physics simulation.

Subsequently, with its current architecture, the GeoDIN cannot accurately predict the well production rates for oil and water. The GeoDIN is based on the concept of interaction networks[21], initially developed and validated for tasks of physical reasoning such as predicting potential energy of *n*-body systems, where *n* interacting objects are of the same type and result in *n(n-1)* relations to learn meaningful interactions caused by exerting distance and mass dependent forces on each other.

As previously described, the GeoDIN graph representation of the reservoir simulation model embodies two types of objects (nodes): grid cells and wells. The dominant interaction dynamics occurs at cell-to-cell level and the three-layer model, used in our training experiments, renders almost 200,000 relations (graph edges in the GeoDIN model) to accurately learn meaningful cell-to-cell flow dynamics by interaction networks.

In GeoDIN, *CFs* are used to one-hot encode wells

Fig. 20 *Results of transmissibility normalization for data points corresponding to active cells, using Box-Cox transformation.*

Fig. 21 *The per cell error distribution for the GeoDIN prediction relative to full physics simulation for* SOIL, SWAT, *and* PRESS, *respectively, in the 85-layer simulation model (Experiment 3), over time.*
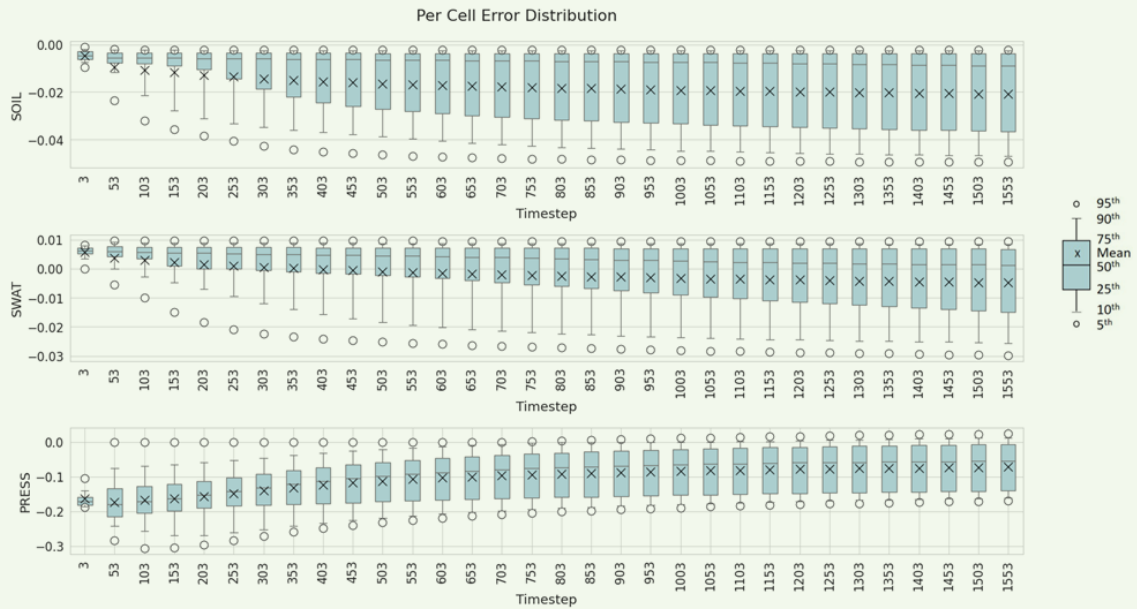
into a network graph. In the three-layer model, used for training, encoding five wells (one injector and four producers), completed top-to-bottom results in 15 well-to-cell relations. This is orders of magnitude lower than the number of cell-to-cell relations and insufficient for interaction networks to learn meaningful well-to-cell dynamics and accurately predict well rates. Alternative approaches can be investigated to improve the prediction of well rates in GeoDIN models: (a) predict flow saturation within drainage regions of perforated/completed well cells with interaction networks (expansion to drainage regions will increase the number of corresponding well-to-cell relations) and use separate machine learning models such as multilayer perception, LSTM, or recurrent NN to predict well rates as time series, and (b) modify the loss function to penalize for the well-to-cell interactions in prediction of well rates.

Conclusions

GeoDIN is a novel proof-of-concept technology with applications to graph learning from reservoir simulation models that carries a game changing potential for rapid prediction of subsurface flow dynamics. For *SOIL* and *SWAT*, the GeoDIN model prediction generalizes efficiently to capture the interaction effects on a larger simulation grid model with distinctively different distribution of subsurface properties, spatially, and by magnitude (Experiment 3). Furthermore, a high degree of generalization has been achieved to account for variable (injector) well locations (Experiment 2). In addition, we demonstrate a significant prediction speed up of the GeoDIN model with respect to full physics simulation reaching almost fivefold acceleration for the largest model simulated, with reduced hardware requirements (two

GPUs vs. 70 CPUs).

When training the GeoDIN model, the GPU memory allocation may become challenging with model scale up. In our experiments with the SPE10 model, the number of graph edges increases almost six times faster than the number of cells in the underlying simulation grid. The graph size may expand at even higher rates when distinctive features that govern reservoir connectivity, e.g., fractures, faults, and high flow units, are encoded. One recommendation would be to utilize the distributed deep learning training framework (Horovod) and leverage state-of-the-art hardware, such as GPU clusters with sufficient memory to perform the training at scale. It is also suggested to build on the learnings from Box-Cox data transformation and perform a rigorous sensitivity and ranking analysis, jointly for network graph object and relation attributes, and with variable well positioning to evaluate their distinctive impact on learning cell-to-cell flow diffusivity.

When compared to fluid dynamics, the reservoir pressure is characterized as the global model property, established several orders of magnitude faster than the fluid convection speed. In interaction networks, which communicate by node-to-node information transfer, the spatiotemporal propagation of pressure is more sensitive to local embeddings, which makes the learning of representative pressure dynamics significantly more challenging. The GeoDIN model is unable to accurately capture meaningful pressure dynamics induced by a single water injector, which results in a larger prediction error when benchmarked with reservoir simulation.

On average, over the three conducted experiments, the error distribution suggests that a great majority (90% to

95%) of grid cells fall within 10% to 30% error bound relative to full physics simulation. The ability of GeoDIN to predict spatial pressure dynamics more accurately could improve if the model is trained with a variable number and use locations of injectors as well as variable injection rates. We may conduct such experiments in the future.

As the way forward, we are currently investigating the application of the state-of-the-art NN architectures, such as graph NNs with advanced feature encoding and augmentation to improve training with clustered and sectorized data, learn highly similar graph structures and embeddings, propagate information across graphs with automated feature learning, and to conserve fluid volumes over long prediction times. Ultimately, our objective is to generalize and scale up the GeoDIN architectures by training with reservoir properties under uncertainty, a variety of scenarios of distinctive reservoir connectivity (faulted and fractured models), complex structure and gridding, e.g., unstructured and locally refined grids, and with modeling different recovery drive mechanisms, improved oil recovery strategies, and well placement and production constraints.

Acknowledgments

References

1. Willcox, K.E., Ghattas, O. and Heimbach, P.: "The Imperative of Physics-Based Modeling and Inverse Theory in Computational Science," *Nature Computational Science*, Vol. 1, March 2021, pp. 166-168.

2. Zhao, Y. and Sarma, P.: "A Benchmarking Study of a Novel Data Physics Technology for Steamflood and SAGD Modeling: Comparison to Conventional Reservoir Simulation," SPE paper 189772, presented at the SPE Canada Heavy Oil Technical Conference, Calgary, Alberta, Canada, March 13-14, 2018.

3. Klie, H., Yan, B. and Klie, A.: "Transfer Learning for Scalable Optimization of Unconventional Field Operations," paper presented at the SPE/AAPG/SEG Unconventional Resources Technology Conference, Virtual, July 20-22, 2020.

4. Zhang, J., Cheung, S.W., Efendiev, Y., Gildin, E., et al.: "Deep Model Reduction Model Learning for Reservoir Simulation," SPE paper 193912, presented at the SPE Reservoir Simulation Conference, Galveston, Texas, April 10-11, 2019.

5. Jin, Z.L., Liu, Y. and Durlofsky, L.J.: "Deep Learning-Based Reduced Order Modeling for Subsurface Flow Simulation," 2019, *arXiv:1906.03729v1*.

6. Al-Sulaimani, T. and Wheeler, M.: "Reduced Order Modeling for Multiphase Flow Using a Physics-Based Deep Learning," SPE paper 203965, presented at the SPE Reservoir Simulation Conference, Galveston, Texas, October 4-6, 2021.

7. Watter, M., Springenberg, J.T., Boedecker, J. and Riedmiller, M.: "Embed to Control: A Locally Linear Latent Dynamics Model for Control from Raw Images," paper presented at the 29th Conference on Neural Information Processing Systems, Montreal, Quebec, Canada, December 7-12, 2015.

8. Fraces, C.G., Papaioannou, A. and Tchelepi, H.: "Physics Informed Deep Learning for Transport in Porous Media. Buckley Leverett Problem," 2020, *arXiv:2001.05172v1*.

9. Wang, N., Zhang, D., Chang, H. and Li, H.: "Deep Learning of Subsurface Flow via Theory-Guided Neural Network," *Journal of Hydrology*, Vol. 584, May 2020.

10. Wang, N., Chang, H. and Zhang, D.: "Efficient Uncertainty Quantification and Data Assimilation via Theory-Guided Convolutional Neural Network," *SPE Journal*, Vol. 26, Issue 6, December 2021, pp. 4128-4156.

11. Thavarajah, R., Zhai, X., Ma, Z. and Castineira, D.: "Fast Modeling and Understanding Fluid Dynamics Systems with Encoder-Decoder Networks," 2020, *arXiv:2006.05409v1*.

12. Cai, S., Mao, Z., Wang, Z., Yin, M., et al.: "Physics-Informed Neural Networks (PINNs) for Fluid Mechanics: A Review," 2021, *arXiv:2105.09506v1*.

13. Fuks, O. and Tchelepi, H.A.: "Limitations of Physics Informed Machine Learning for Nonlinear Two-Phase Transport in Porous Media," *Journal of Machine Learning for Modeling and Computing*, Vol. 1, Issue 1, 2020, pp. 19-37.

14. Zitnik, M., Agrawal, M. and Leskovec, J.: "Modeling Polypharmacy Side Effects with Graph Convolutional Networks," *Bioinformatics*, Vol. 34, Issue 13, July 2018, pp. i457-i466.

15. Hamilton, W.L., Ying, R. and Leskovec, J.: "Representation Learning on Graphs: Methods and Applications," *IEEE Data Engineering Bulletin*, Vol. 40, Issue 3, 2017, pp. 52-74.

16. Halac, D., Bhooshan, S., Chen, M., Abida, K., et al.: "Drive2Vec: Multiscale State-Space Embedding of Vehicular Sensor Data," paper presented at the IEEE International Conference on Intelligent Transportation Systems, Maui, Hawaii, November 4-7, 2018.

17. Cranmer, M.D., Xu, R., Battaglia, P. and Ho, S.: "Learning Symbolic Physics with Graph Networks," 2019, *arXiv:1901.05862v2*.

18. Golmohammadi, A.: "Hybrid Modeling: Challenges and Opportunities in the Subsurface," paper presented at the SPE Workshop: Merging Data-Driven and Physics-Based Models for Enhanced Reservoir Insights and Predictions, San Antonio, Texas, November 19-20, 2019.

19. Sanchez-Gonzalez, A., Godwin, J., Pfaff, T., Ying, R., et al.: "Learning to Simulate Complex Physics with Graph Networks," 2020, *arXiv:2002.09405v2*.

20. Jalving, J, Cao, Y. and Zavala, V.M.: "Graph-Based Modeling and Simulation of Complex Systems," *Computers & Chemical Engineering*, Vol. 125, June 2019, pp. 134-154.

21. Battaglia, P.W., Pascanu, R., Lai, M., Rezende, D., et al.: "Interaction Networks for Learning about Objects, Relations and Physics," paper presented at the 30th Conference on Neural Information Processing Systems, Barcelona, Spain, December 5-10, 2016.

22. Maucec, M., Jalali, R. and Dossary, M.: "Methods and Systems for Generating Graph Neural Networks for Reservoir Grid Models," U.S. Patent Application 2021/0389491 A1, 2021.

23. Sintef: "The 10th SPE Comparative Solution Project, Model 2," 2008, *https://www.sintef.no/projectweb/geoscale/results/msmfem/spe10/*.

24. Dogru, A.H., Fung, L.S.K., Middya, U., Al-Shaalan, T.M., et al.: "New Frontiers in Large-Scale Reservoir Simula-

tion," SPE paper 142297, presented at the SPE Reservoir Simulation Symposium, The Woodlands, Texas, February 21-23, 2011.

25. Equinor: "Equinor/ecl: Software for Reading and Writing the Result Files from the Eclipse Reservoir Simulator," 2021, GitHub repository: *https://github.com/equinor/ecl*.

26. Kingma, D. and Ba, J.: "Adam: A Method for Stochastic Optimization," paper presented at the International Conference on Learning Representations, San Diego, California, May 7-9, 2015.

27. Maucec, M. and Jalali, R.: "Geoscience-Based Deep Interaction Networks for Predicting Flow Dynamics in Reservoir Simulation Models," SPE paper 205952, *SPE Journal*, in press, 2021.

About the Authors

Dr. Marko Maucec

Ph.D. in Nuclear Engineering, University of Ljubljana

Dr. Marko Maucec is a Petroleum Engineering Consultant with the Simulation Group of Saudi Aramco's Reservoir Description and Simulation Department. His main responsibilities cover the development and implementation of methods for uncertainty quantification, dynamic model inversion with assisted history matching, production optimization, and data- and physics-driven predictive modeling into reservoir simulation practices.

Marko has been awarded prestigious postdoctoral research tenures, such as the Fulbright and Marie Curie Fellowships, has worked internationally in the nuclear research and industry as well as formerly in the oil industry with Halliburton/Landmark and Shell International E&P.

He has authored more than 80 peer-reviewed and conference papers. Marko is a coauthored on a reference book, *Intelligent Digital Oil and Gas Fields: Concepts, Collaboration, and Right-Time Decisions*, and is an inventor on 30 U.S. patents and patent applications.

He is an active member of the Society of Petroleum Engineers (SPE), a technical peer reviewer for the *SPE Journal*, and a co-organizer of professional events and forums. Marko is an appointed member in the Reservoir Advisory Committee to the Technical Director for SPE's Reservoir technical discipline, and is currently serving as the co-editor for the InTech Open Book Series publication on Applied Spatial-Temporal Data Analytics and Machine Learning.

He received his B.S. degree in Electrical Engineering from the University of Ljubljana, Ljubljana, Slovenia, his M.S. degree in Nuclear Engineering from the University of Maribor, Maribor, Slovenia, and his Ph.D. degree in Nuclear Engineering from the University of Ljubljana, Ljubljana, Slovenia.

Marko completed his postdoctoral work at Claremont Graduate University, Claremont, CA, and the University of Groningen, Groningen, the Netherlands.

Ridwan S. Jalali

M.S. in Computer Science, King Fahd University of Petroleum and Minerals

Ridwan S. Jalali joined Saudi Aramco in September 2011 as an IT System Analyst. His research areas include data science and machine learning for physical systems, computer vision and cognitive systems, including speech recognition, and natural language understanding.

Ridwan received his B.S. degree in Computer Science from Colorado State University, Fort Collins, CO, and his M.S. degree in Computer Science from King Fahd University of Petroleum and Minerals, Dhahran, Saudi Arabia.

Imaging Subsurface Targets Using Cross-Borehole GPR: A Field and Modeling Approach

Jesus M. Felix Servin and Hussain A. Shateeb

Abstract /

Cross-borehole ground penetrating radar (XBGPR) is a geophysical technique that allows for high-resolution characterization of the interwell region. This method relies on the propagation of electromagnetic (EM) waves — typically in the MHz region — that are analyzed to generate subsurface maps of EM properties, which can be interpreted into fluid saturation maps. We present the results of a large-scale field experiment complemented by 3D numerical simulations evaluating the feasibility of locating small fluid targets of different compositions in the subsurface.

An array of 33 target wells and six observation wells completed with nonconductive, nonmagnetic pipe were used to conduct the experiments. The target wells were filled with different fluids, including dielectrically and magnetically tagged fluids, such as polymer solutions and polymer solutions with magnetite. Time-domain EM measurements were acquired using a 100 MHz XBGPR system in a semi-reciprocal tomographic setup. The acquired waveforms were filtered and processed using bh_tomo, an open source platform for XBGPR analysis. Traveltime and amplitude inversions were performed to obtain velocity and attenuation maps of the surveyed area. In parallel, 3D numerical simulations were conducted using a commercially available finite element modeling package. The simulation results were compared and validated with the experimental results.

The simulations are in overall agreement with the field results; showing the right trend in traveltime and amplitude for the different fluids. All fluids caused an increase in traveltime compared to air filled target wells. Water appears to cause the largest increase, followed by AN-132, xanthan, and finally xanthan with magnetite. The observed traveltime is lower than expected. This may be an indication of the wave going around the holes and partially avoiding the slow fluids, especially because the operating wavelength is comparable to the well spacing.

Another possible explanation is that the actual location of the wells is slightly different from the original design due to inaccurate drilling. Yet another possibility is that the array may behave as a periodic structure, causing modal propagation. The attenuation data shows a clear difference between the empty and the liquid filled target holes, but little difference between the liquids. As a whole, the results prove that our approach can be used to locate relatively small fluid targets via EM tomographic surveys with no previous geological information.

Experimental data of XBGPR is rather limited. Our experiments expand the understanding of the challenges and opportunities that such a technique can offer to the oil and gas industry. We have also developed and validated modeling capabilities that will enable improved planning and quick testing of future surveys.

Introduction

Ground penetrating radar (GPR) is a geophysical technique that allows for high-resolution characterization of the subsurface. GPR uses electromagnetic (EM) propagating waves to probe the subsurface and detect structures and changes in electrical properties via reflection and/or transmission measurements. Comprehensive descriptions of the technique and its applications can be found in the literature[1, 2]. GPR has been used in several fields, such as glacial exploration and monitoring[3, 4], aquifer characterization[5], utility detection[6, 7], mining[8, 9], and voids detection[10], among others.

Signal penetration depends on the operating frequency and propagating media properties, and ranges widely from less than 1 m for clay, to several thousands of meters for ice[11]. Deep investigation is only possible in highly resistive materials and at low operating frequencies (tens of MHz).

GPR surveys can be divided into surface and borehole, depending on the acquisition configuration, and transmission, Fig. 1. Borehole GPR surveys are conducted in reflection mode when only one borehole is available and both the transmitter (Tx) and the receiver (Rx) are sequentially positioned at multiple locations along the same borehole. The reflections, caused by changes in the EM properties of the subsurface, are recorded. When two or

Fig. 1 *A schematic representation of surface GPR (left), reflection borehole GPR (middle), and transmission borehole GPR (right), also known as cross-borehole GRP.*
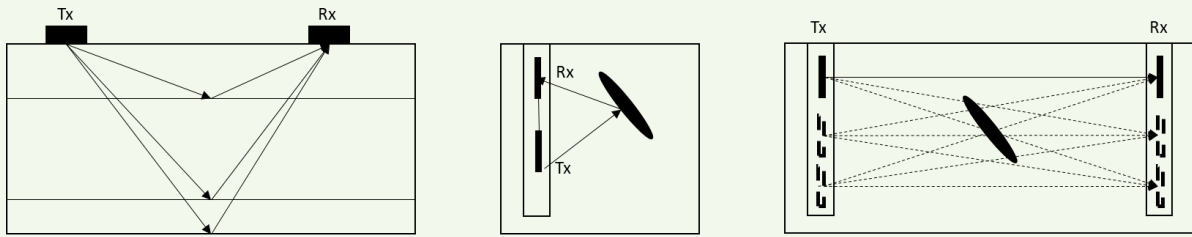
more boreholes are available, the survey can be conducted in transmission mode, also known as cross-borehole GPR (XBGPR).

Our work focuses on XBGPR, in which an EM signal is launched into the medium of interest by a Tx antenna located inside a borehole and the signal is recorded a certain distance away by an Rx antenna located inside a second borehole. Conventionally, the traveltime and first cycle amplitude of the recorded waveforms are picked, Fig. 2, and inverted, to obtain velocity and attenuation maps of the subsurface that can be further interpreted to obtain distribution maps of dielectric permittivity, ε, magnetic permeability, μ, and electric conductivity, σ. More sophisticated techniques to infer subsurface properties from the received waveforms, such as full waveform inversion, have also been explored and show promising results[5, 12-15].

The operating frequency of most borehole GPR systems is between 20 MHz to 250 MHz, with corresponding wavelengths of 5 m to 0.4 m for common geological materials[13, 16, 17]. Similar to surface GPR, the penetration depth ranges from less than a meter in clay, to tens of meters in crystalline rock, and thousands of meters in salt[11]. XBGPR is less common than surface GPR. Nevertheless, this technique has been implemented in multiple areas, such as mining[9], cavity imaging[17], fracture characterization[18], and hydrogeophysical investigations[19].

The application of borehole GPR in the oil and gas context is rather limited. Subsequently, several studies have been performed in recent years to evaluate the feasibility of incorporating this technique to some of the industry's operations. Zhou (2020)[20] investigated the potential use of this technique for well logging and production monitoring. Heigl et al. (2005)[21] performed simulations to determine if mud invasion can be estimated by means of borehole GPR. Miorali et al. (2011a)[22] and (2011b)[23] proposed a method to monitor water and oil movement in smart wells using permanent downhole GPR systems. Oloumi et al. (2015)[24] investigated the feasibility of imaging oil well perforations using borehole GPR in reflection mode. Chen et al. (2002)[25] showed that this technique is suitable for near wellbore imaging and geosteering applications.

Theory

In XBGPR, the traveltime and amplitude of the received signals depend on the EM properties of the media through which they propagate. EM waves propagate through air with the speed of light. Consequently, their speed in the subsurface is a function of the EM properties of the subsurface and the frequency of the wave, as described by Eqn. 1:

$$v = \left\{ \sqrt{\mu\epsilon} \sqrt{\frac{1}{2}\left[\sqrt{1 + \left(\frac{\sigma}{\omega\epsilon}\right)^2} + 1 \right]} \right\}^{-1} ,$$

1

where v is the speed of propagation, ω is the angular frequency, μ is the magnetic permeability, ε is the dielectric permittivity, and σ is the electric conductivity. Moreover, if we assume low conductivity (low loss approximation), Eqn. 1 simplifies to Eqn. 2:

$$v = \frac{1}{\sqrt{\mu\epsilon}} .$$

2

According to the low loss approximation in Eqn. 2, the speed of propagation is inversely proportional to μ and ε. Therefore, increasing either μ, or ε, or both, should result in lower propagation speed and increased signal traveltime. Several processes contribute to signal amplitude reduction, including attenuation, spherical spreading, scattering, as well as reflections at the interfaces. Similar to traveltime, attenuation is a function of the EM properties of the propagating medium as well as the signal frequency, as described by Eqn. 3:

Fig. 2 *A schematic of a received waveform showing the first break, which is used to calculate the traveltime, and the first cycle peak-to-peak amplitude.*

$$\alpha = \omega\sqrt{\mu\epsilon}\sqrt{\frac{1}{2}\left[\sqrt{1 + \left(\frac{\sigma}{\omega\epsilon}\right)^2} - 1\right]}$$

      3
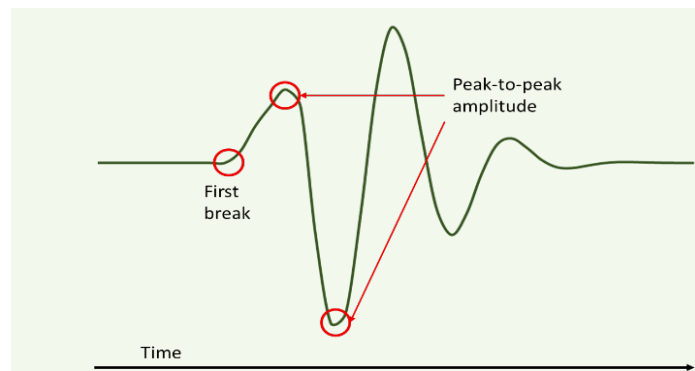
where a is the attenuation constant, ω is the angular frequency, μ is the magnetic permeability, ε is the dielectric permittivity, and σ is the electric conductivity.

In the case of oil reservoir fluids, significant changes in σ and ε are typically observed between oil and brine. Moreover, changes in μ are not usually observed, unless magnetic materials, such as iron oxide, are present in the formation. Therefore, μ may serve as a contrast to label injected fluids such that they can be differentiated from the fluids already present in the reservoir.

The purpose of this work is to investigate the feasibility of labeling fluids using magnetic and dielectric contrast agents, and locating them via XBGPR surveys. A series of large-scale experiments performed using an array of shallow wells are presented.

Testing Platform

An array of shallow wells designed to function as a testing platform for novel EM approaches was used to conduct the experiments. The entire platform consists of 47 wells of different depths and diameters, completed with non-conductive and nonmagnetic casing to be suitable for EM transmissions, Fig. 3. All wells were sealed from the bottom so that no fluids can leak from or into the wellbores. Depending upon the inner diameter, depth, and location, the wells are divided in four categories: deep observation wells (DO1 to DO2), far observation wells (O1 to O6), near observation wells (O7 to O12), and shallow wells (C1-1 to C3-11). Table 1 summarizes

the specifications and number of wells drilled for each category. For this work, only the near observation and shallow wells were used, the other wells are reserved for future tests.

The array design takes into consideration important parameters to improve the quality of the planned EM surveys. In the case of XBGPR, the borehole depth, D, to borehole separation, S, as a rule of thumb should be greater than 2. Meeting this condition maximizes the angle coverage and prevents refracted airwaves from masking direct arrivals[2]. At the same time, it is important to make sure that S is large enough to be in the far field of the antenna radiation, such that Eqn. 4 is met:

$$S > \frac{v}{f}$$

      4

where v is the ground velocity and f is the GPR center frequency.

In our case, the borehole depth is 40 m, and the borehole

Table 1 *A summary of wells drilled and their dimensions.*

Type of Well	Inner Diameter (m)	Depth (m)	# of Wells
Deep observation	0.3048	200	2
Far observation	0.3048	40	6
Near observation	0.1524	40	6
Shallow wells	0.3048	30	33

Fig. 3 *A schematic representation of the testing platform. For the experiments presented in this work, only Wells O7-O12 and C1-1 to C3-11 were used.*
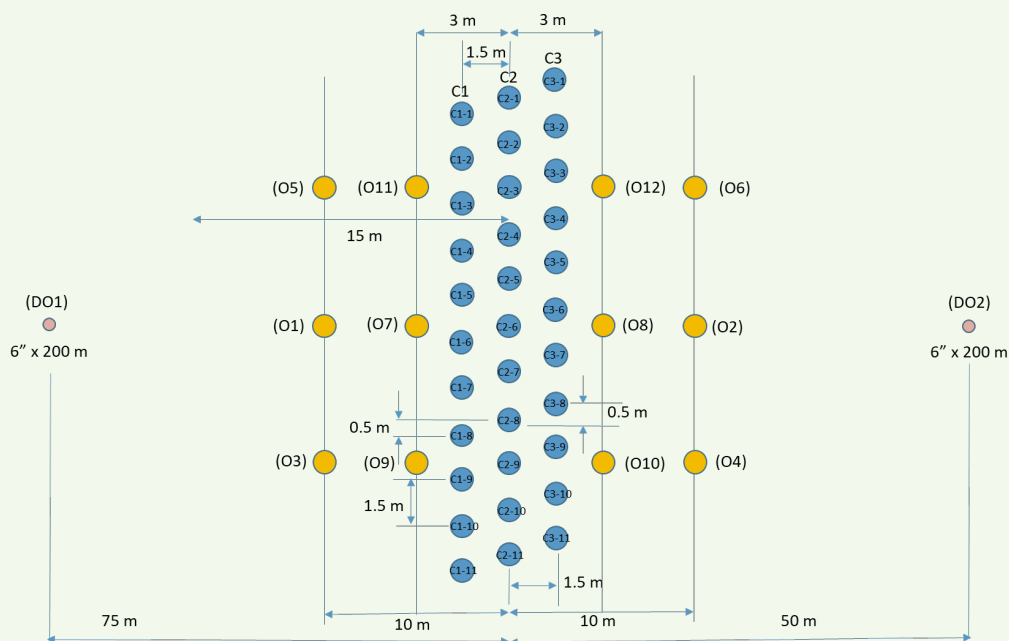
separation is 6 m, yielding a ratio of 6.67, well above the minimum recommendation of 2. The borehole separation is also larger than the velocity to center frequency ratio, which is approximately 1.2. Therefore, the dimensions of our array ensure significant angle coverage and far field conditions for the measurements.

Acquisition System and Procedure

A typical XBGPR system consists of three main components: a control unit, a power supply system, and antennas. For our tests, we used a pair of MALA Borehole 100 MHz Slimhole Antennas coupled to a MALA ProEx control unit. The antennas are powered downhole by batteries, and the data is conveyed to the control unit at the surface via fiber optics to avoid EM interference.

The data was collected in a tomographic manner between pairs of observation wells using a multiple offset gathers approach. To maintain a balance between the time required to conduct each survey and the ray coverage, we opted for a semi-reciprocal acquisition setup, Fig. 4. This approach yields higher resolution in the center and lower resolution close to the wellbore. It also yields higher ray coverage than a sparse setup and it is less time-consuming than a dense setup[16].

Prior to lowering the antennas, the traveltime through

Fig. 4 *A schematic of the three different acquisition setups. Sparse (left) results in ray coverage gaps close to the wellbore, semi-reciprocal (middle) improves ray coverage near to the wellbore, dense (right) results in the best ray coverage, but at increased data size and acquisition effort.*


air for a known distance was recorded, to be used as a time-zero correction. Next, the Tx was lowered 5 m below the surface and the Rx was moved from 5 m above the Tx, to 5 m below it, collecting waveforms every 0.1 m. It has been reported that when the angle between the Tx and Rx is large, the signal is received away from the antenna feed points, leading to errors in velocity estimates[26]. Consequently, we limited the acquisition to 5 m above and below the position of the Tx, which limits the angle to no more than 40°. Then, the Tx was lowered 1 m and the acquisition from 5 m above to 5 m below it every 0.1 m was repeated.

This process continued until the Tx reached a depth of 35 m. Next, both tools were brought to the surface and a second time-zero correction shot was acquired. We then exchanged the Tx and Rx boreholes and repeated the acquisition process previously described. This procedure was repeated for each pair of wells.

Experiments and Fluid Preparation

The experiments involved filling the shallow wells with a certain type of fluid and conducting XBGPR tomographic acquisitions using the near observation wells. Five different experiments were conducted based on the type of fluid filling the shallow boreholes. Table 2 summarizes the composition of each fluid, as well as the approximate EM properties. The well water was obtained from a well in the vicinity of the testing area. The AN-132 polymer was acquired from SNF; the xanthan gum had a technical grade purity level and was acquired from FuFeng; the magnetite was acquired from LKAB under the commercial name of MagnaChem10. All chemicals were used as received.

Mixing for fluids 3 to 5 was performed in a large tank with three rotating blades mounted at the top. The mixing procedure consisted of first filling the tank with water to 80% to 90% of the desired volume. Then, adding the magnetite (if applicable), followed by the polymer (xanthan or AN-132), while mixing. Next, mixing was stopped and the tank was topped up to the final volume. Finally, mixing was resumed and continued for one hour. During that time, the viscosity of the fluid was monitored. Approximately three batches had to be prepared for each experiment. Overall, the fluids looked homogeneous and the viscosity between different batches was comparable.
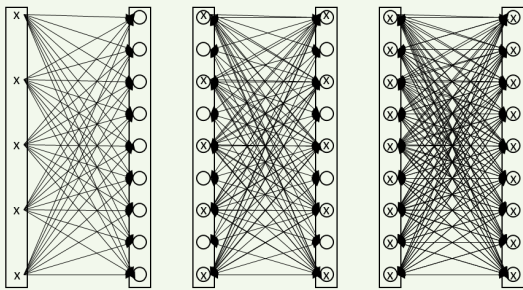
Table 2 *The fluids used to fill the shallow wells for each of the performed experiments.*

#	Name	Fluid	σ [S/m]	ε_r	μ_r
1	Air (baseline)	Air	~0	1	1
2	Water	Well water	0.5	80	1
3	AN-132	2.5 g/L of AN-132 dissolved in well water	0.7	> 80	1
4	Xanthan	5.0 g/L of xanthan dissolved in well water	0.8	> 80	1
5	Magnetite	7.5 g/L of xanthan and 100 g/L of magnetite dissolved in well water	1.0	> 80	> 1

Data Processing Workflow

Data processing and interpretation was done using bh_tomo[27], an open-source platform developed for GPR surveys. The raw data was subjected to the following preprocessing workflow:

1. Filtering: A band pass filter was used to remove noise from the data. The low and high cut frequencies used are 10 MHz and 250 MHz, respectively.

2. Pruning: Stations shallower than 5 m below the surface were removed, to avoid refracted waves propagating through the air. In addition, waveforms with a signal-to-noise ratio (SNR) below 1 were pruned. This process generally removed 30% to 50% of the data.

After filtering and pruning, the data was processed to pick the traveltime and peak-to-peak amplitude for each trace.

Traveltime Analysis

Traveltime picking was done using the semi-automatic traveltime picking module of bh_tomo. This approach entails picking the first break of a series of waveforms that are used to automatically pick the first break of the remaining data using cross correlation. Next, the manual traveltime picking module was used to quickly browse through the picked times and correct obvious mistakes. Most of the errors were due to low SNR. Once the data were picked, we proceeded to compare the traveltimes for different fluids.

Traveltime Difference

The traveltime difference was estimated by comparing the picked traveltime for a given Tx-Rx position for different fluids. This information was used as a first approximation to evaluate if the fluids were having an impact on the signal's traveltime. This may be the best way to see small changes, because traveltime inversion involves smoothing, which could mask small changes in slowness.

Figure 5 shows the traveltime difference between water and air for well pairs O7 and O12. Most of the differences are positive, meaning that the traveltime is longer when the wells are filled with water than when they are filled with air. It should be noted that the traveltime difference

is generally small (< 4 ns). Similar results were obtained when comparing AN-132 and magnetite with air (data not shown).

Traveltime Inversion

The next step involved inverting the traveltime data to obtain a map of slowness. Multiple grid element sizes for the inversion models were tested. The best results were obtained using elements of 0.25 m by 0.25 m, where the bh_tomo offers two different algorithms to perform the inversion, geostatistics and LSQR. For the work presented here, only the latter was used. Table 3 summarizes the parameters used to perform the inversion. In the absence of other constraints, the smoothing weight in x and z were modified until a minimum in the variance of the residuals (σ^2) was obtained, Fig. 6. The inversion generates a map of subsurface velocity between two wells, Fig. 7.

In addition to the regular inversion, bh_tomo has two options that allow for time-lapse evaluation of the data. The first one is simultaneous inversion, in which two data sets are inverted simultaneously while trying to be

Table 3 *The parameters used to perform the traveltime inversion using the LSQR algorithm.*

Parameter	Value
Number of straight rays' iterations	1
Number of curved rays' iterations	2
Solver tolerance	1e-6
Maximum number of solver iterations	100
Constraints weights	1
Smoothing weight x	10
Smoothing weight y	10
Smoothing weight in z	10
Smoothing operator order	2
Maximum model parameter variation per iteration	50%

Fig. 5 *The traveltime difference between water and air for Wells O7 and O12. Since most of the traveltime differences are positive, it can be concluded that overall water is slower than air.*
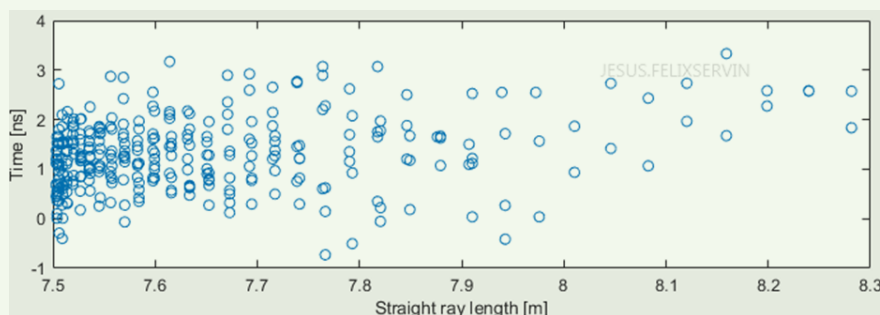
Fig. 6 *The norm of the residuals (top left), residuals histogram (bottom left), residuals as a function of angle with respect to the horizontal (top right) and residuals as a function of Tx and Rx depth (bottom right). The smoothing weights was changed until a minimum in the variance of the residuals was achieved.*
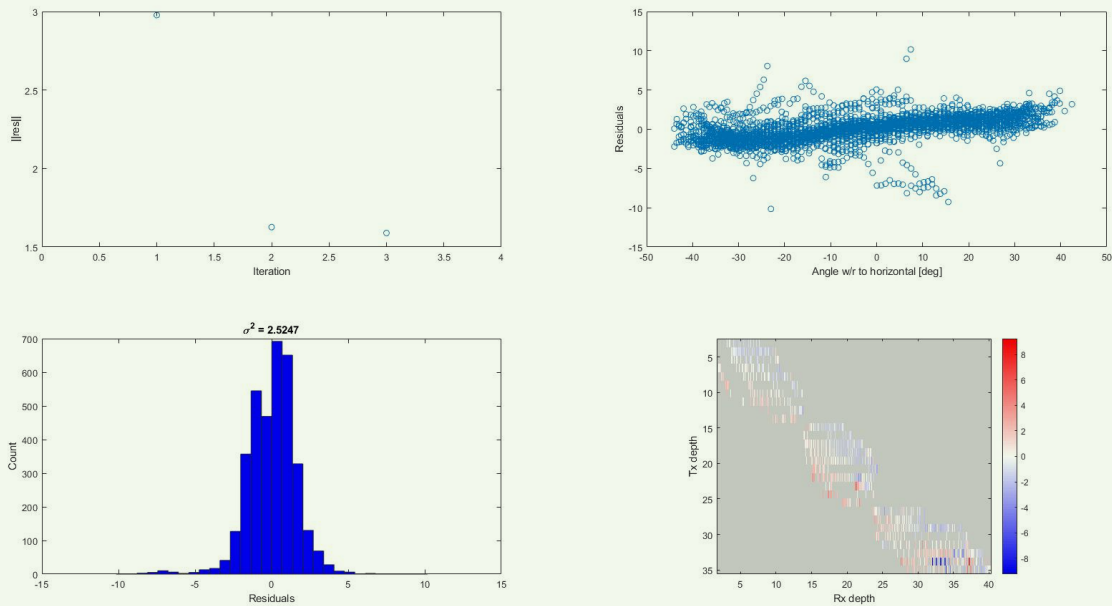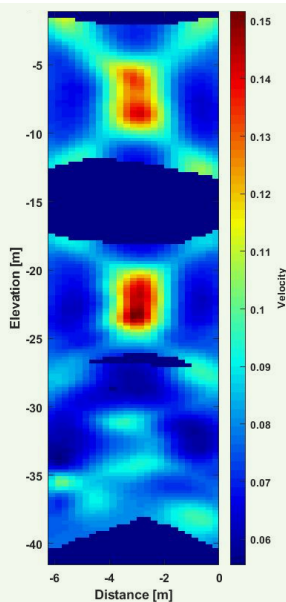

Fig. 7 *The velocity map obtained for the two well panels (O12-O11 and O11-O12) inverted together with air-filled shallow wells. The fast regions are present in the center of the map, corresponding to the location of the shallow wells.*

on inverting the change in traveltime difference rather than the traveltime itself. Both approaches were tested but simultaneous inversion did not generate satisfactory results. We speculate that the differences were too small and were masked by this approach. The second approach is better suited for small changes in traveltime. Subsequently, one limitation is that it assumes the ray paths are the same for both data sets. This assumption is reasonable if the difference in traveltime is small; however, it may not be suitable in situations where the difference in traveltime is large or if the soil conditions significantly changed from one survey to the other. The result of the inversion is a map of percentage change in slowness, Fig. 8. Regions where the change is positive represent portions of the reservoir that became slower in the second survey.

Amplitude Analysis and Inversion

Peak-to-peak amplitude picking was performed using the automatic function provided by bh_tomo. Next, the traces were inspected manually to correct obvious mistakes. Amplitude inversion was done using the LSQR algorithm to obtain maps of attenuation. The fitting parameters are the same used for the traveltime inversion, Table 3, and were optimized to minimize the variance of the residuals. The inversion generates a map of attenuation between two wells, Fig. 9.

Results and Discussion

A subset of six panels corresponding to well pairs O8-O9, O12-O7, and O12-O11 were used to evaluate the results. We begin by investigating the data quality and ray coverage. The data shows low ray coverage in some regions and a complete lack of data for certain intervals,

as close as possible to a reference tomogram; for example, air and water, with air as the reference. In this case, the simultaneous inversion would highlight the differences caused by the water. The second approach consists

Fig. 8 *A map of change in slowness, as a percentage, obtained for Wells O8-O9 and O9-O8 traveltime values of water minus air and using the inversion of air as the reference. Increases in slowness are shown in the central region, where the wells are located. This means that water is causing those regions to become slower than when the wells were empty.*
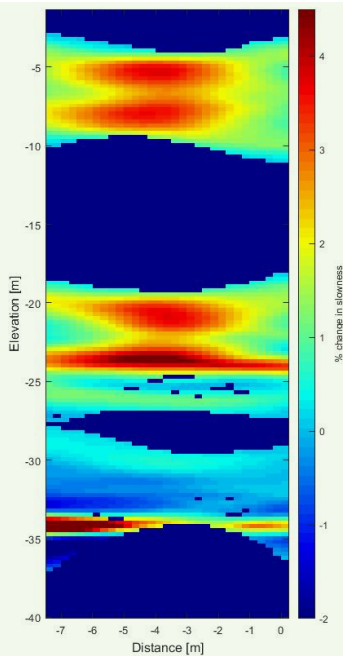

Fig. 9 *An attenuation map obtained for well panels O8-O9 and O9-O8 inverted together with magnetite filled shallow wells. High attenuation regions are present in the center of the map, corresponding to the location of the shallow wells.*
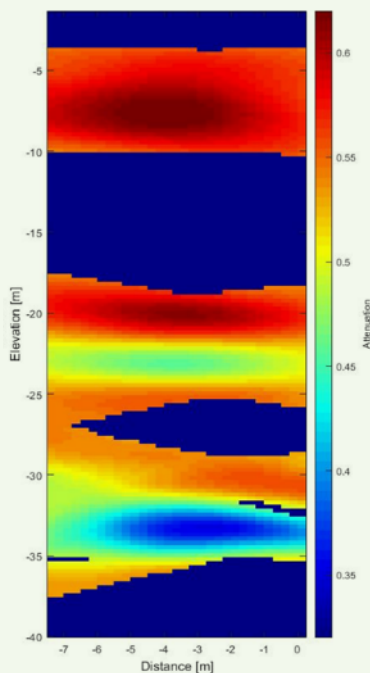

Fig. 10. Based on the resistivity logs of DO1 and DO2, it appears that for values below 50 Ωm, the signal falls below the limit of detection before reaching the Rx. We speculate that these intervals correspond to layers of clay, which are known to result in high attenuation for GPR signals[11]. Based on the ray coverage, we conclude that large variations in resistivity are present within the array. For example, for well pair O12-O7 there is no ray coverage below 25 m, while there is significant coverage for the other two well pairs, especially O12-O11. This suggests that some of the layers may not be continuous across the entire array. Because of the lack of data, the results obtained from regions with low ray coverage will have higher uncertainty.

The traveltime difference data suggests that filling the wells with liquids results in increased traveltime. Figure 11 shows the traveltime difference between water and air (top) and magnetite and water (bottom) for the panels obtained from Wells O7 and O12. Most of the traveltime differences for the first case are positive, meaning that filling the shallow wells with water increases the signal's traveltime.

A similar trend is observed when the wells are filled with fluids 3 to 5. This trend was expected because all liquids have higher ε and/or μ than water, but it must be noted that the traveltime is shorter than anticipated. This may be an indication of the wave going around the wells and partially avoiding the slow fluids, especially because the operating wavelength is comparable to the well spacing. Another factor that may contribute to this discrepancy is that the actual location of the wells is different from the original design due to inaccuracy while drilling.

Consequently, in some cases, only a small portion of a fluid filled well is between the observation wells, rather than the entire well. When we compare magnetite and water, we observe that most of the traveltime differences are negative. This suggests that magnetite reduces the signal travel as compared to just water. A similar trend is observed when fluids 3 and 4 are compared with water. This trend was not expected because the product of ε and μ for fluids 3 to 5 should be higher than for water. Therefore, an increase on signal traveltime for these fluids over water was expected.

The inversion of the traveltime difference shows similar results: an increase in slowness when the shallow wells are filled with liquids, Fig. 12, water showing the greatest increase, followed by AN-132, xanthan, and finally magnetite. Based on the estimated EM properties of the fluids, Table 2, we expected water to result in the shortest traveltime and magnetite in the longest; however, the data shows the opposite.

The attenuation data shows a clear difference between air filled and liquid filled shallow wells, but similar attenuation among the different liquids, with AN-132 showing the lowest attenuation, followed by xanthan, and then water and magnetite, Fig. 13. As expected, filling the wells with conductive liquids increases the signal attenuation.

To understand the potential reasons for the discrepancies observed in the traveltime data, 3D numerical

Fig. 10 *From left to right, the resistivity log for DO2, ray coverage for well panel O9-O8, ray coverage for well panel O12-O7, ray coverage for well panel O12-O11, and the resistivity log for well panel DO1. The intervals of low or null ray coverage seem to correlate with regions where the resistivity is below 50 Ωm.*
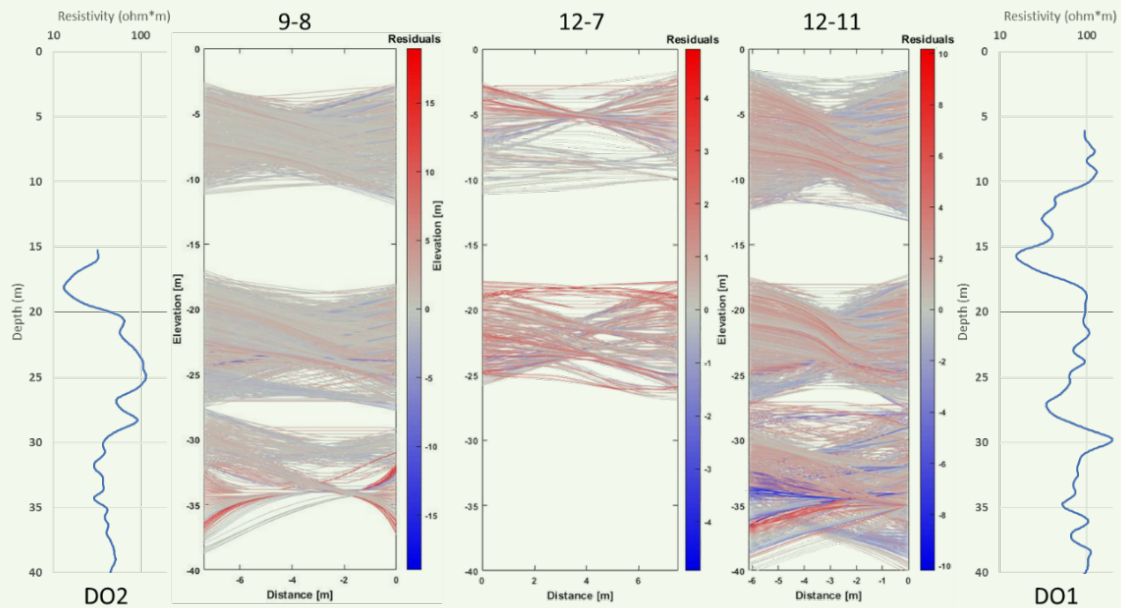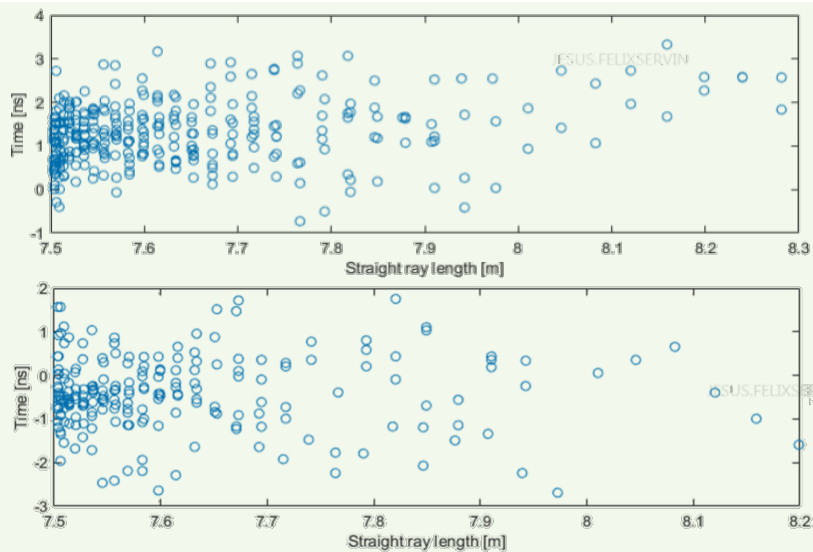

Fig. 11 *The traveltime difference between water and air (top), and magnetite and water (bottom) for Wells O7 and O12.*

simulations that employed parameters similar to those encountered in the field were conducted using a commercially available finite element package. The numerical model was developed using a strategy similar to the one presented by Felix Servin et al. (2019)[28]. The simulation results confirm our experimental results: water appears to be the slowest fluid, followed by xanthan and then magnetite, Fig. 14.

This trend was not anticipated based on the EM

properties of the fluids. We speculate that a likely explanation for such unexpected behavior is that the array is acting as a periodic structure imposing constraints on the propagation mode of the wave, leading to nonmonotonic relationships between the phase speed and the EM properties. Overall, the simulations agree with the experimental results; not only showing that the liquids are slower than air, but also displaying the right trend for the traveltime: water being the slowest, followed by

Fig. 12 *Maps of change in slowness. From left to right, water minus air, AN-132 minus air, xanthan minus air, and magnetite minus air. From top to bottom, well panel 8-9, well panel 12-7, and well panel 12-11.*
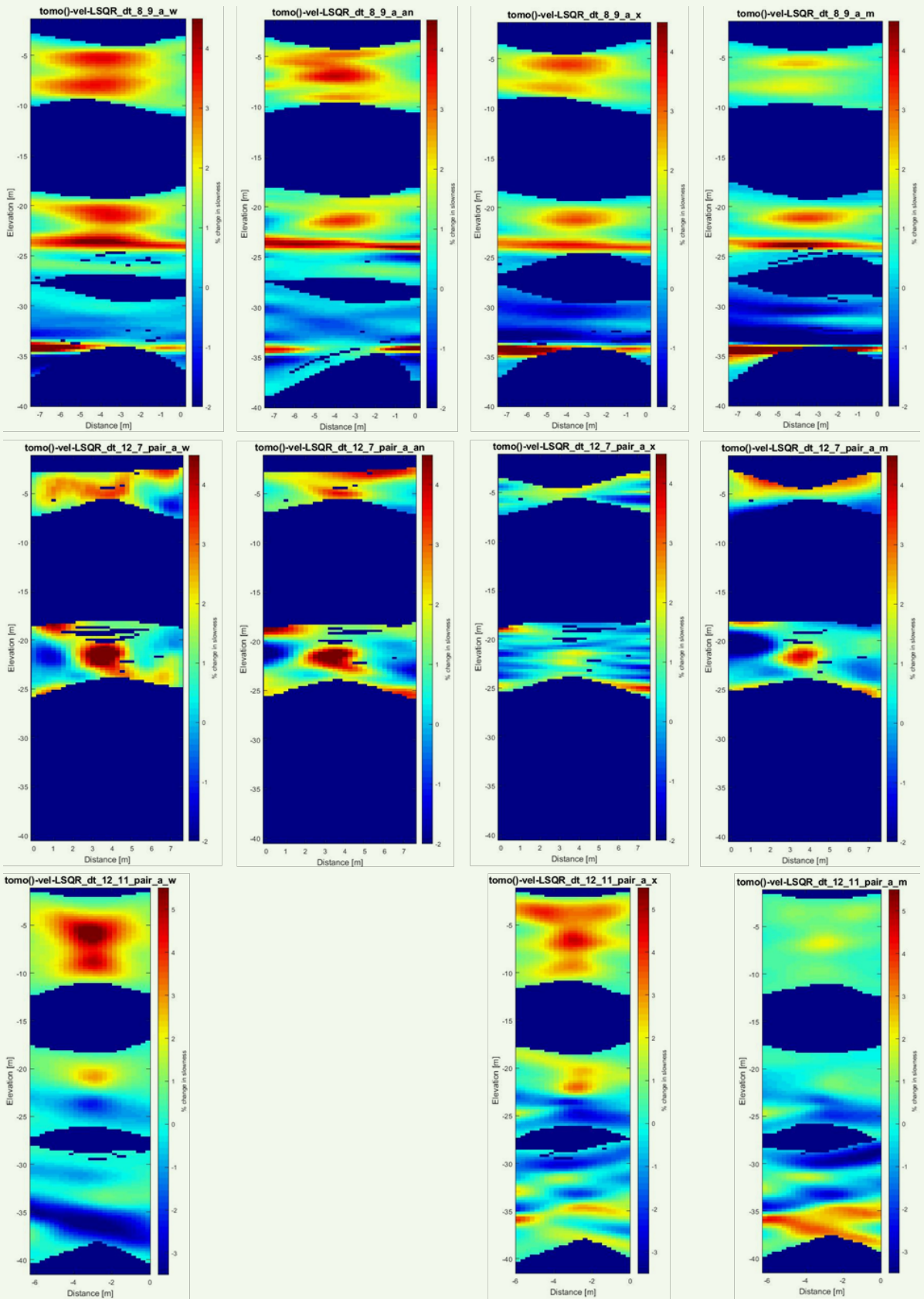
Fig. 13 *From left to right, maps of attenuation for well pair O8-O9 when filled with air, water, AN-132, xanthan, and magnetite, respectively.*
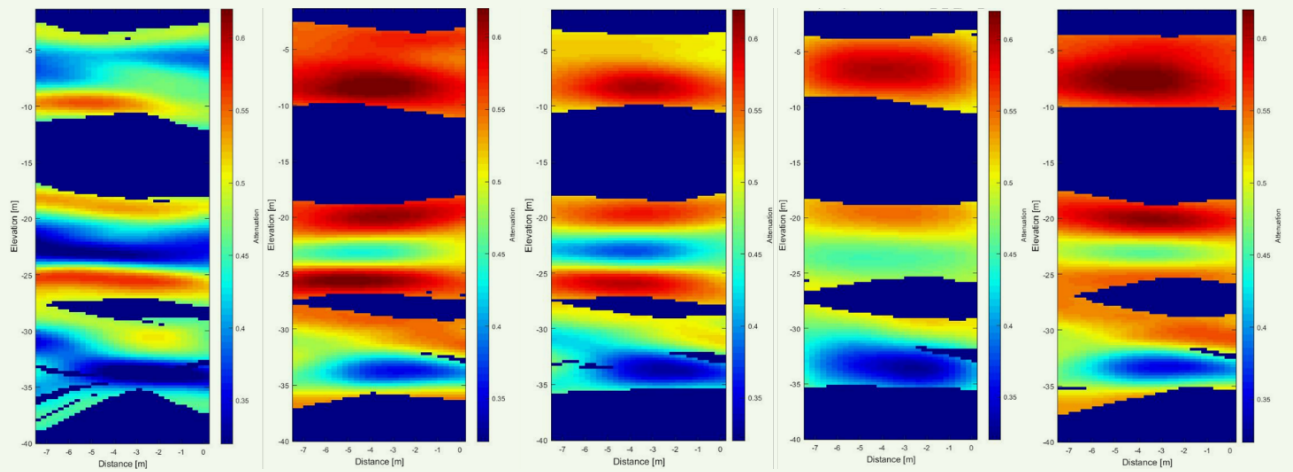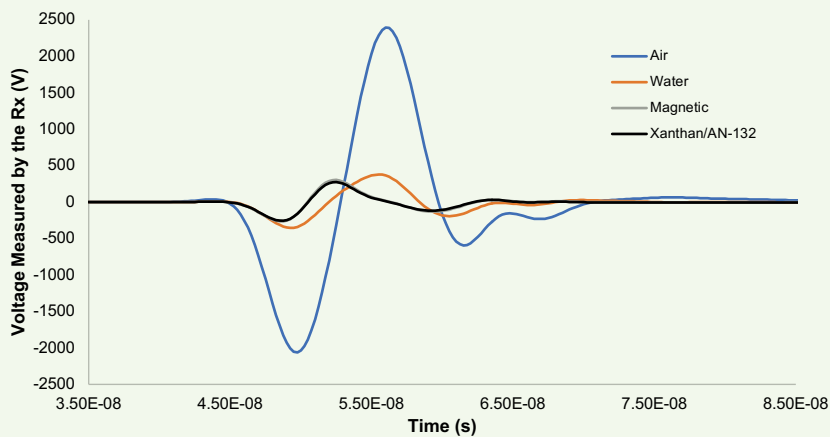

Fig. 14 *The simulated received waveforms for different fluids for a 100 MHz signal.*

AN-132, xanthan, and then magnetite. Based on the simulations, the difference in traveltime between water, AN-132, and xanthan is likely due to the difference in σ. Moreover, the difference in traveltime is observed not on the first arrival, but on the second peak of the signals.

The implications are that the inversion algorithm may have to be modified to account for this. It is also shown that increasing σ reduces traveltime, e.g., water vs. xanthan. This confirms our hypothesis that fluids that are more conductive will prevent the signal from penetrating deep into the wellbore, and therefore will diminish the effect of the fluids on the signal's traveltime.

The simulations also show that while water should result in reduced attenuation, the rest of the liquids should have similar amplitude. The field results show water resulting in attenuation comparable to the other fluids. This could be a consequence of slight changes in the saturation of the matrix due to rain in the days leading

to some of the experiments; however, the results are in overall agreement with the simulations.

Conclusions

The results of these tests prove that XBGPR surveys can be used to locate relatively small targets of fluids via time-lapse tomographic surveys, even with no previous geological information. We were able to demonstrate the effect of μ and/or σ on the signal traveltime and amplitude. Consequently, the traveltime effect is smaller and the trend is different from what was originally anticipated, most likely due to the periodic structure of the array and the difference in σ of the fluids. The observed trends concur with the 3D numerical simulations, highlighting the importance of conducting simulations before and after future tests.

An analysis of the traveltime data enables differentiating between air and liquid targets, and to a lesser degree one

liquid from another. Subsequently, the behavior is not what was expected prior to conducting the experiments. Based on the experimental and simulations results, we conclude that the electrical conductivity of the fluids has a significant effect on traveltime. For a given fluid, increasing the conductivity will reduce the traveltime. Looking at the attenuation data, we conclude that increasing conductivity will also reduce signal amplitude.

Because of the difference in conductivity between the different fluids, it was not possible to quantify how much effect μ had on signal traveltime. Future tests should be designed such that all fluids have as much as possible the same conductivity. Due to the design of the testing platform, sharp changes in EM properties are expected between the rock and the wells. Consequently, inversion involves smoothing, and therefore, is not best suited for sharp changes. It may be worth exploring the possibility of using full waveform inversion. It must also be noted that in the reservoir, such sharp changes are not expected.

Moving forward, we recommend conducting similar experiments in reflection mode, since this setup appears to be more suitable for oil and gas applications, given the rather limited penetration obtained in transmission mode.

Acknowledgments

References

1. Annan, A.P.: "GPR — History, Trends, and Future Developments," *Subsurface Sensing Technologies and Applications*, Vol. 3, October 2002, pp. 253-270.

2. Annan, A.P.: "Ground-Penetrating Radar," Chapter 11 in *Investigations in Geophysics*, Butler, D.K. (ed.), Society of Exploration Geophysicists, 2005, 758 p.

3. Sun, B., Siegert, M.J., Mudd, S.M., Sugden, D., et al.: "The Gamburtsev Mountains and the Origin and Early Evolution of the Antarctic Ice Sheet," *Nature*, Vol. 459, June 2009, pp. 690-693.

4. Lamsters, K., Karušs, J., Rečs, A. and Bērziņš, D.: "Detailed Subglacial Topography and Drumlins at the Marginal Zone of Mulajokull Outlet Glacier, Central Iceland: Evidence from Low Frequency GPR Data," *Polar Science*, Vol. 10, December 2016, pp. 470-475.

5. Klotzsche, A., van der Kruk, J., Meles, G.A., Doetsch, J.A., et al.: "Full Waveform Inversion of Crosshole Ground Penetrating Radar Data to Characterize a Gravel Aquifer Close to the River Thur, Switzerland," *Near Surface Geophysics*, Vol. 8, Issue 6, June 2010, pp. 635-649.

6. Prego Martinez, F.J., Solla, M., Puente, I. and Arias, P.: "Efficient GPR Data Acquisition to Detect Underground Pipes," *NDT & E International*, Vol. 91, June 2017, pp. 22-31.

7. Šarlah, N., Podobnikar, T., Ambrožič, T. and Mušič, B.: "Application of Kinematic GPR-TPS Model with High 3D Georeference Accuracy for Underground Utility Infrastructure Mapping: A Case Study from Urban Sites in Celje, Slovenia," *Remote Sensing*, Vol. 12, Issue 8, April 2020.

8. Cook, J.C.: "Radar Exploration Through Rock in Advance of Mining," *Transactions of the Society Mining Engineers*, Vol. 254, 1976, pp. 140-146.

9. Fullagar, P.K., Livelybrooks, D.W., Zhang, P., Calvert, A.J., et al.: "Radio Tomography and Borehole Radar Delineation of the McConnell Nickel Sulfide Deposit, Sudbury, Ontario, Canada," *Geophysics*, Vol. 65, Issue 6, November 2000, pp. 1920-1930.

10. Rodeick, C.A.: "Roadbed Void Detection by Ground Penetrating Radar," *Highway & Heavy Construction*, Vol. 127, 1984, pp. 60-61.

11. Slob, E., Sato, M. and Olhoeft, G.: "Surface and Borehole Ground Penetrating Radar Developments," *Geophysics*, Vol. 75, Issue 5, September 2010, pp. 75A103-75A120.

12. Klotzsche, A., van der Kruk, J., Vereecken, H., Meles, G.A., et al.: "High Resolution Imaging of the Unsaturated and Saturated Zones of a Gravel Aquifer Using Full Waveform Inversion," paper presented at the 6th International Workshop on Advanced Ground Penetrating Radar, Aachen, Germany, June 22-24, 2011.

13. Klotzsche, A., van der Kruk, J., Meles, G.A. and Vereecken, H.: "Crosshole GPR Full Waveform Inversion of Waveguides Acting as Preferential Flow Paths within Aquifer Systems," *Geophysics*, Vol. 77, Issue 4, July 2012, pp. H57-H62.

14. Klotzsche, A., van der Kruk, J., Linde, N., Doetsch, J., et al.: "3-D Characterization of High Permeability Zones in a Gravel Aquifer Using 2-D Crosshole GPR Full Waveform Inversion and Waveguide Detection," *Geophysical Journal International*, Vol. 195, Issue 2, November 2013, pp. 932-944.

15. Yang, X., Klotzsche, A., van der Kruk, J., Vereecken, H., et al.: "Full-Waveform Inversion of Cross-Hole GPR Data Measured at the Boise Gravel Aquifer," paper presented at the 6th International Workshop on Advanced Ground Penetrating Radar, Aachen, Germany, June 22-24, 2011.

16. Klotzsche, A.: "Full-Waveform Inversion of Crosshole GPR Data for Hydrogeological Applications," Forschungszentrum Jülich, Zentralbibliothek, 2013.

17. Tronicke, J. and Hamann, G.: "Vertical Radar Profiling: Combined Analysis of Traveltimes, Amplitudes, and Reflections," *Geophysics,* Vol. 79, Issue 4, July 2014, pp. H23-H35.

18. Zhou, H., and Sato, M.: "Subsurface Cavity Imaging by Crosshole Borehole Radar Measurements," *IEEE Transactions on Geoscience and Remote Sensing*, Vol. 42, Issue 2, February 2004, pp. 335-341.

19. Jang, H., Kuroda, S. and Kim, H.J.: "Efficient Electromagnetic Imaging of an Artificial Infiltration Process in the Vadose Zone Using Cross-Borehole Radar," *IEEE Geoscience and Remote Sensing Letters*, Vol. 8, March 2011, pp. 243-247.

20. Zhou, F.: "Novel Applications of Ground Penetrating Radar in Oil Fields," Ph.D. thesis, Delft University of Technology, 2020.

21. Heigl, W.M. and Peeters, M.: "Can We Obtain Invasion Depth with Directional Borehole Radar?" *Petrophysics*, Vol. 46, Issue 1, January 2005, pp. 52-61.

22. Miorali, M., Slob, E. and Arts, R.: "A Feasibility Study of Borehole Radar as a Permanent Downhole Sensor," *Geophysical Prospecting*, Vol. 59, Issue 1, January 2011, pp. 120-131.

23. Miorali, M., Zhou, F., Slob, E. and Arts, R.: "Coupling Ground Penetrating Radar and Fluid Flow Modeling for Oil Field Monitoring Applications," *Geophysics*, Vol. 76, Issue 3, May 2011, pp. A21-A25.

24. Oloumi, D., Pettersson, M.I., Mousavi, P. and Rambabu, K.: "Imaging of Oil Well Perforations Using UWB Synthetic Aperture Radar," *IEEE Transactions on Geoscience and Remote Sensing*, Vol. 53, Issue 8, February 2015, pp. 4510-4520.

25. Chen, Y-H. and Oristaglio, M.L.: "A Modeling Study of Borehole Radar for Oil Field Applications," *Geophysics*, Vol. 67, Issue 5, September 2002, pp. 1486-1494.

26. Irving, J.D. and Knight, R.J.: "Effect of Antennas on Velocity Estimates Obtained from Crosshole GPR Data," *Geophysics*, Vol. 70, Issue 5, September 2005, pp. K39-K42.

27. Giroux, B., Gloaguen, E. and Chouteau, M.: "bh_tomo — a Matlab Borehole Georadar 2D Tomography Package," *Computers & Geosciences*, Vol. 33, Issue 1, January 2007, pp. 126-137.

28. Felix Servin, J.M., Deffenbaugh, M., Adams, R. and Riachentsev, V.: "Can we Propagate MHz EM Signals for 1 km through the Subsurface in the Presence of Conductive Media?" *SEG Technical Program Expanded Abstracts 2019,* pp. 1164-1168.

About the Authors

Jesus M. Felix Servin

M.S. in Chemical and Biological Engineering, King Abdullah University of Science and Technology

Jesus M. Felix Servin joined the Reservoir Engineering Technology Division of Saudi Aramco's Exploration and Petroleum Engineering Center – Advanced Research Center (EXPEC ARC) in February 2012. His focus is on the development of electromagnetic methods and nanoparticle-based contrast agents for reservoir characterization and monitoring. Jesus's role has been instrumental in the development and deployment of the Magnetic Nano-Mappers project, including hardware design and in-house fabrication, instrumentation, computer programming, and data processing.

Jesus' interests include the development of nanoscale strategies for reservoir illumination and electromagnetic methods for reservoir description and monitoring.

He received his B.S. degree in Engineering Physics from Instituto Tecnologico y de Estudios Superiores de Monterrey, Monterrey, Mexico, and an M.S. degree in Chemical and Biological Engineering from King Abdullah University of Science and Technology, Thuwal, Saudi Arabia.

Hussain A. Shateeb

A.S. in Industrial Chemistry Technology, Jubail Industrial College

Hussain A. Shateeb joined Saudi Aramco as an Apprentice Technician in the Vocational College Graduates (VCGNE) Training Program in August 2014. Upon attaining his degree in 2016, he then then joined the Reservoir Engineering Technology Division of Saudi Aramco's Exploration and Petroleum Engineering Center – Advanced Research Center (EXPEC ARC), where he works as a Lab Technician.

Hussain received his A.S. degree in Industrial Chemistry Technology from Jubail Industrial College, Jubail, Saudi Arabia.